Exploring the physics of the Earth's core with numerical simulations

Nathanaël Schaeffer

Habilitation à Diriger des Recherches

Université Grenoble Alpes

Exploring the physics of the Earth's core with numerical simulations

Nathanaël Schaeffer

soutenue le 30 septembre 2015, devant le jury composé de :

Emmanuel DORMY	École Normale Supérieure (Paris)	Rapporteur
Bérengère DUBRULLE	Centre d'Études Atomiques (Saclay)	Rapporteur
Johannes WICHT	Max Planck Institute (Göttingen)	Rapporteur
Thierry ALBOUSSIÈRE	Université Claude Bernard (Lyon)	Examinateur
Franck PLUNIAN	Université Grenoble Alpes (Grenoble)	Examinateur

Abstract

In the first chapter of this report, I discuss some of my work of the past 7 years, since I joined the geodynamo team at ISTerre as a CNRS researcher. This work most often involves numerical simulations with codes that I have written.

An important step forward in the efficiency of simulations based on the spherical harmonic transform has come from the matrix-free SHTns library I have designed and written (Schaeffer, 2013).

Numerical simulations linked to the magnetized spherical Couette experiment DTS have been performed to understand its peculiar turbulence (Figueroa et al., 2013) and try to characterize the effect of the small turbulent scales on the induction processes (Cabanes, Schaeffer, and Nataf, 2014a; Cabanes, Schaeffer, and Nataf, 2014b).

Related to the Earth's core dynamics, my simulations helped to characterize the effects of the magnetic field on short timescale flows, leading to strong arguments for quasi-geostrophic (columnar) flows at large spatial scales ($\gtrsim 10$ km) and short timescales ($\lesssim 10$ years) in the core (Gillet, Schaeffer, and Jault, 2011). Smaller length scales evade the rotational constraint because inertial waves are getting too slow. At longer length scales more research is needed, but we have already explored the implications of a deformation of the columns by magnetic fields (Schaeffer, Lora Silva, and Pais, 2016). We have also shown that near the equator, where the columnar flows were expected to wither, the quasi-geostrophy seems strong in the Earth's core (Schaeffer and Pais, 2011).

Prompted by observations, we studied the propagation and reflection of torsional Alfvén waves in the core, and showed the importance of the value of the magnetic Prandtl number (Schaeffer, Jault, et al., 2012). Moreover, an extension of this work to include a conducting solid layer at the top of the core suggests the existence of such a layer with a rather strong conductance in the Earth.

More recently, and as a logical follow-up, I have produced turbulent geodynamo simulations, with interesting implications that will be reported in a future publication, but several facts are already presented in appendix D and will also be discussed here. These simulations have also fed the reflection that resulted in our chapter on core turbulence in the second edition of the Treatise on Geophysics (Nataf and Schaeffer, 2015).

In the second chapter, I present synthetically my ongoing work and projects that develop even further the topics above, but also new projects on the dynamo of the early Moon and further numerical developments.

Contents

Chapter 1

Research summary of selected work

1.1 Introduction

1.1.1 Motivation

Describing and understanding the Deep Earth

The Earth deep interior is impossible to observe directly, but it is possible to probe it using several tools. The seismic waves traveling through our planet yield most of the information we have on its structure, through the travel speed and reflection at the interfaces of the compression and shear waves, but also through the frequency and attenuation of the seismic normal modes. The Earth's rotation variations, which respond to gravitational torques, depend not only on its moment of inertia (the mass distribution), but also whether there are fluid layers and the coupling between the fluid layers and the solid ones. A good example of the usefulness of these measurements is the success of the PREM model (Dziewonski and Anderson, 1981), which included data from seismology (both travel time and normal modes) as well as total mass and moment of inertia.

The magnetic field of our planet is produced by fluid motion in its core, and as such it gives away information about the flow in the core. This flow is arguably driven by convection due to the slow cooling of the Earth. It is also influenced by the magnetic field itself, but also by some details of its boundaries. It is also important to keep in mind that if the mantle near the core-mantle boundary is slightly conducting, there will be some electromagnetic coupling of the core and mantle, which may be important to understand Earth's rotation variations, such as nutation. During the evolution of

the Earth, its magnetic field has been recorded by rocks, sediments or even human artifacts for the latest part. These recording may also constrain the Earth's history.

Planetary magnetic fields

Regarding its magnetic field, the Earth is no exception. Indeed, most planets of the solar system exhibit magnetic fields, with various characteristics (see Jones, 2011, for a review). In the absence of seismic information, these magnetic fields and their dynamics give us important informations on their internal structure. Some peculiar features, such as the strong axisymmetry of Saturn's field are sometimes hard to explain, challenging our comprehension of the planetary magnetic field generation. Similarly, hints toward a strong dynamo on the early Moon currently escapes explanation (Weiss and Tikoo, 2014).

By extensive use of numerical simulations, Christensen and Aubert, 2006 proposed empirical scaling laws for the magnetic field strength of planets. Those numerical simulations were (as all planetary dynamo simulations) operating with parameters remote from the actual viscosities and magnetic diffusivities. The remarkable success of such simulations to reproduce the Earth's field (e.g. Aubert, Finlay, and Fournier, 2013) remains largely unexplained, and the validity of the obtained scaling laws has been questioned (e.g. Oruba and Dormy, 2014).

1.1.2 Governing equations

We consider the following equations that govern the magneto-hydrodynamics (MHD) of an incompressible fluid in a reference frame with angular rotation rate $\mathbf{\Omega_0}$. We use the Boussinesq approximation and treat the density ρ as constant, except in the buoyancy force that arise from small variations of ρ, written using a codensity c. For example if thermal convection is considered, we take $c = \alpha T$, with T the temperature and α the constant thermal expansion coefficient Note also that the magnetic field is measured in units of (Alfvén) velocity so that the magnetic field in Tesla is $\sqrt{\mu_0 \rho}\, b$, with μ_0 the magnetic permeability. The equations governing the evolution of the velocity

field $\mathbf{u}$, the magnetic field $\mathbf{b}$ and the codensity then read:

$$\partial_t \mathbf{u} + (2\mathbf{\Omega_0} + \nabla \times \mathbf{u}) \times \mathbf{u} = -\nabla p^* + \nu \Delta \mathbf{u} + (\nabla \times \mathbf{b}) \times \mathbf{b} + c\mathbf{g} \tag{1.1}$$

$$\partial_t \mathbf{b} = \nabla \times (\mathbf{u} \times \mathbf{b}) + \eta \Delta \mathbf{b} \tag{1.2}$$

$$\partial_t c + \mathbf{u}.\nabla(c + C_0) = \kappa \Delta c \tag{1.3}$$

$$\nabla \mathbf{u} = 0 \tag{1.4}$$

$$\nabla \mathbf{b} = 0 \tag{1.5}$$

The important fluid properties are its kinematic viscosity ν, its magnetic diffusivity $\eta = (\mu_0 \sigma)^{-1}$ (where σ is its conductivity), and the diffusivity of the codensity κ (the thermal diffusivity in the case of thermal convection). p^* is a dynamic pressure (including terms that can be written as a gradient, such as centrifugal force, hydrostatic gravity, ...) and C_0 is the imposed base codensity profile.

Several non-dimensional parameters derive from these equations, for a given length-scale L, typical velocity U and magnetic field B (in velocity units). The following non-dimensional numbers are also used to review some of the physics of planetary interiors.

1.1.3 Control Parameters

The four following parameters are control parameters as their values are required to solve the above equations; they control the physics. However, from a geophysical point of view, some are difficult to determine for the Earth's core, not te speak about other planets, because their values depend on the material properties of the fluid. Not all relevant material properties are well known (Olson, 2015).

The Ekman number

$$E = \frac{\nu}{\Omega L^2} \tag{1.6}$$

measures the ratio between viscous and Coriolis force. It is typically very tiny in planets ($E \sim 10^{-15}$ for the Earth's core). In rotating fluids, thin boundary layers develop where viscous and Coriolis forces balance. These Ekman layers have a thickness of $\sqrt{\nu/\Omega}$ which scales as $E^{1/2}$.

The Rayleigh number

$$Ra = \frac{g \Delta c L^3}{\nu \kappa} \tag{1.7}$$

compares the strength of the unstable stratification compared to damping by viscous and thermal effects. It can be seen as the ratio of thermal diffusion

time $\tau_\kappa = L^2/\kappa$ to the time it would take for a fluid parcel to travel a distance L at its terminal velocity $\tau_u = L/u$ with $u \sim L^2 g \Delta c/\nu$. Here Δc is a typical variation of c across the domain. For $Ra > Ra_c$, convection occurs. In the case of rapidly rotating convection ($E \ll 1$), Ra_c depends on the Ekman number as $Ra_c \sim E^{-4/3}$ (e.g. Busse, 1970; Dormy et al., 2004; Jones, 2015).

It is not so easy to estimate the Rayleigh number in the liquid core, because most of the temperature contrast between the top of the core and its base is due to compression via the equation of state (Olson, 2015). This part defines the adiabatic (or isentropic) temperature profile, and only the density variations in excess of it should be included in c. Since heat conducted along the adiabat is large, it is possible that the Rayleigh number is subcritical ($Ra < Ra_c$) in part of the core. However, as soon as the density profile departs from the adiabat, the Rayleigh number can be very large.

The magnetic Prandtl number

$$Pm = \frac{\nu}{\eta} \tag{1.8}$$

compares the kinematic viscosity to the magnetic diffusivity. For liquid metals it is always small: $Pm \sim 10^{-5}$.

The thermal Prandtl number

$$Pr = \frac{\nu}{\kappa} \tag{1.9}$$

compares the kinematic viscosity to the thermal diffusivity. For liquid metals in the lab we have $Pr \sim 0.1$. For the core, according to Olson (2015), it is less clear cut, with $Pr \lesssim 1$. Note that if one considers chemical convection (due to variable light element concentration), we have $Pr \gg 1$ which is now called the Schmidt number. Most numerical models of the geodynamo combine the effect of thermal and chemical convection into one codensity variable, with a single diffusivity. The choice of $Pr = 1$ then seems reasonable, especially when turbulent transport is invoked. However, the role of a truly double diffusive convection in the Core has gained some renewed interest (e.g. Breuer et al., 2010; Simitev, 2011; Net, Garcia, and Sánchez, 2012; Takahashi, 2014), maybe driven by the findings of Busse (2002).

1.1.4 Diagnostic Parameters

These parameter depend on typical values U, B of the velocity and magnetic fields. They are therefore not known *a priori*. Understanding of the

physics leading to relationships between control and diagnostic parameters, or even empirical laws relating them together are of broad interest to predict the behavior of magnetic fields and flows found on different natural objects. Christensen and Aubert (2006) proposed such scaling laws, based on numerical simulations. They have been successful at explaining planetary and maybe even stellar fields, but some concerns and criticism remain and alternative approaches have been proposed (e.g. Stelzer and Jackson, 2013; Davidson, 2013; Oruba and Dormy, 2014).

The magnetic Reynolds number

$$Rm = \frac{UL}{\eta} \tag{1.10}$$

compares at the largest scale the induction term $\nabla \times (u \times b)$ to the magnetic diffusion. This number is the key parameter for dynamo action, because only if $Rm > Rm_c$ can a magnetic field grow from an infinitesimal seed. The value of Rm_c depends on the details of the flow, but is found in the range 10 to 100 for most efficient flows. Note also that not all flows can generate magnetic fields, regardless of their Rm.

The kinetic Reynolds number

$$Re = \frac{UL}{\nu} \tag{1.11}$$

compares at the largest scale the advection term $u \times \nabla u$ to the viscous dissipation. It is a key parameter for characterizing turbulence. The huge values of Re found in geophysical systems imply a broad range of active flow scales. For planetary cores with a dynamo magnetic field, we must have $Rm \gtrsim 100$ to ensure dynamo action. Because in liquid metals $Pm \sim 10^{-5}$, it implies $Re \gtrsim 10^7$.

The Rossby number

$$Ro = \frac{U}{L\Omega} \tag{1.12}$$

measures the importance of the non-linear advection term over the Coriolis force. It is often small in geophysical contexts ($Ro \sim 10^{-6}$ for the large scale flow of the Earth). It is also the ratio of material speed to Inertial Wave speed, and as such is an analogue of the Mach number for inertial waves. Its low value means that the Coriolis force constrains the flow for a broad range of scales, possibly all scales, as it is argued by Nataf and

Schaeffer (2015, also reproduced in appendix B.7). Note that in laboratory experiments, rotating turbulence is mostly studied at moderate values of Rossby numbers ($Ro \sim 0.1$), possibly not so relevant for $Ro \ll 1$. In the absence of magnetic field, a low Rossby number implies anisotropic flows with elongated structures aligned with the rotation axis. This is reminiscent of the **Taylor-Proudman theorem**: $\mathbf{\Omega_0}.\nabla u = 0$ for an inviscid stationary flow at $Ro = 0$, with forces deriving from a potential only.

The Lehnert number

$$Le = \frac{B}{L\Omega} \tag{1.13}$$

measures the ratio of Alfvén speed to Inertial Wave speed. When small, as in the core where $Le \sim 10^{-3}$, the effect of the Coriolis force is felt well before that of the magnetic field. This leads to short time-scales unaffected by the Lorentz-Laplace force (Jault, 2008; Gillet, Schaeffer, and Jault, 2011).

The Lundquist number

$$S = \frac{2BL}{\eta + \nu} \tag{1.14}$$

compares the Alfvén wave speed B to their damping time. Alfvén waves can be observed only for $S \gg 1$ (Alfvén, 1942). In the Earth's core $S \sim 10^5$, but due to the small Lehnert number Le, Alfvén waves are only manifest in the form of Torsional Waves which are geostrophic motions (Braginsky, 1970; Jault and Légaut, 2005; Roberts and Aurnou, 2011; Jault and Finlay, 2015).

The Elsasser number

$$\Lambda = \frac{B^2}{\eta\Omega} \tag{1.15}$$

compares the Lorentz-Laplace force to the Coriolis force assuming a quasi-static equilibrium and uncorrelated u and b. These assumptions are valid for systems with an imposed magnetic field at low Rm and low S. In the geophysical context it is also an important number but it does not give the real Lorentz-Laplace to Coriolis force. Soderlund, King, and Aurnou (2012) introduce an improved measure and argue that almost all numerical simulations are only weakly influenced by the magnetic field. This contrasts with Jones (2011) who shows a strong effect of the magnetic field on the flow in simulations. In section 2.1.1, we will try to shed some light on this issue.

The Hartmann number

$$Ha = \frac{BL}{\sqrt{\eta\nu}} \tag{1.16}$$

is the square-root of the ratio of the Lorentz force to the viscous force. The thickness of the Hartmann boundary layer (where viscous stress balance electromagnetic stress) is proportional to its inverse. When $Pm \ll 1$, we have $S \simeq Ha\sqrt{Pm}$.

The Alfvén number

$$A = \frac{U}{B} \tag{1.17}$$

compares material velocities to Alfvén wave speed. It is also the square-root of the ratio between kinetic and magnetic energies. In the Earth's core, we have $A \sim 0.01$ so that we are far from the equipartition between kinetic and magnetic energies which is often found in non-rotating dynamos at moderate Pm.

1.1.5 Open questions

Here we list some open questions on how planetary dynamos operate.

- How does the magnetic field affect the flow at various time and length scales? Can we build a reduced model?
- Do the small turbulent scales participate in the dynamo process?
- How relevant are the current numerical geodynamo simulations for planetary cores? What are the implications for the sclaing laws?
- Are there other ways to produce magnetic field in planetary cores, that do not rely on convection (e.g. precession driven dynamos)?
- Is there a stably stratified layer at the top of the core? How does it affect the dynamics?
- Is there an important effect of realistic double-diffusion convection in planetary cores?

Some contributions relevant to these questions are presented in the rest of this document.

1.2 Numerical simulations in spherical geometry

Numerical simulations of planetary interiors is a widely used tool to understand their complex dynamics. At first order, planetary interiors have a spherical shape and this simple geometry is suitable for spectral methods. Indeed, spherical harmonic expansions are convenient to describe a band-limited function $f(\theta, \phi)$ on a sphere using a discrete set of complex coefficient f_ℓ^m:

$$f(\theta, \phi) = \sum_{\ell=0}^{L} \sum_{m=-\ell}^{\ell} f_\ell^m Y_\ell^m(\theta, \phi), \tag{1.18}$$

where $Y_\ell^m(\theta, \phi)$ are the spherical harmonics; ℓ and m are the harmonic degree and order respectively. Moreover, since Y_l^m are eigenfunctions of the Laplace operator on the sphere, the three-dimensional Laplace operator reads

$$\Delta f = \frac{1}{r}\partial_{rr}(rf) - \frac{1}{r^2}\ell(\ell+1)f. \tag{1.19}$$

A variety of Magneto-hydrodynamic (MHD) simulation codes in sphere take advantage of the spherical harmonic decompositions, and they have been benchmarked in several studies (Christensen, Aubert, Cardin, et al., 2001; Marti et al., 2014; Matsui and Heien, 2014). These pseudo-spectral methods transform, at each time-step, the fields back and forth between the spectral domain where the fields really live and evolve and the spatial domain where the non-linear terms can be conveniently evaluated. Details are given by Christensen and Wicht (2015).

Large resolutions are needed not only for non-linear turbulent cases, but also for linear studies where thin vortices or internal shear layers develop at small viscosity.

The viability of spectral methods in the era of massively parallel computing has been questioned in the past. However, as a matter of fact, cartesian spectral simulations of turbulence (using Fourier transform in the three dimensions) are still running with success on world's largest computers. In the unbounded, periodic cube, the fast Fourier transform (FFT) allows to perform the spectral to spatial transforms reasonably quickly, with a number of operation scaling as $N^d \log(N)$, where N is the number of spectral modes in one dimension and d the dimension of the problem. However, in spherical geometry, the existing codes do not use fast spherical transforms, and the number of operation scales as N^3 for the spherical harmonic transform part, instead of $N^2 \log(N)$ if it would be as efficient as the FFT.

1.2.1 Is it possible to improve the SHT?

Several authors have proposed algorithms for Fast Spherical Harmonic transforms (Driscoll and Healy, 1994; Potts, Steidl, and Tasche, 1998; Mohlenkamp, 1999; Suda and Takami, 2002; Healy Jr, Kostelec, and Rockmore, 2004; Tygert, 2008). However, they are complicated or unstable and cannot be used in practice. This was already the conclusion of Lesur and Gubbins (1999). Since the FFT can already be used in the longitudinal direction, the problem lies in finding a fast Legendre transform. We remind that

$$Y_\ell^m(\theta,\phi) = P_\ell^m(\cos\theta)e^{im\phi} \tag{1.20}$$

with

$$P_\ell^m(x) = \begin{cases} p_\ell^m(x), & \text{for even } m \\ \sqrt{1-x^2}\, p_\ell^m(x), & \text{for odd } m \end{cases} \tag{1.21}$$

and $p_\ell^m(x)$ is a polynomial.

Evaluating $p_\ell^m(\cos\theta)$ can be done using the Discrete Cosine Transform (DCT), leading to the semi-naive approach of Healy et al. (2003). In order to improve the DCT-based transform, I introduced the use of a Clenshaw-Curtis quadrature (Clenshaw and Curtis, 1960) for the forward transform, which reduces by a factor of two the number of collocation grid points compared to the usual sampling theorem. The Clenshaw-Curtis quadrature needs $N_\theta > L_{max}+1$, almost the same requirements as the Gauss-Legendre quadrature. However, when transforming quadratic products, dealiasing constraints lead to $N_\theta > 2L_{max}+1$, instead of $N_\theta > 3L_{max}/2$ for the Gauss-Legendre quadrature.

Furthermore, for large m, the so-called polar optimization (see e.g. Schaeffer, 2013, also reproduced in appendix B.4) leads to improved efficiency for large order m, because $P_\ell^m(x)$ is vanishingly small for $|x| > x_c(m)$, with x_c decreasing when m increases. Thus all the values for $|x| > x_c$ can be treated as zero.

As a result, the DCT accelerated transform is efficient for low m and quasi-linear computations where dealiasing is not required. Besides being advantageous only at $m \ll L$, these DCT transforms have another drawback: they need a lot of costly precomputations and storage. This limits their practical interest. Furthermore, using the vector capabilities of modern computers (which means they can apply the same operation on several numbers packed together), the DCT loses its advantage completely.

I implemented the Legendre transform using the Gauss quadrature. Instead of storing the coefficients needed to transform from spectral to spatial

space, I recompute them when needed, on the fly using the basic recurrence relations. Because the performance bottleneck today is memory access, this leads to significant performance gain, especially with hand vectorized code. And as a very welcome side-effect of the on-the-fly computation, the memory requirements have been drastically reduced, opening the possibility of very high resolution simulations based on spherical harmonics. The SHTns library, which is freely available[1], has been successful in significantly improving the performance of simulations code. Indeed, the whole PARODY code runs two times faster since it makes use of SHTns, even at low spherical harmonic resolution (private communication of Julien Aubert).

1.2.2 Improving the performance of spherical codes

Building on top of the efficient spherical harmonic transform, I needed a spherical code that I would enjoy working with[2]. I took inspiration from the axisymmetric code of Dominique Jault, as well as from the numerical methods described by Dormy (1997).

The first version was written in plain C, using shared-memory parallelization (OpenMP) and solving only MHD equations (without buoyancy). It has been used in Gillet, Schaeffer, and Jault (2011, also reproduced in appendix B.1).

It later and progressively evolved to a C++ code, with concentric shells distributed across multiple processes (using MPI) and with the temperature equation (1.3) added. XSHELLS participated in the performance benchmark effort initiated by the american CIG working group (Matsui and Heien, 2014), where it was found to be the fastest code based on finite-differences in radius: for a given number of cores, it is three times faster than the second (which was PARODY before relying on SHTns). Comparison to codes using Chebychev expansions in radius is not straightforward, but I would argue that to solve a given problem, there is still a gap (about a factor of 2 at least).

Although SHTns and XSHELLS work best on intel machines, they have also been ported to the Blue Gene/Q architecture. Figure 1.1 shows the parallel performance on these two types of machines. XSHELLS scales very well up to 1 core per radial shell. This is achieved thanks to a custom radial solver, that only needs communications with nearest neighbors and keeps an optimal low latency (see appendix C.6.2). Scaling beyond this limit (using several cores per radial shell) requires to exploit parallelism within a shell, which is done using the multithreaded spherical harmonic transform provided

[1] https://bitbucket.org/nschaeff/shtns

[2] I dislike Fortran.

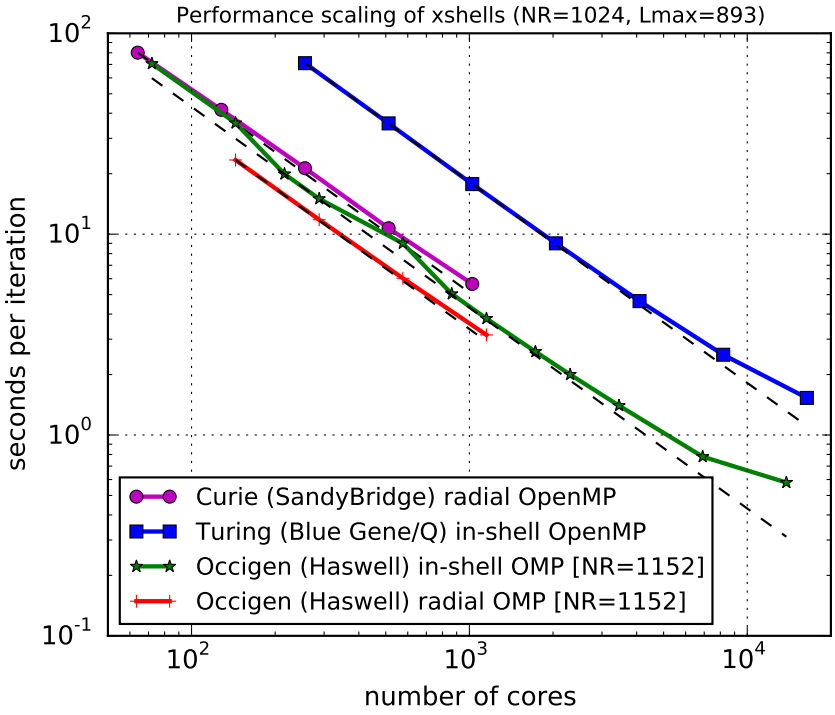

Figure 1.1: Performance scaling of XSHELLS in year 2015, on three french supercomputers with different architectures: *SandyBridge* on *Curie* (thin nodes, TGCC, about 21 Gflops/core), *Haswell* on Occigen (CINES, about 42 Gflops/core), and *Blue Gene/Q* on *Turing* (IDRIS, about 13 Gflops/core). The ideal scaling for each machine is represented by the dashed black lines. On each computer, a geodynamo simulation was run with 1024 or 1152 radial grid points and spherical harmonics truncated after degree 893.

by SHTns in addition to standard OpenMP work sharing within a shell in the XSHELLS code. More details of the code and some specific features can be found in appendix C. XSHELLS is released under the CeCILL Licence with a user manual and a public code repository[3]

It is also interesting to note that XSHELLS can work in full spheres (without inner-core) although load-balancing issues prevent a good scaling in this case. This feature was however used by Monteux et al. (2012) to compute dynamos in sinking spherical diapirs.

[3]XSHELLS code repository: https://bitbucket.org/nschaeff/xshells

1.3 Simulations of the DTS experiment

Figueroa et al. (2013, also reproduced in appendix B.5) performed and analyzed three-dimensional numerical simulations of the DTS (Derviche Tourneur Sodium) experiment (see Brito et al., 2011, and references therein). The conducting solid shells were included in theses simulations at low magnetic Prandtl number ($Pm \sim 0.001$). Note that the fluid is not forced into motion by thermal convection, but rather by differential rotation of the inner and outer sphere, in the so-called spherical Couette configuration (see Wicht, 2014, for the non-magnetic case). This implies that we do not need to solve for the temperature perturbation (eq. 1.3).

We found that turbulent fluctuations were strong near the outer shell, where the magnetic field is weak, and weak near the inner sphere permeated by a strong magnetic field. Nevertheless, magnetic field fluctuations follow the opposite trend, with weak fluctuations in the outer region and strong ones in the inner-region. This is due to the amplitude of the imposed dipolar magnetic field, varying by a factor of more than 20 between the inner sphere and the outer shell. We also showed that, if observed for a long enough time, the turbulent spectra in the simulations exhibit similar bumps as the one observed in experimental spectra (Schmitt et al., 2008). To do this we have performed Fourier transforms in time t and azimuth ϕ of full spatio-temporal fields records. Our results suggest that modes can be excited and observed in developed turbulence.

During the PhD thesis of Simon Cabanes (Cabanes, 2014), we have used XSHELLS to solve the induction equation in a DTS configuration (also including the solid conducting shells). It was the direct model for the framework build by Cabanes, Schaeffer, and Nataf (2014a) to invert the large measurement collection of DTS runs. In particular, at high rotation rate, the Doppler velocity measurements are lost (due to centrifugation of the impurities that reflect ultrasounds), and Simon was able to constrain the mean flow using the other types of measurements (electric potential probes and magnetometers) and its inversion procedure.

In an attempt to go beyond the determination of the mean flow $\langle \mathbf{U} \rangle$, Cabanes, Schaeffer, and Nataf (2014b, also reproduced in appendix B.6) added mean electro-motive force (EMF) represented by an α and β coefficient to account for the effect of turbulence on the mean induction equation. In the mean-field theory framework, the mean magnetic field $\langle \mathbf{B} \rangle$ obeys:

$$\partial_t \langle \mathbf{B} \rangle = \nabla \times (\langle \mathbf{U} \rangle \times \langle \mathbf{B} \rangle + \mathcal{E}) + \eta \Delta \langle \mathbf{B} \rangle \tag{1.22}$$

Furthermore, provided there is a scale separation between turbulent and mean flows (which seems to be the case in the numerics, see 1.2), the EMF

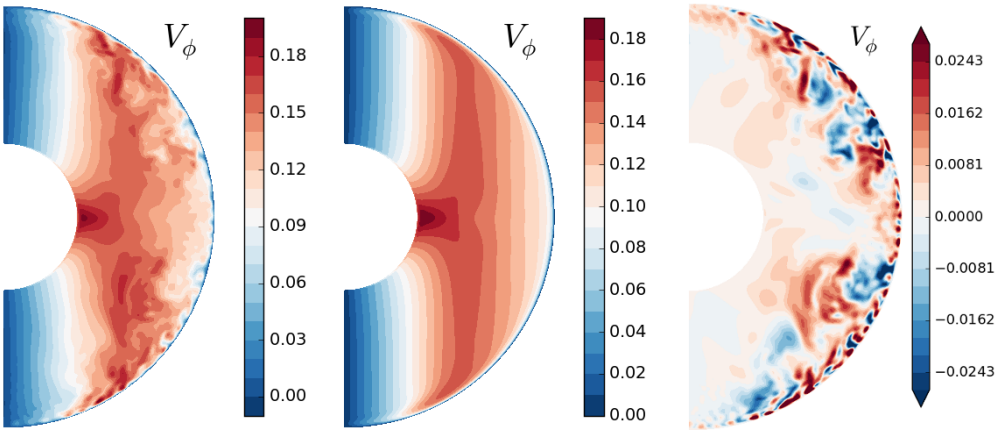

Figure 1.2: Azimuthal flow in a meridional cut of a direct numerical simulation of the DTS experiment ($Re = 2\pi f r_o^2/\nu = 2.9 \times 10^4, Rm = 29, Pm = 10^{-3}$), showing the decomposition of the flow $u_\phi(t) = \langle u_\phi \rangle + u'_\phi(t)$. Left: instantaneous snapshot $u_\phi(t)$; Middle: mean flow $\langle u_\phi \rangle$; Right: fluctuations $u'_\phi(t)$.

can be approximated by the use of α and β tensors. For simplifications, we decided to approximate the EMF $\mathcal{E}$ by

$$\mathcal{E} = \alpha(r)\langle \mathbf{B} \rangle - \beta(r)\nabla \times \langle \mathbf{B} \rangle. \tag{1.23}$$

where $\alpha(r)$ and $\beta(r)$ are scalars, leading to

$$\partial_t \langle \mathbf{B} \rangle = \nabla \times (\langle \mathbf{U} \rangle \times \langle \mathbf{B} \rangle + \alpha \langle \mathbf{B} \rangle - (\eta + \beta)\nabla \times \langle \mathbf{B} \rangle) \tag{1.24}$$

Accordingly, we have introduced these $\alpha(r)$ and $\beta(r)$ terms into XSHELLS to account for them in the inversion of the experimental measurements. We found that the non-rotating DTS is described by a relatively weak $\alpha(r)$ and a strong negative $\beta(r)$ (almost 50% reduction in effective magnetic diffusivity).

Rodion Stepanov alerted us on the fact that for our antisymmetric imposed dipolar field, our parameterization leads to anti-symmetric contributions by α and symmetric contributions by β to the EMF. We thus also tested an alternate parameterization of the EMF $\mathcal{E}$, where α and β give rise to symmetric contributions if $\langle \mathbf{B} \rangle$ is anti-symmetric. Namely:

$$\mathcal{E} = \alpha(r)\, \mathbf{e_r} \times \langle \mathbf{B} \rangle - \beta(r)\nabla \times \langle \mathbf{B} \rangle. \tag{1.25}$$

which can be seen as the contribution of the antisymmetric part of the α tensor. The $\beta(r)$ profile was barely changed, and the misfit to the data was slightly worse.

In addition, we have performed direct numerical simulations (without α and β) of the DTS experiment with a realistic magnetic Reynolds number $Rm = 29$ at $Pm = 10^{-3}$ leading to a rather turbulent regime at $Re = 2\pi f r_o^2/\nu = 2.9 \times 10^4$, where f is the rotation frequency of the inner-sphere, while r_o is the outer radius. In this simulation, field snapshots were recorded and the mean EMF computed. We then have extracted the best fitting α and β.

Note that in the paper published in PRL, we made a confusion in the sign of β. After checking the codes, it appears that the β inverted from the experiments has the correct sign. Only very recently did we realize that the β obtained from direct numerical simulations was plotted with the wrong sign in Cabanes, Schaeffer, and Nataf (2014b, figure 2). We corrected the mistake in an Erratum (Cabanes, Schaeffer, and Nataf, 2015) as well as in appendix B.6. This removes the strong support of the numerical simulations to the negative β in the interior region, and calls for further investigation of this effect in DTS.

1.4 Simulations motivated by observations

Hannes Alfvén first showed the theoretical existence, in an inviscid fluid of infinite electrical conductivity, of hydromagnetic waves that couple fluid motion and magnetic field (Alfvén, 1942). The propagation of torsional Alfvén waves (TAW) in the Earth's fluid core was thereafter predicted by Braginsky (1970). Such waves arise in rapidly rotating spheres or spherical shells in the presence of a magnetic field. In torsional Alfvén waves, the motions are geostrophic and consist in the rotation $\omega_g(s)$ of nested cylinders centered on the rotation axis. They thus depend only on the distance s to the rotation axis.

Torsional waves with much shorter periods have now been extracted from time series of core surface flows for the time interval 1955-1985 (Gillet, Jault, et al., 2010). If this discovery is confirmed, the period of the fundamental modes is of the order of 6 years and, as such, is much shorter than initially calculated. In their study, the TAW seemed to originate near the inner-core ($s = 0.35$) and propagate toward the equator ($s = 1$), as can be seen in figure 1.3. However, no reflection could be clearly identified.

1.4.1 Reflection of Alfvén waves

This prompted us to study the reflection of TAW, that we published in Schaeffer, Jault, et al. (2012, also reproduced in appendix B.3). First, we recall some of the results of Schaeffer, Jault, et al. (2012) obtained in the

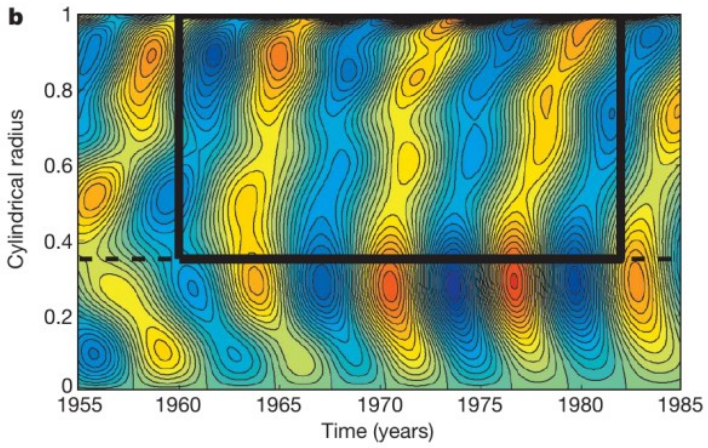

Figure 1.3: Time versus cylindrical radius map of angular velocity in the Earth's core, filtered around a 6 year period, as obtained by Gillet, Jault, et al., 2010, their figure 2b.

case of an insulating wall, before extending them to conducting walls.

We first introduce the problem through the example of simple Alfvén waves, transverse to a uniform magnetic field in an homogeneous and electrically conducting fluid, hitting a solid wall perpendicular to the imposed magnetic field (Roberts, 1967). The imposed uniform magnetic field B_0 is along the x-axis, while the induced magnetic field $b(x,t)$ and the velocity field $u(x,t)$ are transverse to this field, along y. Assuming invariance along y and z axes, the problem reduce to a 1-dimensional problem, u and b depending only on x. Projecting the Navier-Stokes equation and the induction equation on the y direction (on which the pressure gradient and the non-linear terms do not contribute), one obtains the following equations:

$$\partial_t u = B_0 \partial_x b + \nu \partial_{xx} u \tag{1.26}$$

$$\partial_t b = B_0 \partial_x u + \eta \partial_{xx} b \tag{1.27}$$

where η is the magnetic diffusivity and ν the kinematic viscosity. Note that magnetic fields are scaled to Alfvén speed units (see sec. 1.1.2).

Elsasser variables

Much comprehension can be gained by transforming the above equation set with the introduction of the two Elsasser variables $h_\pm = u \pm b$. Equation of momentum and of magnetic induction combine into

$$\partial_t h_\pm \mp V_A \partial_x h_\pm - \frac{\eta+\nu}{2} \partial_{xx} h_\pm = \frac{\nu-\eta}{2} \partial_{xx} h_\mp \tag{1.28}$$

where $V_A = B_0$ is the Alfvén wave speed. It is already apparent that when $\nu = \eta$, the right hand side of the previous equation vanishes, in which case h_+ and h_- are decoupled. One can also show that h_- travels in the direction of the imposed magnetic field, while h_+ travels in the opposite direction.

Introducing a length scale L and the time-scale L/V_A, the previous equations take the following non-dimensional form:

$$\partial_t h_\pm \mp \partial_x h_\pm - \frac{1}{S} \partial_{xx} h_\pm = \frac{1}{S} \frac{Pm-1}{Pm+1} \partial_{xx} h_\mp \tag{1.29}$$

where we recall the Lundquist number S and the magnetic Prandtl number Pm are defined as:

$$S = \frac{2 V_A L}{\eta + \nu} \qquad \text{and} \qquad Pm = \frac{\nu}{\eta}$$

The propagation of Alfvén waves requires that the dissipation is small enough, which is ensured by $S \gg 1$.

The fact that $(Pm-1)/(Pm+1) = -(Pm^{-1}-1)/(Pm^{-1}+1)$ establishes a fundamental symmetry of these equations: when changing Pm into Pm^{-1}, only the sign of the coupling term (right hand side of equations 1.29) changes.

For $Pm = 1$ the equations for h_+ and h_- are fully decoupled, regardless of the value of S:

$$\partial_t h_\pm = \pm\partial_x h_\pm + \frac{1}{S}\partial_{xx} h_\pm \tag{1.30}$$

Then, only the boundary condition can possibly convert h_+ to h_-, leading to reflection.

Insulating wall

These equations must be completed by boundary conditions. If the wall is electrically insulating, and the fluid velocity vanishes at the solid boundary (no-slip boundary condition), we have $b = 0$ and $u = 0$, leading to $h_\pm = 0$.

This boundary condition does not couple h_+ and h_-. As a result, reflection is not allowed at an insulating boundary when $Pm = 1$, because reflection requires change of traveling direction, and thus transformation of h_+ into h_- and vice versa. The energy carried by the wave has to be dissipated in the boundary layer.

For $Pm \neq 1$ the equations are coupled: for very small diffusivities (that is large Lundquist number S), the coupling will be effective only in a thin boundary layer. In addition the coupling will be more efficient as Pm is far from 1. This gives a mechanism for reflection of Alfvén waves on an insulating boundary when $Pm \neq 1$.

Another combination of boundary conditions inhibits reflection for $Pm = 1$: for a stress-free ($\partial_x u = 0$) and perfectly conducting wall ($\partial_x b = 0$), which translates into $\partial_x h_+ = 0$ and $\partial_x h_- = 0$, the fields h_+ and h_- are decoupled, as for a no-slip insulating wall.

Schaeffer, Jault, et al. (2012) go further and compute the reflection coefficient R, which reads, for a no-slip and insulating wall,

$$R = \frac{1-\sqrt{Pm}}{1+\sqrt{Pm}} \tag{1.31}$$

.

Conducting wall

We now insert a solid conducting layer of thickness ϵ between the solid insulator and the conducting fluid. A schematic setup is shown on figure 1.4. Equations 1.26 and 1.27 in the fluid must be complemented with

$$\partial_t b = \eta_W \partial_{xx} b \tag{1.32}$$

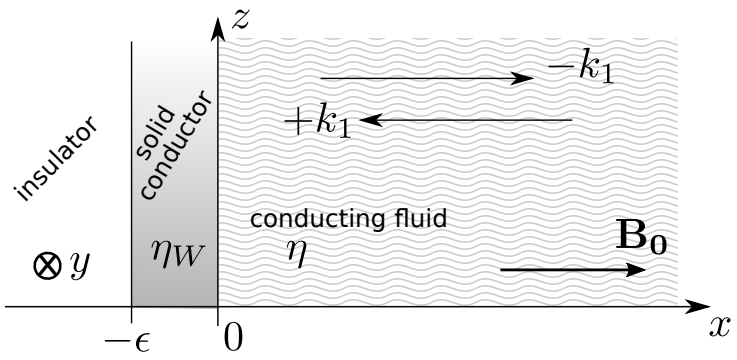

Figure 1.4: Schematic one-dimensional setup for the propagation of Alfvén waves interacting with a conducting wall. The imposed field B_0 is normal to the wall, which has a thickness ϵ. The fluid and the solid wall have respective magnetic diffusivities η and η_W. The incoming wave has wavenumber $+k_1$ and the reflected wave has wavenumber $-k_1$. Everything is independent of y and z.

in the solid wall of magnetic diffusivity η_W.

At the solid-liquid interface ($x = 0$), the velocity vanishes: $u(0) = 0$. The magnetic field is continuous, $[b] = 0$ and the electric field also. Since the electric field $\mathbf{E}$ is related to the electric current $\mathbf{j} = j\mathbf{e_z} = \partial_x b\mathbf{e_z}$ by Ohm's law, and because $u(0) = 0$, we have: $[j/\sigma] = 0$ which translates into

$$\eta_W \, \partial_x b|_{x=0^-} = \eta \, \partial_x b|_{x=0^+} \tag{1.33}$$

At the insulator, we have $b(-\epsilon) = 0$.

We seek solution in the form of plane waves $u, b = u_0, b_0 \exp(i\omega t + ikx)$ at a given frequency ω. Following Schaeffer, Jault, et al. (2012) we define the reflection coefficient $R = u^-/u^+$, which is the ratio of the outgoing fluid velocity amplitude over the incoming one, at the wall. Matching the solution in the solid conducting region and the liquid conducting region, we find the following expression:

$$\frac{1+R}{1-R} = \sqrt{\frac{S_W}{2}} \, F\left(\frac{\epsilon}{\lambda}\right) \left(\frac{1}{S} - i\right)(1+i) + \sqrt{Pm} \tag{1.34}$$

with

$$F(x) = \frac{1 - e^{-2x(1+i)}}{1 + e^{-2x(1+i)}} \qquad \lambda = \sqrt{\frac{2\eta_W}{\omega}} \qquad S_W = \frac{V_A^2}{\omega \eta_W} \qquad S = \frac{V_A^2}{\omega \eta}$$

In the case of an electrical conductor good enough for Alfvén waves to

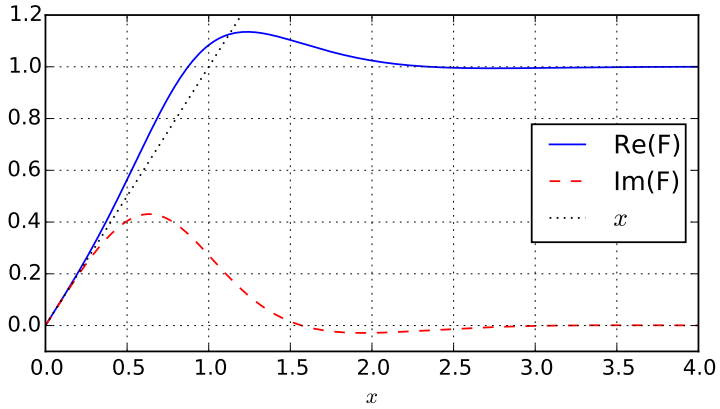

Figure 1.5: Graphic representation of the real and imaginary parts of function $F(x)$ that enters the reflection coefficient of Alfvén waves on a conducting wall (eq. 1.34). For $x \lesssim 0.3$, it is well approximated by $F(x) \sim x(1+i)$

propagate ($S \gg 1$), it reduces to a complex-valued reflection coefficient:

$$\frac{1+R}{1-R} \simeq \sqrt{\frac{S_W}{2}}\, F\left(\frac{\epsilon}{\lambda}\right)\,(1-i) + \sqrt{Pm}$$

The function $F(x)$ is represented in figure 1.5. When the thickness ϵ is small compared to the electromagnetic skin-depth λ, we can use the approximation $F(x \to 0) \sim x(1+i)$. This leads to a simple reflection coefficient in the case of a thin, low conductivity wall:

$$R \simeq \frac{1 - Q_W - \sqrt{Pm}}{1 + Q_W + \sqrt{Pm}} \qquad \text{for } \epsilon \lesssim 0.3\,\lambda \tag{1.35}$$

where

$$Q_W = \frac{V_A \epsilon}{\eta_W} = V_A\, \mu_0 \sigma_W \epsilon \tag{1.36}$$

is a Lundquist number constructed with the Alfvén speed in the fluid but with the wall thickness and the wall magnetic diffusivity. Note that in this case R is a real number between -1 and $+1$, and is independent of the frequency ω. When $\sigma_W = 0$ we have $Q_W = 0$ and we recover the reflection coefficient of the insulating wall. In this limit, Q_W depends only on the wall conductance $\sigma_W \epsilon$.

In the case of a liquid metal, we may consider the case $\sqrt{Pm} \ll Q_W$ which reduces further to

$$R \simeq \frac{1 - Q_W}{1 + Q_W}$$

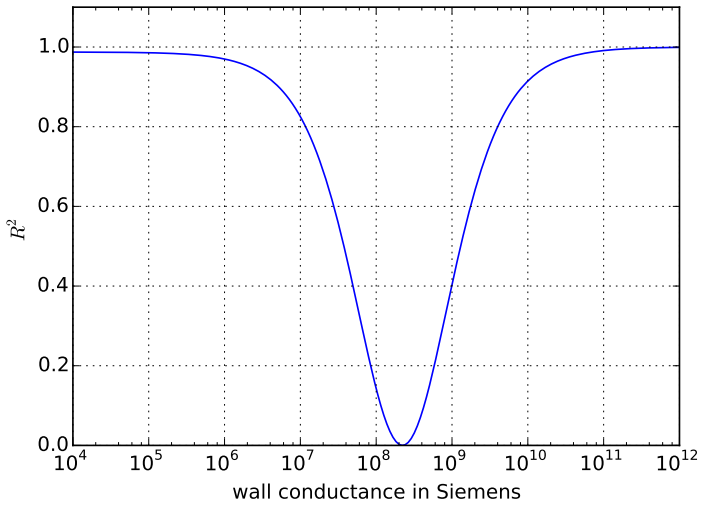

Figure 1.6: Reflected energy of an Alfvén wave as a function of the conductance of the wall. We set $V_A = 3.6 \times 10^{-3}$ m/s corresponding to $B_0 = 4 \times 10^{-4}$ T and $Pm = 10^{-5}$, which are representative for the Earth's core.

and is now independent of the fluid conductivity. It also shows that when $Q_W \sim 1$, no reflection will be observed.

Application to Torsional Alfvén Waves in the Earth's core

Schaeffer, Jault, et al. (2012) have shown that the one-dimensional plane wave theory was relevant for Torsional waves in the spherical geometry of the Earth's core, although there are some differences. Hence, they argued that in the case of numerical simulations, all performed with $Pm \sim 1$, there will be no significant reflection of Torsional Alfvén waves. This also prevents the existence of eigen-modes, which will be damped.

In the case of the Earth, since we do not observe reflection of the torsional waves, we argue that Q_W should be close to 1, which places a constraint on the conductance of the conducting layer at the base of the mantle. Indeed, taking Earth-like values, the reflected energy has a minimum for a layer at the base of the mantle with a conductance of around 10^8 Siemens, as seen in figure 1.6. This would translate to a layer of about $\epsilon \sim 100$ meters with the same conductivity as the core. We check that in that case the skin-depth is $\lambda = 8$km, leading to $\epsilon/\lambda \sim 0.01$, validating our approximation of $F(x)$.

With Alexandre Capron (Master student), we performed numerical simulations of the propagation of a torsional Alfvén wave pulse in a spherical shell

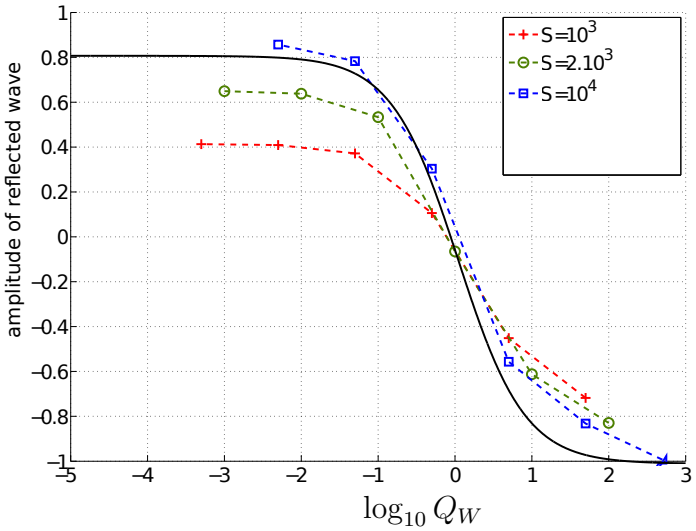

Figure 1.7: Reflection coefficient R as a function of parameter Q_W measured for torsional Alfvén waves in a spherical shell numerical simulation. With $Pm = 0.01$ and three values of the Lundquist number S. The black curve corresponds to equation 1.35 which assumes $S \gg 1$.

permeated by a externally applied axial quadrupole magnetic field. These simulations are the same as the ones done by Schaeffer, Jault, et al. (2012, reproduced in appendix B.3), except for the conducting solid layer surrounding the fluid. We have used various conductivities for this layer, and the reflection coefficient is in agreement with the simple 1-dimensional Alfvén wave hitting a wall at $S \to \infty$, especially for $Q_W \sim 1$ as shown by figure 1.7.

1.4.2 Quasi-geostrophic flows in the Earth's core?

Geostrophic flows decribe a perfect balance between Coriolis and pressure (possibly including other forces deriving from a potential, see e.g. Greenspan, 1968):

$$2\boldsymbol{\Omega_0} \times \mathbf{u} = -\nabla p. \tag{1.37}$$

In a sphere, the only geostrophic flows are stationary zonal azimuthal flows invariant along the rotation axis.

Flows dominated by this balance, but where other forces are present at next order are called quasi-geostrophic (QG). An emblematic one is probably

the flow at the onset of thermal convection in a sphere (Busse, 1970), which are known as "Busse columns". These columns are symmetric with respect to the equator: the velocity field perpendicular to the rotation axis (the z-axis) is (almost) invariant along the rotation axis, while the axial velocity is anti-symmetric, varying (almost) linearly with z.

I want to emphasize that another mode for thermal convection has been studied by Roberts (1968) which has the opposite symmetry, relevant for the convection inside the Tangent Cylinder (the cylinder tangent to the inner-core and parallel to the rotation axis), where the gravity is (almost) parallel to the rotation axis, a setup widely studied, leading to a reduced set of equations in the asymptotic limit of high rotation rate (Sprague et al., 2006). It appears that the reduced quasi-geostrophic model of Sprague et al., 2006, which derives from a multi-scale analysis is hard (if not impossible) to fit properly into a spherical shell.

Inspired by Busse (1970), a simpler, two-dimensional quasi-geostrophic model (or columnar model) has been used for rotating thermal convection (Cardin and Olson, 1994; Aubert, Gillet, and Cardin, 2003; Gillet et al., 2007a; Calkins et al., 2012), for rotating magnetoconvection (Gillet et al., 2007b), for kinematic dynamos (Schaeffer and Cardin, 2006) and for inferring core flows from geomagnetic data (Pais and Jault, 2008; Gillet, Schaeffer, and Jault, 2011). This two-dimensional quasi-geostrophic model, described in details by Gillet, Schaeffer, and Jault (2011, also reproduced in appendix B.1) has a few shortcomings: (i) it accounts only for the symmetric part, and is therefore irrelevant inside the Tangent Cylinder; (ii) it is valid for small slopes only, and is thus expected to fail when approaching the equator, where the slope of the sphere becomes very large; (iii) it does not allow any deviations to rigid columns, which are due to the action of other forces (buoyancy and Lorentz for example).

Are such columnar flows a significant component of core flows?

Schaeffer and Pais, 2011, also reproduced in appendix B.2 use numerical simulations to show that depending on the symmetry of the forcing, symmetric or anti-symmetric QG flows are observed. We thus produced core flow maps at the surface of the core, and examine the distribution of symmetric and antisymmetric energy as a function of latitude.

Table 1.4.2 shows a trend for large scales ($\ell \leq 10$) to be more symmetric than small scales. It also shows remarkably that inside the TC, the symmetric flow is much less pronounced than outside, and that, maybe surprisingly, the equator remains fairly symmetric. Note that no special assumption were made within the tangent cylinder: the whole core surface is treated equally.

ℓ_{tr}	6	10	13	18	26
inside TC	0.63	0.79	0.38	0.27	0.22
outside TC	0.84	0.80	0.77	0.71	0.68
equator	0.91	0.91	0.83	0.67	0.65

Table 1.1: Ratio of symmetric kinetic energy over total energy for the core flow of Schaeffer and Pais (2011) truncated at different spherical harmonic degree ℓ_{tr} and integrated over the whole core surface, inside the Tangent Cylinder (TC), and also over a band centered on the equator and spanning 40° of latitude.

It is thus also remarkable that our core flows exhibit a sharp transition at the location of the tangent cylinder, suggesting that the geomagnetic data is sensible to the polar vortex already found by Olson and Aurnou (1999).

How does the magnetic field affect QG flows?

In another paper (Gillet, Schaeffer, and Jault, 2011, also reproduced in appendix B.1), I use direct numerical simulations to complement the geophysical evidence that core flows using the QG assumption reproduce equally well the data using less free parameters. These simulations, at low viscosity and magnetic diffusivity ($S \gg 1$) follow the propagation of a torsional wave through a non-axisymmeric magnetic field, at low Rossby and Lehnert number, as in the Earth's core. Note that there are no buoyancy force taken into account here.

An example of flow in a meridional section is represented in figure 1.8. It shows that where the magnetic field is strong, small-scale Alfvén waves can propagate, but otherwise inertial waves quickly enforce quasi-geostrophy. I want to emphasize that this is a short time-scale behavior. For long time-scales, Buoyancy forces and Lorentz forces are expected to play an important role, leading to thermal winds and magnetostrophy (Aubert, 2005). The time-scale of the transition is not known, but the Alfvén time-scale might be relevant.

Beyond quasi-geostrophy

Sreenivasan and Jones (2011) introduce the effect of the Lorentz force in the classic asymptotic model of thermal convection (e.g. Jones, Soward, and Mussa, 2000; Dormy et al., 2004). The typical time-scale of the thermal convection flow considered here is $\tau_{conv} \sim E^{-1/3} T_\Omega$, where T_Ω is the rotation period. For the Earth's core, this means $\tau_{conv} \sim 100$ years. This is much

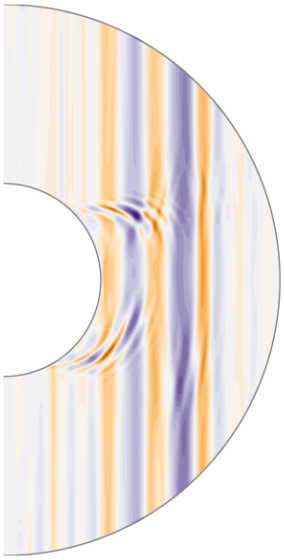

Figure 1.8: Meridional slice showing the cylindrical radial component of the flow (perpendicular to the rotation axis, which is vertical in the figure), when torsional waves travels through a non-axisymmetric magnetic field. The simulation (case A of Gillet, Schaeffer, and Jault, 2011) has input parameters $Le = 2.9 \times 10^{-4}$, $\Lambda = 1.5$, $S = 1.6 \times 10^4$, $Pm = 1$, $E = 5.7 \times 10^{-8}$. The flow shown here has $Ro \sim 10^{-7}$.

larger than the Alfvén time of 6 years in the core (Gillet, Jault, et al., 2010), and our previous argument for QG flows in the presence of strong magnetic field (Gillet, Schaeffer, and Jault, 2011) does not hold anymore. On centenial time-scales the Lorentz force can balance the Coriolis force, and strict quasi-geostrophy may not be the best ansatz. Indeed Sreenivasan and Jones (2011) show that for Elsasser number $\Lambda \sim 1$ the columns are deformed and a magnetic-pumping flow is introduced. Schaeffer, Lora Silva, and Pais (2016, also reproduced in appendix B.8) use their analytical results to crudely parameterize the effect of the Lorentz force on the quasi-geostrophic columns. We compute a surface core flow inverted from geomagnetic field data, that is downward continued into the bulk using our new parameterization. The resulting flow (see figure 1.9 for an example) is put into a kinematic dynamo code.

Not that by solving only the induction equation we can also use realistic parameters ($Rm \sim 1000$), unlike full featured geodynamo simulations. We observe growing magnetic fields in a region delimited by $Rm > 90$ and $\Lambda > 0.25$. Since our flow does not contain scales smaller than about 800 km, our kinematic dynamo calculations show that the geodynamo does not need to

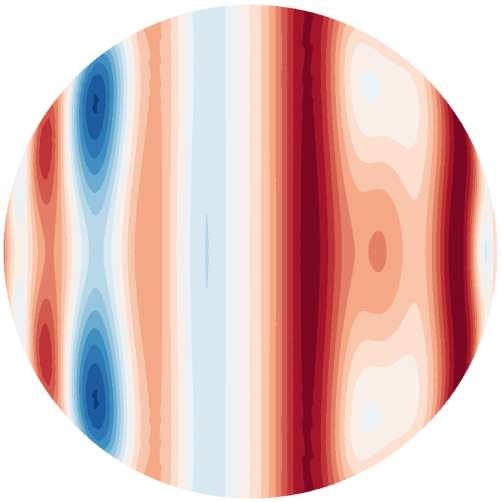

Figure 1.9: Meridional cut showing the flow (component perpendicular to the plane) deformed by the magnetic pumping introduced by Schaeffer, Lora Silva, and Pais (2016) at $\Lambda = 0.9$.

rely on small-scales to produce a magnetic field comparable to the one we observe. In particular, there is no need for turbulent electro-motive force.

Temporary conclusion

We have shown, through dedicated numerical simulations, that short time-scale and large length-scale flows are likely to be quasi-geostrophic in the Earth's core, despite the strong magnetic field (Jault, 2008; Gillet, Schaeffer, and Jault, 2011). The effect of buoyancy at theses short time-scale is arguably small, at least near the onset of convection. Short time-scale is still fuzzy, but period of a few years or less should qualifiy.

On centennial time-scales, the flow may be considered quasi-static, and the Elsasser number controls the deformation of columns. This deformation enhances flow helicity and the generation of dipolar magnetic field (Sreenivasan and Jones, 2011; Schaeffer, Lora Silva, and Pais, 2016). A self-consistent parameterization of this deformation, as well as the effect of buoyancy would be a great addition to the current quasi-geostrophic model, resulting in a model that could account for a wide range of time-scales.

1.5 Turbulence in the Core

Earth's magnetic field is generated by a turbulent flow of liquid metal in the core. Estimates of viscosity, electrical conductivity, as well as core flow and internal magnetic field estimations (Olson, 2015; Gillet, Jault, et al., 2010) draw the picture of a turbulent core spanning many time- and length-scales. Nataf and Schaeffer (2015, reproduced in appendix B.7) discuss the expected turbulent state of the core based on length-scale dependent non-dimensional numbers (e.g. replace L with the length-scale ℓ of your choice in the number defined in sections 1.1.3 and 1.1.4). We have also introduced a new kind of regime diagrams that present the same information than turbulent spectra, but using actual length-scales and time-scales instead, enabling direct correspondence to real physical systems.

1.5.1 Waves

To introduce the rather complicated diagram for the Earth's core, we have represented what we know in figure 1.10, putting an emphasis on waves. Waves are responses to perturbations, and transmit the corresponding information across the system. For instance, sound waves transmit pressure unbalance, which is restored once the waves have traveled across the system. Hence, slow enough flows can be considered incompressible (or anelastic in the presence of strong stratification). This is translated into an horizontal line in figure 1.10, which represents the time for a sound perturbation to propagate across the core. Similarly, we argue that above the "Inertial" line, quasi-geostrophy rules (Jault, 2008; Gillet, Schaeffer, and Jault, 2011). The presence of a magnetic field leads to Magneto-Coriolis waves with a fast branch corresponding to almost unaltered inertial (and Rossby) waves and a slow branch (Magnetostrophic waves, labeled "Slow MC") at $Le = B_0/\ell\Omega \ll 1$. These branches progressively merge into Alfvén waves at $Le \gtrsim 10^{-2}$ (e.g. Schmitt, 2010; Galtier, 2014; Canet, Finlay, and Fournier, 2014). It is not yet clear what happens at longer time-scales, on which the magnetic field can act (above the Alfvén line ?) Indeed, there are too many constraints for them to be satisfied simultaneously.

For a flow $u(\ell)$, staying above the "Inertial" lines means

$$Pd(\ell) < \frac{u(\ell)L}{\Omega\ell^2} = 1 \tag{1.38}$$

This Proudman number (let's call it that way), which compares the time to form a Taylor column to the vortex turn-over time, may control the transition from columnar flow to anisotropic and still rotation-dominated turbulence (in

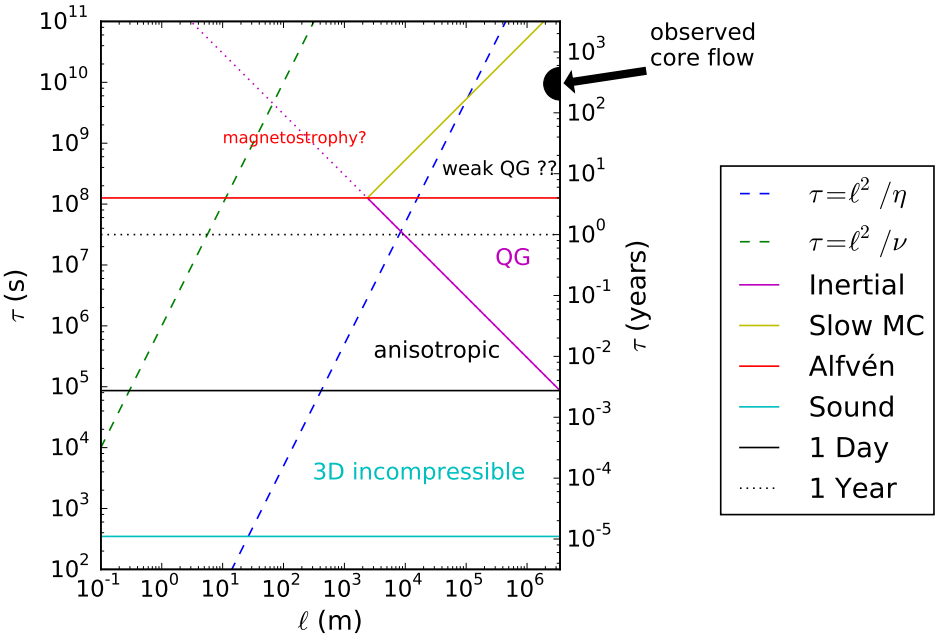

Figure 1.10: Regime diagram for the Earth's core, highlighting the various possible transitions. Thick lines are core transit times for different waves of length scale ℓ (non-dispersive waves result in horizontal lines). Sound waves propagate at $\sim$ 10 km/sec, so that they need a few minutes to cross the core. Alfvén waves need $\sim$ 4 years to cross the outer core (Gillet, Jault, et al., 2010). Inertial waves are dispersive, with a group velocity $\sim \ell\Omega$. Slow Magneto-Coriolis waves have group velocity $\sim B_0^2/\ell\Omega$. Dashed lines mark the magnetic and viscous diffusive times. Above the "Sound" line, the flow can be considered incompressible. Rotationally constrained turbulence (anisotropic) is expected above the "1 Day" line ($Ro < 1$). Quasi-geostrophic (columnar) motion is expected in the triangle labeled "QG" (short time-scale at $Le(\ell) < 1$, see Jault, 2008; Gillet, Schaeffer, and Jault, 2011). In the upper-right part, where the large-scale core flow is observed, constraints from both magnetic field and rotation may matter. "Observed core flow" corresponds to a large-scale flow at 15 km/year.

the absence of magnetic field or buoyancy force), as suggested by figure 1.10. For $Pd < 1$, the material speed is slower than Rossby waves (slow inertial waves with $k.\Omega \sim 0$) at the same scale, and therefore these waves should make up the flow, leading to some Rossby wave turbulence.

1.5.2 Inferred regimes for the core

These $\tau - \ell$ diagrams also make it easy to determine the dissipated power, which can in turn be compared to actual constraints we have on natural systems. Speculating above the turbulent spectra in the core, the figure 8 of Nataf and Schaeffer (2015) (reproduced here in figure 1.11) gives a plausible diagram for the Earth's core, which satisfy the constraints on dissipated power. We want to emphasize that according to the observed core flow and estimated field strength, the flow time-scale is always very longer than a day (small local Rossby number), excluding three-dimensional turbulence at all spatial scales. The u-line ($\tau_u = \ell/u$) is almost always above the Rossby line, meaning that quasi-geostrophic columns could span the whole core (the flow time-scale is larger than the time $T = L/\ell\Omega$ to form the Taylor column). Note also that in order to keep the total dissipation comparable to the estimated heat flux extracted from the core (a few TW), it could not be otherwise.

1.5.3 Turbulence in geodynamo simulations?

In most numerical simulations, turbulence is weak or absent because it is technically challenging to obtain turbulence with today's computers. Indeed, to reach the dynamo regime we need $Rm \gtrsim 100$, and because $Rm = Re\,Pm$, large Re are needed for the low Pm regime relevant for the core.

In their pioneering work, Glatzmaier and Roberts (1995) have obtained a self-sustained magnetic field from a self-consistent geodynamo model. Their model, limited by the computing power of that time, was restricted to the large scales and they employed hyperviscosity to damp the small scales of the fields. They also used a magnetostrophic balance argument to remove inertia, effectively filtering out inertial and Alfvén waves. Arguably, their model was adequate to represent the long-term balance of the geodynamo, including reversals, which was a remarkable feature of their simulation. More recently, high resolution simulations have pushed the parameters toward more realistic ones (Kageyama, Miyagoshi, and Sato, 2008; Sakuraba and Roberts, 2009), but most of the papers focus on reproducing observable features of the geomagnetic field (e.g. Aubert, Labrosse, and Poitou, 2009; Christensen, Aubert, and Hulot, 2010; Christensen, 2011; Aubert, Finlay, and Fournier, 2013) while sacrificing the small-scale flow and rapid dynamics. Figure 1.12

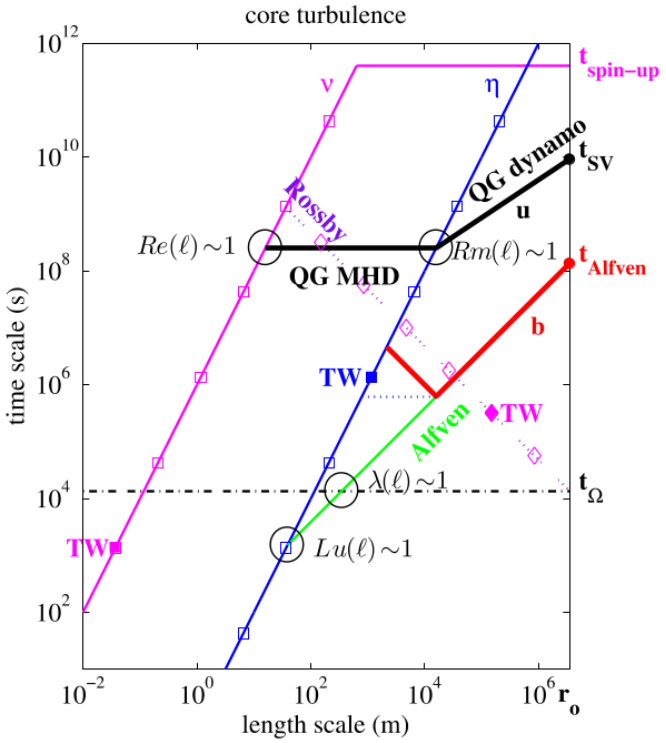

Figure 1.11: Regime diagram for the Earth's core (figure 8 of Nataf and Schaeffer, 2015, see also appendix B.7). The slopes are rather arbitrary since we do not know much about turbulence in this kind of system. Yet, based on time-scales observed for large-scale flow (turn-over time of 300 years) and magnetic field (Alfvén time-scale of 6 years), and the total dissipation (a few TW) we are able to predict roughtly what time-scales and length-scales are expected for the flow.

shows a broad selection of geodynamo simulations in two planes of the parameter space. A rather convincing trend is that when lowering $Em = E/Pm$, small A are achieved (ie large relative magnetic fields). Small discs tend to have smaller A, at least for $Pm > 1$. Looking at the A vs Pm representation, it rather difficult to state that most geodynamo simulations are in the correct asymptotic regime. However, some recent efforts by Sheyko (2014) as well as our own ongoing work (labeled Highway, see appendix D) seem to start to reach out to the Earth's core.

When trying to compute numerical simulations of the geodynamo as close as possible to the parameters of the Earth's core, the computation cost increases not only because of the higher and higher spatial resolution required, but also because the time-step is smaller and smaller compared to the mag-

netic diffusion time. Hence, in order to reach a statistically stationary dynamo regime, the time needed for a simulation to run increases prohibitively.

To reach extreme parameters in our simulations, we propose a technique that avoids to compute long transients by choosing initial conditions that are close to the statistical equilibrium state. Those initial conditions are obtained by applying previously established scaling laws to the output of a lower resolution simulation at parameter further from the Earth's core. This procedure can be repeated to achieve simulations that are closer and closer to the conditions of the Earth's core, paving the road of a numerical highway to the Earth's core.

We have been able to reach strongly forced dynamos at low Ekman number, where the magnetic energy becomes larger than the kinetic energy. Fast variations of the magnetic field can be observed at the Earth's surface, while the flow exhibits tall and thin structures under the effect of the strong global rotation, with a wide range of excited scales. Analysis of these simulations is ongoing work and some preliminary results are discussed in section 2.1, while more details and a gallery of interesting features can be found in appendix D.

The regime diagram (see Nataf and Schaeffer, 2015) of our most turbulent simulation is represented in figure 1.13. The intersection of the "Inertial" line with the ℓ/u line happens at

$$Pd(\ell) = \frac{u(\ell)L}{\Omega\ell^2} = 1 \tag{1.39}$$

This Proudman number (let's call it that way), which compares the time to form a Taylor column to the vortex turn-over time, may control the transition from columnar flow to anisotropic and still rotation-dominated turbulence (in the absence of magnetic field or buoyancy force), as suggested by figure 1.10. For $Pd < 1$, the material speed is slower than Rossby waves (ie slow inertial waves with $k.\Omega \sim 0$) at the same scale, and therefore these waves should make up the flow, leading to some Rossby wave turbulence.

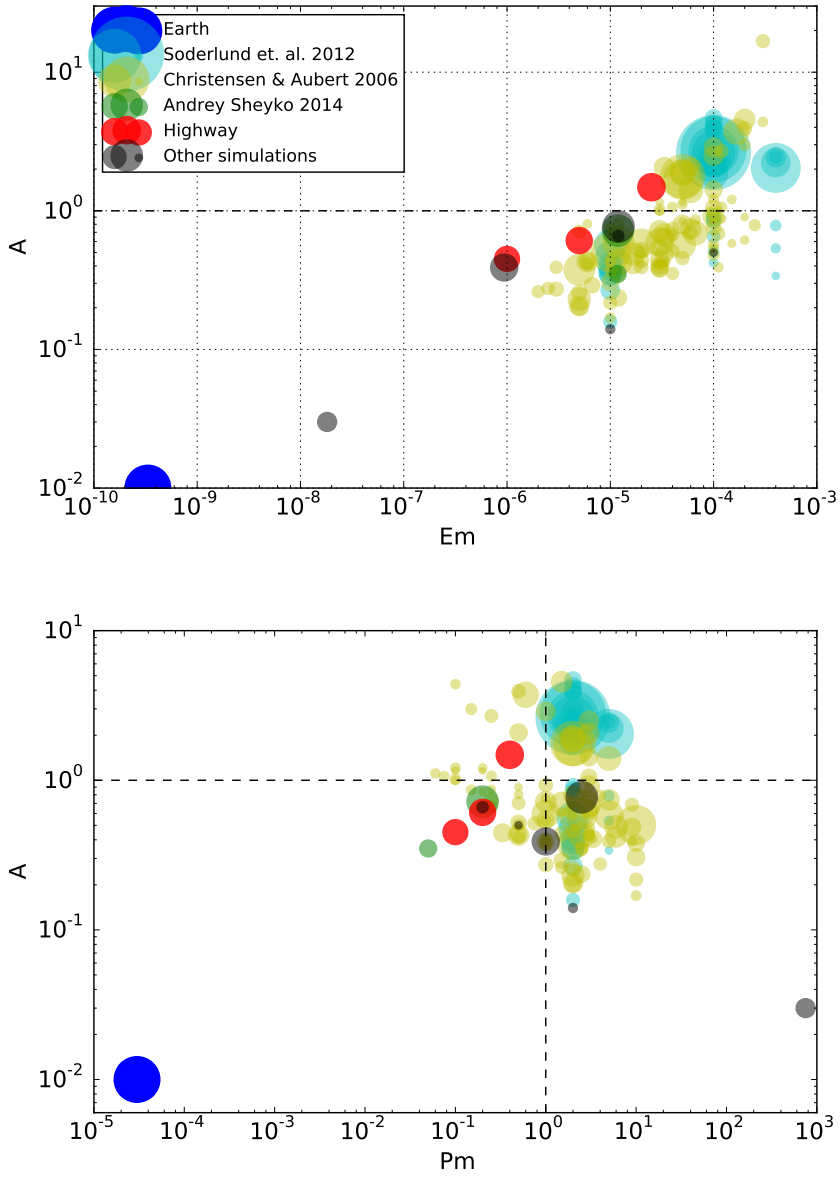

Figure 1.12: Numerical simulations reaching towards the Earth's core. The Alfvén number A (see eq. 1.17) is on the y-axis and the magnetic Reynolds number Rm (see eq. 1.10) is proportional to the surface of the plotted discs. These parameters are plotted as a function of two input parameters $E_m = E/Pm$ (top), and Pm (bottom), for a selection of geodynamo numerical simulations and the Earth. Our own simulations are in red (and more details about them can be found in appendix D).

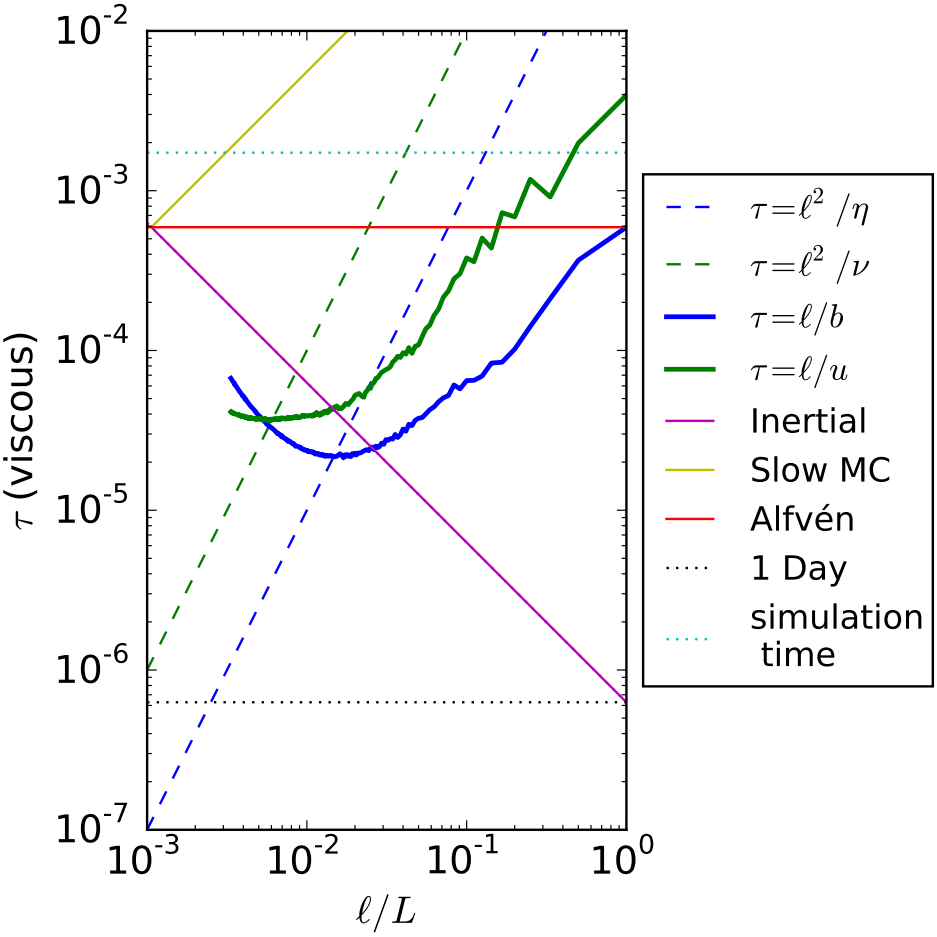

Figure 1.13: Regime diagram for my most extreme numerical simulation $E = 10^{-7}, Pm = 0.1, Pr = 1, Ra/Ra_c \sim 4200$. In addition to the wave transit times (see also fig. 1.10, p. 30), the actual spectrum of both velocity and magnetic field has been translated into $\tau - \ell$ space. Although the scales are not separated as much as in the Earth, they respect the correct ordering. The corresponding spectrum is also represented in figure D.2.

Chapter 2

Research projects and ongoing work

2.1 Understanding Turbulent dynamos

There are several open questions arising as to how do turbulent dynamos operate in planetary cores. Does the magnetic field generation happen at large scales? Do the small scales contribute? How does the magnetic field affect the rotating turbulence? Is it possible to produce a useful reduced model? What kind of force balances govern the various time and length-scales?

In the context of the ANR AVSGeomag and in collaboration with Alexandre Fournier, Dominique Jault and Julien Aubert, I have produced numerical simulations at low viscosity and strong convective forcing leading to rather turbulent spherical dynamos. Our simulations can contribute to the answer at the previous open questions. We are currently analyzing the large amount of data (about 4 Tb), and as a teaser some figures are collected in appendix D.

2.1.1 Force balances

Unlike standard, non-rotating, non-magnetic turublence, there are several additional terms in our Navier-Stokes equation (eq. 1.1). An interesting output of our simulations is the force balance as a function of frequency and length scales, which may guide us to develop reduced models and improve our understanding. In practice, we compute and store the various curl of force densities (ie terms in the vorticity equation) for a collection of fields at different times (with constant time interval). Taking the curl allows to eliminate the main geostrophic balance between Coriolis and pressure gradient. As in Figueroa et al. (2013), we then compute temporal Fourier transform

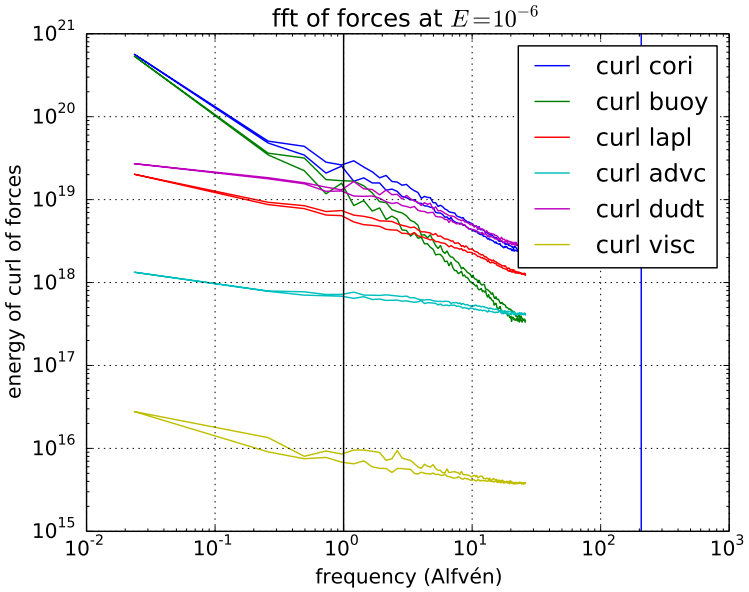

Figure 2.1: Force balance vs frequency considering large scales of the fields only (which were truncated at spherical harmonic degree $\ell = 30$ before computing the forces). Note that boundary layers were also removed. Simulation parameters are $E = 10^{-6}, Pm = 0.2, Pr = 1, Ra/Ra_c = 4500$ (jump 1 in table D.1). We represent the rms value (integrated over the whole spatial domain) of the curl of the following force densities: Coriolis (curl cori), buoyancy (curl buoy), Lorentz-Laplace (curl lapl), advection (curl advc), $\partial_t u$ (curl dudt), viscous diffusion (curl visc). The black vertical line marks the Alfvén frequency, and the blue vertical line marks the Coriolis frequency.

of the full curled force fields. Preliminary results considering only the large scales of the fields (truncated to spherical harmonic degree $\ell \leq 30$ before computing the forces) are represented on figure 2.1.1. It appears that the average (long-term) balance in the vorticity equation is an equilibrium between Coriolis and buoyancy. It contrasts with the short time-scale balance which implies $\partial t\omega$ and Coriolis, suggesting that inertial waves (which include the slow quasi-geostrophic Rossby waves) dominate at these scales. The Lorentz-Laplace force is always sub-dominant, although less so at shorter time scales where it overtakes buoyancy. Advection and viscous terms are almost negligible at theses scales. Although it is more difficult because of the large amount of storage and memory required, small spatial scale balances will be computed similarly and analyzed soon.

2.1.2 Mean fields

There are interesting features in these dynamo runs. Considering the mean axisymmetric flow (time and ϕ-averaged), it appears that both the meridional and azimuthal components are progressively suppressed outside the tangent cylinder as the viscosity is reduced (see figure D.3). A strong polar vortex is confined inside the tangent cylinder (the cylinder touching the equator of the inner-core) while small-scale convection stirs the outside (figures D.2-D.2). Similarly, the mean toroidal field concentrates in the polar regions while the poloidal field is stronger outside the tangent cylinder. This suggests that the strong poloidal magnetic field inhibits the zonal flows seen in other studies (e.g Aubert, 2005) and that the thermal wind balance is restricted to the tangent cylinder. To confirm this, we plan to compute force balances separately inside an outside the tangent cylinder.

Turning to the non-axisymmetric mean flow, we were quite pleased to observe the formation of large scale, non-zonal flows in our most turbulent case (see figure D.3). This suggest the presence of an inverse cascade from the energetic small-scale convection to large eddies. Interestingly, the flow seems to follow magnetic field features. Does it minimize the induction ? Is it possible to derive constraints that could replace the arbitrary regularizations used to invert the flow at the surface of the Earth's core from geomagnetic field variations ?

It is also interesting to note that these large scales are fairly symmetric, except in some places were the magnetic field is strong, suggesting that quasi-geostrophy is challenged by the magnetic field at these large time-scales. As we have advocated in Schaeffer, Lora Silva, and Pais (2016, also reproduced in appendix B.8), a quasi-geostrophic model that accounts for the effect of a moderate magnetic field would be a great tool, and I hope to be able to contribute to it.

2.1.3 Can we do better?

Pushing the parameters even further will be hard. Our $E = 10^{-7}$ dynamo, probably the most turbulent dynamo ever computed, spans 1600 rotation periods, which also corresponds to about 30 turn-over times of the small convective scale, 2.5 Alfvén times, but only 1.5% of a magnetic diffusion time (see table D.1 and figure 1.13).

However, it seems that the large scale flow generation and the correct ordering of all time and length-scales suggest that we may have almost reached a regime where the viscosity does not dictate all the dynamics. I think that pushing the parameters further will require improved numerical methods,

especially the time scheme. See section 2.6 for some propositions.

2.2 MagLune: the dynamo of the Moon

The ANR funded project "MagLune" aims at improving our knowledge on the former dynamo of the Moon. The Moon has a mean radius of 1737 km, a liquid iron core of about $r_o = 330 \pm 20$ km and a solid inner-core of about $r_i = 240 \pm 10$ km (Weber et al., 2011). The aspect ratio $r_i/r_o = 0.7$ is much larger than in the Earth.

Although there is no hint for a magnetic field on the Moon today, measurements on lunar rock samples retrieved by the Apollo missions suggest the presence of a strong magnetic field (about 20 to 30 times stronger than the current field at the Earth's surface) about 4 billion years. This magnetic field inferred from rock samples requires a dynamo in the small iron core of the Moon, but the scaling laws of Christensen and Aubert (2006) predict a field that is smaller by at least an order of magnitude. Moreover, at recent epochs, a weaker field has been recorded in lunar rocks. This change of regime is intriguing and calls for an explanation. Could it be associated with the nucleation of the inner-core? In the case of the Earth's history, Aubert, Labrosse, and Poitou (2009) conclude that the inner-core nucleation had no significant effect on the surface field. More details about the lunar dynamo are given by Weiss and Tikoo (2014).

During this 4 year project, which has started in 2015, one team will make new measurements on Apollo samples to improve our confidence in the past field. With David Cébron, we plan to run new numerical simulations of convection powered by the crystallization of the lunar core on one hand and precession on the other hand. By varying the size of the inner-core from no inner-core (full sphere) to large inner-core (the current moon has a plausible relative radius ratio of 0.7), we will cover the whole range of lunar history.

2.2.1 Convective dynamos

Laneuville et al. (2014) use thermodynamic arguments to suggest that a dynamo powered by the crystallization of the inner-core of the moon could provide a long lasting dynamo. The remaining problem is that of the too low intensity and that of the stopping of the dynamo. We plan to revisit thermal convection driven dynamos ($Pr \ll 1$) in full-sphere as well as the dynamos driven by light-element release ($Pr \gg 1$) at the inner-core boundary by the freezing process, with various sizes of the inner-core.

The effect of inner-core nucleation in the Earth has been studied by

Aubert, Labrosse, and Poitou (2009), who found that it did not influence significantly the field seen at the Earth's surface. However, they did not consider the influence of the Prandtl number.

For large Pr dynamos, Simitev and Busse (2005) suggest that stronger dipole field are obtained, which is a desirable feature for the Moon. This may well be a way to obtain a strong-field magnetostrophic dynamo regime at low Pm.

We also plan to study the effect of realistic double-diffusive convection dynamos. Indeed, Busse (2002) suggest that double-diffusive effects can lower the threshold of convection significantly. There are only a few dynamo simulations with two different equations for composition and temperature. On one hand Glatzmaier and Roberts (1996) and Roberts and Glatzmaier (2001) include realistic boundary conditions for temperature and composition equations, but use the same (turbulent) diffusivities[1]. On the other hand there are studies considering different diffusivities for thermal and compositional equations, but with simplified boundary conditions that impose independent composition and heat fluxes at the inner-core boundary (e.g. Manglik, Wicht, and Christensen, 2010). Low viscosity dynamo models in a realistic double-diffusive regime are yet to be produced.

2.2.2 Precession dynamos in spherical shells

Only little is known on precession dynamos (Tilgner, 2005; Tilgner, 2015). We plan to do a wide parameter survey, varying the precession rate, the precession angle, the viscosity, and the magnetic diffusivity, for different sizes of the inner-core, reflecting various epochs of a planet's history.

The goal is multiple: (i) to map the parameter region where dynamo action is possible; (ii) to gain physical insights in the possibly various mechanism found; (iii) to derive scaling laws that could be applied for planets and the moon. An example of the magnetic field obtained in a precessing sphere is shown on figure 2.2. Some feature are reminiscent of the diapir dynamos studied by Monteux et al. (2012).

It is not straightforward that the resulting magnetic fields are geophysically relevant. Indeed, a small-scale dynamo as the one shown in figure 2.2 is not a good candidate to explain the large-scale magnetic field at the surface of the moon. In addition, the time-scale of magnetic field variations should also be long enough to prevent being filtered out by a slightly conducting mantle (Tilgner, 2015). We hope that at the end of this project we

[1]Note that Roberts and Glatzmaier (2001) use rather extreme parameters with $Pr = Pm = 725$!

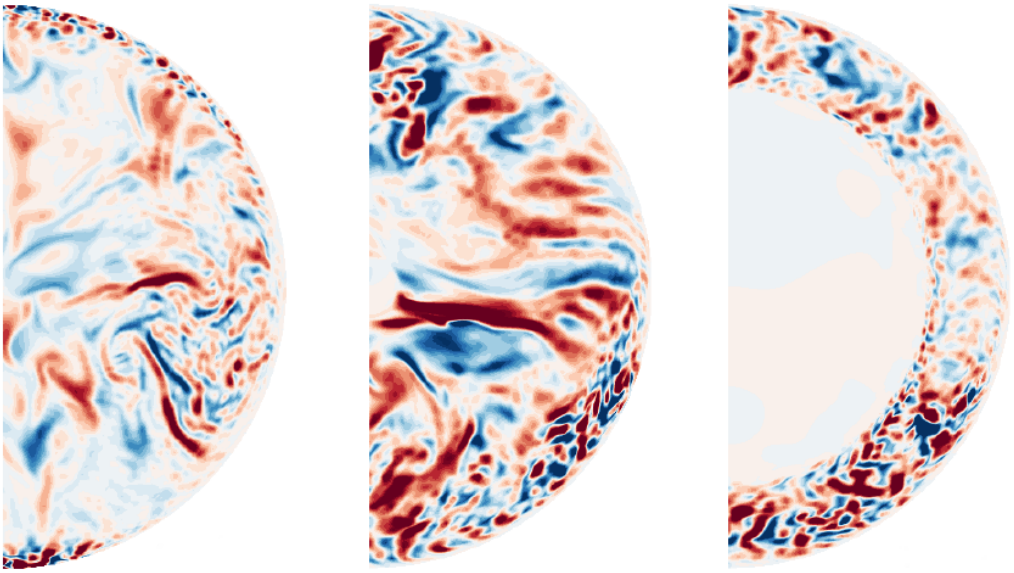

Figure 2.2: Radial magnetic field obtained in three precessing dynamos with no inner-core (left), small inner-core (middle) and large inner-core (right). Parameters were set to $E = 3 \times 10^{-5}$, $Pm = 1$, with a precessing rate of $0.1\Omega_0$ and a precessing angle of 90°.

can depict precession driven dynamos in an asymptotic regime relevant for planetary interiors.

2.3 Simulation of experiments

The DTS experiment has just restarted in the rapidly rotating regime, with unprecedented instrumentation. With Elliot Kaplan, we are currently running simulations to accompany these experiments.

2.3.1 DTS

The strong turbulence in the outer region limits our parameter range. We could adopt an approach similar to Cabanes, Schaeffer, and Nataf (2014b) by adjusting a turbulent viscosity depending on the radius, in order to reproduce the experimental results. Such a turbulent viscosity would be a crude model of sub-grid scale turbulence.

data assimilation

Since it is impossible to simulate the real parameters, data assimilation seems an interesting way to analyze experimental data. Usually (as in meteorology), the numerical model is not too bad, and the initial conditions are the variables that are assimilated, also because the model is not run longer than a typical correlation time. In our type of experiments, the initial conditions are forgotten quickly, and we are interested instead in the statistical equilibrium and the fluctuations around it.

We plan to go one step further than Cabanes, Schaeffer, and Nataf (2014b), and use a full dynamical model (including both Navier-Stokes and induction equation) in which we would use data assimilation to adjust the control parameters and possibly inhomogeneous diffusivities. This would require to build a robust assimilation framework on top of XSHELLS, probably using Python and PETSc. Furthermore, allowing diffusivities to vary not only along the radius but also with angle would require more generic implicit schemes, probably matrix-free. This needs some effort to adapt the current version of XSHELLS, but would also be useful for other sort of studies.

Note that we have also proposed to apply such kind of data assimilation technique on the *Big Sister* experiment (this is how we call the 3 m diameter spherical Couette experiment in Maryland).

2.3.2 ZoRo

The rapidly rotating convection experiment dedicated to the study of the formation of zonal jets in non-linear convection will also benefit from numerical simulations. The quasi-geostrophic model of Guervilly (2010) can produce these alternating zonal jets. A validation by 3D simulations would add some weight to it. In the geodynamo team and in collaboration with Mathieu Dumberry, we are currently planning a strategy to develop a common tool and model for quasi-geostrophic simulations of convection, possibly using the Dedalus code[2].

2.4 Eigenmodes with magnetic fields

Following the discussion of sections 1.4.2 and 1.5, it is not clear how the magnetic field affects the flow structure and dynamics in the Earth's core. Computing eigenmodes influenced by a magnetic field at low viscosity would

[2] http://dedalus-project.org/

shed some light on the issue. Of course, one must not forget that in a dynamo regime, the magnetic field is not imposed but dynamically linked to the fluid.

With PhD student Jéremie Vidal, we have computed gravito-inertial modes in spherical shells (Vidal and Schaeffer, 2015). The numerical method uses sparse matrices with the PETSc and SLEPc libraries (Hernandez, Roman, and Vidal, 2005) and is therefore scalable, allowing to compute modes at very low viscosity. We have also added the effect of a magnetic field, but calculating the non-zero matrix entries describing the coupling is tedious and error-prone, even assisted by computer algebra systems, and must be carried out again if the imposed magnetic field is changed. Schmitt (2010) used a dense matrix formulation, which is very convenient for arbitrary magnetic fields, but is not parallel and cannot reach the low viscosities relevant for the core.

A possible solution would be to use iterative matrix-free methods. This would allow much more flexibility. The results of such a study could guide us to take into account the effect of the magnetic field in quasi-geostrophic dynamic models.

2.5 From spheres to ellipsoids

Mechanically driven flows (precession, libration, tides, ...) are significantly different if the container is a sphere or an ellipsoid. Then, because of the non-symmetric shape, pressure torques can efficiently entrain the fluid, instead of the weak viscous coupling in the case of the sphere. Currently, local methods are used to compute the fluid dynamics in ellipsoids (e.g. Favier et al., 2015). If we could extend the efficient spectral methods to ellipsoids without loosing their significant speed advantage, we would have a tool to study efficiently MHD and dynamo action in these bodies.

Lorenzani and Tilgner (2001) applied a global homothetic transformation to map a spheroid onto a sphere. The major inconvenience with this method is that the ellipticity is constant across the domain: no smooth match to a spherical domain is possible, nor having different ellipticities for the mantle and the inner-core. In addition the method does not generalize well to ellipsoids, and the implementation of magnetic field boundary conditions is problematic.

At least two alternate ways exist. First, a non-orthogonal coordinate system (also known as Clairaut coordinates, see e.g. Kopal, 1980; Ivers and Phillips, 2001; Rogister and Rochester, 2004; Rieutord and Espinosa Lara, 2013) could be used and mapped to the sphere in order to use spherical harmonics. The resulting equations are complicated but seem tractable. The

numerous couplings introduced by such an approach for the ellipsoid would almost certainly require an iterative matrix-free solver. This method could also be generalized to arbitrary topography at the boundaries.

Second, modified boundary conditions could also be used in principle (Rieutord and Zahn, 1997). They have the main advantage that they would change only the boundary conditions (in a non-trivial way) requiring only matrix-based generalized solvers in the spheroidal case. Note however that this method is an approximation expected to be valid only for small deformations, whereas the previous one is exact.

An important part of the PhD of Jérémie Vidal is dedicated to design and implement this kind of method, and to apply it to general topography and mechanically forced dynamos in non-spherical shells.

2.6 Improving the numerical methods

2.6.1 More flexible implicit time-schemes

Almost all geodynamo codes treat the Coriolis force explicitly. This results in a stringent CFL condition because of the fast inertial waves that must be resolved, resulting in small time-steps. Treating the Coriolis force implicitly is possible, although the matrix to inverse now becomes complex and a general LU solver must be employed, at the cost of increased memory requirements and computation time. Hopefully the increased computation time for one time step is more than compensated by the increased size of the time-step. However there are other terms in the equations that can limit the time-step if treated explicitly, such as the Lorentz-Laplace force or a small grid size in the boundary layers. Treating the magnetic field implicitly will be difficult and would most certainly require a non-linear fully implicit solver. This kind of fully-implicit methods have already been implemented for Cartesian dynamos (Schmalzl and Hansen, 2000), plasma physics (Chacón, 2008; Lütjens and Luciani, 2010). In the geodynamo context, some effort has also been reported (Zhan et al., 2014).

If the time-step is limited by the small boundary layers, a possible solution would be to parameterize the Ekman layers, using the formulas of (Greenspan, 1968) and that I have already implemented in a quasi-geostrophic model (Schaeffer and Cardin, 2005). The main problem to overcome in a spherical shell is the singularity at the equator. I plan to study the feasibility of this idea.

Even if we treat the non-linear terms (including Lorentz-Laplace) explicitly, having a generic semi-implicit solver that does not rely on a banded-

matrix structure (which is the structure of the diffusion operator) would also enable interesting features like non-spherically symmetric diffusivities or complex boundary conditions coupling different fields or harmonic degrees. Non-spherically symmetric diffusivity will have interesting applications in further studying the effect of mantle conductivity on the velocity and magnetic fields (see Jault, 2015). Complex boundary conditions are needed for realistic double-diffusion convection and also to approximate spheroidal boundaries.

2.6.2 Matrix-free implicit methods

Couplings between harmonic degrees as well as orders (as an ellipsoidal shape would require) will not be possible using matrix based methods. Indeed, the matrices would become very large, and the efficient parallelization will be difficult for both matrix solvers and the computation of non-linear terms.

Iterative solvers only require a function that compute the result of applying a linear operator on a vector. The function could be complicated, with spherical transforms involved, although it would make it costly. This makes it possible to design matrix-free time schemes, where no matrix is ever formed, saving a lot of memory. One must however bear in mind that iterative methods like GMRES are efficient only if we have a good preconditioner (an approximate of the inverse of our linear operator). Generic preconditioners (like ILU) require a matrix representation of the linear operator, which we would rather avoid. Or we could leave the azimuthal coupling outside the preconditionner to keep small enough local matrices. We also plan to investigate other types of preconditioners in collaboration with Ludovic Métivier (LJK, Université de Grenoble).

Appendix A

Vitae

Nathanaël Schaeffer, 37 years.
Currently **chargé de recherche (CR1)** at CNRS – ISTerre UMR 5275

Studies and diplomas

Juin 1996 : Bac S, mention bien.

1996-98 : CPGE à Strasbourg (PC*), intégration de l'ENS Lyon.

1998-01 : Magistère des Sciences de la Matière à l'ENS Lyon, mention bien.

2000-01 : DEA en Mécanique des Fluides (Centrale Lyon / EPF Lausanne), mention très bien.

2001-04 : Thèse : Instabilités, turbulence et dynamo dans une couche de fluide cisaillée en rotation, (LGIT, Grenoble) avec Philippe Cardin et Henri-Claude Nataf, soutenue le 10/12/2004.

Academic career

2005 : Post-doc at LGIT (Grenoble) : Quasi-geostrophic turbulence. (10 months).

2005-06 : Post-doc at IRPHE (Marseille) : Elliptic instability (1 year).

2006-07 : Post-doc at CEA Cadarache : Plasma stability in Tokamaks (13 months).

déc. 2007– : Chargé de Recherche at ISTerre (ex-LGIT), Grenoble.

A.1 Teaching & advising

PhD theses

- Simon Cabanes, 2011–2014, TUE, H-C Nataf + N Schaeffer : Contributions des fluctuations turbulentes au champ magnétique induit dans une expérience en sodium liquide.
- Jérémie Vidal, 2014–, TUE, N Schaeffer + D Cébron : Forçages mécaniques et déformations topographiques dans les noyaux planétaires: écoulements et dynamo.

Post-docs

- Aldo Figueroa 2011, H-C Nataf + N Schaeffer. Simulations numériques de l'expérience DTS (Couette sphérique magnétisé en sodium liquide).
- Elliot Kaplan 2015, H-C Nataf + N Schaeffer. Simulations numériques et turbulence dans l'expérience DTS.

Internships

- Marie Drouard 2011, **M2R** TUE, F Plunian + N Schaeffer : Régime de propagation d'ondes dans un modèle de noyau terrestre.
- Jérémie Vidal 2014, **M2R** TUE, N. Schaeffer : Ondes quasi-géostrophiques en présence de stratification à l'interface noyau-manteau.
- Marie Parrens 2009, **M1** TUE, N Schaeffer : Les inversions du champ magnétique terrestre.
- Marie Parrens 2009 **M1** TUE, F Plunian + N Schaeffer (stage d'été optionnel) : Prédiction du nombre de tâches solaires
- Alexandre Capron 2013 **M1**, Ondes de torsion d'Alfvén dans le noyau terrestre : influence de la conductivité du manteau.
- Patrick Zitzke 2014 **M1** ENS Lyon, F Plunian + N Schaeffer : Analysis and editing of geodynamo simulation data.
- Rizka Zakiah Drajat 2015 **M2R** TUE, L Métivier + N Schaeffer : Comparison of Numerical Time-stepping Schemes for Inertial Waves Model in the Earth's Core.

Lectures

2009-2014 : Lecture "*Dynamique des Fluides Géophysiques*" in the M2R TUE of Université Joseph Fourier (Grenoble).

2010 : Lecture "Géodynamo" for *l'école doctorale TUE* (Grenoble).

2010 : Invited lecture for *l'École thématique systèmes complexes*, Rennes (France) : "Magnétohydrodynamique & Dynamo : Turbulence et Ordre"

A.1.1 Other responsibilities

Team leader of the geodynamo team since September 2012. On January the 1st, 2015, the team was made of 8 researchers, and 3 engineers.

Reviewer for *Geophysical Research Letters*, *Geophysical Journal International*, *Journal of Fluid Mechanics*, *Earth and Planetary Science Letters*, *Physics of the Earth and Planetary Interiors*, *Physics of Fluids*, *Progress in Earth and Planetary Science*, *Astronomy & Astrophysics*.

Communication correspondant for the laboratory from 2009 to 2011.

A.2 Publications

- 18 articles published in peer-reviewed journals (rang A)
- 276 citations (google scholar)
- h-index 9 (google scholar)

A.2.1 Refereed articles

Schaeffer, N., Lora Silva, E., Pais, M. A., (2016). "Can Core Flows inferred from Geomagnetic Field Models explain the Earth's Dynamo?" In: *Geophysical Journal International*.

Pais, M. A., Morozova, A. L., **Schaeffer, N.,** (2015). "Variability modes in core flows inverted from geomagnetic field models". In: *Geophysical Journal International* 200.1, pp. 402–420.

Vidal, J., **Schaeffer, N.,** (2015). "Quasi-geostrophic modes in the Earth's fluid core with an outer stably stratified layer". In: *Geophysical Journal International* 202.3, pp. 2182–2193.

Cabanes, S., **Schaeffer, N.**, Nataf, H.-C., (2014a). "Magnetic induction and diffusion mechanisms in a liquid sodium spherical Couette experiment". In: *Physical Review E* 90.4, p. 043018.
— (2014b). "Turbulence Reduces Magnetic Diffusivity in a Liquid Sodium Experiment". In: *Physical Review Letters* 113, p. 184501.
Marti, P., **Schaeffer, N.**, Hollerbach, R., Cébron, D., Nore, C., Luddens, F., Guermond, J.-L., Aubert, J., Takehiro, S., Sasaki, Y., (2014). "Full sphere hydrodynamic and dynamo benchmarks". In: *Geophysical Journal International* 197.1, pp. 119–134.
Figueroa, A., **Schaeffer, N.**, Nataf, H.-C., Schmitt, D., (2013). "Modes and instabilities in magnetized spherical Couette flow". In: *Journal of Fluid Mechanics* 716, pp. 445–469.
Schaeffer, N., (2013). "Efficient spherical harmonic transforms aimed at pseudospectral numerical simulations". In: *Geochemistry, Geophysics, Geosystems* 14.3, pp. 751–758.
Guervilly, C., Cardin, P., **Schaeffer, N.**, (2012). "A dynamo driven by zonal jets at the upper surface: Applications to giant planets". In: *Icarus* 218.1, pp. 100–114.
Monteux, J., **Schaeffer, N.**, Amit, H., Cardin, P., (2012). "Can a sinking metallic diapir generate a dynamo?" In: *Journal of Geophysical Research: Planets* 117.E10.
Schaeffer, N., Jault, D., Cardin, P., Drouard, M., (2012). "On the reflection of Alfvén waves and its implication for Earth's core modeling". In: *Geophysical Journal International* 191.2, pp. 508–516.
Gillet, N., **Schaeffer, N.**, Jault, D., (2011). "Rationale and geophysical evidence for quasi-geostrophic rapid dynamics within the Earth's outer core". In: *Physics of the Earth and Planetary Interiors*.
Schaeffer, N., Pais, M. A., (2011). "On symmetry and anisotropy of Earth-core flows". In: *Geophysical Research Letters* 38.10.
Schaeffer, N., Le Dizès, S., (2010). "Nonlinear dynamics of the elliptic instability". In: *Journal of Fluid Mechanics* 646, pp. 471–480.
Roy, C., **Schaeffer, N.**, Le Dizès, S., Thompson, M., (2008). "Stability of a pair of co-rotating vortices with axial flow". In: *Physics of Fluids* 20, p. 094101.
Schaeffer, N., Cardin, P., (2006). "Quasi-geostrophic kinematic dynamos at low magnetic Prandtl number". In: *Earth and Planetary Science Letters* 245.3-4, pp. 595–604.
— (2005a). "Quasigeostrophic model of the instabilities of the Stewartson layer in flat and depth-varying containers". In: *Physics of Fluids* 17, p. 104111.

Schaeffer, N., Cardin, P., (2005b). "Rossby-wave turbulence in a rapidly rotating sphere". In: *Nonlinear Processes in Geophysics* 12.6, pp. 947–953.

Schaeffer, N., Manga, M., (2001). "Interaction of rising and sinking mantle plumes". In: *Geophysical research letters* 28.3, pp. 455–458.

A.2.2 Book chapter

Nataf, H.-C.**, Schaeffer, N.,** (2015). "8.06 - Turbulence in the Core". In: *Treatise on Geophysics (Second Edition)*. Ed. by G. Schubert. Second Edition. Oxford: Elsevier, pp. 161–181.

A.2.3 Invited talks

Schaeffer, N., Fournier, A., Jault, D., Aubert, J., (2015a). "High resolution geodynamo simulations with strongly-driven convection and low viscosity". In: *EGU General Assembly*. Vienna (Austria), p. 7376.

— (2015b). "High resolution geodynamo simulations with strongly-driven convection and low viscosity". In: *AGU/CGU Joint Assembly*. Montreal (Canada).

Schaeffer, N., (2015). "Geodynamo Simulations with XSHELLS + SHTns". In: *Geodynamo Benchmarking Workshop*. Boulder, Colorado.

Schaeffer, N., Fournier, A., Aubert, J., Jault, D., Plunian, F., Zitzke, P., (2014). "Rotating dynamo turbulence: theoretical and numerical insights". In: *Mathematics of Turbulence: Geophysical and Astrophysical Turbulence*. IPAM, Los Angeles (USA).

Fournier, A.**, Schaeffer, N.**, Aubert, J., (2012). "Fast transients in 3D dynamo models". In: *AGU Fall Meeting*. San Francisco (US).

Schaeffer, N., Drouard, M., Gillet, N., Jault, D., Pais, A., Plunian, F., (2011). "Quasi-Geostrophic Flows in the Earth Core as a Source for the Secular Variation". In: *EGU*. Vienna (Austria).

A.2.4 Software

Developed and distributed under the free software CeCILL Licence:

SHTns is a high performance library for Spherical Harmonic Transform written in C, aimed at numerical simulation (fluid flows, mhd, ...) in spherical geometries. This library is used by researchers from various fields, as shown by the citations to the associated paper (Schaeffer, 2013).

XSHELLS is a high performance simulation code for the rotating Navier-Stokes equation in spherical shells, optionally coupled to the induction and temperature equation. A user manual is available.

A.2.5 Participation to conferences

I attended many international conferences. For the past 5 years, I have been to EGU (2015), AGU/CGU (2015), ETC14 (2013), SEDI (2012), EGU (2011), EPSC-DPS (2011), and CNFGG (2010).

Appendix B

Selection of papers

Physics of the Earth and Planetary Interiors 202–203 (2012) 78–88

Contents lists available at SciVerse ScienceDirect

Physics of the Earth and Planetary Interiors

journal homepage: www.elsevier.com/locate/pepi

Rationale and geophysical evidence for quasi-geostrophic rapid dynamics within the Earth's outer core

Nicolas Gillet, Nathanaël Schaeffer *, Dominique Jault

ISTerre, CNRS, Université Joseph-Fourier, BP 53, 38041 Grenoble Cedex 9, France

ARTICLE INFO

Article history:
Available online 22 June 2012
Guest edited by: Keke Zhang.
Edited by: M. Jellinek

Keywords:
Earth's core
Quasi-geostrophy
Geomagnetic secular variation
Core flow

ABSTRACT

We present arguments supporting the hypothesis that the flow in the Earth's core, for the time scales of the historical secular variation, is well described by a quasi-geostrophic (QG) model, almost invariant along the rotation axis. A previous study showed that for axisymmetric motions, the dimensionless number appropriate to compare magnetic and rotation forces is independent of magnetic diffusivity, increases with decreasing length scales, and takes value much smaller than unity for lengths about 10^6 m. Here, we extend this result to non-axisymmetric motions, and give a criterion for QG to hold based on length scale, rotation rate and magnetic field intensity. The numerical simulations exhibit a columnar behaviour at parameters representative of the Earth's core, supporting the quasi-geostrophic hypothesis for fast, large length-scale motions. In addition, we present the results of several inversions of the core flow from geomagnetic field models, showing that (a) the energy of the motions symmetrical with respect to the equatorial plane represents about 80% of the total energy when no symmetry is assumed a priori; (b) for the same number of parameters, an equatorially symmetric (QG) flow model explains more of the secular variation than a flow without specified geometry.

1. Background geophysical knowledge

Combining the accuracy of satellite observations (Lesur et al., 2008; Olsen et al., 2009) and the quasi-geostrophic (QG) hypothesis for rapid core flows has made possible a much improved description of the core surface flows responsible for the secular variation (SV) of the Earth's magnetic field. Thus, Pais and Jault (2008) argued for the presence of a planetary scale, eccentric and anticyclonic gyre within the Earth's fluid core. Also, using an ensemble approach to account for the large scale (harmonic degree less than 13) secular variation produced from the invisible small scale radial magnetic field gave a realistic estimate of the variance of the core flow coefficients (Gillet et al., 2009). Moreover, using magnetic field data from the pre-satellite era together with the quasi-geostrophic hypothesis, gave indications on the temporal spectrum of the core flows (Gillet et al., 2010a). Finally, the QG hypothesis has been shown to be compatible with abrupt secular variation changes recorded at observatories (Gillet et al., 2009).

However, the QG hypothesis can be challenged. Recent studies about either the chemical interactions between the Earth's lower mantle and the fluid outer core (Buffett and Seagle, 2010), or the density of the topmost 300 km of the outer core inferred from observed seismic wave speeds (Helffrich and Kaneshima, 2010), have sparked renewed investigations of a stratified layer at the top of the core. If the stratification is strong enough, the motions in the layer should be decoupled from the interior flow with small horizontal scale (Takehiro and Lister, 2001). There is also some evidence that the heat flux at the core-mantle boundary is not laterally uniform (Lay et al., 2008). Then, a steady thermal wind could be driven at the top of the core (Amit et al., 2008) and may contribute to the geomagnetic secular variation. Finally, it has been suggested, on the basis of geodynamo numerical simulations, that magnetic diffusion plays an important role in the geomagnetic secular variation (Amit and Christensen, 2008). But it is in the context of negligible magnetic diffusion that the QG core flow hypothesis has been advocated (Jault, 2008).

Therefore, we find it important to introduce new empirical tests of the quasi-geostrophic core flow hypothesis. We follow different lines of argument. At the core surface, QG flows are particular tangentially geostrophic (TG, Le Mouël, 1984) core flows that are symmetrical with respect to the equatorial plane outside the trace C, at the core surface, of the tangent cylinder (the cylinder tangent to the inner core and parallel to the rotation axis). Furthermore, QG flows do not cross the two curves C. Hence, we can compare how well QG and TG core surface flows individually predict the observed secular variation for different epochs. From calculations of TG core flows, we can also simply investigate whether QG flows

DOI of original article: http://dx.doi.org/10.1016/j.pepi.2011.01.005
* Corresponding author. Tel.: +33 476 635 180.
E-mail addresses: nathanael.schaeffer@gmail.com, nicolas.gillet@obs.ujf-grenoble.fr (N. Schaeffer).

0031-9201/$ - see front matter © 2011 Elsevier B.V. All rights reserved.
http://dx.doi.org/10.1016/j.pepi.2012.03.006

are predominant in the TG solutions. Furthermore, we can study whether the proportion of QG flows among the calculated TG flows increases with the accuracy of magnetic field data. For that latter purpose, we have found it necessary to use a magnetic field model which includes the last decades and accurately records the successive improvements of observatory series.

Lehnert (1954) introduced the number

$$\lambda_\ell = \frac{B}{\ell\Omega\sqrt{\rho\mu_0}}, \tag{1}$$

which measures the ratio between the inertial wave period and the Alfvén wave period, and gives the magnitude of the magnetic force relative to the rotation force when magnetic diffusion is unimportant (Ωe_z is the rotation vector with e_z the unit vector along the rotation axis, ℓ is the characteristic length-scale, B the magnetic field strength, ρ the density and μ_0 the free space magnetic permeability). The Lehnert number λ_ℓ is of the order of 510^{-4} in the Earth's core for $\ell\sim10^6$ m and B of the order of a few mT (Aubert et al., 2009; Gillet et al., 2009, 2010a). Jault (2008) gave different examples drawn from the literature of the occurrence of axially invariant flows in spherical shells for small values of λ_ℓ. He also investigated numerically the fluid response, in a rapidly rotating spherical shell permeated by an axisymmetric (with respect to e_z) magnetic field, to an impulsive rotation of the inner sphere. That transient response amounts to the propagation of two geostrophic shear layers from the tangent cylinder towards the equator of the outer sphere on the one hand and the rotation axis on the other hand. It contrasts with the zonal motions produced by a steady forcing, in which case the appropriate number to compare magnetic and rotation forces is the Elsasser number $\Lambda = \sigma B^2/\rho\Omega$ instead of the Lehnert number (σ is the electrical conductivity). For $\Lambda > O(1)$, the contours of equal differential rotation tend to follow the magnetic field lines of force, following Ferraro's law. In this paper, we generalize the study of Jault (2008) to non axisymmetric magnetic fields. We obtain again geostrophic shear layers propagating away from the tangent cylinder but also, superimposed on the geostrophic circulation, motions that are not axisymmetric. We find that they are mostly quasi-geostrophic for $\lambda_\ell \ll 1$.

After a brief introduction of the quasi-geostrophic approximation, we devote the following section to the numerical study, whereby we document the emergence of transient quasi-geostrophic flows for $\lambda_\ell \ll 1$. We argue in the fourth section that our core flow inversions support the QG hypothesis. The description of the magnetic field model that we have used for this study is left for the Appendix C. In the last section, we discuss important open questions.

2. The quasi-geostrophic approximation

The quasi-geostrophic approximation was first developed in the context of thin fluid geophysical envelopes (ocean, atmosphere, see e.g. Gill, 1982). It was later on adapted to thick spherical shells such as the Earth's outer core (Hide, 1966). QG models have given physical insight into the dynamics of rotating systems with varying height parallel to the axis or, in the case of thin shells, varying inclination of the rotation vector with respect to the local vertical. That latter ingredient is at the origin of phenomena such as Rossby waves, or generation of zonal motions through anisotropic turbulence (Smith and Waleffe, 1999; Read et al., 2004). It sets the QG model apart from a simple two-dimensional Navier–Stokes flow.

The quasi-geostrophic equations govern the evolution of the geostrophic velocity field $\boldsymbol{u}^g$ that satisfies the geostrophic equilibrium:

$$2\Omega\boldsymbol{e}_z \times \boldsymbol{u}^g = -\nabla\Pi^g \;\Rightarrow\; \boldsymbol{u}^g = \frac{1}{2\Omega}\boldsymbol{e}_z \times \nabla\Pi^g(s,\phi). \tag{2}$$

($\boldsymbol{e}_s, \boldsymbol{e}_\phi, \boldsymbol{e}_z$) are unit vectors in the cylindrical coordinates (s, ϕ, z), and Π^g is the reduced geostrophic pressure. The so-called barotropic flow $\boldsymbol{u}^g$ satisfies to the Proudman–Taylor constraint, $\partial\boldsymbol{u}^g/\partial z = 0$. The flow and pressure fields are completed by an ageostrophic (or baroclinic) component $\boldsymbol{u}^a$ and Π^a:

$$[\boldsymbol{u}, \Pi](s,\phi,z,t) = [\boldsymbol{u}^g, \Pi^g](s,\phi,t) + [\boldsymbol{u}^a, \Pi^a](s,\phi,z,t). \tag{3}$$

We find from (2) that $\boldsymbol{u}^g$ is divergence-free, which implies

$$\nabla\cdot\boldsymbol{u}^a = 0. \tag{4}$$

The QG model offers a way to investigate dynamics in a spherical shell, such as the Earth's core. It is formally justified for small Rossby numbers $Ro = \frac{\mathcal{U}}{\Omega\ell}$, where $\mathcal{U}$ is the typical velocity. The Coriolis term associated with the ageostrophic flow $\boldsymbol{u}^a$ in the momentum equation cannot remain unbalanced. *The QG approach consists in neglecting the ageostrophic contributions in the momentum equation that regroups the main perturbations to*(2)*, except for the Coriolis and pressure terms*:

$$\frac{d\boldsymbol{u}^g}{dt} + 2\Omega\boldsymbol{e}_z\times\boldsymbol{u}^a = -\nabla\Pi^a + \frac{\boldsymbol{F}}{\rho} + \nu\nabla^2\boldsymbol{u}^g. \tag{5}$$

$\boldsymbol{F}$ stands for the bulk forces and ν is the kinematic viscosity. Note that baroclinic instabilities are filtered in the above momentum equation. However, even in contexts where it does not formally apply ($Ro\sim1$, presence of baroclinic waves), the QG approximation happens to give a useful framework, as shown by Williams et al. (2010).

Taking the curl of (5), in order to eliminate the pressure gradient, averaging along the z component, and taking advantage of the incompressibility condition (4), permits to write an equation for the geostrophic pressure:

$$\frac{d}{dt}\nabla^2\Pi^g + \frac{\beta}{s}\frac{\partial\Pi^g}{\partial\phi} = \frac{\Omega}{\rho H}\int_{-H}^{+H}\boldsymbol{e}_z\cdot(\nabla\times\boldsymbol{F})dz + \nu(\nabla^2)^2\Pi^g, \tag{6}$$

for which we have used the boundary condition

$$\boldsymbol{u}\cdot\boldsymbol{e}_{r|z=\pm H} = 0 \Rightarrow \forall(s,\phi), \quad \boldsymbol{u}_{z|\pm H} = \pm\frac{dH}{ds}\boldsymbol{u}^g_s. \tag{7}$$

$H(s) = \sqrt{r_o^2 - s^2}$ is the half-height of a fluid column, ($\boldsymbol{e}_r$, $\boldsymbol{e}_\theta$, $\boldsymbol{e}_\phi$) are unit vectors in spherical coordinates (r, θ, ϕ), and r_0 is the outer core radius. The slope of the container, which enters the expression for the parameter $\beta(s) = (2\Omega/H)(dH/ds)$, is at the origin of Rossby waves.

Eq. (6) must be coupled to an equation for the source term (density anomaly for buoyancy, magnetic field for the Lorentz force). Some variants of the QG set of equations for magnetized fluids, in which variations of the magnetic field with respect to z are ignored, have been put forward (Hide, 1966; Busse and Finocchi, 1993; Diamond et al., 2007). They formed the basis of numerical models of the outer core rapid dynamics (Hide, 1966) and of the solar tachocline (Tobias et al., 2007). Canet et al. (2009) relied on the z-averaging of the Lorentz forces, as Gillet et al. (2007) before them, in order to write modified QG equations valid for a more general magnetic field in a spherical shell. Their model requires $\lambda_\ell \ll 1$ and that the field is much weaker at the fluid boundaries than in the interior. It has not been studied numerically yet.

As derived above, the QG model also gives an insight on the ageostrophic flow: crossing (5) with $\boldsymbol{e}_z$ before taking the z-derivative and eliminating the pressure term, through another application of (5), gives:

$$\frac{\partial\boldsymbol{u}^a_e}{\partial z} = \frac{1}{2\rho\Omega}\boldsymbol{e}_z\times\left[\nabla_e\boldsymbol{F}_z - \frac{\partial\boldsymbol{F}_e}{\partial z}\right]. \tag{8}$$

This is the thermal or magnetic wind equation, depending on $\boldsymbol{F}$. In the presence of axial variations of the magnetic field, the flows, which participate to the magnetostrophic balance (Taylor, 1963;

Table 1
Parameters for the numerical experiments. Λ and λ are based on the maximum value of the magnetic field in the fluid domain. The root-mean-squared values of these numbers is displayed for information. n_{max} and m_{max} are the truncation degree and order of the spherical harmonic expansion, N_r is the number of radial grid points.

Case	n_{max}	m_{max}	N_r	E_m	Λ	Λ_{rms}	λ	λ_{rms}	S
A	240	20	600	5.7×10^{-8}	15	1.5	9.1×10^{-4}	2.9×10^{-4}	1.6×10^{4}
B	240	20	600	5.7×10^{-8}	2	0.2	3.4×10^{-4}	1.1×10^{-4}	6.0×10^{3}
C	240	20	1000	1.0×1.0^{-8}	12	1.2	3.4×10^{-4}	1.1×10^{-4}	3.4×10^{4}

Fearn, 1998) between Coriolis and magnetic forces, also present variations with respect to the z coordinate. Nonetheless, these can be considered as part of the QG model defined above. In the QG framework, the contribution of the magnetostrophic flows to$\partial \boldsymbol{u}/\partial t$ is omitted.

Neglecting the vertical shear in (8) implies that u_z^a varies linearly with z, as a result of (4). Then using (7), we are able to describe the vertical flow not only at the boundaries, but also in the core interior:

$$\forall (s,\phi,z), u_z^a(s,\phi,z) = \frac{z}{H}\frac{dH}{ds} u_s^g(s,\phi). \tag{9}$$

Here, we have considered a fluid element outside the cylindrical surface tangent to the inner core (see Pais and Jault, 2008 for the QG equations valid inside the tangent cylinder). In some sense, by using (2) and (9) to describe the flow we focus on the rapidly changing barotropic motions.

Hence, from a kinematical point of view, a QG velocity field is characterized by (*i*) equatorial components u_s and u_ϕ independent of z, and (*ii*) a vertical component u_z that obeys Eq. (9). Pais and Jault (2008) (see their section 4.3) show that theses two conditions imply the tangential geostrophy constraint at the core-mantle boundary:

$$\nabla_H \cdot (\boldsymbol{u}\ cos\ \theta) = 0. \tag{10}$$

At this point, we have enough information to continue the velocity fields $\boldsymbol{u}(\theta, \phi)$ calculated at the core surface into the core interior, provided (i) that the surface velocity obeys (10), (ii) that it is symmetrical with respect to the equatorial plane outside the tangent cylinder, and (iii) that

$$u_\theta\left(\arcsin\left(\frac{r_i}{r_0}\right), \phi\right) = 0, \tag{11}$$

where r_i is the inner core radius.

Schaeffer and Cardin (2005) proposed an alternative derivation of the QG approximation in a sphere, whereby the equatorial flow $\boldsymbol{u}_e$ is assumed to be z-invariant, the vertical flow u_z is still deduced from u_s using (9), but

$$\nabla \cdot \boldsymbol{u}_e = -\frac{\partial u_z}{\partial z}, \tag{12}$$

whereas definition (2) yields $\nabla \cdot \boldsymbol{u}_e^g = 0$ instead. At the core surface and outside the tangent cylinder, (12) and (9) imply the constraint $\nabla_H \cdot \boldsymbol{u} = 2 \tan\theta u_\theta$, first derived by Amit and Olson (2004) as the "columnar flow" constraint (see their Appendix A). Pais and Jault (2008) remarked that (9) and (12) imply a different constraint (their expression A8) inside the tangent cylinder TC. Thus, a consistent implementation of (12) requires either two different descriptions of the velocity field, respectively, inside and outside TC or ignoring the solid inner core altogether. Outside the tangent cylinder, Pais and Jault (2008) have found no major difference between flow models derived using either (2) or (12).

3. Quasi-geostrophic transient motions

We already know from the previous study of Jault (2008) that transient axisymmetric motions that arise in a sphere permeated by an axisymmetric magnetic field are geostrophic and thus remarkably invariant along the rotation axis, even though the imposed magnetic field is not. Here, we extend this result to non-axisymmetric flows and magnetic fields. All the numerical experiments involve an electrically conducting fluid that occupies a spherical shell that is rotating at angular velocity $\boldsymbol{\Omega}$ and is immersed in an imposed steady magnetic field $\boldsymbol{B}_0$. From a state of rest in the rotating frame (neglecting a possible background flow $\boldsymbol{U}_0$), we then perform a small and short displacement of the conducting inner sphere around the axis of rotation. The angular velocity of the inner sphere reaches a maximum value $\Delta\Omega$ and slows down back to rest during a few global rotation periods $T_\Omega = 2\pi/\Omega$. In contrast with the previous study of Jault (2008), $\boldsymbol{B}_0$ is not purely axisymmetric, leading to non-axisymmetric fluid motions.

Our three-dimensional spherical code (using second order finite differences in radius, pseudo-spectral spherical harmonic expansion and an Adams–Bashforth scheme in time) performs the time-stepping of the momentum equation of the fluid and of the induction equation, both in the conducting solid inner body and in the fluid spherical shell. We use no-slip boundary conditions. The region outside the spherical shell is electrically insulating and the solid inner body has the same electrical conductivity as the liquid in the spherical cavity.

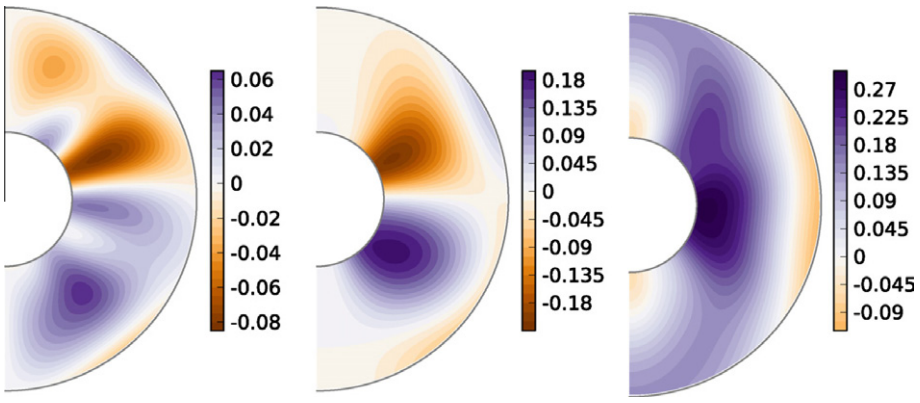

Fig. 1. Meridional cross-section of the imposed magnetic field, in max($|\boldsymbol{B}_0|$) units. From left to right the cylindrical components (s, ϕ, z) of the magnetic field at $\phi = 25°$.

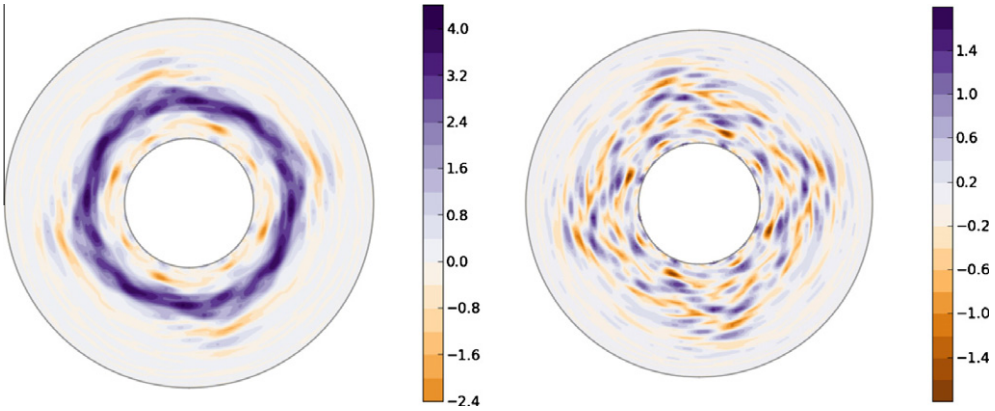

Fig. 2. Equatorial cross-section of azimuthal component of the total (left) and non-axisymmetric (right) velocity field u_ϕ at $t = 183T_\Omega$ after the impulse (case A). The velocities are in units of $r_o\Delta\Omega/1000$.

Choosing the outer core radius r_o as the length-scale, $B_0 = \max(|\boldsymbol{B}_0|)$ as the magnetic field unit, the Alfvén time $\tau_a = r_o\sqrt{\rho\mu_0}/B_0$ as the time-scale, and B_0^2/μ_0 as the pressure unit, we obtain the following non-linear dimensionless equations for the perturbations of the fluid velocity field $\boldsymbol{u}$ and of the magnetic field $\boldsymbol{b}$:

$$\frac{d\boldsymbol{u}}{dt} + \frac{2}{\lambda_{r_0}}\boldsymbol{e}_z \times \boldsymbol{u} = -\nabla\Pi + (\boldsymbol{j} + \boldsymbol{J}_0) \times (\boldsymbol{b} + \boldsymbol{B}_0) - \boldsymbol{J}_0 \times \boldsymbol{B}_0 + \frac{p_m}{S}\nabla^2\boldsymbol{u} \tag{13}$$

$$\frac{\partial \boldsymbol{b}}{\partial t} = \nabla \times [(\boldsymbol{u} + \boldsymbol{U}_f) \times (\boldsymbol{B}_0 + \boldsymbol{b})] + \frac{1}{s}\nabla^2\boldsymbol{b}, \tag{14}$$

where Π is the reduced pressure, $\boldsymbol{j} = \nabla \times \boldsymbol{b}$ and $\boldsymbol{J}_0 = \nabla \times \boldsymbol{B}_0$ are the electrical currents associated respectively with the induced and imposed magnetic field. The imposed velocity field of the solid inner sphere is $\boldsymbol{U}_f(t) = r\sin\theta\Delta\Omega\exp[-(t/T_f - 3)^2]\boldsymbol{e}_\phi$ for $r < r_i$ with $T_f = 5T_\Omega$. Since the amplitude of $\Delta\Omega$ is tiny, the nonlinear inertial term $(\boldsymbol{u}\cdot\nabla)\boldsymbol{u}$ does not play any important role. Note also that the model does not include the Lorentz force $\boldsymbol{J}_0 \times \boldsymbol{B}_0$ that drives the background flow $\boldsymbol{U}_0$ omitted in this study.

The Lundquist number $S = \tau_\eta/\tau_a = r_oB_0/\eta\sqrt{\rho\mu}$, ratio of the magnetic dissipation time $\tau_\eta = r_{o2}/\eta$ to the Alfvén wave time-scale, is of the order of 10^5 in the Earth's core, with η the magnetic diffusivity. The magnetic Prandtl number $P_m = \nu/\eta$, which is the ra-

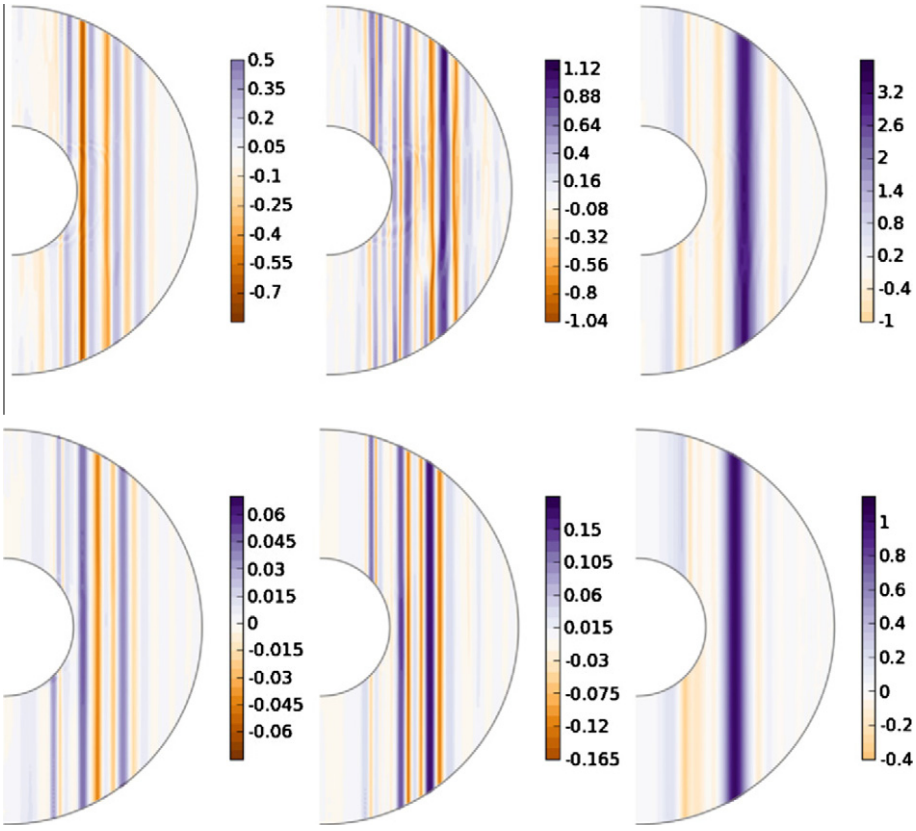

Fig. 3. Meridional cross-sections of the velocity field. From left to right: the non-axisymmetric components of the velocity field u_s (cylindrical radial) and u_ϕ (azimuthal) at $\phi = 25°$; and the axisymmetric component $u_\phi^{m=0}$. Velocities are in units of $r_o\Delta\Omega/1000$. Top: case A at $t = 183T_\Omega$ after the impulse. Bottom: case B at $t = 366T_\Omega$ after the impulse.

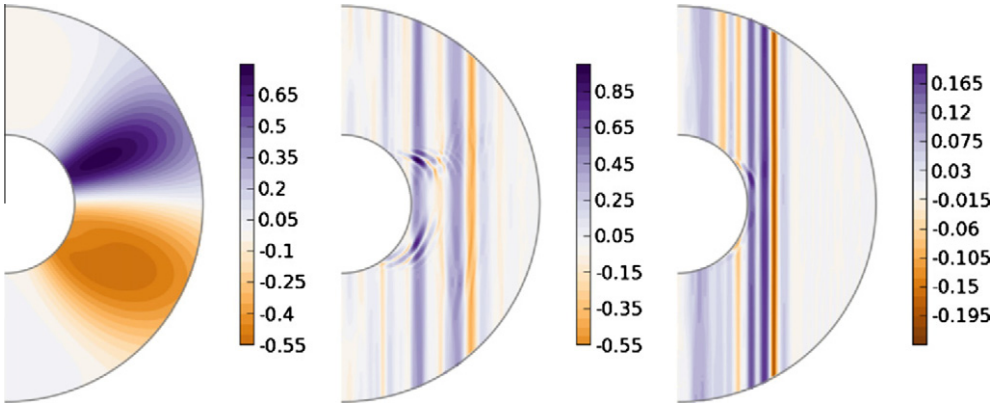

Fig. 4. Meridional cross-section at $\phi = 0^\circ$, where the magnetic field almost reaches its strongest intensity. Left: cylindrical radial component of the imposed magnetic field. Middle to right, cylindrical radial component u_s for cases A and B, respectively at $t = 183T_\Omega$ and $t = 366T_\Omega$ after the impulse. The magnetic field is in max($|B_0|$) units. Velocities are in units of $r_o\Delta\Omega/1000$.

tio of the viscous over magnetic dissipation times, is of the order of 10^{-5} in the Earth's core. To keep as close as possible to the Earth, we use an aspect ratio $r_i/r_o = 0.35$. The magnetic field intensity is chosen such that $10^{-4} \leq \lambda \leq 10^{-3}$, the magnetic diffusivity such that $10^3 \leq S \leq 10^4$ and $\Lambda = O(1)$. These three parameter values are chosen to be similar to those found in the Earth's core. As a consequence we reach magnetic Ekman number $E_m = \lambda/S = \eta/\Omega r_{o2} < 10^{-7}$. To keep the problem computationally tractable, we set $Pm = 1$. Table 1 gives the parameter values for the different numerical experiments.

The imposed magnetic field $\boldsymbol{B}_0$ is composed of an axisymmetric part (1/3 of the magnetic energy) and a non-axisymmetric part (2/3 of the magnetic energy) that has an azimuthal wave number $m = 4$. There are no other symmetries imposed (the field contains both equatorially symmetric and antisymmetric components, see Appendix A for details). Meridional cross sections of the imposed field $\boldsymbol{B}_0$ are displayed in Fig. 1.

At the very beginning, just after the short displacement of the inner-core, most of the signal consists of inertial waves mainly propagating inside the tangent cylinder. Their effect is to quickly (in a few rotation periods $T_\Omega = 2\pi/\Omega$) form two strongly z-invariant, mostly axisymmetric and zonal jets, that propagate slowly as torsional Alfvén waves (Braginsky, 1970) away from the equator of the inner core. As already shown by Jault (2008), the axisymmetric component is geostrophic. We thus focus on the non-axisymmetric part of the flow, which arises because of the non-zonal component of the imposed magnetic field. It is illustrated with the equatorial cross-section shown in Fig. 2 for case A.

Fig. 3 displays meridional cross-sections of the non-zonal flow for the cases A and B, respectively 183 and 366 T_Ω after the impulse. The flow contours are almost z-invariant: the quasi-geostrophic hypothesis holds well for transient non-axisymmetric motions, even though the Elsasser number Λ reaches values up to 15 (see Table 1).

There are, however, localized motions which are not z-invariant. Fig. 4 shows, for the cases A and B, the cylindrical radial velocity at the same time but in another meridional cross-section where the magnetic field is locally about ten times stronger than in the cross-sections previously shown in Fig. 3. The QG hypothesis is locally violated in areas where the Elsasser number is about 10 and the local Lehnert number (based on the local length scale of the flow) is about 0.01.

For the same meridional plane, a more quantitative description is given by the velocity profiles of Fig. 5 for the strongest magnetic field case (case A, $\phi = 0$, where the Elsasser number based on the maximum B_s in this plane would be about $\Lambda_{\rm loc} = 6.3$). It seems that the large scales of the flow are more z-invariant than its small scales.

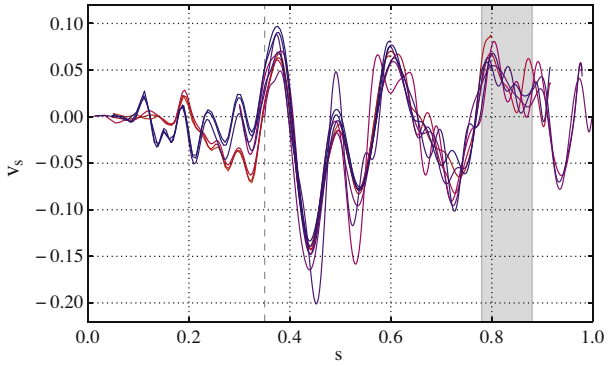

Fig. 5. Velocity profiles (u_s) as a function of cylindrical radius for different fixed height ($-0.8 \leq z \leq 0.8$ with steps of 0.2, from blue to red) after $366T_\Omega$, and at $\phi = 0^\circ$ for case A. The shaded area indicates the location of the main torsional wave, and the velocities are in units of $r_o\Delta\Omega/1000$. (For interpretation of the references to colour in this figure legend, the reader is referred to the web version of the article.)

Fig. 6 (case A) further contrasts the large scale and the small scale motions. The former are outstandingly z-invariant whereas the latter manifestly deviate from quasi-geostrophy. This result can be interpreted in terms of the value of the local Lehnert number (Eq. (1)), which depends on the length scale. Quasi-geostrophy holds well, in Fig. 6, for length scales larger than 0.08 which means $\lambda_\ell \lesssim 0.01$. Of course, this also corresponds to an Elsasser number, and in order to discriminate between a limit given by the Elsasser number or by the Lehnert number, we use a filtering technique (see Appendix B) to determine the length scale above which the flow is QG. The results, reported in Table 2, show that non-QG flow arise when the local Lehnert number $\lambda_{\rm loc} \lesssim 0.01$, with no influence of the Elsasser number. A similar estimation is provided by Jault (2008) in the axisymmetrical case. Applied to the Earth core, we would expect the liquid iron flow of length scale larger than 5×10^4 m to be strongly QG, corresponding to a spherical harmonic degree at the core surface of about 200.

We have thus exhibited flows that are both quasi-geostrophic and non axisymmetric, excited by an impulse on the rotation of the inner core. We find that the flows are even more QG when they are large length-scale as anticipated from the expression (1) for the Lehnert number. This also implies that the small scale, non-QG flows dissipate faster than the large scale QG flow. All our findings support the idea that the large scale flow in the Earth core should be quasi-geostrophic. In the following section, we search for empirical evidence of quasi-geostrophy of the large scale core flows inferred from geomagnetic data.

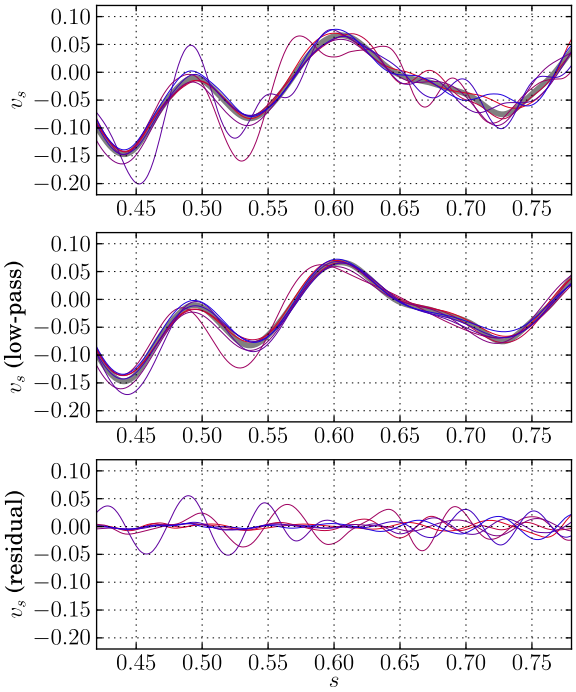

Fig. 6. The data of Fig. 5 in the range $s\epsilon[0.42, 0.78]$ (top), after filtering out the scales smaller than 0.08 (middle), and the residual small scales (bottom). The bold grey curve is a z-average excluding the two most differing curves. Most of the departure from QG is contained in the small scales.

4. Tangentially versus quasi-geostrophic surface core flow models

From the magnetic model obtained in Appendix C, we derive time-dependent core flow models spanning from year 1840.5 to 2008. The spherical harmonic representation $m(t)$ of the Earth's magnetic field is considered as "data". It is used only up to degree $N_b = 11$, since high degree coefficients are controlled by damping. The flow is calculated at the core surface. There, its toroidal and poloidal expansions (see e.g. Holme, 2007) $\boldsymbol{u}(t) = \{t_{nm}^{s,c}(t), s_{nm}^{s,c}(t)\}_{n\epsilon[1,N_u],m\epsilon[0,n]}$, truncated at degree $N_u = 22$, are expanded in time onto the same cubic B-spline basis as that used for the magnetic model. We follow an ensemble approach (Gillet et al., 2009), with ensemble size $K = 20$, to account for the impact on the secular variation of unresolved main field coefficients of degree $n \in [N_b + 1, \ldots, 3N_b]$. We generate a set of random, time-correlated small-scale magnetic field models $\{\tilde{\mathbf{m}}^k(t)\}_{k=1,\ldots,K}$. For each realization in the ensemble, flow coefficients are linked to magnetic field coefficients through the forward problem

$$\partial_t \mathbf{m} = \mathsf{A}(\mathbf{m} + \tilde{\mathbf{m}}^k)\boldsymbol{u}^k + \boldsymbol{e}^k, \tag{15}$$

where $\mathbf{e}^k$ is the secular variation errors vector. We use a strong form (Jackson, 1997; Gillet et al., 2009) to impose the tangentially geostrophic constraint (10) (Le Mouël, 1984). Extra topological constraints on the core surface flow derived from the QG approximation (equatorial symmetry outside the tangent cylinder plus zero cylindrical radial flow at the tangent cylinder) are applied with a weak form (Pais and Jault, 2008; Gillet et al., 2009). We then minimize a penalty function of the form

$$J(\boldsymbol{u}^k) = \frac{1}{t_e - t_s}\int_{t_s}^{t_e} \{\left\|\partial_t \mathbf{m} - \mathsf{A}(\mathbf{m} + \tilde{\mathbf{m}}^k)\boldsymbol{u}^k\right\|_{\mathsf{C_m}}^2 + \alpha\|\boldsymbol{u}^k(t)\|_{\mathsf{R}}^2 + \mu\|\boldsymbol{u}^k(t)\|_{\mathsf{Q}}^2\}dt \tag{16}$$

with the generic notation $\|\mathbf{v}\|_{\mathsf{M}^2} = \mathbf{v}^T\mathsf{M}^{-1}\mathbf{v}$. A constant noise level of 10 $(\mathrm{nT/y})^2$ at the Earth surface has been considered to calculate the covariance matrix $\mathsf{C_m}$. Diagonal elements of the regularization matrix R are proportional to $(2n+1)/[n(n+1)]^2$, i.e. we use a penalization function intermediate between the kinetic energy norm and the "strong" norm (Holme, 2007). The TG and QG models analysed in the remaining of this section have been obtained with Eq. (16) and a coefficient α multiplying the regularizing norm set as $\alpha = 10^{-5}$. We have previously noticed that the average of the ensemble of realizations, obtained using this norm, presents weak sensitivity to the damping parameter α over a wide range of α for degrees $n \leq 10$ (Gillet et al., 2009). TG flows are obtained with $\mu = 0$, whereas for QG flows μ is set to a value large enough so that the solution does not vary when μ is further increased.

We first investigate the equatorial symmetry of the calculated TG flows. We note that the relative proportion of the flow component symmetrical about the equatorial plane (ES) increases with time as the data become more accurate (Fig. 7). We also plot the kinetic energy spectra for recent epochs (Fig. 8). The energy of the flow component antisymmetrical about the equatorial plane (EA) is smaller than the energy associated with ES coefficients at low harmonic degrees ($n < 10$), as was already qualitatively remarked, 20 years ago, by Hulot et al. (1990) who wrote that their EA flows present no apparent global organization. We also find that most of EA coefficients are not resolved, since their dispersion is larger than their average value.

Then we compare the ability of TG and QG flows to account for the observed SV. We calculate surface core flows and then only keep the coefficients of degree $n \leq N$ of the resulting models. The part of the SV which is not explained by the flow models – the misfit – decreases with N. We thus obtain a relationship between the

Table 2
For the three different parameter set, we have determined the length scale δ_{QG} above which the flow is QG, and the corresponding Lehnert number (expression (1)). Even though the Elsasser number spans almost one decade, λ_δ does not vary significantly.

Case	E_m	Λ	λ	δ_{QG}	λ_δ
A	5.7×10^{-8}	15	9.1×10^{-4}	0.10	9.1×10^{-3}
B	5.7×10^{-8}	2	3.4×10^{-4}	0.04	8.5×10^{-3}
C	1.0×10^{-8}	12	3.4×10^{-4}	0.05	7.5×10^{-3}

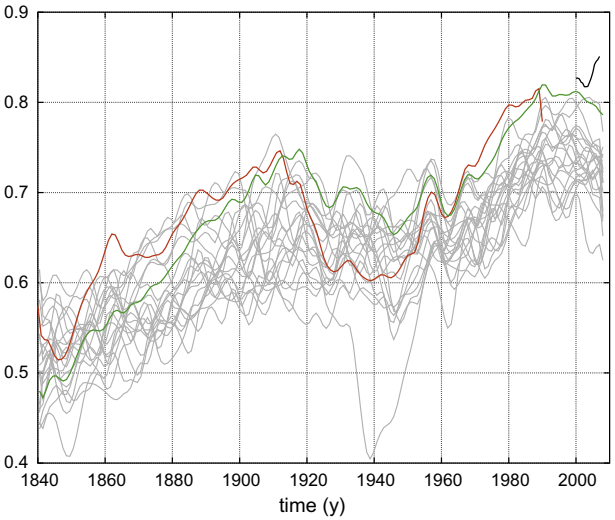

Fig. 7. Time evolution of the fraction of ES kinetic energy for average TG flow models built from *gufm1* (red), xCHAOS (black) and the model proposed in Appendix C (green). In grey: time evolution of the fraction of ES kinetic energy for all the realisations of flow obtained with our model. (For interpretation of the references to colour in this figure legend, the reader is referred to the web version of the article.)

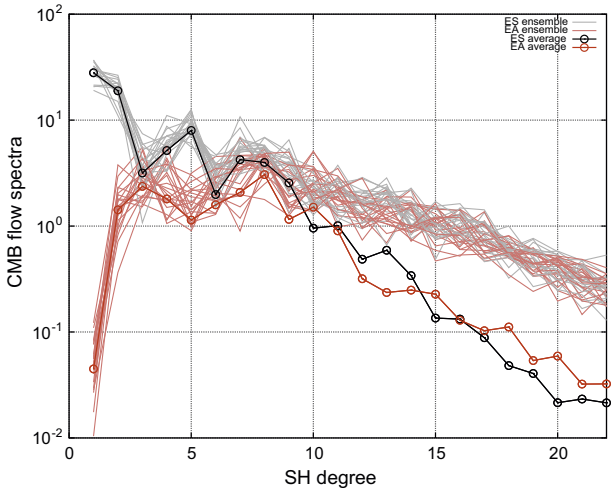

Fig. 8. CMB flow spectra (time averaged over 1990–2000) for TG models: EA (red circles: average, light red: ensemble) and ES (black circles: average, grey: ensemble) flow components, in $(km/y)^2$.

number P of coefficients of the truncated flow model and the misfit (see Appendix D for the calculation of P for TG and QG flow models). Fig. 9 shows that for the same value of P, QG flows show a better fit to SV data than TG flows. This result is significant as the average flow models do not depend on the damping parameter for the resolved low degrees. As a consequence there is no difficulty for QG flows to predict sharp SV changes at observatory locations, as illustrated in Fig. 10, and the delays observed for such events that depend on the observatory latitude or longitude (see e.g. Pinheiro and Jackson, 2008) cannot be used as an argument against the QG hypothesis.

We have already observed that the ES component of TG flows is enhanced when the quality of geomagnetic data, thus the accuracy of geomagnetic models, improves. Assuming this equatorial symmetry when calculating QG flows, we also find that the average of the ensemble of core flow models becomes more and more energetic as data quality increases, leaving less and less flow coefficients unconstrained. This is illustrated in Fig. 11 that displays, as a function of time, the ratio between kinetic energies in the dispersion and the average of the ensemble, a kind of noise/signal ratio in the flow reconstruction. The decrease in the dispersion in the ensemble indicates that SV models are more easily predicted under the QG hypothesis when they are better constrained by geomagnetic data: when SV models are better constrained by geomagnetic data, less dispersion is observed in the ES component. We have checked that this observation does not depend on the choice of damping parameter α. Gillet et al. (2009) had already pointed out this improving ability of QG flows at predicting SV data for the period 1960–2002, looking at the time evolution of the misfit between SV data and predictions. We extend here this analysis over the past 150 years. Our diagnostic is more rigorous than that used by Gillet et al. (2009), since the normalized quantity shown in Fig. 11 is less impacted by the 60–80 years apparent pulsation present in geomagnetic time series (Roberts et al., 2007).

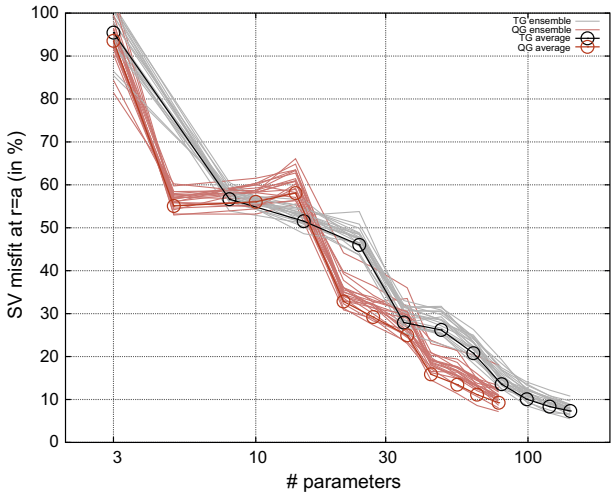

Fig. 9. Misfit to the SV data (time averaged over 1990–2000) as a function of the number of parameters for TG (black circles: average, grey: ensemble) and QG (red circles: average; light red: ensemble) flow models truncated at different harmonic degrees. (For interpretation of the references to colour in this figure legend, the reader is referred to the web version of the article.)

5. Geophysical and methodological perspectives

Our numerical models do suggest that large scale transient flows in the Earth's core are mostly quasi-geostrophic. We have not, however, accounted for the magnetostrophic velocity, which is formally part of the QG model (Eq. (8)). Extensions of our numerical model are thus desirable. Before restoring the $\boldsymbol{J}_0 \times \boldsymbol{B}_0$ term that we have neglected, we need to ensure that the prescribed magnetic fields used for the numerical experiment is in a Taylor state, namely that the circulation of the Lorentz force along geostrophic contours vanish when integrated over any geostrophic cylinder (Taylor, 1963; Livermore et al., 2010). Otherwise, fast geostrophic torsional waves will first develop. It would enable us to specify both the length scale and time scale at which the flow ceases to be axially invariant. We may also estimate the range of parameters for which the QG hypothesis holds by studying freely decaying turbulence or the response to a small scale turbulent forcing. As an example, one can wonder whether dipole changes on centennial time scales can be the result of QG dynamics (see the difficulty to reproduce the dipole trend from TG flow predictions according to Jackson, 1997).

For the purpose of this study, we have focused on the z-invariance of the motions that arise in our numerical experiment. However, as we pointed out in Section 2, there are two different variations of the quasi-geostrophic model, leading to slightly different constraints on core-surface flows, especially in the equatorial region and in the vicinity of the tangent cylinder. Three-dimensional numerical simulations will be useful in pondering the validity of these constraints.

The ensemble technique of Gillet et al. (2009) was originally developed for satellite magnetic field models. In that context, there is a relatively well defined truncation level $N_b \backsimeq 13$ above which the magnetic field emanating from the core experiences too much geometric attenuation to be measurable at the Earth's surface in the presence of the crustal field. Here, we have only changed N_b to $N_b = 11$ to adapt the technique to a model derived from observatory and land survey data. That modification does not suffice to take the poor distribution of this type of data into account satisfactorily. Our suggestion is to forgo the customary but non-physical strong regularization of magnetic field models (as noted by Backus, 1988) and to generate the ensemble of magnetic field models used to calculate core flows from the covariance matrix of the field coefficients (following the stochastic approach of McLeod, 1996). That approach requires prior information on the magnetic field coefficients. A solution consists of extrapolating the empirical spatial spectra of the magnetic field and its secular variation calculated for low spherical harmonic degrees from recent satellite data to all degrees up to an arbitrarily large truncation degree. We plan

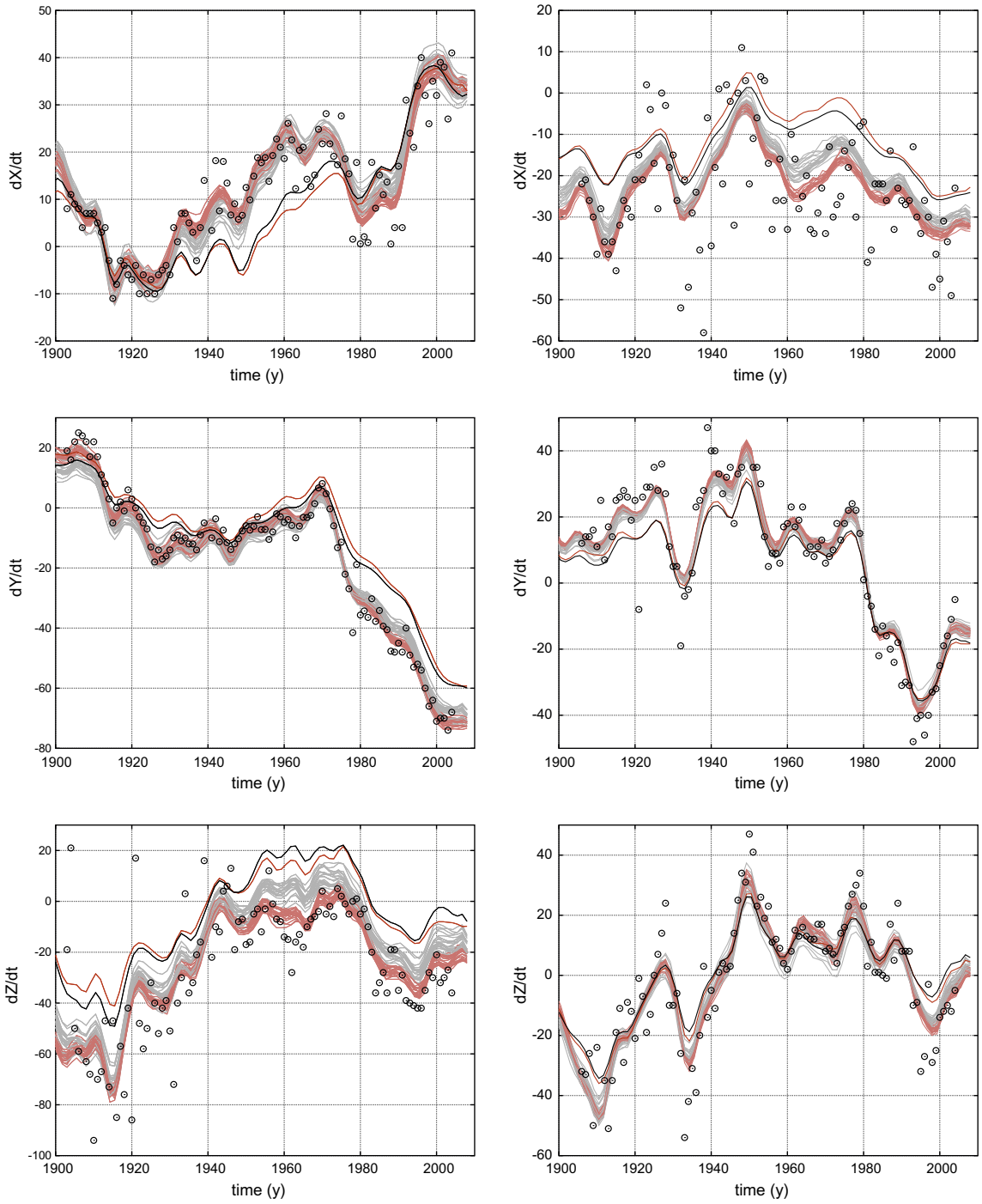

Fig. 10. Comparison between SV predictions and first differences of annual means (black circles) recorded at the Sitka (Northern America, left) and Apia (South West Pacific, right) observatories in the X (top), Y (middle) and Z (bottom) directions. Full lines correspond to predictions from QG flow models obtained with damping parameters $\alpha = 10^{-5}$ (ensemble: light red; average: red) and $\alpha = 10^{-4}$ (ensemble: grey; average: black). (For interpretation of the references to colour in this figure legend, the reader is referred to the web version of the article.)

then to reconsider the comparison between the observed and predicted length-of-day (LOD) changes over the 20th century. Indeed, the ensemble of core flows that are discussed in this paper tend to over predict the actual LOD changes. This is an indication that the largest scales of our time-varying flows have too high a velocity, probably as a consequence of the physically unjustified penalization of the small scale flows. As noted by Gillet et al. (2010b), the high degree SV coefficients of models derived from land data are less variable than the low degree coefficients which may unduly yield too variable large scale modelled core flows. Hopefully, introducing a priori information on the variability of the Gauss coefficients may counter that undesirable effect.

Acknowledgements

We are very grateful to Christopher Finlay and Andy Jackson for sharing with us the updated magnetic data sets used to build our magnetic model. We thank Phil Livermore, whose review helped

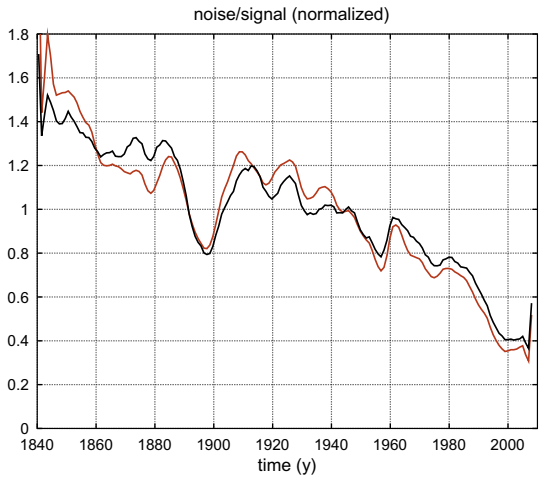

Fig. 11. Time evolution of the ratio between the kinetic energy of the dispersion in the ensemble (variance) and the kinetic energy of the ensemble average, for damping parameters $\alpha = 10^{-5}$ (black) and $\alpha = 10^{-4}$ (red). Since our inversion technique only provides a relative estimate of the variance in the ensemble of core flow models (see Gillet et al., 2010a, supplementary information) we normalized both curves by their time average in order to obtain a meaningful comparison. (For interpretation of the references to colour in this figure legend, the reader is referred to the web version of the article.)

improve the quality of the manuscript. This work has been supported by grants from the French Agence Nationale de la Recherche, Research programme VS-QG (Grant Number BLAN06-2.155316) and Centre National d'Études Spatiales. The simulations were run at the Service Commun de Calcul Intensif de l'Observatoire de Grenoble (SCCI).

Appendix A. The imposed magnetic field

Explicitly, we set $\boldsymbol{B}_0 = \nabla \times \nabla \times (P\mathbf{r})$ with

$$P = (j_1(\beta_{11} r) - 0.3 j_1(\beta_{12} r)\left(Y_1^0 + \alpha \frac{1}{81} r^2 Y_9^4\right) - 0.2 j_3(\beta_{31} r)\left(Y_3^0 + \alpha \frac{1}{144} r^2 Y_{12}^4\right) \quad \text{(A1)}$$

(r, θ, ϕ) are the spherical coordinates. The j_n's are the spherical Bessel functions of the first kind, with β_{nk} the k-th root of j_{n-1}. $Y_n^m(\theta, \phi,)$ is the Schmidt semi-normalized spherical harmonic of degree n and order m. Finally, α is a parameter that allows us to adjust the ratio of axisymmetric over non-axisymmetric components. In this study, $\alpha = 1$ whilst $\alpha = 0$ would reproduce the field of Jault (2008).

Appendix B. Length scale separation in the numerical solution

In our spherical code, the fields are defined by their spherical harmonic coefficients $A_l^m(r)$. Defining a spatial scale δ and the corresponding fractional spherical harmonic degree $l_\delta(r) = \pi r/\delta$, we can compute

$$\hat{A}_l^m(r) = e - (l^2/3l(2/\delta)(r))\left(\int e^{-3}(r'-r)^2/\delta^2 dr'\right)^{-1} \times \int A_l^m(r') e^{-3}(r'-r)^2/\delta^2 dr' \quad \text{(A2)}$$

which has the scales smaller than δ almost isotropically filtered out. δ_{QG} is then the smallest δ for which the cylindrical components of the flow along the ϕ and s direction do not show any significant variation in the z direction.

Appendix C. The geomagnetic model for 1840–2008 used in the study

In order to document the impact, on core flow models reconstructed from geomagnetic field models, of increases in data quality that occured in the past century (use of proton magnetometers after 1960, digital acquisition introduced in the following decades), our study requires a continuous historical model covering the past century or so. This also makes possible to directly compare flow reconstructions estimated from models derived with or without satellite data of the past decade. Among the available models, *gufm1* (Jackson et al., 2000) ends in 1990, whereas CM4 (Sabaka et al., 2004) only starts in 1960 and ends in 2002. We then decided to build an ad hoc new model covering 1840.5–2008 using a conventional approach. It starts in 1840 when intensity data become available (Gubbins et al., 2006; Finlay, 2008). We use extended data sets compared to that used for *gufm1*, adding in particular: first differences of observatory annual means up to 2006, and

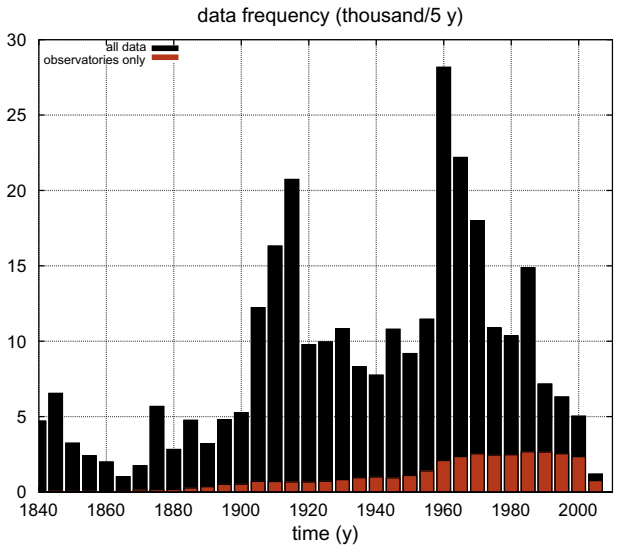

Fig. C1. Data frequency as a function of time, for all data (black), and observatory annual means only (red). (For interpretation of the references to colour in this figure legend, the reader is referred to the web version of the article.)

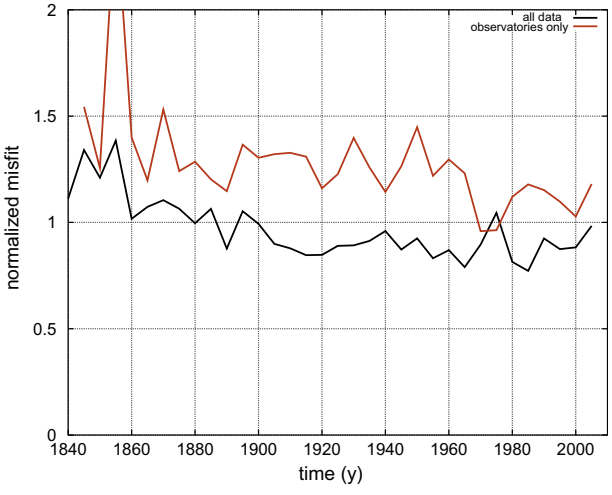

Fig. C2. Normalized misfit $\mathcal{M}$ as a function of time, for all data (black), and observatory annual means only (red). (For interpretation of the references to colour in this figure legend, the reader is referred to the web version of the article.)

survey data up to 2005 from the BGS website (courtesy Susan MacMillan). The temporal evolution of the data frequency is displayed in Fig. C1.

As the method we follow is very similar to that used to build *gufm1*, we only recall here the main features. Under the insulating mantle hypothesis, the magnetic field derives from a potential. We perform a classical (Langel, 1987) spherical harmonics decomposition (degree n, order m) of the radial magnetic field B_r at the core-mantle boundary, with truncation degree $N = 14$. It defines the magnetic model $\mathbf{m}(t) = \{g_{nm}^{s,c}(t)\}_{n\epsilon[1,N],m\epsilon[0,n]}$. The time representation is similar to that of *gufm1*, using cubic B-spline basis (De Boor, 2001) with knots every 2.5 years regularly spanning $[t_s, t_e] = [1840.5, 2008]$. $\mathbf{y}^o = \{y_i\}_{i=1,\dots,N^o}$ is the data vector, with N° the number of data. The geomagnetic forward problem is $\mathbf{y}^o = \mathrm{H}(\mathbf{m}) + \mathbf{e}^o$, with $\mathbf{e}^\circ$ the data error vector (with the associated error covariance matrix C) and H the forward operator (see e.g. Gubbins and Roberts, 1983; Bloxham et al., 1989). We minimize a penalty function of the form

$$J(\mathbf{m}) = \chi^2 + \frac{1}{t_e - t_s}\int_{t_s}^{t_e} \{\alpha_s \|\mathbf{m}(t)\|_{\mathrm{R_s}}^2 + \alpha_T \|\mathbf{m}(t)\|_{\mathrm{R_T}}^2\} dt. \tag{C1}$$

$\chi^2 = \| \mathbf{y}^o - \mathrm{H(m)} \|_{\mathrm{C_2}}$ is the measure of the misfit to the data, with the notation $\|\mathbf{x}\|_{\mathrm{M}^2} = \mathbf{x}^T\mathbf{M}^{-1}\mathbf{x}$. $\mathrm{R_S}$ is the spatial damping matrix corresponding to the heating norm (Gubbins, 1975). $\mathrm{R_T}$ is the temporal damping matrix penalizing for second time derivative (or secular acceleration) $\partial_{t2}B_r$.

Our model is rather conservative: damping parameters $(\alpha_S, \alpha_T) = (10^{-10}, 5 \times 10^{-2})$ have been chosen such that main field (MF), secular variation (SV) and secular acceleration (SA) norms and spectra are close to those obtained for *gufm1* (see Figs. C3 and C4). This choice of damping parameters provides a normalized misfit $\mathcal{M} = \sqrt{\chi^2/N^o}$ close to unity. Its temporal evolution is displayed in Fig. C2. The CMB power spectra and norms for the main field are defined as

$$\mathcal{S}_{mf}(n,t) = (n+1)\left(\frac{a}{c}\right)^{2n+4} \sum_{m=0}^{N} \left[g_{nm}^s(t)^2 + g_{nm}^c(t)^2\right], \tag{C.2}$$

$$\mathcal{N}_{mf}(t) = \sqrt{4\pi \sum_{n=1}^{N} \frac{n+1}{2n+1} \mathcal{S}_{mf}(n,t)}, \tag{C.3}$$

with similar expressions for the SV and SA.

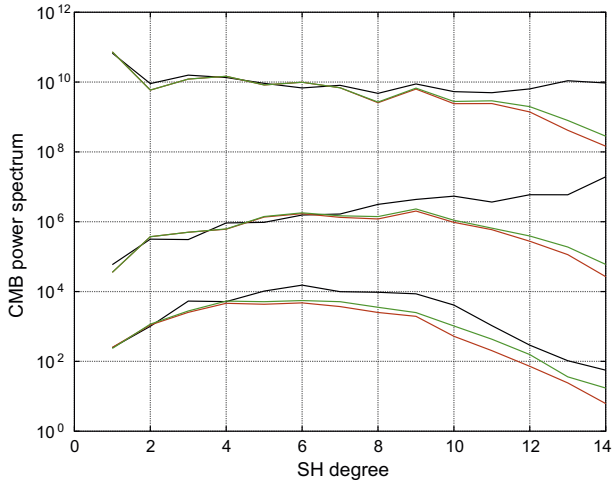

Fig. C3. From top to bottom: MF (nT^2), SV (nT^2/y^2) and SA (right, nT^2/y^4) spectra, time averaged respectively over 1900–1980 for the model derived for this work (green) and *gufm1* (red), and over 2000–2006 for xCHAOS (black). (For interpretation of the references to colour in this figure legend, the reader is referred to the web version of the article.)

Appendix D. The number of parameters for TG and QG flow models

There are $N_u(N_u + 4)$ independent constraints for a TG model expanded up to degree N_u, so that remain N_{u2} degrees of freedom (Le Mouël et al., 1985; Jackson, 1997). However, $2N_u$ constraints involve the poloidal coefficients $s_{N_u,m\neq 0}^{s,c}$, which are set to zero. These

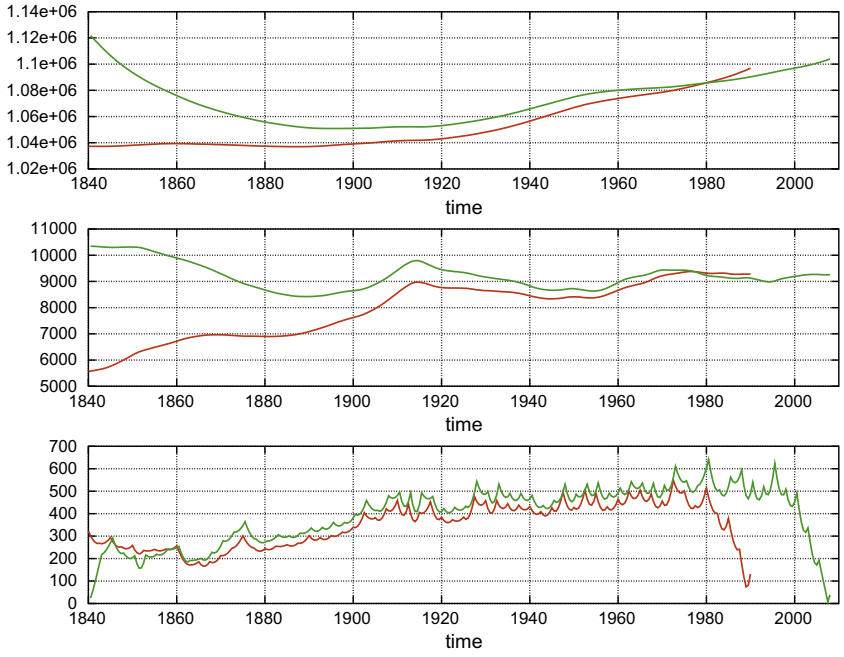

Fig. C4. From top to bottom: magnetic field (nT), secular variation (nT/y) and secular acceleration (right, nT/y^2) norms for the model used in this study (green) and *gufm1* (red). (For interpretation of the references to colour in this figure legend, the reader is referred to the web version of the article.)

cannot be calculated with the geostrophic chain (see Backus and Le Mouël, 1986) as they require coefficients of degree $n > N_u$ that do not enter the flow model description. As a consequence, when truncating such a model at degree $N \leq N_u$, one actually finds that TG flow models contain $P = N(N+2)$ independent coefficients. We approximate P for QG flows as the number of ES coefficients of a TG flow truncated at the degree N: $P = N(N+3)/2$ for N even and $P = N(N+3)/2 + 1$ for N odd. That estimate is not exact as we do not impose the equatorial symmetry constraint inside the tangent cylinder (which leaves more degrees of freedom, but concerns a small area), and we impose a constraint on the cylindrical radial flow at the tangent cylinder (which reduces the degrees of freedom)

References

Amit, H., Aubert, J., Hulot, G., Olson, P., 2008. A simple model for mantle-driven flow at the top of Earth's core. Earth Planet. Space 60, 845–854.

Amit, H., Christensen, U., 2008. Accounting for magnetic diffusion in core flow inversions from geomagnetic secular variation. Geophys. J. Int. 175 (3), 913–924.

Amit, H., Olson, P., 2004. Helical core flow from geomagnetic secular variation. Phys. Earth Planet. Inter. 147, 1–25.

Aubert, J., Labrosse, S., Poitou, C., 2009. Modelling the palaeo-evolution of the geodynamo. Geophys. J. Int. 179, 1414–1428. http://dx.doi.org/10.1111/j.1365-246X.2009.04361.x.

Backus, G.E., 1988. Bayesian inference in geomagnetism. Geophys. J. 92, 125–142.

Backus, G.E., Le Mouël, J.-L., 1986. The region on the core-mantle boundary where a geostrophic velocity field can be determined from frozen-flux magnetic data. Geophys. J. R. Astron. Soc. 85, 617–628.

Bloxham, J., Gubbins, D., Jackson, A., 1989. Geomagnetic secular variation. Phil. Trans. R. Soc. Lond. A 329, 415–502.

Braginsky, S.I., 1970. Torsional magnetohydrodynamic vibrations in the Earth's core and variations in day length. Geomag. Aeron. 10, 1–8.

Buffett, B., Seagle, C., 2010. Stratification of the top of the core due to chemical interactions with the mantle. J. Geophys. Res. 115 (B4), B04407.

Busse, F., Finocchi, F., 1993. The onset of thermal convection in a rotating cylindrical annulus in the presence of a magnetic field. Phys. Earth Planet. Inter. 80 (1–2), 13–23.

Canet, E., Fournier, A., Jault, D., 2009. Forward and adjoint quasi-geostrophic models of the geomagnetic secular variation. J. Geophys. Res. 114, B11101. http://dx.doi.org/10.1029/2008JB006189.

De Boor, C., 2001. A practical guide to splines. Appl. Math. Sci. 27, Springer, New York.

Diamond, P., Itoh, S., Itoh, K., Silvers, L., 2007. β-plane MHD turbulence and dissipation in the solar tachocline. In: Hughes, D., Rosner, R., Weiss, N. (Eds.), The Solar Tachocline. Cambridge University Press, pp. 213–239.

Fearn, D., 1998. Hydromagnetic flow in planetary cores. Rep. Prog. Phys. 61, 175.

Finlay, C.C., 2008. Historical variations of the geomagnetic axial dipole. Phys. Earth Planet. Int., 70.

Gill, A.E., 1982. Atmosphere–Ocean Dynamics. Academic Press, London.

Gillet, N., Brito, D., Jault, D., Nataf, H.-C., 2007. Experimental and numerical studies of magnetoconvection in a rapidly rotating spherical shell. J. Fluid Mech. 580, 123–143.

Gillet, N., Jault, D., Canet, E., Fournier, A., 2010a. Fast torsional waves and strong magnetic field within the Earth's core. Nature 465, 74–77.

Gillet, N., Lesur, V., Olsen, N., 2010b. Geomagnetic core field secular variation models. Space Sci. Rev. 155 (1), 129–145. http://dx.doi.org/10.1007/s11214-009-9586-6.

Gillet, N., Pais, M.A., Jault, D., 2009. Ensemble inversion of time-dependent core flow models. Geochem. Geophys. Geosyst. 10 (6), Q06004. http://dx.doi.org/10.1029/2008GC002290.

Gubbins, D., 1975. Can the Earth's magnetic field be sustained by core oscillation? Geophys. Res. Lett. 2, 409–412.

Gubbins, D., Jones, A.L., Finlay, C., 2006. Fall in Earth's magnetic field is erratic. Science 312, 900–903.

Gubbins, D., Roberts, N., 1983. Use of the frozen flux approximation in the interpretation of archeomagnetic and paleomagnetic data. Geophys. J. R. Astron. Soc. 73, 675–687.

Helffrich, G., Kaneshima, S., 2010. Outer-core compositional stratification from observed core wave speed profiles. Nature, 807–810.

Hide, R., 1966. Free hydromagnetic oscillations of the Earth's core and the theory of geomagnetic secular variations. Phil. Trans. R. Soc. Lond. A 259, 615–646.

Holme, R., 2007. Large scale flow in the core. In: Olson, P., Schubert, G. (Eds.), Treatise in Geophysics. Core Dynamics, vol. 8, pp. 107–129.

Hulot, G., Le Mouël, J.-L., Jault, D., 1990. The flow at the core-mantle boundary: symmetry properties. J. Geomag. Geoelectr. 42, 857–874.

Jackson, A., 1997. Time-dependency of tangentially geostrophic core surface motions. Phys. Earth Planet. Inter. 103, 293–311.

Jackson, A., Jonkers, A.R.T., Walker, M.R., 2000. Four centuries of geomagnetic secular variation from historical records. Phil. Trans. R. Soc. Lond. A 358, 957–990.

Jault, D., 2008. Axial invariance of rapidly varying diffusionless motions in the Earth's core interior. Phys. Earth Planet. Int. 166, 67–76.

Langel, R.A., 1987. The main field. In: Jacobs, J.A. (Ed.), Geomagnetism, vol. I. Academic Press, London.

Lay, T., Hernlund, J., Buffett, B.A., 2008. Core-mantle boundary heat flux. Nat. Geosci. 1, 25–32.

Le Mouël, J.-L., 1984. Outer core geostrophic flow and secular variation of Earth's geomagnetic field. Nature 311, 734–735.

Le Mouël, J.-L., Gire, C., Madden, T., 1985. Motions of the core surface in the geostrophic approximation. Phys. Earth Planet. Inter. 39, 270–287.

Lehnert, B., 1954. Magnetohydrodynamic waves under the action of the Coriolis force. Astrophys. J. 119, 647–654.

Lesur, V., Wardinski, I., Rother, M., Mandea, M., 2008. GRIMM: the GFZ Reference Internal Magnetic Model based on vector satellite and observatory data. Geophys. J. Int. 173, 382–394.

Livermore, P., Ierley, G., Jackson, A., 2010. The construction of exact Taylor states. II: The influence of an inner core. Phys. Earth Planet. Int. 178, 16–26.

McLeod, M.G., 1996. Spatial and temporal power spectra of the geomagnetic field. J. Geophys. Res. 101, 2745–2763.

Olsen, N., Mandea, M., Sabaka, T.J., Tøffner-Clausen, L., 2009. CHAOS-2: a geomagnetic field model derived from one decade of continuous satellite data. Geophys. J. Int. 179, 1477–1487.

Pais, M.A., Jault, D., 2008. Quasi-geostrophic flows responsible for the secular variation of the Earth's magnetic field. Geophys. J. Int. 173, 421–443.

Pinheiro, K., Jackson, A., 2008. Can a 1-D mantle electrical conductivity model generate magnetic jerk differential time delays? Geophs. J. Int. 173, 781–792.

Read, P.L., Yamazaki, Y.H., Lewis, S.R., Williams, P.D., Miki-Yamazaki, K., Sommeria, J., Didelle, H., Fincham, A., 2004. Jupiter's and Saturn's convectively driven banded jets in the laboratory. Geophys. Res. Lett. 31. http://dx.doi.org/10.1029/2004GL020106.

Roberts, P.H., Yu, Z.J., Russel, C.T., 2007. On the 60-year signal from the core. Geophys. Astrophys. Fluid Dyn. 101 (1), 11–35.

Sabaka, T.J., Olsen, N., Purucker, M.E., 2004. Extending comprehensive models of the Earth's magnetic field with Oersted and CHAMP data. Geophys. J. Int. 159, 521–547.

Schaeffer, N., Cardin, P., 2005. Quasi-geostrophic model of the instabilities of the Stewartson layer in flat and depth varying containers. Phys. Fluids 17, 104111.

Smith, L.M., Waleffe, F., 1999. Transfer of energy to two-dimensional large scales in forced, rotating three-dimensional turbulence. Phys. Fluids 11, 1608–1622.

Takehiro, S., Lister, J., 2001. Penetration of columnar convection into an outer stably stratified layer in rapidly rotating spherical fluid shells. Earth Planet. Sci. Lett. 187 (3–4), 357–366.

Taylor, J.B., 1963. The magnetohydrodynamics of a rotating fluid and the Earth's dynamo problem. Proc. R. Soc. Lond. A 274, 274–283.

Tobias, S.M., Diamond, P.H., Hughes, D.W., 2007. β-plane magnetohydrodynamics turbulence in the solar tachocline. Astrophys. J. 667, 113–116.

Williams, P.D., Read, P.L., Haines, T.W.N., 2010. Testing the limits of quasi-geostrophic theory: application to observed laboratory flows outside the quasi-geostrophic regime. J. Fluid. Mech. 49, 187–203.

On symmetry and anisotropy of Earth-core flows

N. Schaeffer[1] and M. A. Pais[2]

Received 26 January 2011; revised 4 April 2011; accepted 6 April 2011; published 26 May 2011.

[1] Quasi-geostrophic (QG) flows are a recently developed and very promising paradigm for modeling decadal secular variation (SV). Here we examine the effects of allowing anisotropy and departures of the flow from quasigeostrophy. We perform dedicated numerical experiments of the flow dynamics and magnetic induction inside the Earth's liquid core at time scales characteristic of secular variation of the geomagnetic field. Obtained results motivate new flow inversion regularization featuring an equatorially anti-symmetric component superimposed to quasi-geostrophic columns, and stronger latitudinal than longitudinal flow gradients. Applying these constraints allows to explain the observed SV for the whole period 1840–2010, and most significantly, provides a clearly improvement in prediction for decadal length-of-day variations for the period 1980–2000. Furthermore, the trace of the inner-core appears clearly without any assumption for the 1997–2010 period covered by satellite geomagnetic data. Our results support QG being the appropriate description of the force balance within the core on decadal time scales and large spatial scales. **Citation:** Schaeffer, N., and M. A. Pais (2011), On symmetry and anisotropy of Earth-core flows, *Geophys. Res. Lett.*, *38*, L10309, doi:10.1029/2011GL046888.

1. Introduction

[2] The secular variation of the magnetic field of the Earth is due to the flow of liquid metal advecting the magnetic field inside the Earth's core. A large number of studies have focused on inference of the core surface flow from geomagnetic field data [*Holme*, 2007]. Recently, it has been advocated that Quasi-Geostrophic (QG) flows should give a good description of the flow in the core [*Jault*, 2008], and kinematic properties of this type of flow have already been used to constrain the core surface flow models inferred from magnetic field data to be symmetric with respect to the equator and purely azimuthal at the rim of the tangent cylinder [*Pais and Jault*, 2008; *Gillet et al.*, 2009].

[3] Still, some unclear points persist, and our study tries to shed some light on three of them: (i) The QG hypothesis has been justified for asymptotically small slopes [e.g., *Jones*, 2007], and the question arises as to its validity in the vicinity of the equator of both inner core and core-mantle boundary. For example, a flow crossing the equator line, like under the Indian ocean and Brazil in models where the tangential geostrophy of flows was not imposed [*Olsen and Mandea*, 2008], could not be captured by a QG model, which imposes a purely azimuthal flow at the equator. (ii) Even though the global amount of equatorial symmetry of core surface flow models has been in general increasing with time during the period 1840–2010 [*Gillet et al.*, 2011], no analysis has been made to identify which are the spatial features that can be associated to QG dynamics. (iii) Recent efforts have been made to also take into account the uncertainties due to the advection of an unknown small scale geomagnetic field by an unresolvable small scale flow [*Eymin and Hulot*, 2005; *Pais and Jault*, 2008]. However, these small scales are poorly constrained [*Gillet et al.*, 2009] and no useful information has been obtained from them. Underparameterization of core flow models due to regularizations penalizing too strongly small length scales may be the cause of the overestimation of decade length of day variations (ΔLOD) seen in most studies. We investigate the possibility that this may be due to aliasing of small scales (which do not carry angular momentum in the model we use [*Jault et al.*, 1988]) to large scales, by comparing estimations using different regularizations.

[4] The paper is organized as follows. Section 2 presents results of direct numerical simulations which serve as motivation to propose new core surface constraints in section 3. Specific features of our flow inversion are also stated there. The resulting core surface flow models are examined in section 4 and compared with previously published models by testing their ability in estimating ΔLOD. The mean flow model computed from CHAOS-3 is examined. A summary of our findings is presented in the Conclusion.

2. Direct Numerical Simulations

[5] In order to gain insight into the kinematics of the flow inside the Earth core, we run full three dimensional numerical simulations in a spherical shell of radius a, rotating at period $T = 2\pi/\Omega$, and with a solid inner core of radius $0.35a$. The conducting fluid of density ρ, viscosity ν and magnetic diffusivity $\eta = \nu$ is permeated by a constant, toroidal and axisymmetric magnetic field $\mathbf{B}_0 = B_0 \nabla \times (4r(a - r)\mathbf{r}/a^3)$, with B_0 such that the Lehnert number $\lambda = B_0(\sqrt{\mu_0 \rho} a \Omega)^{-1}$ (the ratio of the Alfvén wave to the inertial wave speeds) is set to 10^{-3}, close to its value inside the Earth's core. A small λ is important to resolve propagating inertial and Alfvén waves, both having a crucial role on SV dynamics [*Jault*, 2008]. We solve the Navier-Stokes equation (including the Coriolis and Lorentz force) together with the induction equation. The Ekman number $E = \nu(a^2\Omega)^{-1}$ is set to 10^{-6} and we use stress-free boundaries. The mantle and the inner-core are insulators in these calculations, although the boundary condition has no visible impact on the geometry of the flow. Details about the code are given by *Gillet et al.* [2011].

[6] The simulation is performed in two steps. First, from a state of rest, we impose a localized bulk force field $\mathbf{F}^{\pm}(\mathbf{r}) = F_0 \nabla \times [\mathbf{r} \exp(-|\mathbf{r} - \mathbf{r}_+|^2 / \delta^2) \pm \mathbf{r} \exp(-|\mathbf{r} - \mathbf{r}_-|^2 / \delta^2)]$, where $\mathbf{r}_\pm = (0.675a, \pi/4, \pm a/2)$ in cylindrical coordinates (s, ϕ, z)

[1]ISTerre, CNRS, University Joseph Fourier, Grenoble, France.
[2]CFC, Physics Department, University of Coimbra, Coimbra, Portugal.

0094-8276/11/2011GL046888

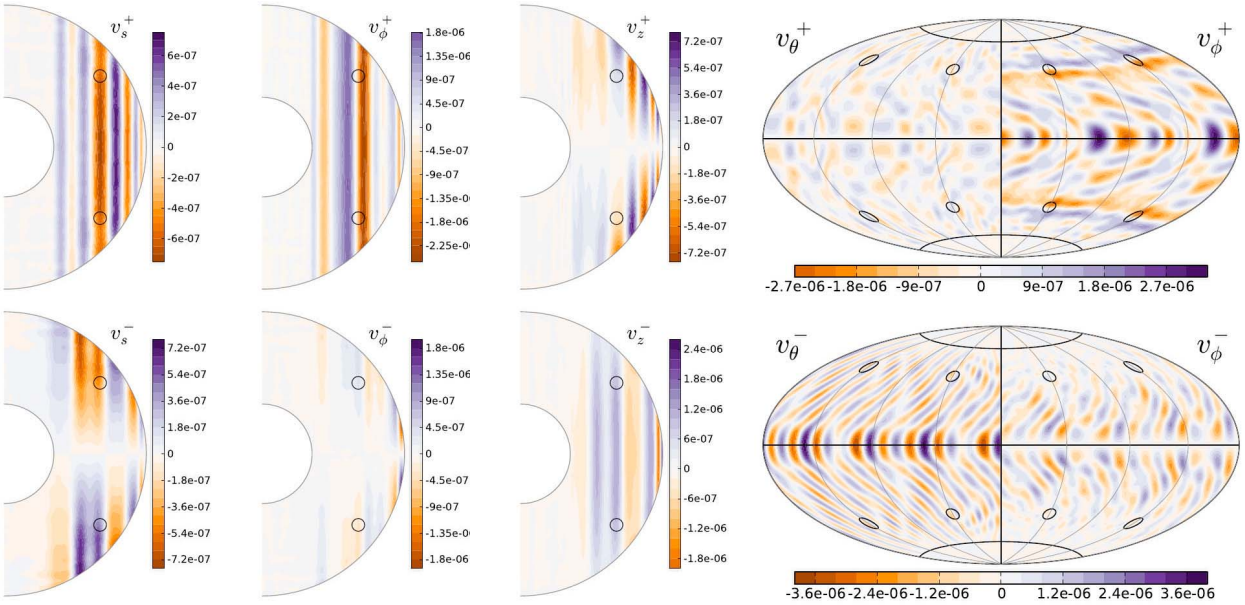

Figure 1. Flows resulting from a (top) symmetric or (bottom) anti-symmetric forcing followed by $110T$ of free decay. From left to right: the cylindrical components (v_s, v_ϕ, v_z) in the meridional plane containing $\mathbf{r}_\pm$, and the spherical components (v_θ, v_ϕ) at the core-surface (note on the right the use of a 4-fold symmetry in the simulation). The circles indicate the location of the applied forcing in the meridian plots, and its projection along the z-axis on the surface plots. The surface projection of the equator of the inner-core is also drawn. Velocities are expressed in units of $a\Omega$.

with origin O in the center of the sphere, and Oz parallel to the global rotation axis. The forcing length-scale is set to $\delta = 0.045a$, while its amplitude F_0 is chosen so that the resulting flow $\mathbf{v}$ is of low amplitude: $v \ll a\Omega$. After a duration $\Delta t = 6T$ allowing for the formation of Taylor columns through the propagation of inertial waves, we stop the forcing and let the flow freely decay during the second step of the simulation.

[7] Figure 1 shows the flow after 110 periods of free decay, in the two forcing cases: either symmetric ($\mathbf{F}^+$) or anti-symmetric ($\mathbf{F}^-$) with respect to the equator. We observe that these flows have undistinguishable decay rates. As expected for low values of λ, the symmetric forcing leads to a flow $\mathbf{v}^+$ that is nearly QG: v_s^+, v_ϕ^+ are independent of z, satisfying the Taylor-Proudman (TP) constraint $\partial_z \mathbf{v} = 0$, while $v_z^+ \propto z$ ensures the impermeability of the boundaries. The anti-symmetric flow $\mathbf{v}^-$ is certainly less known: v_z^- satisfies the TP constraint but induces v_s^- and v_ϕ^- that do not, in order to ensure the impenetrability of the boundaries. Furthermore, it appears that $\mathbf{v}^+$ is dominated by v_ϕ^+ and a tendency to zonation, while $\mathbf{v}^-$ has higher values at large s or low latitude, where it is dominated by v_z^- (or v_θ^-). The increasingly large boundary slope when $s \to 1$ reduces the amount of v_s^- produced by v_z^- at the boundaries. Finally, in spite of a localized forcing, both $\mathbf{v}^+$ and $\mathbf{v}^-$ tend to spread over the whole volume outside the cylinder tangent to the inner-core equator (TC). We obtain similar results when replacing the toroidal forcing $\mathbf{F}^\pm$ with a poloidal one, except for v_z^- which is weaker and has a more complex dependence on z.

3. Proposed Constraints for Inverting the Core Flow and Methodology

[8] We propose to translate the results obtained for $\mathbf{v}$ in the previous section to surface core flows $\mathbf{u}$ which can be computed from geomagnetic field models. The $\mathbf{v}^+$ QG flow (also referred to as a columnar flow) leads to the following relation at the core surface [*Amit and Olson*, 2004]:

$$\nabla_H \cdot \mathbf{u}^+ = 2u_\theta^+ \tan\theta \tag{1}$$

The axial component of the $\mathbf{v}^-$ flow comprises, besides a z-invariant term, other anti-symmetric contributions that cannot be separated at the core surface. This precludes the derivation of a kinematic constraint for $\mathbf{u}^-$. We will thus invert for flows that, besides a symmetric component $\mathbf{u}^+$ satisfying (1), will also include an antisymmetric component $\mathbf{u}^-$ which has no particular kinematical constraint imposed.

[9] In the Earth core, due to the very small viscosity and high electrical conductivity, we do not expect any significant damping effect on the flow at the scales that can be probed by magnetic field models. However, observations and numerical results for different natural rotating flow systems, with or without magnetic fields, show a tendency for the flow to develop preferably along parallels, in the form of thin zonal jets. This leads to anisotropic structures elongated in the azimuthal direction but showing small scales in the radial direction. The most emblematic case is the banded atmosphere of Jupiter, but there is also evidence for alternating jets in the Ocean [*Maximenko et al.*, 2005]. Numerical simulations of thermal convection also exhibit this kind of flow [*Christensen*, 2002] and recent geodynamo simulations by *Miyagoshi et al.* [2010] show the formation of low-latitude zonal flows at low Ekman numbers. Inspired by these results, we propose a penalization of the azimuthal gradients, by minimizing the integral over the core-mantle surface (CMB):

$$R_A = \int_{\mathrm{CMB}} \left[\frac{1}{\sin\theta}\frac{\partial \mathbf{u}}{\partial \phi}\right]^2 dS. \tag{2}$$

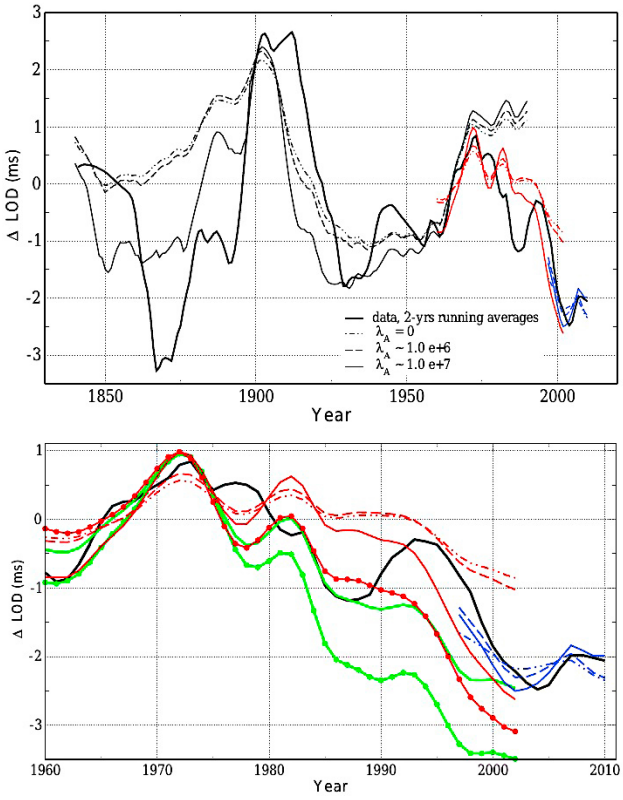

Figure 2. Observed (thick black line) and estimated ΔLOD. (top) Estimates for gufm1 (thin black lines), CM4 (red) and CHAOS-3 (blue), for 3 different degrees of flow anisotropy. (bottom) Blow up of Figure 2 (top) for the most recent period. Also shown, for CM4, estimates from large-scale $\mathbf{u}^+$ (green line with circles), small-scale $\mathbf{u}^+$ (green line) and large scale $\mathbf{u}^\pm$ (red line with circles).

This anisotropic norm can be shown to depend both on spherical harmonic degree ℓ and order m as ℓm^2. Because it does not restrain zonal flows (and hence torsional oscillations), we superimpose an isotropic penalization of the mean squared velocities over the core surface ($\int_{CMB}\mathbf{u}^2 dS$, referred to as ℓ^1 norm).

[10] To cover a time interval as large as possible and treat different geomagnetic field models, we invert the gufm1 [*Jackson et al.*, 2000], the comprehensive CM4 [*Sabaka et al.*, 2004] and the satellite derived CHAOS-3 [*Olsen et al.*, 2010] geomagnetic field models up to degree $\ell = 13$. We obtain snapshots of core surface fluid flow up to $\ell = 26$ that can, by advecting the field, explain the secular variation models (frozen-flux hypothesis). The adopted methodology is described by *Holme* [2007]. We look for a regularized weighted least squares flow solution that explains snapshots of the geomagnetic field model up to some degree of confidence, which comprises both the information on the noise level of the SV data ($\sigma^d(\ell)$) and an estimation of the SV signal produced by a non-parameterized contribution of the magnetic field small scales (representativity error, $\sigma^r(\ell)$) [*Gillet et al.*, 2009]. Assuming these two kinds of errors are uncorrelated, we then construct a diagonal predictive data covariance matrix with elements $\sigma^d(\ell)^2 + \sigma^r(\ell)^2$. The term representing the confidence on the SV model, $\sigma^d(\ell)^2$, is given by $\eta(2\ell + 1)^{-1}(\ell + 1)^{-1}$, where we use as noise level η the value 0.4 $(\text{nT/yr})^2$ for gufm1 and CM4 models (assuming that SV degrees $\ell < 10$ contain relevant information in both these models [*Gillet et al.*, 2010]), and 0.01 $(\text{nT/yr})^2$ for the satellite derived model CHAOS-3 [*Olsen et al.*, 2010]. The representativity errors are assumed to be independent of time and we use the law $\sigma^r(\ell)^2 = 36\exp(-\ell)$, close to those derived by *Pais and Jault* [2008] and *Gillet et al.* [2009].

[11] The inversion is stabilized using regularization presented above. Condition (1) is converted into a quadratic norm that is introduced in the global objective functional to be minimized by the flow solution. This condition constrains only but $\mathbf{u}^+$ using a very high Lagrange multiplier. We test the relevance of $\mathbf{u}^-$ by also inverting for purely symmetric flows that obey condition (1). Norm R_A (equation (2)) is used to introduce anisotropy, in conjunction with the isotropic ℓ^1 norm. To compare with more standard procedures where stronger regularizations are used, we also invert for flows using only an ℓ^3 norm, which penalizes the mean squared velocity gradients over the CMB [*Gillet et al.*, 2009].

[12] In order to test the sensitivity of geomagnetic field models to the boundary of the TC, we use the same regularizations over the whole core surface.

4. Inverted Flow Models

[13] The new regularizing norms are tested for a possible improvement of estimates of ΔLOD. We concentrate on the 1960–2002 epoch covered by the CM4 model, for which the

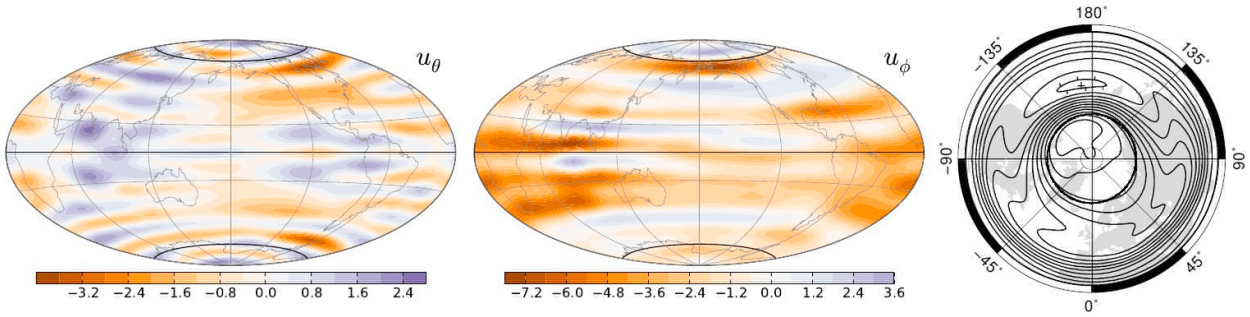

Figure 3. Inverted flow $\overline{\mathbf{u}}^\pm$ using $\lambda_A = 8 \times 10^6$ averaged over the CHAOS-3 era. Components (left) u_θ and (middle) u_ϕ in km/yr, and (right) the stream-function ξ of the symmetric part $\overline{\mathbf{u}}^+$ viewed from north-pole defined by $\overline{\mathbf{u}}^+ = (\cos\theta)^{-2}\,\mathbf{r} \times \nabla\xi$. The parallel corresponding to the trace of the TC is drawn (as well as ±20°, related to Table 1).

Table 1. Ratio of Symmetric Kinetic Energy Over Total Energy $E^+/(E^+ + E^-)$ for the Flow $\overline{\mathbf{u}}^{\pm}$ (Figure 3) Truncated at Different Spherical Harmonic Degree ℓ_{tr} and Integrated Over the Whole Core Surface, Inside the TC, and Also Over a Band Centered on the Equator and Spanning 40° of Latitude

ℓ_{tr}	Core Surface	Inside TC	Equator
6	0.84	0.63	0.91
10	0.80	0.79	0.91
13	0.76	0.38	0.83
18	0.70	0.27	0.67
26	0.66	0.22	0.65

imposed anisotropy is responsible for the most clear improvement. It is known that standard flow predictions do recurrently introduce a stronger decaying trend of ΔLOD than observed during this period [*Gillet et al.*, 2009]. We test the hypothesis that this poor estimation may be due to aliasing caused by underparameterization of small scales. This would deteriorate estimation of large scale coefficients, in particular t_1^0 and t_3^0 (which carry the core angular momentum) and more importantly deteriorate the accuracy of their time variations. In Figure 2 we show estimates produced by $\mathbf{u}^+$ flows and flows supporting an equatorial antisymmetric component besides the QG symmetric one ($\mathbf{u}^{\pm}$ flows), with different small scale penalization strength. The ΔLOD predicted by a large scale $\mathbf{u}^+$ flow model produces a too strong negative trend (normalized squared misfit $\chi^2 = 1.2$). When using a weaker regularization the results are clearly improved ($\chi^2 = 0.7$). But the best result is obtained when allowing for $\mathbf{u}^-$ and imposing lower longitudinal gradients ($\chi^2 = 0.55$).

[14] We further check the importance of norm R_A in improving the estimations. In Figure 2 we show estimations for different degrees of anisotropy, quantified by different values of the regularizing parameter λ_A weighting R_A: from $\lambda_A = 0$ (only the ℓ^1 norm is used) to the maximum degree of anisotropy achieved while still explaining the SV model to a reasonable level. We note that using solely the isotropic regularization ℓ^1 produces too low amplitude estimations, and that increasing the anisotropy constraint (and decreasing the isotropic one) improves the results. This is because the flow energy can be more freely distributed among different length-scales of the zonal flow coefficients, including those contributing to the core angular momentum.

[15] We quantify the maximum anisotropy imposed on flow models computing $\alpha = (R_A^0 - R_A^*)/R_A^0$, where R_A^0 and R_A^* are values of R_A computed respectively for flows inverted with $\lambda_A = 0$ (no anisotropy) and for the maximum achieved λ_A. We find α increasing from 0.8 to 0.9 during the 1840–2010 period. The good recovery of the trend and the amplitude of oscillations in ΔLOD is not specific to inversions of CM4, and we show in Figure 2 the good results obtained for gufm1 (1840–1990) and CHAOS-3 (1997–2010).

[16] We proceed to identify the core surface regions where the $\mathbf{u}^-$ component is more important, as accounted by SV models in the frozen-flux approximation. We concentrate on the more recent CHAOS-3 model (derived from very recent satellite data and revised observatory monthly mean values) and compute the corresponding mean anisotropic flow model $\overline{\mathbf{u}}^{\pm}$, represented in Figure 3. Its rms velocity is 9.7 km/yr during the 1997–2010 period. We note the important contribution of u_θ^- in the equatorial region, where the crossing of the equator under Indonesia is quite obvious. However, only small scales are affected by the breakdown of QG near the equator, while the large scale flow remains highly symmetric outside the TC (see Table 1). Most striking is the sharpness with which the $\overline{\mathbf{u}}^+$ flow model perceives the inner-core, as shown by its streamfunction (ξ, Figure 3, right).

5. Conclusion

[17] Our direct numerical simulations show that for short time-scale symmetric forcing, the flow response is quasi-geostrophic in Earth's core conditions. For an anti-symmetric forcing, an anti-symmetric counterpart of the QG flow could account for flows crossing the core-mantle boundary equator. As this component seems to decay at the same rate as the QG component, we argue that the presence of anti-symmetric flows at the core surface depends mainly on the amount of anti-symmetric forcing (whether buoyant, turbulent or magnetic) in the Earth core. Our simulations also show the development of longitudinal structures for the symmetric part, and a clear separation between the regions inside and outside the tangent cylinder. These results have inspired new constraints that we used for inverting the flow at the core surface from geomagnetic field models.

[18] Our flow models, with improved estimations of ΔLOD and the natural emergence of symmetric large scale features including the trace of the tangent cylinder, support three main implications: (i) the large scale flow in the Earth core responsible for SV is very likely dominated by QG motions; (ii) significant deviations to QG are expected for smaller scales and in the equatorial region; (iii) SV models seem to detect anisotropic flows in the Earth core, with zonation and strong latitudinal gradients.

[19] **Acknowledgments.** We would like to thank Dominique Jault and Nicolas Gillet for fruitful discussions, and Nils Olsen for kindly sending us the CHAOS-3 main field coefficients. This research work was made possible by a joint FCT/CNRS grant. The simulations were run at the Service Commun de Calcul Intensif de l'Observatoire de Grenoble (SCCI).

[20] The Editor thanks Hagay Amit and an anonymous reviewer for their assistance in evaluating this paper.

References

Amit, H., and P. Olson (2004), Helical core flow from geomagnetic secular variation, *Phys. Earth Planet. Inter.*, *147*, 1–25.

Christensen, U. R. (2002), Zonal flow driven by strongly supercritical convection in rotating spherical shells, *J. Fluid Mech.*, *470*, 115–133.

Eymin, C., and G. Hulot (2005), On core surface flows inferred from satellite magnetic data, *Phys. Earth Planet. Inter.*, *152*, 200–220.

Gillet, N., M. A. Pais, and D. Jault (2009), Ensemble inversion of time-dependent core flow models, *Geochem. Geophys. Geosyst.*, *10*, Q06004, doi:10.1029/2008GC002290.

Gillet, N., V. Lesur, and N. Olsen (2010), Geomagnetic core field secular variation models, *Space Sci. Rev.*, *155*(1), 129–145, doi:10.1007/s11214-009-9586-6.

Gillet, N., N. Schaeffer, and D. Jault (2011), Rationale and geophysical evidence for quasi-geostrophic rapid dynamics within the Earth's outer core, *Phys. Earth Planet. Inter.*, doi:10.1016/j.pepi.2011.01.005, in press.

Holme, R. (2007), Large scale flow in the core, in *Treatise on Geophysics*, vol. 8, *Core Dynamics*, edited by G. Schubert, pp. 107–130, Elsevier, Amsterdam.

Jackson, A., A. Jonkers, and M. Walker (2000), Four centuries of geomagnetic secular variation from historical records, *Philos. Trans. R. Soc. London, Ser. A*, *358*, 957–990.

Jault, D. (2008), Axial invariance of rapidly varying diffusionless motions in the Earth's core interior, *Phys. Earth Planet. Inter.*, *166*, 67–76, doi:10.1016/j.pepi.2007.11.001.

Jault, D., C. Gire, and J. L. Le Mouel (1988), Westward drift, core motions and exchanges of angular momentum between core and mantle, *Nature*, *333*(6171), 353–356, doi:10.1038/333353a0.

Jones, C. A. (2007), Thermal and compositional convection in the outer core, in *Treatise on Geophysics*, vol. 8, *Core Dynamics*, edited by G. Shubert, pp. 131–185, Elsevier, Amsterdam.

Maximenko, N. A., B. Bang, and H. Sasaki (2005), Observational evidence of alternating zonal jets in the world ocean, *Geophys. Res. Lett.*, *32*, L12607, doi:10.1029/2005GL022728.

Miyagoshi, T., A. Kageyama, and T. Sato (2010), Zonal flow formation in the Earth's core, *Nature*, *463*(7282), 793–796, doi:10.1038/nature08754.

Olsen, N., and M. Mandea (2008), Rapidly changing flows in the Earth's core, *Nat. Geosci.*, *1*, 390–394.

Olsen, N., M. Mandea, T. J. Sabaka, and L. Tøffner-Clausen (2010), The CHAOS-3 geomagnetic field model and candidates for the 11th generation IGRF, *Earth Planets Space*, *62*, 719–729, doi:10.5047/eps.2010.07.003.

Pais, M. A., and D. Jault (2008), Quasi-geostrophic flows responsible for the secular variation of the Earth's magnetic field, *Geophys. J. Int.*, *173*, 421–443, doi:10.1111/j.1365-246X.2008.03741.x.

Sabaka, T. J., N. Olsen, and M. E. Purucker (2004), Extending comprehensive models of the Earth's magnetic field with Ørsted and CHAMP data, *Geophys. J. Int.*, *159*, 521–547.

M. A. Pais, CFC, Physics Department, University of Coimbra, P-3004-516 Coimbra, Portugal. (pais@fis.uc.pt)

N. Schaeffer, ISTerre, CNRS, University Joseph Fourier, BP 53, F-38041 Grenoble CEDEX 9, France. (nathanael.schaeffer@ujf-grenoble.fr)

Geophysical Journal International

Geophys. J. Int. (2012) **191,** 508–516 doi: 10.1111/j.1365-246X.2012.05611.x

On the reflection of Alfvén waves and its implication for Earth's core modelling

Nathanaël Schaeffer,[1] Dominique Jault,[1,2] Philippe Cardin[1] and Marie Drouard[1]

[1]*ISTerre, Université de Grenoble* 1*, CNRS,* F-38041 *Grenoble, France. E-mail: nathanael.schaeffer@ujf-grenoble.fr*
[2]*Earth and Planetary Magnetism Group, Institut für Geophysik, Sonnegstrasse* 5*, ETH Zürich,* CH-8092*, Switzerland*

Accepted 2012 July 11. Received 2012 July 11; in original form 2011 December 19

SUMMARY

Alfvén waves propagate in electrically conducting fluids in the presence of a magnetic field. Their reflection properties depend on the ratio between the kinematic viscosity and the magnetic diffusivity of the fluid, also known as the magnetic Prandtl number Pm. In the special case, $Pm = 1$, there is no reflection on an insulating, no-slip boundary, and the incoming wave energy is entirely dissipated in the boundary layer.

We investigate the consequences of this remarkable behaviour for the numerical modelling of torsional Alfvén waves (also known as torsional oscillations), which represent a special class of Alfvén waves, in rapidly rotating spherical shells. They consist of geostrophic motions and are thought to exist in the fluid cores of planets with internal magnetic field. In the geophysical limit $Pm \ll 1$, these waves are reflected at the core equator, but they are entirely absorbed for $Pm = 1$. Our numerical calculations show that the reflection coefficient at the equator of these waves remains below 0.2 for $Pm \geq 0.3$, which is the range of values for which geodynamo numerical models operate. As a result, geodynamo models with no-slip boundary conditions cannot exhibit torsional oscillation normal modes.

Key words: Numerical solutions; Dynamo: theories and simulations; Rapid time variations; Core, outer-core and inner-core; Planetary interiors.

1 INTRODUCTION

Hannes Alfvén first showed the theoretical existence, in an inviscid fluid of infinite electrical conductivity, of hydromagnetic waves that couple fluid motion and magnetic field (Alfvén 1942). The propagation of torsional Alfvén waves in the Earth's fluid core was, thereafter, predicted by Braginsky (1970). Such waves arise in rapidly rotating spheres or spherical shells in the presence of a magnetic field. In torsional Alfvén waves, the motions are geostrophic and consist in the rotation $\omega_g(s)$ of nested cylinders centred on the rotation axis. They, thus, depend only on the distance s to the rotation axis. The period of the fundamental modes of torsional Alvén waves in the Earth's fluid core was first estimated to be about 60 yr. This timescale was inferred from the analysis of the decadal length of day changes since the first half of the 19th century (Jordi *et al.* 1994) and of the geomagnetic secular variation after 1900 (Braginsky 1984). With hindsight, these time-series were not long enough to show convincingly variations with 60 yr periodicity. Torsional waves with much shorter periods have now been extracted from time-series of core surface flows for the time interval 1955–1985 (Gillet *et al.* 2010). If this discovery is confirmed, the period of the fundamental modes is of the order of 6 yr and, as such, is much shorter than initially calculated.

Several authors have searched for torsional Alfvén waves in geodynamo simulations. Using stress-free boundary conditions, Dumberry & Bloxham (2003) and Busse & Simitev (2005) illustrated some parts of the torsional wave mechanism. Dumberry & Bloxham (2003) found that the whole length of the geostrophic cylinders accelerates azimuthally as if they were rigid. The inertial forces, in their simulation, are however, so influential that they dominate the Lorentz forces. Torsional Alfvén waves (TAW) have finally been detected in a set of numerical simulations of the geodynamo with no-slip boundary conditions, for $0.5 \leq Pm \leq 10$, by Wicht & Christensen (2010) (the magnetic Prandtl number Pm is the ratio of kinematic viscosity over magnetic diffusivity). In both the geophysical ($Pm \sim 10^{-5}$) and the numerical studies, there seems to be no reflection of the TAW upon their arrival at the equator. However, experimental studies in liquid metals have shown resonance effects on Alfvén normal modes (Jameson 1964) as well as reflection of wave packets (Alboussière *et al.* 2011).

In this paper, we elaborate on the remark that reflection of Alfvén waves is controlled not only by the boundary condition, but also by the magnetic Prandtl number of the fluid in which they propagate (see Jameson 1961, p. 23,24). In the next section, we discuss the governing equations for 1-D Alfvén waves and the associated boundary conditions for a solid and electrically insulating wall. We remark that for $Pm = 1$ all the energy of the incident Alfvén wave is dissipated in a boundary layer, resulting in no reflected wave. In the following section, we change geometry to further emphasize our point and briefly present a direct numerical simulation of propagation

and reflection of Alfvén wave in a non-rotating spherical shell. That introduces the section devoted to the geophysical application, where we investigate TAW in the Earth's core, modelled as a rapidly rotating spherical shell, calculating the energy loss on reflection at the Equator as a function of *P*m. Finally, we discuss the implications concerning the ability of geodynamo simulations to produce torsional eigenmodes and waves which are expected in the Earth's core.

2 REFLECTION OF ONE-DIMENSIONAL ALFVÉN WAVES

We introduce the problem through the example of Alfvén waves, transverse to a uniform magnetic field in an homogeneous and electrically conducting fluid, hitting a solid wall perpendicular to the imposed magnetic field (Roberts 1967). The imposed uniform magnetic field B_0 is along the x-axis, whereas the induced magnetic field $b(x, t)$ and the velocity field $u(x, t)$ are transverse to this field, along y. Assuming invariance along y- and z-axes, the problem reduce to a 1-D problem, u and b depending only on x. Projecting the Navier–Stokes equation and the induction equation on the y direction (on which the pressure gradient and the non-linear terms do not contribute), one obtains the following equations:

$$\partial_t u = \frac{B_0}{\mu_0 \rho}\partial_x b + \nu \partial_{xx} u, \tag{1}$$

$$\partial_t b = B_0 \partial_x u + \frac{1}{\mu_0 \sigma}\partial_{xx} b, \tag{2}$$

where μ_0 is the magnetic permeability, ρ is the fluid density, ν the kinematic viscosity and σ the electrical conductivity.

2.1 Elsasser variables

Introducing the two Elsasser variables $h_\pm = u \pm b/\sqrt{\mu_0 \rho}$, the equation of momentum (1) and the equation of magnetic induction (2) can be combined into

$$\partial_t h_\pm \mp V_\mathrm{A} \partial_x h_\pm - \frac{\eta + \nu}{2}\partial_{xx} h_\pm = \frac{\nu - \eta}{2}\partial_{xx} h_\mp, \tag{3}$$

where $V_\mathrm{A} = B_0/\sqrt{\mu_0 \rho}$ is the Alfvén wave speed, and $\eta = (\mu_0 \sigma)^{-1}$ is the magnetic diffusivity. It is already apparent that when $\nu = \eta$, the right-hand side of the previous equation vanishes, in which case h_+ and h_- are fully decoupled. One can also show that h_- travels in the direction of the imposed magnetic field, whereas h_+ travels in the opposite direction.

Introducing a length scale L and the timescale L/V_A, the previous equations take the following non-dimensional form:

$$\partial_t h_\pm \mp \partial_x h_\pm - \frac{1}{S}\partial_{xx} h_\pm = \frac{1}{S}\frac{P\mathrm{m} - 1}{P\mathrm{m} + 1}\partial_{xx} h_\mp, \tag{4}$$

where the Lundquist number S and the magnetic Prandtl number Pm are defined as

$$S = \frac{2 V_\mathrm{A} L}{\eta + \nu} \qquad P\mathrm{m} = \frac{\nu}{\eta}.$$

The propagation of Alfvén waves requires that the dissipation is small enough, which is ensured by $S \gg 1$.

The fact that $(P\mathrm{m} - 1)/(P\mathrm{m} + 1) = -(P\mathrm{m}^{-1} - 1)/(P\mathrm{m}^{-1} + 1)$ establishes a fundamental symmetry of these equations: when changing Pm into $P\mathrm{m}^{-1}$, only the sign of the coupling term (right-hand side of eq. 4) changes.

2.2 Physical boundary conditions and reflection of Alfvén waves

These equations must be completed by boundary conditions. We assume that the wall is electrically insulating, and that the fluid velocity vanishes at the solid boundary (no-slip boundary condition), which translate to $b = 0$ and $u = 0$, leading to $h_\pm = 0$.

For $P\mathrm{m} = 1$ the equations for h_+ and h_- are fully decoupled, regardless of the value of S

$$\partial_t h_\pm = \pm \partial_x h_\pm + \frac{1}{S}\partial_{xx} h_\pm. \tag{5}$$

In addition, for an insulating solid wall, the boundary condition $h_\pm = 0$ does not couple h_+ and h_- either. As a result, reflection is not allowed at an insulating boundary when $P\mathrm{m} = 1$, because reflection requires change of travelling direction, and thus transformation of h_+ into h_- and vice versa. The energy carried by the wave has to be dissipated in the boundary layer.

For $P\mathrm{m} \neq 1$ the equations are coupled: for very small diffusivities (that is large Lundquist number S), the coupling will be effective only in a thin boundary layer. In addition the coupling will be more efficient as Pm is further from 1. This gives a mechanism for reflection of Alfvén waves on an insulating boundary when $P\mathrm{m} \neq 1$. Before giving a numerical illustration, it is instructive to consider the boundary conditions in the two limits $P\mathrm{m} = 0$ and $P\mathrm{m} = \infty$, with $S \gg 1$ (dissipationless interior).

In the limit $P\mathrm{m} = 0$, there is no viscous term and the boundary condition, at the wall $x = x_0$, reduces to

$$b(x_0, t) = 0 \quad \Rightarrow \quad h_+(x_0, t) = h_-(x_0, t). \tag{6}$$

There is perfect reflection. The incident (+) and reflected (−) waves have equal velocities and opposite magnetic fields. This also corresponds to a stress-free boundary condition for the velocity field in combination with an insulating wall (infinitely small vorticity sheet at the wall), leading to perfect reflection regardless of the value of Pm used in eq. (4). In this case the boundary condition for the velocity field is $\partial_x u = 0$, which translates into $\partial_x(h_+ + h_-) = 0$ and $h_+ - h_- = 0$, effectively coupling h_+ and h_-.

In the limit $P\mathrm{m} = \infty$, the boundary condition, at the wall $x = x_0$, reduces instead to

$$u(x_0, t) = 0 \quad \Rightarrow \quad h_+(x_0, t) = -h_-(x_0, t). \tag{7}$$

The incident and reflected waves have opposite velocities and equal magnetic fields. This also corresponds to a no-slip boundary condition for the velocity field in combination with a perfectly conducting wall (infinitely small current sheet at the wall), leading to perfect reflection regardless of the value of Pm used in eq. (4). In this case, the boundary condition for the magnetic field is $\partial_x b = 0$, which couples h_+ and h_-.

Another combination of boundary conditions inhibits reflection for $P\mathrm{m} = 1$: for a stress-free ($\partial_x u = 0$) and perfectly conducting wall ($\partial_x b = 0$), which translates into $\partial_x h_+ = 0$ and $\partial_x h_- = 0$, the fields h_+ and h_- are decoupled, as for a no-slip insulating wall. Note finally that a wall with finite conductivity will allow some weak reflection, as illustrated by Fig. 4(h).

2.3 Numerical simulations

We have performed a numerical simulation in a channel $0 \leq x \leq x_0$ with a 1-D finite difference scheme. The Lundquist number is chosen large enough so that dissipation can be neglected in the interior. The boundary conditions were set to be electrically insulating

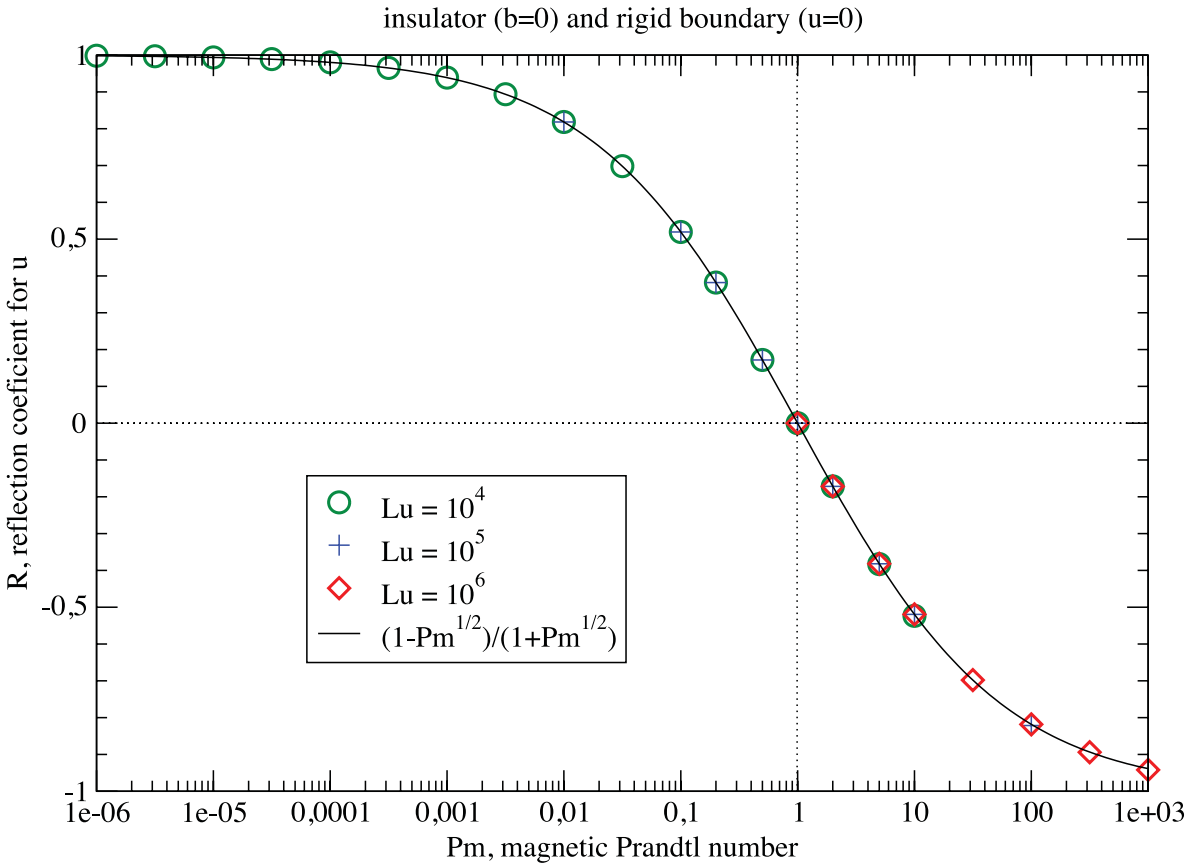

Figure 1. Reflection coefficient for a 1-D Alfvén wave packet hitting an insulating boundary with normal incidence, as a function of Pm and for different magnetic Lundquist numbers $Lu = V_a L/\eta$. The theoretical value for plane waves $R(Pm) = (1 - \sqrt{Pm})/(1 + \sqrt{Pm})$ fits the numerical simulation results perfectly.

and no-slip. The grid is refined next to the boundaries, to have at least 4 points in each boundary layer, which are Hartmann layers of thickness $\delta = \sqrt{\nu\eta}/V_A$ (see Appendix A).

From the simulation of the travelling wave, we compute the transmission coefficient as the ratio of the velocity amplitude of the reflected and incident waves for different values of Pm and S. The results are reported on Fig. 1.

As expected, there is full dissipation for $Pm = 1$ and energy conservation for $Pm \gg 1$ or $Pm \ll 1$. Furthermore, the reflection coefficient R is independent of S, and exhibits the expected symmetry $R(Pm^{-1}) = -R(Pm)$. The measured values of R match perfectly the theoretical reflection coefficient $R(Pm) = (1-\sqrt{Pm})/(1+\sqrt{Pm})$ derived for plane waves, because R depends neither on the pulsation ω, nor on the wavenumber k (see Appendix A).

3 REFLECTION OF A LOCALIZED ALFVÉN WAVE PACKET ON A SPHERICAL BOUNDARY

The peculiar case where no reflection occurs is not specific to the planar, 1-D ideal experiment. Here, we run an axisymmetric simulation in a spherical shell permeated by a non-uniform magnetic field, without global rotation. The imposed magnetic field is the same as in Jault (2008), and is represented by the dashed field lines of Fig. 2. Contrary to the simplest case of the previous section, it is a non-uniform magnetic field, which is not perpendicular to the boundaries. The observed behaviour of Alfvén wave packets hitting the curved boundaries should therefore apply to many systems.

The numerical pseudo-spectral code is the one used in Gillet *et al.* (2011), but restrained to axisymmetry. It uses the SHTns library (Schaeffer 2012) for spherical harmonic expansion (Legendre polynomials) in the latitudinal direction, and second-order finite differences in radius with many points concentrated near the boundaries. It time steps both induction and momentum equation in the sphercial shell using a semi-implicit Crank–Nicholson scheme for the diffusive terms, whereas the coupling and (negligible) nonlinear terms are handled by an Adams–Bashforth scheme (second order in time). The number of radial gridpoints is set to 500 and the maximum degree of Legendre polynomials to 120.

The Alfvén wave packets are generated mechanically by spinning the conducting inner core for a very short duration (compared to the Alfvén propagation time). Since the imposed magnetic field strength is not uniform, the wave front deforms as it propagates along the field lines. When the wave packet hits the outer insulating spherical shell, it does reflect and propagates back towards the inner shell for $Pm = 0.1$ and $Pm = 10$ but there is no reflection for $Pm = 1$. This is illustrated by the snapshots of Fig. 2.

4 REFLECTION OF TORSIONAL ALFVÉN WAVES

Finding evidence of propagation of TAW in the Earth's fluid core may open a window on the core interior. Properties of TAW in the

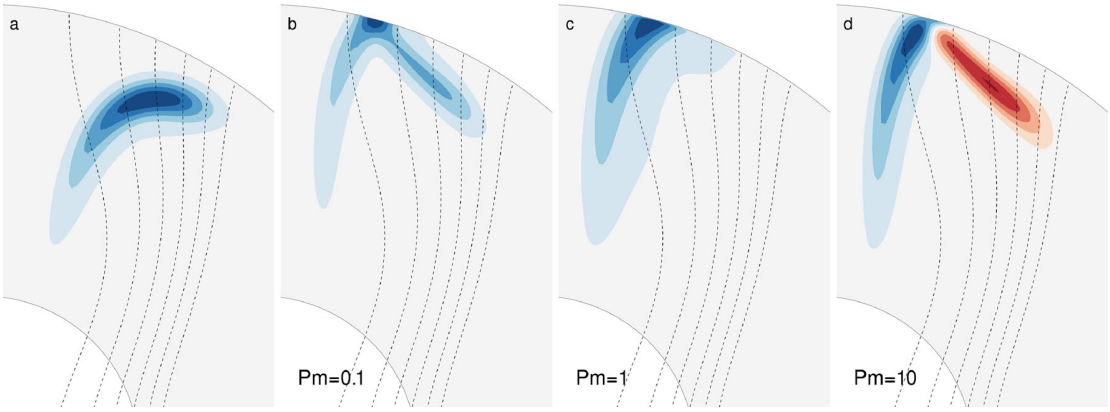

Figure 2. Snapshot of the azimuthal velocity component of Alfvén waves propagating in a non-rotating spherical shell. The dashed-lines are the imposed magnetic field lines. From left-hand panel to right-hand panel: Panel (a) the incoming waves travelling from the inner shell to the outer shell along magnetic field lines; Panel (b) case $Pm = 0.1$, $S = 1800$ showing reflection with the same sign; Panel (c) case $Pm = 1$, $S = 1000$ with total absorption at the wall; Panel (d) case $Pm = 10$, $S = 1800$ showing reflection with opposite sign.

Earth's core have, thus, been thoroughly investigated after the initial study of Braginsky (1970). They have been recently reviewed by Jault (2003) and Roberts & Aurnou (2011).

4.1 Model of torsional Alfvén waves

To model TAW, magnetic diffusion and viscous dissipation are neglected in the interior of the fluid. The Earth's fluid core is modelled as a spherical shell of inner radius r_i, outer radius r_o and rotation rate Ω. Rapid rotation introduces an asymmetry between the velocity and magnetic fields and makes the velocity geostrophic, provided that $\lambda \equiv V_A/\Omega r_o \ll 1$ (Jault 2008). Note that the Lehnert number λ is about 10^{-4} in the Earth's core. Geostrophic velocity in a spherical shell consists of the rotation $\omega_g(s)$ of nested cylinders centred on the rotation axis. It, thus, depends only on the distance s from the rotation axis (in r_o units). A 1-D wave equation for the geostrophic velocity $s\omega_g(s)$ is obtained after elimination of the magnetic field b

$$L\frac{\partial^2\omega_g(s)}{\partial t^2} = \frac{\partial}{\partial s}\left[L\tilde{V}_A^2\frac{\partial\omega_g(s)}{\partial s}\right], \tag{8}$$

with $L = s^3H(s)$ and $H(s) = \sqrt{1-s^2}$ the half-height of the geostrophic cylinders, and $\tilde{V}_A^2$ involves only the z-average of the squared s-component of the imposed magnetic field. Braginsky (1970) derived (8) rigorously in the geophysical case for which the viscous Ekman layer is thin compared to the magnetic diffusion layer located at the top and bottom rims of the geostrophic cylinders. This condition amounts to $Pm\lambda \ll 1$. Then, the velocity remains geostrophic in the magnetic diffusion layer. We have written the eq. (8) in its simplest form, when the imposed magnetic field is axisymmetric, the mantle is insulating and Ekman friction at the rims of the geostrophic cylinders is neglected. The eq. (8) needs to be completed by two boundary conditions, which can be derived when either $Pm \ll 1$ or $Pm \gg 1$.

Interestingly, the eq. (8) may be valid in the limit $Pm \ll 1$ but also in the limit $Pm \gg 1$ (provided $Pm\lambda \ll 1$). In the specific case $Pm \ll 1$, the appropriate boundary condition on the geostrophic velocity at the equator (on the inner edge of the Hartmann boundary layer) can be inferred from the boundary condition on the magnetic field. For an insulating outer sphere, it yields $\partial_s\omega_g|_{s=1} = 0$ which corresponds to a stress-free boundary, as in the 1-D wave case with $Pm \to 0$. In the case $Pm \gg 1$, the appropriate boundary condition is $\omega_g|_{s=1} = 0$ as the angular velocity of the outermost geostrophic cylinder is immediately synchronized with the rotation of the solid outer sphere in the course of a spin-up experiment. This is equivalent to a no-slip boundary, as for the 1-D wave case with $Pm \to \infty$.

4.2 Normal modes

Assuming that ω_g varies with time as e^{ict}, the eq. (8) can be transformed into a normal mode equation

$$-c^2\omega_g(s) = \frac{1}{L}\frac{\partial}{\partial s}\left[L\tilde{V}_A^2\frac{\partial\omega_g(s)}{\partial s}\right]. \tag{9}$$

Transmission and reflection of TAW on the geostrophic cylinder tangent to the inner core set a special problem that we do not address here. As an intermediate step, we simply illustrate our discussion with results for the full sphere case, imposing $\partial_s\omega_g|_{s=\varepsilon} = 0$, with $\varepsilon \ll 1$ (we have checked the convergence of the numerical results as $\varepsilon \to 0$). It is of interest to write the solution of this equation in the case $c = 0$ and $\tilde{V}_A$ uniform

$$\omega_g(s) = \frac{1}{2}\alpha_1\left[-\frac{\sqrt{1-s^2}}{s^2} - \log\left(\sqrt{1-s^2}+1\right) + \log(s)\right] + \alpha_2. \tag{10}$$

A non-zero solution (uniform rotation $\omega_g(s) = \alpha_2$) exists for the boundary condition $\partial_s\omega_g|_{s=1} = 0$ but not for the condition $\omega_g|_{s=1} = 0$ that applies when $Pm \gg 1$. We are interested in this latter case, despite its lack of geophysical realism, as contrasting the two boundary conditions sheds light on the nature of the constraint $\partial_s\omega_g|_{s=1} = 0$ that has always been used in TAW studies.

In the general case ($c \neq 0$, non-uniform $\tilde{V}_A$), it remains easy to calculate numerically a solution of (9) for $0 < s < 1$. We have successfully checked our numerical results against the eigenvalues listed in the table C1 of Roberts & Aurnou (2011), that have been obtained analytically for $\partial_s\omega_g|_{s=1} = 0$ and $\tilde{V}_A = 1$. Then, the first eigenvalues are (0, 5.28, 8.63, 11.87, 15.07, ..), whereas in the case $\tilde{V}_A = 1$ and $\omega_g|_{s=1} = 0$ they are (2.94, 6.35, 9.58, 12.78, 15.95, ..). In the latter case, we recover our previous observation that 0 is not an eigenvalue.

In contrast with an often-made statement (Buffett 1998; Jault 2003; Roberts & Aurnou 2011), the study of the case $Pm \gg 1$ shows that it is not required to have $\partial_s\omega_g|_{s=1} = 0$ to obtain solutions with bounded values of ω_g for $s \leq 1$. On the other hand, the singularity of $\partial_s L$ at $s = 1$ implies a singularity of $\partial_s\omega_g$ (which is $O((1-s)^{-1/2})$

as $s \to 1$) . That points to significant viscous dissipation once the viscous term is reintroduced.

When Pm is neither very small nor very large, it is not possible to separate the interior region (where (9) applies) and the Hartmann boundary layer.

We can conclude the discussion of normal modes by noting that the solutions for the two cases $Pm \ll 1$ and $Pm \gg 1$ differ in a significant way at the equator. In both cases, solutions are obtained which satisfy the appropriate boundary conditions and with bounded values of ω_g for s in the interval [0, 1]. However, reintroducing dissipation modifies the eigensolutions in the vicinity of the equator and the eigenvalues in the second case only.

4.3 Numerical experiments

To determine the reflection coefficient of TAW at the equator of the outer shell, we use a set-up that resembles the Earth's core. The code is the same as the one described in Section 3, but this time with imposed global rotation. The total number of radial points is typically 1200 and the maximum degree of Legendre polynomials is set to 360.

For reflection to occur, there must be a non-zero imposed magnetic field B_s at the equator. Hence, we set the simplest potential quadrupolar field (generated from outside the sphere): $B_s = B_0 s$, $B_z = 2B_0 z$ and $B_\phi = 0$. This ensures a local travelling speed $V_A(s) = B_s(s)/\sqrt{\mu_0 \rho}$ that is large near the reflection point ($s = 1$). The Lehnert number is small and always set to $\lambda = V_A/(\Omega r_o) = 5 \times 10^{-4}$, so that λPm is also small.

The initial velocity field is along the azimutal direction ϕ and depends only on the cylindrical radius s: $u_\phi(s) = s\omega_g(s) = u_0 s \exp(-(s - s_0)^2/\ell^2)$ with $s_0 = 0.675$. We used two different width $\ell = 0.02$ and $\ell = 0.063$. This initial velocity field splits into a TAW packet propagating inwards that we do not consider here, and another travelling outwards that we carefully follow and we focus on the reflection of this wave packet at the equator of the outer shell ($s = 1$). The Lundquist number S based on the size of the spherical shell ranges from 6×10^2 to 8×10^4 and the Ekman number $E = \nu/\Omega r_o^2$ and magnetic Ekman number $Em = \eta/\Omega r_o^2$ are both always very low and range from 5×10^{-10} to 5×10^{-7} over a wide range of magnetic Prandtl number: from $Pm = 10^{-3}$ to $Pm = 10^2$.

We measure the extremum of the velocity field in the wave packet before and after the reflection, a_i and a_r respectively, at a fixed radius ($s = 0.925$ for $\ell = 0.02$ and $s = 0.75$ for $\ell = 0.063$), from which we compute the corresponding reflection coefficient $R = a_r/a_i$, reported in Fig. 3 for an insulating outer shell. We found no significant dependence with the Lundquist number S or the width of the initial pulse ℓ (R varies by less than 0.03).

As expected from the discussion of Alfvén waves equations, the combination $Pm = 1$, no-slip boundary condition and insulating wall corresponds to a special case whereby no reflection at all occurs at the equator (see also Fig. 4g).

However, there are differences with the planar case. First, the reflection coefficient is not symmetric with respect to $Pm = 1$, as expected from our discussion of torsional eigenmodes in spherical geometry in the previous section. For large Pm there is high dissipation and very little reflection compared to low Pm. Second, the reflection coefficient is not as large.

Space–time diagrams of the reflection of the wave at the equator are presented in Fig. 4 for a few representative cases. The highest reflection coefficient occurs for the stress-free insulating case at

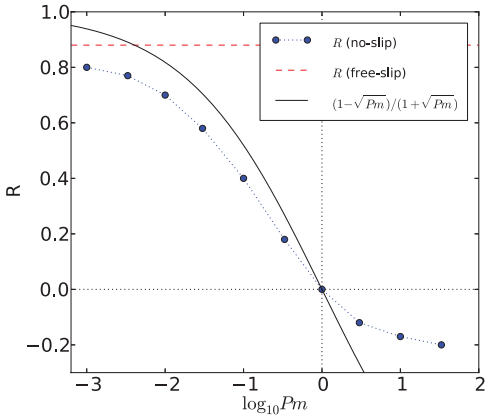

Figure 3. Reflection coefficient for a TAW for insulating and no-slip boundary conditions, as a function of Pm. The Lundquist number is always large ($S > 5000$ for $Pm \geq 0.01$ and $S > 600$ otherwise). For reference, the black curve is the planar Afvén wave reflection coefficient $(1-\sqrt{Pm})/(\sqrt{Pm}+1)$, and the red line marks the reflection coefficient for a stress-free boundary (obtained with $Pm = 1$ but which is theoretically independent of Pm and corresponds to a no-slip boundary with $Pm \to 0$).

$Pm = 1$: from $R = 0.86$ at $S = 1000$ to $R = 0.88$ at $S = 1.5 \times 10^4$. In this case (Figs 4a and b) one can also see the amplification of the velocity field very near the boundary, as the magnetic field must vanish, doing so by producing the reflected wave, just as in the planar case. This is not a boundary layer, but simply the superposition of the incident and reflected wave (see also Appendix A). The Hartmann boundary layer is too small to be seen on these plots, but we checked that its size and relative amplitude for velocity and magnetic fields do match the analytic theory developed in Appendix A.

For $Pm = 0.1$, the reflected wave carries only 16 per cent of the energy, the remaining being dissipated in the boundary layer. The magnetic field changes sign at the reflection, whereas the velocity keeps the same sign (Figs 4c and d). For $Pm = 10$, the reflected energy drops to 3 per cent and the small reflected velocity field has opposite sign, whereas the magnetic field (barely visible on Fig. 4) keeps the same sign (Figs 4e and f). During its propagation, the incoming wave is also much more damped than for $Pm = 0.1$, even in the case where S or E have comparable values. This is due to strong dissipation at the top and bottom boundaries, which increases as the wave propagates toward the equator (visible in Fig. 4e) for $Pm > 1$. This may not be unrelated to the previously discussed singularity for normal modes in the case $Pm > 1$. A consequence of this large dissipation, is the difficulty to clearly identify the reflected wave, and to properly define a reflection coefficient. The values reported in Fig. 3 are, thus, not very precise for $Pm > 1$.

It may also be worth noting that changing the magnetic boundary from insulating to a thin conducting shell allows weak reflection for $Pm = 1$ and no-slip velocity (Fig. 4h), in agreement with the analysis of the governing equations (Section 2.2).

4.4 Energy dissipation and normal modes

We want to emphasize that when no reflection occurs, the energy of the wave is dissipated very quickly. However, for liquid metals ($Pm \ll 1$), only a small amount of the wave energy is absorbed in the event of a reflection, but many successive reflections can lead to significant dissipation. Using the theoretical reflection coefficient, we can estimate the timescale of dissipation of an Alfvén wave due

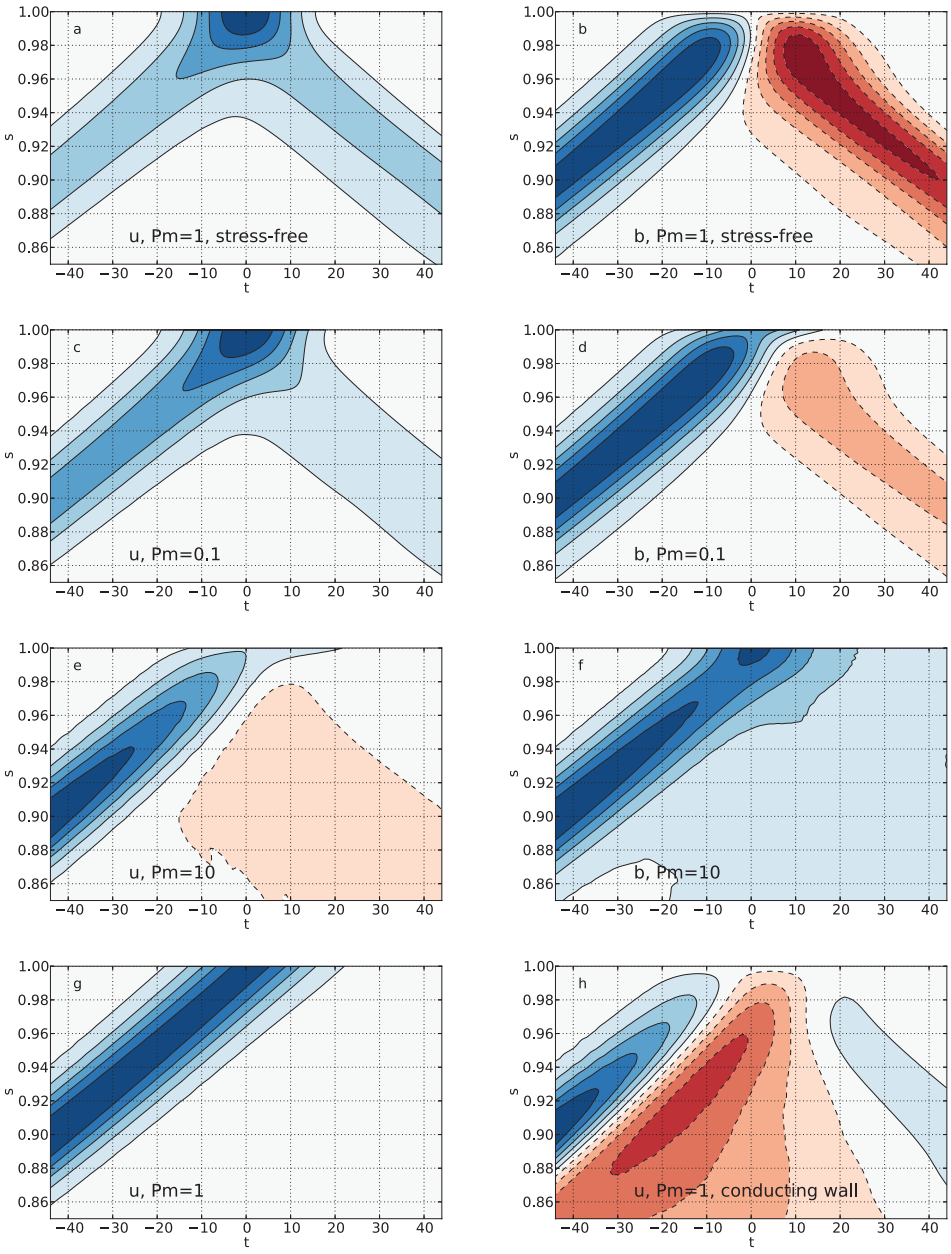

Figure 4. Space–time diagrams of the reflection of a TAW for $S \simeq 10^4$ and $\ell = 0.02$ recorded in the equatorial plane, near the equator. *Top row*: stress-free boundary with $P\mathrm{m} = 1$ ($R = 0.88$), (a) the azimuthal angular velocity u_ϕ/s and (b) the azimuthal magnetic field b_ϕ (changing sign). *Second row*: No-slip boundary with $P\mathrm{m} = 0.1$ ($R = 0.40$), (c) the azimuthal angular velocity u_ϕ/s and (d) the azimuthal magnetic field b_ϕ (changing sign). *Third row*: No-slip boundary with $P\mathrm{m} = 10$ ($R = -0.17$), (e) the azimuthal angular velocity u_ϕ/s (changing sign) and (f) the azimuthal magnetic field b_ϕ. *Bottom row*: (g) azimuthal angular velocity u_ϕ/s for no-slip boundary with $P\mathrm{m} = 1$ showing no reflection ($R = 0$) for insulating boundary, (h) and little reflection when the insulator is replaced by a solid conductive layer.

to its reflections at the boundaries. In the case of an Alfvén wave turbulence (many wave packets) in a spherical shell of radius L with homogeneous mean energy e, permeated by a magnetic field of rms intensity B_0, any wave packet will reach the outer insulating boundary once (on average) in the time interval L/V_A. When it reflects on the boundary, it loses the fraction $1 - R^2(P\mathrm{m})$ of its energy, where $R(P\mathrm{m})$ is the reflection coefficient (in amplitude). We can then estimate the dissipation rate of energy e due to this process

$$\partial_t e \sim \left[R^2(P\mathrm{m}) - 1\right] \frac{B_0}{L\sqrt{\mu_0 \rho}}\, e. \tag{11}$$

Hence, the timescale of dissipation at the boundaries

$$\tau_s = \frac{L}{V_\mathrm{A}} \frac{1}{1 - R^2(P\mathrm{m})}, \tag{12}$$

which is inversely proportional to the strength of the magnetic field, and depends on the diffusivities only through $P\mathrm{m}$.

We can compare this to the dissipation of Alfvén waves of length scale ℓ in the bulk of the fluid: $\tau_v = 2\ell^2/(\eta + \nu)$. It appears that the length scale ℓ where surface and bulk dissipation are comparable is such that

$$L/\ell = \sqrt{S}\sqrt{1 - R^2}. \tag{13}$$

Hence, for the Earth's core with $S \sim 10^4$, and $R \sim 0.9$ (the stress-free value which gives a good approximation of the low Pm value), the dissipation of Alfvén waves is dominated by the partial absorption at the boundaries for length scales larger than $L/45$. For numerical simulations of the geodynamo with $S \sim 10^3$ ans $R \sim 0.2$, we have $L/\ell \sim 30$.

These timescales are also relevant for torsional normal modes. In 1-D, normal modes are a superposition of waves propagating in opposite directions. Hence, if the dissipation of waves is dominated by their reflection, so will it be for the normal modes. From the previous estimation of L/ℓ in the Earth's core, we expect the dissipation of large wavelength TAW (the ones that can be observed) to be dominated by the effect of reflection. Furthermore, to detect a normal mode, its dissipation time must be much larger than its period $T = 2\pi L(cV_A)^{-1}$. The pulsation c of the first torsional normal modes are given in section 4.2 in Alfvén frequency units, and their dissipation time can be estimated by τ_s for the large-scale normal modes. We define a quality factor for torsional normal modes by

$$Q = \frac{\tau_s}{T} = \frac{c}{2\pi}\frac{1}{1-R^2}. \tag{14}$$

Presence of normal modes requires $Q \gg 1$. Assuming $R = 0.9$ (stress-free value) in the Earth's core, we find $Q_E \simeq 0.8\,c$ and for no-slip numerical simulations of the geodynamo we find $Q_{\rm sim} < 0.16\,c$. Considering the largest modes (with $c \simeq 5$ to 15), torsional oscillations could therefore persist in the Earth's core for a few Alfvén times, but are completely absent even from the best current geodynamo simulations.

5 DISCUSSION: IMPLICATION FOR NUMERICAL GEODYNAMO MODELS AND THE EARTH-CORE

We showed that numerical simulations conducted for $Pm \sim 1$ cannot adequately reproduce the boundary conditions for TAW in the Earth's core (where $Pm \ll 1$). The small reflection coefficient observed for TAW (Fig. 3) means that it is hard to observe TAW reflection at the equator in numerical simulations of the geodynamo which currently operate with $0.1 < Pm < 10$ (e.g. Takahashi *et al.* 2008; Sakuraba & Roberts 2009), where the waves are moreover mixed with thermal convection.

As for possible torsional eigenmodes, it is almost impossible to observe them with such low reflection coefficients. Unfortunately, that severely limits the ability of geodynamo simulations to exhibit torsional oscillation normal modes, because normal modes require a large reflection coefficient to be observable: their period (of order L/V_A) must be much larger than the energy dissipation time τ_s (see expression 12). A few studies have tried to pin down torsional eigenmodes (Dumberry & Bloxham 2003; Sakuraba & Roberts 2008; Wicht & Christensen 2010) but even though they report waves propagating with the appropriate speed, they report neither reflection of these waves, nor eigenmodes.

Another issue for geodynamo models with very low diffusivities, is that the part of the energy carried by Alfvén waves (regular or torsional) is dissipated very quickly (on an Alfvén wave timescale), so that an Alfvén wave turbulence would be damped much faster, and the turbulent state may be far from what we would expect in the Earth's core.

Changing the boundary condition to stress-free simulates the case $Pm = 0$ with a high reflection coefficient ($R = 0.88$), but still lower than the planar case. Even though this may still be problematic to observe eigenmodes, numerical models that use stress-free boundaries (e.g. Kuang & Bloxham 1999; Dumberry & Bloxham 2003; Busse & Simitev 2006; Sreenivasan & Jones 2011) are intrinsically much more suited for the study of torsional normal modes. Quasi-geostrophic dynamo models that can compute dynamo models at very low magnetic Prandtl numbers ($Pm < 10^{-2}$ in Schaeffer & Cardin 2006), could also provide an interesting tool to study torsional oscillations.

In the case of the Earth's core, a recent study (Gillet *et al.* 2010) found no clear evidence for reflection at the equator, although this has yet to be confirmed. One might want to invoke turbulent viscosity (see the contrasted views of Deleplace & Cardin (2006) and Buffett & Christensen (2007) in a different context) to explain this fact, leading to an effective Pm close to 1 and inhibiting reflection of TAW. This would make numerical models more relevant, but is rather speculative. A solid conductive layer at the top of the core can also have a damping effect on the propagation and reflection of torsional waves, and we plan to investigate these matters in a forthcoming study.

ACKNOWLEDGMENTS

The numerical simulations were run at the Service Commun de Calcul Intensif de l'Observatoire de Grenoble (SCCI). We want to thank Mathieu Dumberry and an anonymous reviewer for their help in improving this paper, and Henri-Claude Nataf for useful comments.

REFERENCES

Alboussière, T., Cardin, P., Debray, F., La Rizza, P., Masson, J.P., Plunian, F., Ribeiro, A. & Schmitt, D., 2011. Experimental evidence of Alfvén wave propagation in a gallium alloy, *Phys. Fluids,* **23**(9), 096 601-1–096601-10, doi:10.1063/1.3633090.

Alfvén, H., 1942. Existence of electromagnetic-hydrodynamic waves, *Nature,* **150,** 405–406.

Braginsky, S., 1984. Short-period geomagnetic secular variation, *Geophys. Astrophys. Fluid Dyn.,* **30**(1–2), 1–78.

Braginsky, S.I., 1970. Torsional magnetohydrodynamic vibrations in the Earth's core and variations in day length, *Geomagn. Aeron.,* **10,** 1–8.

Buffett, B.A., 1998. Free oscillations in the length of day: inferences on physical properties near the core mantle boundary, in *The Core–Mantle Boundary Region,* Geodynamics Series, Vol. 28, pp. 153–165, eds Gurnis, M., Wysession, M.E., Knittle, E. & Buffett, B.A., AGU, Washington, D.C.

Buffett, B.A. & Christensen, U.R., 2007. Magnetic and viscous coupling at the core-mantle boundary: inferences from observations of the Earth's nutations, *Geophys. J. Int.,* **171,** 145–152.

Busse, F.H. & Simitev, R.D., 2005. Convection in rotating spherical fluid shells and its dynamo states, in *Fluid Dynamics and Dynamos in Astrophysics and Geophysics,* pp. 359–392, eds Jones, C.A., Soward, A.M., Hughes, D.W. & Weiss, N.O., CRC Press, Boca Raton.

Busse, F.H. & Simitev, R.D., 2006. Parameter dependences of convection-driven dynamos in rotating spherical fluid shells, *Geophys. Astrophys. Fluid Dyn.,* **100**(4), 341–361.

Deleplace, B. & Cardin, P., 2006. Viscomagnetic torque at the core mantle boundary, *Geophys. J. Int.,* **167,** 557–566.

Dumberry, M. & Bloxham, J., 2003. Torque balance, Taylor's constraint and torsional oscillations in a numerical model of the geodynamo, *Phys. Earth planet. Inter.,* **140**(1–3), 29–51.

Gillet, N., Jault, D., Canet, E. & Fournier, A., 2010. Fast torsional waves and strong magnetic field within the Earth's core, *Nature,* **465**(7294), 74–77.

Gillet, N., Schaeffer, N. & Jault, D., 2011. Rationale and geophysical evidence for quasi-geostrophic rapid dynamics within the Earth's outer core, *Phys. Earth planet. Inter.,* **187**(3–4), 380–390.
Jameson, A., 1961. Magnetohydrodynamic waves, *PhD thesis*, University of Cambridge, Cambridge.
Jameson, A., 1964. A demonstration of Alfvén waves part 1. generation of standing waves, *J. Fluid Mech.,* **19**(04), 513–527.
Jault, D., 2003. Electromagnetic and topographic coupling, and LOD variations., in *Earth's Core and Lower Mantle,* pp. 56–76, eds Jones, C.A., Soward, A.M. & Zhang, K., Taylor & Francis, Oxford.
Jault, D., 2008. Axial invariance of rapidly varying diffusionless motions in the Earth's core interior, *Phys. Earth planet. Inter.,* **166,** 67–76.
Jordi, C., Morrison, L., Rosen, R., Salstein, D. & Rossello, G., 1994. Fluctuations in the earth's rotation since 1830 from high-resolution astronomical data, *Geophys. J. Int.,* **117**(3), 811–818.
Kuang, W. & Bloxham, J., 1999. Numerical modeling of magnetohydrodynamic convection in a rapidly rotating spherical shell: weak and strong field dynamo action, *J. Comput. Phys.,* **153**(1), 51–81.
Roberts, P.H., 1967. *An Introduction to Magnetohydrodynamics,* Elsevier, New York, NY.
Roberts, P.H. & Aurnou, J.M., 2011. On the theory of core-mantle coupling, *Geophys. Astrophys. Fluid Dyn.,* **106,** 1–74.
Sakuraba, A. & Roberts, P., 2008. Torsional oscillations in a numerical geodynamo operating in a regime of low ekman and magnetic prandtl numbers, in *AGU Fall Meeting Abstracts,* pp. A1773+, AGU, Washington, D.C.
Sakuraba, A. & Roberts, P.H., 2009. Generation of a strong magnetic field using uniform heat flux at the surface of the core, *Nat. Geosci.,* **2**(11), 802–805.
Schaeffer, N., 2012. Efficient Spherical Harmonic Transforms aimed at pseudo spectral numerical simulations, preprint, arXiv:1202.6522.
Schaeffer, N. & Cardin, P., 2006. Quasi-geostrophic kinematic dynamos at low magnetic Prandtl number, *Earth planet. Sci. Lett.,* **245**(3–4), 595–604.
Sreenivasan, B. & Jones, C.A., 2011. Helicity generation and subcritical behaviour in rapidly rotating dynamos, *J. Fluid Mech.,* **688,** 5–30.
Takahashi, F., Matsushima, M. & Honkura, Y., 2008. Scale variability in convection-driven MHD dynamos at low ekman number, *Phys. Earth planet. Inter.,* **167**(3–4), 168–178.
Wicht, J. & Christensen, U.R., 2010. Torsional oscillations in dynamo simulations, *Geophys. J. Int.,* **181**(3), 1367–1380.

APPENDIX A: ANALYTIC ALFVÉN WAVE SOLUTIONS IN ONE DIMENSION

A1 Plane wave solutions

Following Jameson (1961, p. 15–18), we look for plane wave solutions of eqs (1) and (2), substituting $u = Ue^{i(\omega t + kx)}$ and $b = \sqrt{\mu_0 \rho}\, Be^{i(\omega t + kx)}$

$$\left(i\omega + \nu k^2\right) U = V_A ikB, \tag{A1}$$

$$\left(i\omega + \eta k^2\right) B = V_A ikU, \tag{A2}$$

which we can combine into

$$\nu\eta\, k^4 + \left(V_\mathrm{A}^2 + i\omega(\eta + \nu)\right) k^2 - \omega^2 = 0, \tag{A3}$$

for which the exact solutions are

$$k^2 = -\frac{V_\mathrm{A}^2}{2\nu\eta}(1 + 2i\epsilon)\left(1 \pm \sqrt{1 + \frac{4\omega^2\nu\eta}{V_A^4(1 + 2i\epsilon)^2}}\right), \tag{A4}$$

where ϵ is the reciprocal Lundquist number based on the frequency

$$\epsilon = \frac{\omega(\eta + \nu)}{2V_a^2}. \tag{A5}$$

In the regime where Alfvén waves do propagate, we have $\epsilon \ll 1$ and also $\omega\sqrt{\nu\eta}/V_\mathrm{A}^2 \ll 1$ so we can approximate the square root by its first-order Taylor expansion, which leads to two solutions k_1^2 and k_2^2

$$k_1^2 = \frac{\omega^2}{V_\mathrm{A}^2}(1 + 2i\epsilon)^{-1} \qquad k_2^2 = -\frac{V_\mathrm{A}^2}{\nu\eta}(1 + 2i\epsilon). \tag{A6}$$

The solutions $k = \pm k_1 = \pm\omega/V_\mathrm{A}(1 - i\epsilon)$, correspond to the propagation in both directions of an Alfvén wave at the speed V_A and with attenuation on a length scale $V_\mathrm{A}/(\epsilon\omega)$. The solutions $k = \pm k_2 \simeq \pm i/\delta$ correspond to a Hartmann boundary layer of thickness $\delta \equiv \sqrt{\nu\eta}/V_\mathrm{A}$.

Finally, from eqs (A1) and (A2) we know that U and B are related for each k by

$$\frac{B}{U} = \frac{ikV_a}{i\omega + \eta k^2} = \frac{i\omega + \nu k^2}{ikV_a} \equiv \alpha_k, \tag{A7}$$

and for the solutions $k = \pm k_1$ and $k = \pm k_2$, it reduces to

$$\alpha_{\pm k_1} \simeq \pm 1 \qquad \alpha_{\pm k_2} \simeq \pm\sqrt{\frac{\nu}{\eta}} = \pm\sqrt{P\mathrm{m}}. \tag{A8}$$

This means that for the travelling wave solution, U and B have always the same amplitude and the same phase when propagating in the direction opposite to the imposed magnetic field, or opposite phase when propagating in the same direction. For the boundary layers, in the limit $P\mathrm{m} \ll 1$ they involve the velocity field alone, whereas for $P\mathrm{m} \gg 1$ they involve only the magnetic field.

A2 Reflection coefficient at an insulating wall

To derive the reflection coefficient, we consider an insulating wall at $x = 0$ with an incoming Afvén wave from the $x > 0$ region ($k = +k_1$), giving rise to a reflected wave ($k = -k_1$). The boundary conditions are matched by a boundary layer ($k = +k_2$) localized near $x = 0$ (the solution $k = -k_2$ is growing exponentially for $x > 0$ and has to be rejected for this problem). The solution to this problem reads

$$u = e^{i\omega t}\left[e^{ik_1 x} + Re^{-ik_1 x} + \beta e^{ik_2 x}\right], \tag{A9}$$

$$b = e^{i\omega t}\left[\alpha_{k_1}\left(e^{ik_1 x} - Re^{-ik_1 x}\right) + \alpha_{k_2}\beta e^{ik_2 x}\right]\sqrt{\mu_0\rho}, \tag{A10}$$

where we have taken into account the fact that $\alpha_{-k_1} = -\alpha_{k_1}$ (see eq. A8).

The boundary conditions $u = 0$ and $b = 0$ at $x = 0$ lead to

$$1 + R + \beta = 0 \qquad \alpha_{k_1}(1 - R) + \alpha_{k_2}\beta = 0,$$

from which we find the amplitude β of the velocity boundary layer contribution, and the reflection coefficient R of the amplitude of the velocity component

$$\beta = \frac{-2}{1 + \alpha_{k_2}/\alpha_{k_1}} \qquad R = \frac{1 - \alpha_{k_2}/\alpha_{k_1}}{1 + \alpha_{k_2}/\alpha_{k_1}}.$$

We are left to evaluate $\alpha_{k_2}/\alpha_{k_1}$ using eqs (A8), which gives $\alpha_{k_2}/\alpha_{k_1} = \sqrt{\nu/\eta}$ at leading order in ϵ, and thus

$$R = \frac{1 - \sqrt{P\mathrm{m}}}{1 + \sqrt{P\mathrm{m}}}, \tag{A11}$$

which is independent of ω and V_A. In the case $P\mathrm{m} = 1$, we then have $R = 0$ and $\beta = -1$ which means that no reflection occurs and that the amplitude of the incoming wave is canceled by the boundary layer alone.

It may be worth emphasizing that, although the boundary layer has the same thickness δ in the velocity and the magnetic field components, in the limit $Pm \to 0$, we have $\beta \to -2$ and $\alpha_{k_2}\beta \to 0$, so that the boundary layer is apparent only in the velocity field component (eq. A9), whereas in the limit $Pm \to \infty$, we have $\beta \to 0$ and $\alpha_{k_2}\beta \to -2$, so that the boundary layer is apparent only in the magnetic field component (eq. A10).

Finally, we remark that if one sets $\nu = 0$ or $\eta = 0$ from the beginning in eqs (A1) and (A2), the solution corresponding to the boundary layer does not exist anymore.

Efficient Spherical Harmonic Transforms aimed at pseudo-spectral numerical simulations

Nathanaël Schaeffer
ISTerre, Université de Grenoble 1, CNRS, F-38041 Grenoble, France

June 19, 2015
published in *Geochemistry, Geophysics, Geosystems* **14**, doi:10.1002/ggge.20071 (2013)

Abstract

In this paper, we report on very efficient algorithms for the spherical harmonic transform (SHT). Explicitly vectorized variations of the algorithm based on the Gauss-Legendre quadrature are discussed and implemented in the `SHTns` library which includes scalar and vector transforms. The main breakthrough is to achieve very efficient on-the-fly computations of the Legendre associated functions, even for very high resolutions, by taking advantage of the specific properties of the SHT and the advanced capabilities of current and future computers. This allows us to simultaneously and significantly reduce memory usage and computation time of the SHT. We measure the performance and accuracy of our algorithms. Even though the complexity of the algorithms implemented in `SHTns` are in $\mathcal{O}(N^3)$ (where N is the maximum harmonic degree of the transform), they perform much better than any third party implementation, including lower complexity algorithms, even for truncations as high as $N = 1023$. `SHTns` is available at `https://bitbucket.org/nschaeff/shtns` as open source software.

1 Introduction

Spherical harmonics are the eigenfunctions of the Laplace operator on the 2-sphere. They form a basis and are useful and convenient to describe data on a sphere in a consistent way in spectral space. Spherical Harmonic Transforms (SHT) are the spherical counterpart of the Fourier transform, casting spatial data to the spectral domain and vice versa. They are commonly used in various pseudo-spectral direct numerical simulations in spherical geometry, for simulating the Sun or the liquid core of the Earth among others (Glatzmaier, 1984; Sakuraba, 1999; Christensen et al., 2001; Brun and Rempel, 2009; Wicht and Tilgner, 2010).

All numerical simulations that take advantage of spherical harmonics use the classical Gauss-Legendre algorithm (see section 2) with complexity $\mathcal{O}(N^3)$ for a truncation at spherical harmonic degree N. As a consequence of this high computational cost when N increases, high resolution spherical codes currently spend most of their time performing SHT. A few years ago, state of the art numerical simulations used $N = 255$ (Sakuraba and Roberts, 2009).

However, there exist several asymptotically fast algorithms (Driscoll and Healy, 1994; Potts et al., 1998; Mohlenkamp, 1999; Suda and Takami, 2002; Healy et al., 2003; Tygert, 2008), but the overhead for these fast algorithms is such that they do not claim to be effectively faster for $N < 512$. In addition, some of them lack stability (the error becomes too large even for moderate N) and flexibility (e.g. $N + 1$ must be a power of 2).

Among the asymptotically fast algorithms, only two have open-source implementations, and the only one which seems to perform reasonably well is `SpharmonicKit`, based on the algorithms described by Healy et al. (2003). Its main drawback is the need of a latitudinal grid of size $2(N+1)$ while the Gauss-Legendre quadrature allows the use of only $N + 1$ collocation points. Thus, even if it were as fast as the Gauss-Legendre approach for the same truncation N, the overall numerical

simulation would be slower because it would operate on twice as many points. These facts explain why the Gauss-Legendre algorithm is still the most efficient solution for numerical simulations.

A recent paper (Dickson et al., 2011) reports that carefully tuned software could finally run 9 times faster on the same CPU than the initial non-optimized version, and insists on the importance of vectorization and careful optimization of the code. As the goal of this work is to speed-up numerical simulations, we have written a highly optimized and explicitly vectorized version of the Gauss-Legendre SHT algorithm. The next section recalls the basics of spherical harmonic transforms. We then describe the optimizations we use and we compare the performance of our transform to other SHT implementations. We conclude this paper by a short summary and perspectives for future developments.

2 Spherical Harmonic Transform (SHT)

2.1 Definitions and properties

The orthonormalized spherical harmonics of degree n and order $-n \leq m \leq n$ are functions defined on the sphere as:

$$Y_n^m(\theta, \phi) = P_n^m(\cos\theta)\, \exp(im\phi) \tag{1}$$

where θ is the colatitude, ϕ is the longitude and P_n^m are the associated Legendre polynomials normalized for spherical harmonics

$$P_n^m(x) = (-1)^m \sqrt{\frac{2n+1}{4\pi}} \sqrt{\frac{(n-|m|)!}{(n+|m|)!}}\, (1-x^2)^{|m|/2}\, \frac{d^{|m|}}{dx^{|m|}} P_n(x) \tag{2}$$

which involve derivatives of Legendre Polynomials $P_n(x)$ defined by the following recurrence:

$$\begin{aligned} P_0(x) &= 1 \\ P_1(x) &= x \\ nP_n(x) &= (2n-1)\, x\, P_{n-1}(x) \;-\; (n-1) P_{n-2}(x) \end{aligned}$$

The spherical harmonics $Y_n^m(\theta, \phi)$ form an orthonormal basis for functions defined on the sphere:

$$\int_0^{2\pi} \int_0^{\pi} Y_n^m(\theta, \phi) \overline{Y_l^k}(\theta, \phi) \sin\theta \, d\theta \, d\phi = \delta_{nl} \delta_{mk} \tag{3}$$

with δ_{ij} the Kronecker symbol, and $\overline{z}$ the complex conjugate of z. By construction, they are eigenfunctions of the Laplace operator on the unit sphere:

$$\Delta Y_n^m = -n(n+1) Y_n^m \tag{4}$$

This property is very appealing for solving many physical problems in spherical geometry involving the Laplace operator.

2.2 Synthesis or inverse transform

The Spherical Harmonic synthesis is the evaluation of the sum

$$f(\theta, \phi) = \sum_{n=0}^{N} \sum_{m=-n}^{n} f_n^m Y_n^m(\theta, \phi) \tag{5}$$

up to degree $n = N$, given the complex coefficients f_n^m. If $f(\theta, \phi)$ is a real-valued function, $f_n^{-m} = \overline{f_n^m}$.

The sums can be exchanged, and using the expression of Y_n^m we can write

$$f(\theta,\phi) = \sum_{m=-N}^{N} \left(\sum_{n=|m|}^{N} f_n^m P_n^m(\cos\theta) \right) e^{im\phi} \tag{6}$$

From this last expression, it appears that the summation over m is a regular Fourier Transform. Hence the remaining task is to evaluate

$$f_m(\theta) = \sum_{n=|m|}^{N} f_n^m P_n^m(\cos\theta) \tag{7}$$

or its discrete version at given collocation points θ_j.

2.3 Analysis or forward transform

The analysis step of the SHT consists in computing the coefficients

$$f_n^m = \int_0^{2\pi} \int_0^{\pi} f(\theta,\phi)\overline{Y_n^m}(\theta,\phi)\sin\theta\, d\theta\, d\phi \tag{8}$$

The integral over ϕ is obtained using the Fourier Transform:

$$f_m(\theta) = \int_0^{2\pi} f(\theta,\phi)e^{-im\phi}\, d\phi \tag{9}$$

so the remaining Legendre transform reads

$$f_n^m = \int_0^{\pi} f_m(\theta)P_n^m(\cos\theta)\sin\theta\, d\theta \tag{10}$$

The discrete problem reduces to the appropriate quadrature rule to evaluate the integral (10) knowing only the values $f_m(\theta_j)$. In particular, the use of the Gauss-Legendre quadrature replaces the integral of expression 10 by the sum

$$f_n^m = \sum_{j=1}^{N_\theta} f_m(\theta_j)P_n^m(\cos\theta_j)w_j \tag{11}$$

where θ_j and w_j are respectively the Gauss nodes and weights (Temme, 2011). Note that the sum equals the integral if $f_m(\theta)P_n^m(\cos\theta)$ is a polynomial in $\cos\theta$ of order $2N_\theta - 1$ or less. If $f_m(\theta)$ is given by expression 7, then $f_m(\theta)P_n^m(\cos\theta)$ is always a polynomial in $\cos\theta$, of degree at most $2N$. Hence the Gauss-Legendre quadrature is exact for $N_\theta \geq N + 1$.

A discrete spherical harmonic transform using Gauss nodes as latitudinal grid points and a Gauss-Legendre quadrature for the analysis step is referred to as a Gauss-Legendre algorithm.

3 Optimization of the Gauss-Legendre algorithm

3.1 Standard optimizations

Let us first recall some standard optimizations found in almost every serious implementation of the Gauss-Legendre algorithm. All the following optimizations are used in the `SHTns` library.

Use the Fast-Fourier Transform The expressions of section 2 show that part of the SHT is in fact a Fourier transform. The fast Fourier transform (FFT) should be used for this part, as it improves accuracy and speed. `SHTns` uses the `FFTW` library(Frigo and Johnson, 2005), a portable, flexible and highly efficient FFT implementation.

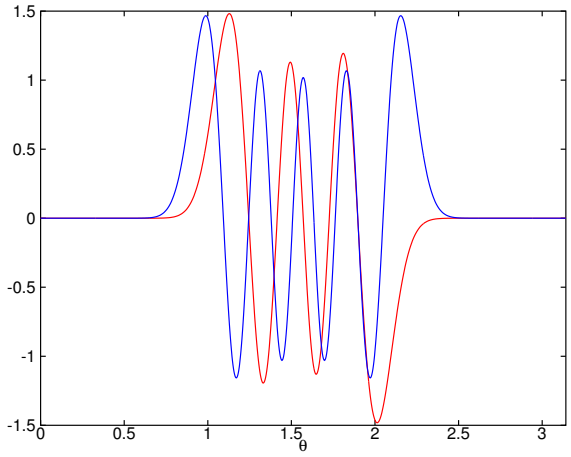

Figure 1: Two associated Legendre polynomials of degree $n = 40$ and order $m = 33$ (blue) and $m = 36$ (red), showing the localization near the equator.

Take advantage of Hermitian symmetry for real data When dealing with real-valued data, the spectral coefficients fulfill $f_n^{-m} = \overline{f_n^m}$, so we only need to store them for $m \geq 0$. This also allows the use of faster real-valued FFTs.

Take advantage of mirror symmetry Due to the defined symmetry of spherical harmonics with respect to a reflection about the equator

$$P_n^m(\cos(\pi - \theta)) = (-1)^{n+m} P_n^m(\cos\theta)$$

one can reduce by a factor of 2 the operation count of both forward and inverse transforms.

Precompute values of P_n^m The coefficients $P_n^m(\cos\theta_j)$ appear in both synthesis and analysis expressions (7 and 10), and can be precomputed and stored for all (n,m,j). When performing multiple transforms, it avoids computing the Legendre polynomial recursion at every transform and saves some computing power, at the expense of memory bandwidth. This may or may not be efficient, as we will discuss later.

Polar optimization High order spherical harmonics have their magnitude decrease exponentially when approaching the poles as shown in Figure 1. Hence, the integral of expression 10 can be reduced to

$$f_n^m = \int_{\theta_0^{mn}}^{\pi-\theta_0^{mn}} f_m(\theta) P_n^m(\cos\theta) \sin\theta \, d\theta \tag{12}$$

where $\theta_0^{mn} \geq 0$ is a threshold below which P_n^m is considered to be zero. Similarly, the synthesis of $f_m(\theta)$ (eq. 7) is only needed for $\theta_0^{mn} \leq \theta \leq \pi - \theta_0^{mn}$. `SHTns` uses a threshold θ_0^{mn} that does not depend on n, which leads to around 5% to 20% speed increase, depending on the desired accuracy and the truncation N.

3.2 On-the-fly algorithms and vectorization

It can be shown that $P_n^m(x)$ can be computed recursively by

$$P_m^m(x) = a_m^m \left(1 - x^2\right)^{|m|/2} \tag{13}$$
$$P_{m+1}^m(x) = a_{m+1}^m \, x P_m^m(x) \tag{14}$$
$$P_n^m(x) = a_n^m \, x P_{n-1}^m(x) + b_n^m \, P_{n-2}^m(x) \tag{15}$$

with

$$a_m^m = \sqrt{\frac{1}{4\pi}\prod_{k=1}^{|m|}\frac{2k+1}{2k}} \tag{16}$$

$$a_n^m = \sqrt{\frac{4n^2-1}{n^2-m^2}} \tag{17}$$

$$b_n^m = -\sqrt{\frac{2n+1}{2n-3}\,\frac{(n-1)^2-m^2}{n^2-m^2}} \tag{18}$$

The coefficients a_n^m and b_n^m do not depend on x, and can be easily precomputed and stored into an array of $(N+1)^2$ values. This has to be compared to the order N^3 values of $P_n^m(x_j)$, which are usually precomputed and stored in the spherical harmonic transforms implemented in numerical simulations. The amount of memory required to store all $P_n^m(x_j)$ in double-precision is at least $2(N+1)^3$ bytes, which gives 2Gb for $N = 1023$. Our on-the-fly algorithm only needs about $8(N+1)^2$ bytes of storage (same size as a spectral representation f_n^m), that is 8Mb for $N = 1023$. When N becomes very large, it is no longer possible to store $P_n^m(x_j)$ in memory (for $N \gtrsim 1024$ nowadays) and on-the-fly algorithms (which recompute $P_n^m(x_j)$ from the recurrence relation when needed) are then the only possibility.

We would like to stress that even far from that storage limit, on-the-fly algorithm can be significantly faster thanks to vector capabilities of modern processors. Most desktop and laptop computers, as well as many high performance computing clusters, have support for Single-Instruction-Multiple-Data (SIMD) operations in double precision. The SSE2 instruction set is available since year 2000 and currently supported by almost every PC, allowing to perform the same double precision arithmetic operations on a vector of 2 double precision numbers, effectively doubling the computing power. The recently introduced AVX instruction set increases the vector size to 4 double precision numbers. This means that $P_n^m(x)$ can be computed from the recursion relation 15 (which requires 3 multiplications and 1 addition) for 2 or 4 values of x simultaneously, which may be faster than loading pre-computed values from memory. Hence, as already pointed out by Dickson et al. (2011), it is therefore very important to use the vector capabilities of modern processors to address their full computing power. Furthermore, when running multiple transforms on the different cores of a computer, the performance of on-the-fly transforms (which use less memory bandwidth) scales much better than algorithms with precomputed matrices, because the memory bandwidth is shared between cores. Superscalar architectures that do not have double-precision SIMD instructions but have many computation units per core (like the POWER7 or SPARC64) could also benefit from on-the-fly transforms by saturating the many computation units with independent computations (at different x).

Figure 2 shows the benefit of explicit vectorization of on-the-fly algorithms on an intel Xeon E5-2680 (*Sandy Bridge* architecture with AVX instruction set running at 2.7GHz) and compares on-the-fly algorithms with algorithms based on precomputed matrices. With the 4-vectors of AVX, the fastest algorithm is always on-the-fly, while for 2-vectors, the fastest algorithm uses precomputed matrices for $N \lesssim 200$. In the forthcoming years, wider vector architecture are expected to become widely available, and the benefits of on-the-fly vectorized transforms will become even more important.

Runtime tuning We have now two different available algorithms: one uses precomputed values for $P_n^m(x)$ and the other one computes them on-the-fly at each transform. The `SHTns` library compares the time taken by those algorithms (and variants) at startup and chooses the fastest, similarly to what the `FFTW` library(Frigo and Johnson, 2005) does. The time overhead required by runtime tuning can be several order of magnitude larger than that of a single transform. The observed performance gain varies between 10 and 30%. This is significant for numerical simulations, but runtime tuning can be entirely skipped for applications performing only a few transforms, in which case there is no noticeable overhead.

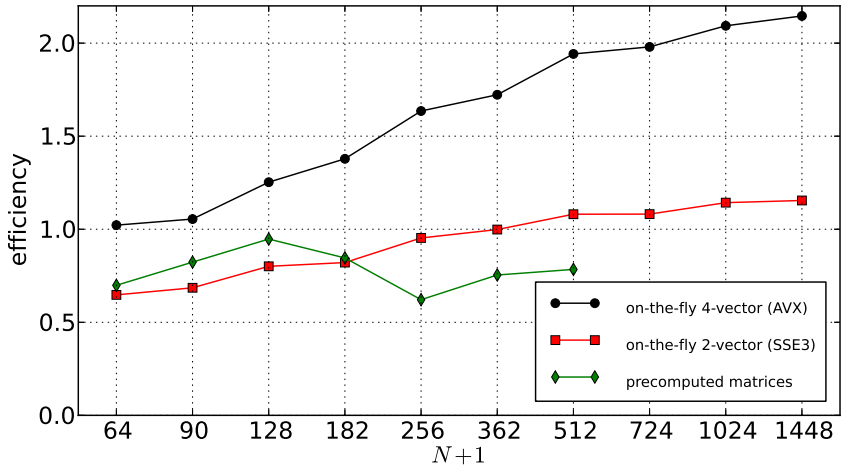

Figure 2: Efficiency $(N+1)^3/(2tf)$ of various algorithms, where t is the execution time and f the frequency of the Xeon E5-2680 CPU (2.7GHz). On-the-fly algorithms with two different vector sizes are compared with the algorithm using precomputed matrices. Note the influence of hardware vector size for on-the-fly algorithms (AVX vectors pack 4 double precision floating point numbers where SSE3 vectors pack only 2). The efficiency of the algorithm based on precomputed matrices drops above $N = 127$ probably due to cache size limitations.

3.3 Multi-threaded transform

Modern computers have several computing cores. We use OpenMP to implement a multi-threaded algorithm for the Legendre transform including the above optimizations and the *on-the-fly* approach. The lower memory bandwidth requirements for the *on-the-fly* approach is an asset for a multi-threaded transform because if each thread would read a different portion of a large matrix, it can saturate the memory bus very quickly. The multi-threaded Fourier transform is left to the FFTW library.

We need to decide how to share the work between different threads. Because we compute the P_n^m on the fly using the recurrence relation 15, we are left with each thread computing different θ, or different m. As the analysis step involve a sum over θ, we choose the latter option.

From equation 7, we see that the number of terms involved in the sum depends on m, so that the computing cost will also depend on m. In order to achieve the best workload balance between a team of p threads, the thread number i $(0 \leq i < p)$ handles $m = i + kp \leq N$, with integer k from 0 to $(N+1)/p$.

For different thread number p, we have measured the time $T_s(p)$ and $T_a(p)$ needed for a scalar spherical harmonic synthesis and analysis respectively (including the FFT).

Figure 3 shows the speedup $T(1)/T(p)$, where $T(p)$ is the largest of $T_s(p)$ and $T_a(p)$, and $T(1)$ is the time of the fastest single threaded tranform. It shows that there is no point in doing a parallel transform with N below 128. The speedup is good for $N = 255$ or above, and excellent up to 8 threads for $N \geq 511$ or up to 16 threads for very large transform ($N \geq 2047$).

3.4 Performance comparisons

Table 1 reports the timing measurements of two SHT libraries, compared to the optimized Gauss-Legendre implementation found in the `SHTns` library (this work). We compare with the Gauss-Legendre implementation of `libpsht` (Reinecke, 2011), a parallel spherical harmonic transform library targeting very large N, and with `SpharmonicKit` 2.7 (DH) which implements one of the Driscoll-Healy fast algorithms (Healy et al., 2003). All the timings are for a complete SHT, which includes the Fast Fourier Transform. Note that the Gauss-Legendre algorithm is by far (a factor of order 2) the fastest algorithm of the `libpsht` library. Note also that `SpharmonicKit`

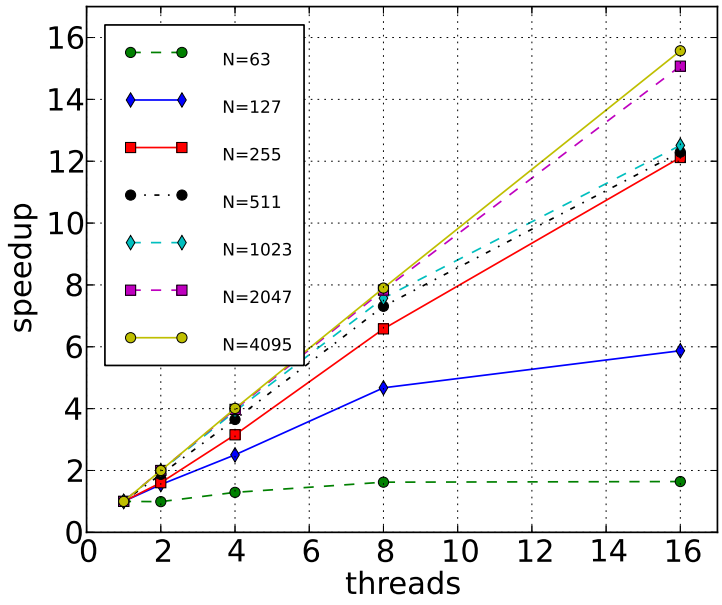

Figure 3: Speedup obtained with multiple threads using OpenMP (`gcc` 4.6.3) on a 16 core intel Xeon E5-2680 (*Sandy Bridge* architecture with AVX instruction set running at 2.7 GHz).

N	63	127	255	511	1023	2047	4095
`libpsht` (1 thread)	1.05 ms	4.7 ms	27 ms	162 ms	850 ms	4.4 s	30.5 s
DH (fast)	1.1 ms	5.5 ms	21 ms	110 ms	600 ms	NA	NA
`SHTns` (1 thread)	0.09 ms	0.60 ms	4.2 ms	28 ms	216 ms	1.6 s	11.8 s

Table 1: Comparison of execution time for different SHT implementations. The numbers correspond to the average execution time for forward and backward scalar transform (including the FFT) on an Intel Xeon X5650 (2.67GHz) with 12 cores. The programs were compiled with `gcc 4.4.5` and `-O3 -march=native -ffast-math` compilation options.

is limited to $N+1$ being a power of two, requires $2(N+1)$ latitudinal colocation points, and crashed for $N = 2047$. The software library implementing the fast Legendre transform described by Mohlenkamp (1999), `libftsh`, has also been tested, and found to be of comparable performance to that of `SpharmonicKit`, although the comparison is not straightforward because `libftsh` did not include the Fourier Transform. Again, that fast library could not operate at $N = 2047$ because of memory limitations. Note finally that these measurements were performed on a machine that did not support the new AVX instruction set.

In order to ease the comparison, we define the efficiency of the SHT by $(N+1)^3/(2Tf)$, where T is the execution time (reported in Table 1) and f the frequency of the CPU. Note that $(N+1)^3/2$ reflects the number of computation elements of a Gauss-Legendre algorithm (the number of modes $(N+1)(N+2)/2$ times the number of latitudinal points $N+1$). An efficiency that does not depend on N corresponds to an algorithm with an execution time proportional to N^3.

The efficiency of the tested algorithms are displayed in Figure 4. Not surprisingly, the Driscoll-Healy implementation has the largest slope, which means that its efficiency grows fastest with N, as expected for a fast algorithm. It also performs slightly better than `libpsht` for $N \geq 511$. However, even for $N = 1023$ (the largest size that it can compute), it is still 2.8 times slower than the Gauss-Legendre algorithm implemented in `SHTns`. It is remarkable that `SHTns` achieves an efficiency very close to 1, meaning that almost one element per clock cycle is computed for $N =\geq 511$. Overall, `SHTns` is between two and ten times faster than the best alternative.

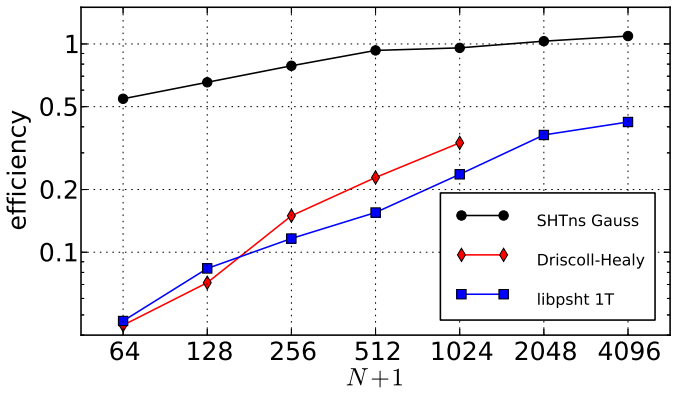

Figure 4: Efficiency $(N+1)^3/(2Tf)$ of the implementations from Table 1, where T is the execution time and f the frequency of the Xeon X5650 CPU (2.67GHz) with 12 cores.

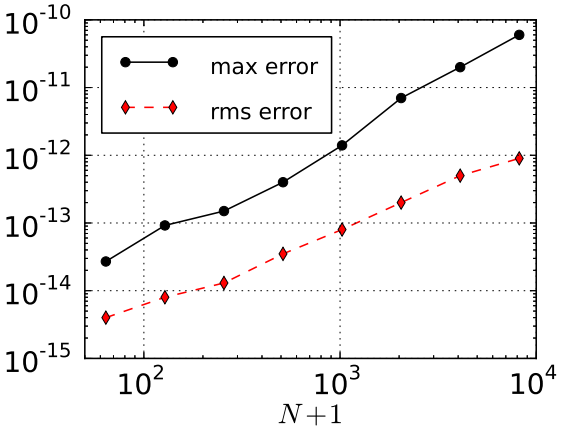

Figure 5: Accuracy of the on-the-fly Gauss-Legendre algorithm with the default polar optimization.

3.5 Accuracy

One cannot write about an SHT implementation without addressing its accuracy. The Gauss-Legendre quadrature ensures very good accuracy, at least on par with other high quality implementations.

The recurrence relation we use (see §3.2) is numerically stable, but for $N \gtrsim 1500$, the value $P_m^m(x)$ can become so small that it cannot be represented by a double precision number anymore. To avoid this underflow problem, the code dynamically rescales the values of $P_n^m(x)$ during the recursion, when they reach a given threshold. The number of rescalings is stored in an integer, which acts as an enhanced exponent. Our implementation of the rescaling does not impact performance negatively, as it is compensated by dynamic polar optimization: these very small values are treated as zero in the transform (eq. 7 and 11), but not in the recurrence. This technique ensures good accuracy up to $N = 8191$ at least, but partial transforms have been performed successfully up to $N = 43600$.

To quantify the error we start with random spherical harmonic coefficients Q_n^m with each real part and imaginary part between -1 and $+1$. After a backward and forward transform (with orthonormal spherical harmonics), we compare the resulting coefficients R_n^m with the originals Q_n^m. We use two different error measurements: the maximum error is defined as

$$\epsilon_{max} = \max_{n,m} |R_n^m - Q_n^m|$$

while the root mean square (rms) error is defined as

$$\epsilon_{rms} = \sqrt{\frac{2}{(N+1)(N+2)} \sum_{n,m} |R_n^m - Q_n^m|^2}$$

The error measurements for our on-the-fly Gauss-Legendre implementation with the default polar optimization and for various truncation degrees N are shown in Figure 5. The errors steadily increase with N and are comparable to other implementations. For $N < 2048$ we have $\epsilon_{max} < 10^{-11}$, which is negligible compared to other sources of errors in most numerical simulations.

4 Conclusion and perspectives

Despite the many fast spherical harmonic transform algorithms published, the few with a publicly available implementation are far from the performance of a carefully written Gauss-Legendre algorithm, as implemented in the `SHTns` library, even for quite large truncation ($N = 1023$). Explicitly vectorized on-the-fly algorithms seem to be able to unleash the computing power of nowadays and future computers, without suffering too much of memory bandwidth limitations, which is an asset for multi-threaded transforms.

The `SHTns` library has already been used in various demanding computations (eg. Schaeffer et al., 2012; Augier and Lindborg, 2013; Figueroa et al., 2013). The versatile truncation, the various normalization conventions supported, as well as the scalar and vector transform routines available for C/C++, Fortran or Python, should suit most of the current and future needs in high performance computing involving partial differential equations in spherical geometry.

Thanks to the significant performance gain, as well as the much lower memory requirement of vectorized on-the-fly implementations, we should be able to run spectral geodynamo simulations at $N = 1023$ in the next few years. Such high resolution simulations will operate in a regime much closer to the dynamics of the Earth's core.

Acknowledgements

The author thanks Alexandre Fournier and Daniel Lemire for their comments that helped to improve the paper. Some computations have been carried out at the Service Commun de Calcul Intensif de l'Observatoire de Grenoble (SCCI) and other were run on the PRACE Research Infrastructure *Curie* at the TGCC (grant PA1039).

References

Augier, P., Lindborg, E., Nov. 2013. A new formulation of the spectral energy budget of the atmosphere, with application to two high-resolution general circulation models. submitted to J. Atmos. Sci. arXiv:1211.0607.
URL `http://arxiv.org/abs/1211.0607`

Brun, A., Rempel, M., Apr. 2009. Large scale flows in the solar convection zone. Space Science Reviews 144 (1), 151–173.
URL `http://dx.doi.org/10.1007/s11214-008-9454-9`

Christensen, U. R., Aubert, J., Cardin, P., Dormy, E., Gibbons, S., Glatzmaier, G. A., Grote, E., Honkura, Y., Jones, C., Kono, M., Matsushima, M., Sakuraba, A., Takahashi, F., Tilgner, A., Wicht, J., Zhang, K., Dec. 2001. A numerical dynamo benchmark. Physics of The Earth and Planetary Interiors 128 (1-4), 25–34.
URL `http://dx.doi.org/10.1016/S0031-9201(01)00275-8`

Dickson, N. G., Karimi, K., Hamze, F., Jun. 2011. Importance of explicit vectorization for CPU and GPU software performance. Journal of Computational Physics 230 (13), 5383–5398.
URL http://dx.doi.org/10.1016/j.jcp.2011.03.041

Driscoll, J., Healy, D. M., June 1994. Computing fourier transforms and convolutions on the 2-sphere. Advances in Applied Mathematics 15 (2), 202–250.
URL http://dx.doi.org/10.1006/aama.1994.1008

Figueroa, A., Schaeffer, N., Nataf, H. C., Schmitt, D., Jan. 2013. Modes and instabilities in magnetized spherical couette flow. Journal of Fluid Mechanics 716, 445–469.
URL http://dx.doi.org/10.1017/jfm.2012.551

Frigo, M., Johnson, S. G., Feb. 2005. The design and implementation of FFTW3. Proceedings of the IEEE 93 (2), 216–231.
URL http://www.fftw.org/fftw-paper-ieee.pdf

Glatzmaier, G. A., Sep. 1984. Numerical simulations of stellar convective dynamos. i. the model and method. Journal of Computational Physics 55 (3), 461–484.
URL http://dx.doi.org/10.1016/0021-9991(84)90033-0

Healy, D. M., Rockmore, D. N., Kostelec, P. J., Moore, S., July 2003. Ffts for the 2-sphere-improvements and variations. Journal of Fourier Analysis and Applications 9 (4), 341–385.
URL http://dx.doi.org/10.1007/s00041-003-0018-9

Mohlenkamp, M. J., 1999. A fast transform for spherical harmonics. The Journal of Fourier Analysis and Appications 5 (2/3).
URL http://www.springerlink.com/content/n01v8q03m5584253/

Potts, D., Steidl, G., Tasche, M., Oct. 1998. Fast algorithms for discrete polynomial transforms. Mathematics of Computation 67, 1577–1590.
URL http://adsabs.harvard.edu/abs/1998MaCom..67.1577P

Reinecke, M., Feb. 2011. Libpsht – algorithms for efficient spherical harmonic transforms. Astronomy & Astrophysics 526, A108+.
URL http://arxiv.org/abs/1010.2084

Sakuraba, A., Feb. 1999. Effect of the inner core on the numerical solution of the magnetohydrodynamic dynamo. Physics of The Earth and Planetary Interiors 111 (1-2), 105–121.
URL http://dx.doi.org/10.1016/S0031-9201(98)00150-2

Sakuraba, A., Roberts, P. H., Oct. 2009. Generation of a strong magnetic field using uniform heat flux at the surface of the core. Nature Geoscience 2 (11), 802–805.
URL http://dx.doi.org/10.1038/ngeo643

Schaeffer, N., Jault, D., Cardin, P., Drouard, M., 2012. On the reflection of alfvén waves and its implication for earth's core modelling. Geophysical Journal International 191 (2), 508–516.
URL http://arxiv.org/abs/1112.3879

Suda, R., Takami, M., 2002. A fast spherical harmonics transform algorithm. Mathematics of Computation 71 (238), 703–715.
URL http://dx.doi.org/10.1090/S0025-5718-01-01386-2

Temme, N. M., Aug. 2011. Gauss quadrature. In: Digital Library of Mathematical Functions (DLMF). National Institute of Standards and Technology (NIST), Ch. 3.5(v).
URL http://dlmf.nist.gov/3.5.v

Tygert, M., Jan. 2008. Fast algorithms for spherical harmonic expansions, II. Journal of Computational Physics 227 (8), 4260–4279.
URL http://dx.doi.org/10.1016/j.jcp.2007.12.019

Wicht, J., Tilgner, A., May 2010. Theory and modeling of planetary dynamos. Space Science Reviews 152 (1), 501–542.
URL http://dx.doi.org/10.1007/s11214-010-9638-y

J. Fluid Mech. (2013), *vol.* 716, *pp.* 445–469.
doi:10.1017/jfm.2012.551

Modes and instabilities in magnetized spherical Couette flow

A. Figueroa‡, N. Schaeffer, H.-C. Nataf† and D. Schmitt

ISTerre, Université de Grenoble 1, CNRS, F-38041 Grenoble, France

(Received 8 May 2012; revised 10 September 2012; accepted 6 November 2012)

Several teams have reported peculiar frequency spectra for flows in a spherical shell. To address their origin, we perform numerical simulations of the spherical Couette flow in a dipolar magnetic field, in the configuration of the *DTS* experiment. The frequency spectra computed from time-series of the induced magnetic field display similar bumpy spectra, where each bump corresponds to a given azimuthal mode number m. The bumps appear at moderate Reynolds number ($\simeq$2600) if the time-series are long enough ($>$300 rotations of the inner sphere). We present a new method that permits retrieval of the dominant frequencies for individual mode numbers m, and extraction of the modal structure of the full nonlinear flow. The maps of the energy of the fluctuations and the spatio-temporal evolution of the velocity field suggest that fluctuations originate in the outer boundary layer. The threshold of instability is found at $Re_c = 1860$. The fluctuations result from two coupled instabilities: high-latitude Bödewadt-type boundary layer instability, and secondary non-axisymmetric instability of a centripetal jet forming at the equator of the outer sphere. We explore the variation of the magnetic and kinetic energies with the input parameters, and show that a modified Elsasser number controls their evolution. We can thus compare with experimental determinations of these energies and find a good agreement. Because of the dipolar nature of the imposed magnetic field, the energy of magnetic fluctuations is much larger near the inner sphere, but their origin lies in velocity fluctuations that are initiated in the outer boundary layer.

Key words: boundary layer stability, geodynamo, MHD turbulence

1. Introduction

It is now well established that the magnetic field of most planets and stars is generated by the dynamo mechanism (Larmor 1919; Elsasser 1946). Motions within an electrically conducting medium can amplify infinitesimally small magnetic field fluctuations up to a level where the Lorentz force that results is large enough to stop their amplification. This is possible for large enough values of the magnetic Reynolds number $Rm = UL/\eta$ (where U is a typical flow velocity, L a typical length, and η is the magnetic diffusivity of the medium).

† Email address for correspondence: Henri-Claude.Nataf@ujf-grenoble.fr

‡ Current address: Facultad de Ciencias, Universidad Autónoma del Estado de Morelos, 62209, Cuernavaca Morelos, México

Analytical (Busse 1975) and numerical (Glatzmaier & Roberts 1995) convective dynamo models, in which the flow is driven by the buoyancy force of thermal or compositional origin, have demonstrated the relevance of the dynamo mechanism for generating the Earth's magnetic field. Other forcings, due to precession, tides or impacts are also invoked to explain the fields of some other planets (Le Bars *et al.* 2011).

In 2000, two experiments demonstrated dynamo action in the lab (Gailitis *et al.* 2001; Stieglitz & Müller 2001). In both cases, the forcing was mechanical, with a dominant large-scale flow. Efforts to produce dynamo action with a highly turbulent flow are still underway (Frick *et al.* 2010; Kaplan *et al.* 2011; Lathrop & Forest 2011), while a rich variety of dynamo behaviours have been discovered in the von Kármán sodium (VKS) experiment (Berhanu *et al.* 2007; Monchaux *et al.* 2007) when ferromagnetic disks stir the fluid.

All these experiments use liquid sodium as a working fluid. The magnetic Prandtl number $Pm = \nu/\eta$ of liquid sodium is less than 10^{-5} (ν is the kinematic viscosity), so that experiments that achieve Rm of order 50 (as required for dynamo action) have kinetic Reynolds number $Re = UL/\nu$ in excess of 10^6. This contrasts with numerical simulations, which require lengthy computations with 1024^3 grid points to reach $Re = 10^4$. Since Reynolds numbers of flows in planetary cores and stars are much larger, we have to rely on theory to bridge the gap. Dynamo turbulence is a crucial issue because dissipation is very much dependent upon the scale and strength of turbulent fluctuations. The question of instabilities and turbulence is also central in the study of accretion disks (Balbus & Hawley 1991). Laboratory experiments can bring some constraints since they exhibit intermediate Reynolds numbers.

In that respect, the observation in several experiments of very peculiar frequency spectra, characterized by a succession of peaks or bumps, deserves some attention. Such bumpy spectra have been obtained in both spherical and cylindrical geometries, when rotation or/and magnetic fields are present, two ingredients that also play a major role in natural systems.

Kelley *et al.* (2007) were the first to observe a bumpy spectrum in a rotating spherical Couette experiment. A small axial magnetic field was applied and the induced field was used as a marker of the flow. The authors showed that the frequency and pattern of the modes correspond to a set of inertial modes. Inertial modes are the oscillatory linear response of a fluid to a time-dependent perturbation where the Coriolis force is the restoring force. Two hypotheses have been put forward to explain the excitation of inertial modes in these experiments: overcritical reflection off the inner Stewartson layer (Kelley *et al.* 2010), and turbulence from the tangent cylinder on the inner sphere (Matsui *et al.* 2011). Most recently, Rieutord *et al.* (2012) presented data recorded in the 3 m diameter spherical Couette experiment of Dan Lathrop's group at the University of Maryland, and proposed a new interpretation. They stress that there is a critical Rossby number below which modes of a given azimuthal mode number m are no longer excited, and show that this happens when the frequency of the mode is equal to the fluid velocity in the Stewartson layer above the equator of the spinning inner sphere. This interpretation in terms of a critical layer opens new perspectives that need to be investigated in more detail.

Bumpy frequency spectra were also reported by Schmitt *et al.* (2008) in the Derviche Tourner sodium (DTS) magnetized spherical Couette flow experiment (Cardin *et al.* 2002; Nataf *et al.* 2006, 2008; Brito *et al.* 2011). An example is shown in figure 1(*a*). Schmitt *et al.* (2008) could show, by correlating signals measured at several longitudes, that each bump is characterized by a given azimuthal

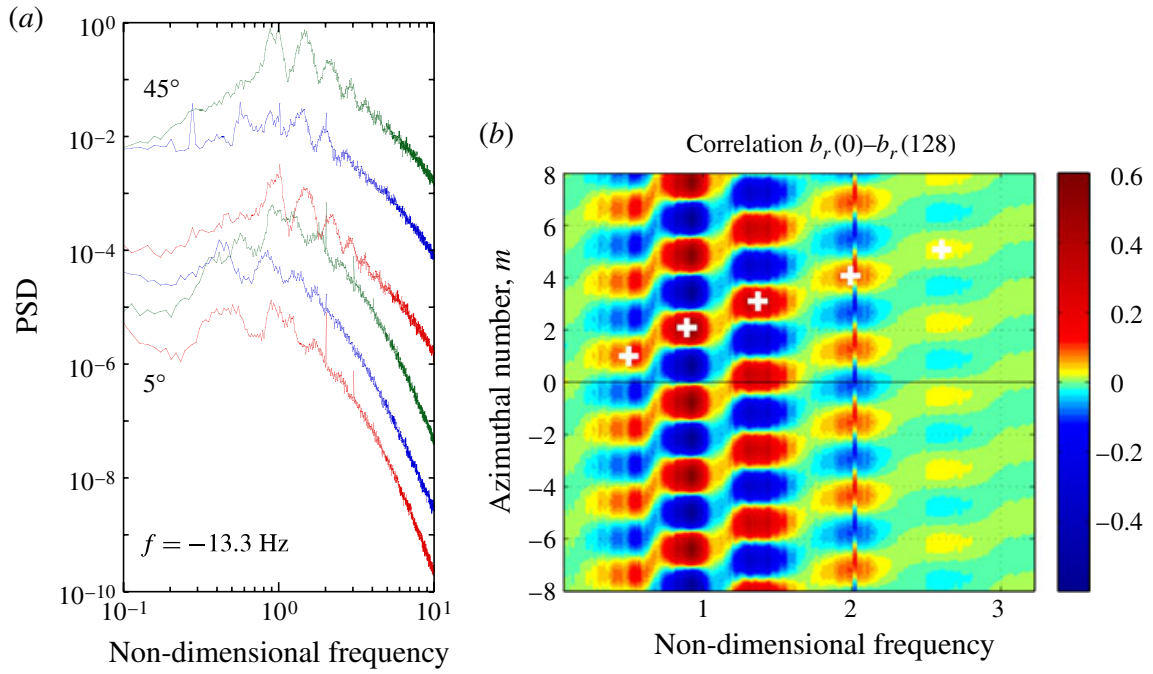

FIGURE 1. (Colour online) Spectral bumps in the *DTS* magnetized spherical Couette flow experiment. (*a*) Frequency spectra of the three components of the surface magnetic field (b_r, b_θ, b_φ in this order, bottom to top) measured at two different latitudes (5° and 45° as indicated). The time window used is 4000 turns. Frequencies (x-axis) are normalized by the rotation frequency of the inner sphere ($f = -13.3$ Hz). The spectral energy density (y-axis) is normalized as in § 4.1 to facilitate the comparison with the corresponding simulation results. The vertical scale applies to the lowest spectrum and successive spectra are shifted by one decade for clarity (two decades between different latitudes). Note the succession of bumps that dominate the spectra. (*b*) Covariance between two b_r time-series recorded at points 128° apart in longitude (same latitude $= -35°$), in a frequency–azimuthal mode number (m) plot. This plot shows that each spectral bump in (*a*) corresponds to a well-defined integer m, which increases with frequency (step-wise succession of positive covariance values starting at $m = 0$) (marked with a white '+') .

wavenumber m (figure 1*b*). Schmitt *et al.* (2013) further investigated the properties of the bumps and showed a good correspondence with linear magneto-inertial modes, in which both the Coriolis and the Lorentz forces play a leading role.

Finally, modes of azimuthal wavenumber $m = 1$ were observed in two magnetized Couette flow experiments aimed at detecting the magneto-rotational instability (MRI): in spherical geometry in Maryland (Sisan *et al.* 2004) and in cylindrical geometry in Princeton (Nornberg *et al.* 2010). Sisan *et al.* (2004) discovered magnetic modes that appeared only when the imposed magnetic field was strong enough and interpreted their observations as evidence for the MRI, even though the most unstable mode is expected to be axisymmetric ($m = 0$) in their geometry. Rotating spherical Couette flow in an axial magnetic field was studied numerically by Hollerbach (2009), who suggested that instabilities of the meridional circulation in the equatorial region could account for some of the modes observed by Sisan *et al.* (2004). Gissinger, Ji & Goodman (2011) further investigated this situation and showed that the instabilities that affect the Stewartson layer around the inner sphere, modified by the imposed magnetic field, have properties similar to the MRI. In contrast to the standard MRI, the instabilities found by Hollerbach (2009) and Gissinger *et al.* (2011) are inductionless.

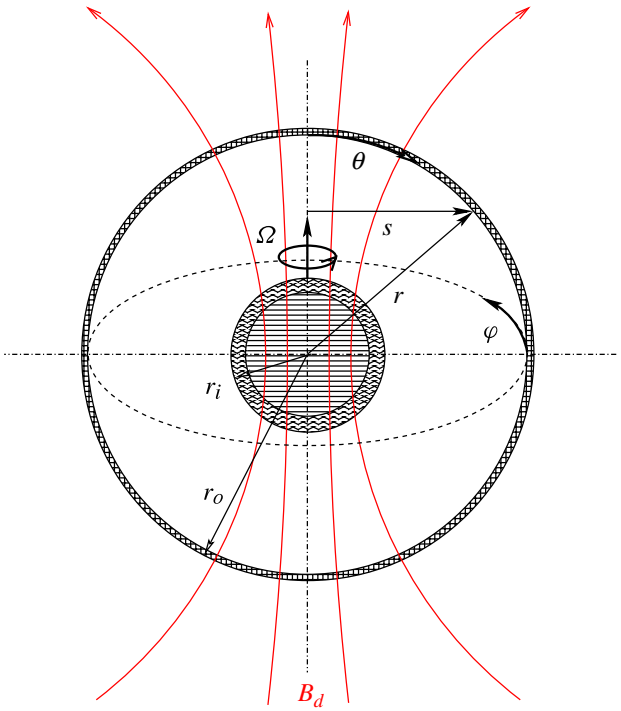

FIGURE 2. (Colour online) Sketch of the *DTS* experiment as modelled in this article. The inner sphere of radius r_i rotates around the vertical axis at angular velocity Ω. It consists of a copper shell enclosing a permanent magnet, which produces the imposed dipolar magnetic field $\boldsymbol{B}_d$. Liquid sodium of electric conductivity σ fills the gap between the inner sphere and the stainless steel outer shell of inner radius r_o. The spherical coordinate system we use is shown.

In the cylindrical Taylor–Couette geometry with a strong imposed axial field, Nornberg *et al.* (2010) observed $m = 1$ rotating modes. They claimed that these modes could be identified with the fast and slow magneto-Coriolis waves expected to develop when both the Coriolis and Lorentz forces have a comparable strength. Considering the fast magnetic diffusion in their experiment (Lundquist number of about 2), this interpretation was rather questionable, and indeed Roach *et al.* (2012) have recently reinterpreted these observations in terms of instabilities of an internal shear layer, in the spirit of the findings of Gissinger *et al.* (2011).

Clearly, magnetized Couette flows display a rich palette of modes and instabilities, and it is important to identify the proper mechanisms in order to extrapolate to natural systems. Hollerbach has investigated the instabilities of magnetized spherical Couette flow in a series of numerical simulations (Hollerbach & Skinner 2001; Hollerbach, Canet & Fournier 2007; Hollerbach 2009). However, bumpy spectra as observed by Schmitt *et al.* (2008) were never mentioned. In this article, we perform numerical simulations in the geometry of the *DTS* experiment, and focus on the origin of these bumpy spectra. The observations of Schmitt *et al.* (2008) are illustrated by figure 1, but the reader should refer to their article for a more detailed presentation. More specifically, we wish to answer the following major questions: How and where are the various modes excited? Are these spectra observed because of the large value of the Reynolds number?

We present the numerical model and the mean flow in § 2. We perform spectral analyses in § 3, and investigate fluctuations and instabilities in § 4. A discussion concludes the article.

2. Numerical model and mean flow

The *DTS* experiment that we wish to model is a spherical Couette flow experiment with an imposed dipolar magnetic field. Liquid sodium is used as the working fluid. It is contained between an inner sphere and a concentric outer shell, from radius $r = r_i$ to $r = r_o$ ($r_i = 74$ mm, $r_o = 210$ mm). The inner sphere consists of a 15 mm-thick copper shell, which encloses a permanent magnet that produces the imposed magnetic field, whose intensity reaches 175 mT at the equator of the inner sphere. The stainless steel outer shell is 5 mm thick. The inner sphere can rotate around the vertical axis (which is the axis of the dipole) at rotation rates $f = 2\pi\Omega$ up to 30 Hz. Although the outer shell can also rotate independently around the vertical axis in *DTS*, we only consider here the case when the outer sphere is at rest.

All these elements are taken into account in the numerical model, which is sketched in figure 2. In particular, we reproduce the ratio in electric conductivity of the three materials (copper, sodium, stainless steel). In the experiment, the inner sphere is held by 25 mm-diameter stainless steel shafts, which are not included in the numerical model.

2.1. *Equations*

We solve the Navier–Stokes and magnetic induction equations that govern the evolution of the velocity and magnetic fields of an incompressible fluid in a spherical shell:

$$\frac{\partial \boldsymbol{u}}{\partial t} + (\boldsymbol{u}\cdot\boldsymbol{\nabla})\boldsymbol{u} = -\frac{1}{\rho}\boldsymbol{\nabla} p + \nu\nabla^2\boldsymbol{u} + \frac{1}{\mu_0\rho}(\boldsymbol{\nabla}\times\boldsymbol{B})\times\boldsymbol{B}, \tag{2.1}$$

$$\frac{\partial \boldsymbol{B}}{\partial t} = \boldsymbol{\nabla}\times(\boldsymbol{u}\times\boldsymbol{B}) - \boldsymbol{\nabla}\times(\eta(r)\boldsymbol{\nabla}\times\boldsymbol{B}), \tag{2.2}$$

$$\boldsymbol{\nabla}\cdot\boldsymbol{u} = 0, \quad \boldsymbol{\nabla}\cdot\boldsymbol{B} = 0, \tag{2.3}$$

where $\boldsymbol{u}$ and p stand for the velocity and pressure fields respectively. Time is denoted by t, while ρ and ν are the density and kinematic viscosity of the fluid. The magnetic diffusivity $\eta(r)$ is given by $\eta(r) = (\mu_0\sigma(r))^{-1}$ where $\sigma(r)$ is the electric conductivity of the medium (fluid or solid shells) and μ_0 the magnetic permeability of vacuum. In the fluid, the conductivity $\sigma(r) = \sigma_{Na}$ is constant. The last term of (2.1) is the Lorentz force. $\boldsymbol{B}$ is the magnetic field. It contains the imposed dipolar magnetic field $\boldsymbol{B}_d$ given by:

$$\boldsymbol{B}_d = B_0\frac{r_o^3}{r^3}(2\cos\theta\boldsymbol{e}_r + \sin\theta\boldsymbol{e}_\theta), \tag{2.4}$$

where θ is the colatitude, $\boldsymbol{e}_r$ and $\boldsymbol{e}_\theta$ are the unitary vectors in the radial and orthoradial directions. B_0 is the intensity of the field at the equator on the outer surface of the fluid ($r = r_o$).

2.2. *Boundary conditions*

We use no-slip boundary conditions for the velocity field on the inner and outer surfaces:

$$\boldsymbol{u} = \Omega r\sin\theta\boldsymbol{e}_\varphi \quad \text{for } r \leqslant r_i, \quad \boldsymbol{u} = \boldsymbol{0} \quad \text{for } r \geqslant r_o. \tag{2.5}$$

We model the copper shell that holds the magnet in *DTS* as a conductive shell with electric conductivity $\sigma_{Cu} = 4.2\sigma_{Na}$. The outer stainless steel shell is modelled as a shell of conductivity $\sigma_{SS} = \sigma_{Na}/9$. These values reproduce the experimental

conductivity contrasts. The conductivity jumps are implemented by taking a continuous radial conductivity profile with sharp localized variations at both interfaces (grid point density increased by a factor 3–5). The internal magnet and the medium beyond the outer stainless steel shell are modelled as electric insulators. The magnetic field thus matches potential fields at the inner and outer surfaces.

2.3. *Numerical scheme*

Our three-dimensional spherical code (XSHELLS) uses second-order finite differences in radius and a pseudo-spectral spherical harmonic expansion, for which it relies on the very efficient spherical harmonic transform of the `SHTns` library (Schaeffer 2012). It performs the time stepping of the momentum equation in the fluid spherical shell, and the time stepping of the induction equation both in the conducting walls and in the fluid. It uses a semi-implicit Crank–Nicholson scheme for the diffusive terms, while the nonlinear terms are handled by an Adams–Bashforth scheme (second-order in time). The simulations that we present typically have 600 radial grid points (with a significant concentration near the interfaces) while the spherical harmonic expansion is carried up to degree 120 and order 40.

2.4. *Dimensionless parameters*

We define in table 1 the dimensionless numbers that govern the solutions in our problem. We pick the outer radius r_o as a length scale, and B_0, the intensity of the magnetic field at the equator of the outer surface, as a magnetic field scale. Note that, due to the dipolar nature of the imposed magnetic field, its intensity is 23 times larger at the equator of the inner sphere. The angular velocity of the inner sphere yields the inverse of the time scale. We choose $U = \Omega r_i$, the tangential velocity at the equator of the inner sphere, as typical velocity.

The solutions are governed by three independent dimensionless numbers but several combinations are possible and we try to pick the most relevant ones. The magnetic Prandtl number Pm compares the diffusion of momentum to that of the magnetic field. It is small in both the simulations and the experiment. The Reynolds number Re is of course essential, as it determines the level of fluctuations. It is not feasible to run numerical simulations with Reynolds numbers as large as in the *DTS* experiment.

However, one of the main findings of Brito *et al.* (2011) is that, because of the imposed dipolar magnetic field, the time-averaged flow is mainly governed by the balance between the Lorentz and the Coriolis forces, where the latter is due to the global rotation of the fluid, which is very efficiently entrained by the inner sphere, even when the outer sphere is at rest. That balance is measured by the Elsasser number Λ. Brito *et al.* (2011) showed that one can recover the proper balance at achievable values of Re by reducing the influence of the magnetic field, keeping the effective Elsasser number Λ as in the experiment.

Nevertheless, Cardin *et al.* (2002) introduced another number λ (named the Lehnert number by Jault (2008)), which provides a better measure of this balance for fast time-dependent phenomena. The Lehnert number λ compares the period of Alfvén waves to that of inertial waves. It is given by:

$$\lambda = \frac{B_0}{\Omega r_i \sqrt{\rho \mu_0}}. \tag{2.6}$$

In the Earth's core, this number is of order 10^{-4} and inertial waves dominate. They force the flow to be quasi-geostrophic on short time scales (Jault 2008). However,

Symbol	Expression	Simulations fixed Ha	Simulations fixed Re	*DTS* $f = [3–30]$ Hz	Earth's core
Pm	ν/η	$\mathbf{10}^{-3}$	10^{-3}	7×10^{-6}	10^{-6}
Re	$\Omega r_i r_o/\nu$	[**2611**–10 100]	2611	$[0.45–4.5] \times 10^{6}$	10^{9}
Λ	$\sigma B_0^2/\rho\Omega$	$[\mathbf{3.4}–0.9] \times 10^{-2}$	$[0.21–13.1] \times 10^{-2}$	$[3–0.3] \times 10^{-2}$	10
Ha	$r_o B_0/\sqrt{\rho\mu_0\nu\eta}$	**16**	[4–31]	200	10^{8}

TABLE 1. Typical values of the dimensionless numbers in the numerical simulations, in the *DTS* experiment (computed for $f = \Omega/2\pi = 3–30$ Hz) and in the Earth's core. The dimensionless numbers of our reference simulation are in bold.

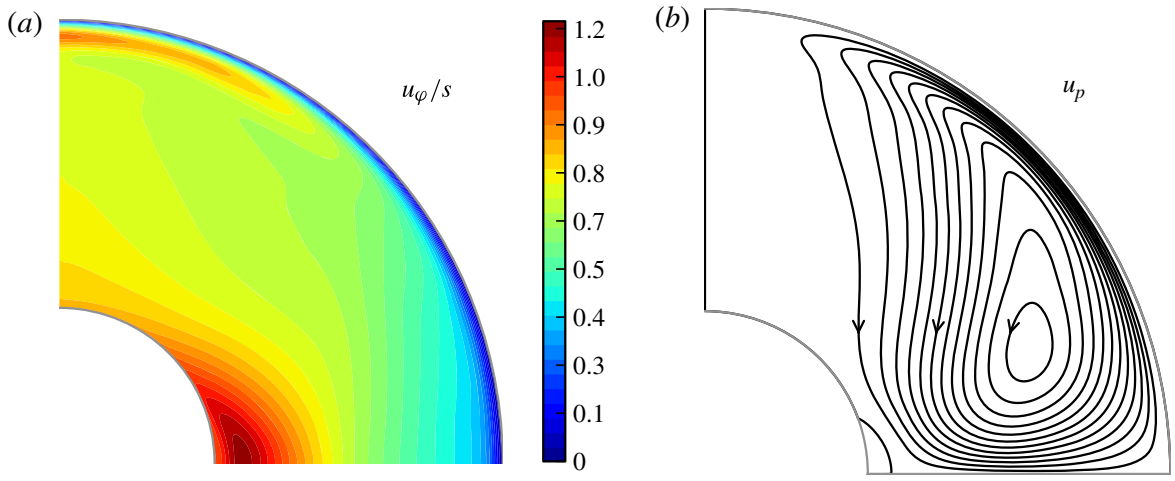

FIGURE 3. (Colour online) Time-averaged meridional slice of the velocity field. (*a*) Angular velocity isovalues. Note the zone of super-rotation near the inner sphere. (*b*) Meridional streamlines. The maximum meridional velocity is 0.4. $Pm = 10^{-3}$, $Re = 2611$, $\Lambda = 3.4 \times 10^{-2}$.

magnetic diffusion severely limits the propagation of Alfvén waves in the *DTS* experiment. This is measured by the Lundquist number, which is the ratio of the magnetic diffusion time to the typical transit time of an Alfvén wave across the sphere, here given by:

$$Lu = \frac{r_o B_0}{\eta \sqrt{\rho \mu_0}}, \tag{2.7}$$

which is taken as $Lu = 0.5$ in the numerical simulations, in agreement with the experimental value.

We therefore follow the same strategy as Brito *et al.* (2011), and try to keep the Elsasser number of the numerical simulations similar to its experimental value. Our reference case thus has: $Pm = 10^{-3}$, $Re = 2611$ and $\Lambda = 3.4 \times 10^{-2}$. The Hartmann number is $Ha = 16$, much smaller that its experimental counterpart ($Ha = 200$). It follows that $\lambda = 6.8 \times 10^{-2}$ and $Rm = RePm = 2.6$ for the reference case. Most results shown in this article relate to our reference case, but we also present some results computed for other Reynolds and Hartmann numbers, as indicated in table 1.

2.5. *Mean flow*

The time-averaged properties of the magnetized spherical Couette flow have been investigated in detail by Brito *et al.* (2011), and we simply recall here a few key observations. We plot in figure 3 the time-averaged velocity field in a meridional plane, for our reference simulation ($Pm = 10^{-3}$, $Re = 2611$ and $\Lambda = 3.4 \times 10^{-2}$). Two distinct regions show up in the map of mean angular velocity (figure 3*a*): an outer almost geostrophic region, where the angular velocity predominately varies with the cylindrical radius s; and an inner region that tends to obey Ferraro's law (Ferraro 1937) around the equator: namely, the angular velocity is nearly constant along field lines of the imposed dipolar magnetic field. Note the presence of a thin boundary layer at the outer surface. The poloidal streamlines (figure 3*b*) display a circulation from the equator towards the poles beneath the outer surface, where the polewards velocity reaches $0.4\Omega r_i$.

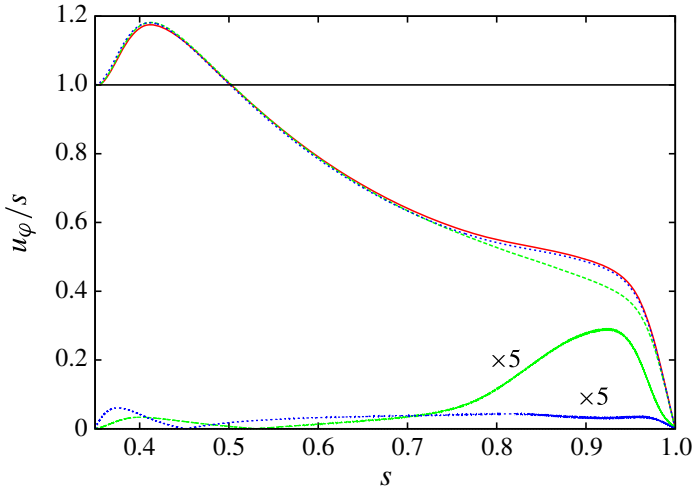

FIGURE 4. (Colour online) Radial profiles of time-averaged angular velocity in the equatorial plane for different simulations with the same parameters ($Pm = 10^{-3}$, $Re = 2611$ and $\Lambda = 3.4 \times 10^{-2}$). Dotted line: axisymmetric equatorially symmetric solution of Brito *et al.* (2011); solid line: axisymmetric solution computed with our XSHELLS code; dashed line: 3D solution from XSHELLS. The curves at the bottom give the unsigned difference between the three-dimensional solution and the axisymmetric one (upper), and between the two axisymmetric solutions (lower), scaled up by a factor 5.

To check our numerical set-up, we compare the time-averaged velocity field of our simulation with that obtained by Brito *et al.* (2011) using an independent axisymmetric equatorially symmetric code. The parameters and boundary conditions are identical, except that the magnetic boundary condition at $r = r_o$ is treated in the thin-shell approximation in Brito *et al.* (2011).

Figure 4 compares the radial profile of the angular velocity in the equatorial plane computed by Brito *et al.* (2011) to our axisymmetric solution, averaged over 50 rotation times, and to our three-dimensional spherical solution, averaged over 100 rotation times. The two axisymmetric solutions agree very well, while the three-dimensional solution exhibits a slightly lower angular velocity near the outer surface. Note that the angular velocity of the fluid reaches values as high as 20 % larger than that of the inner sphere. This phenomenon of *super-rotation* was first predicted by Dormy, Cardin & Jault (1998) in the same geometry (also see Starchenko 1997), but in their linear study, the zone of super-rotation was enclosed in the magnetic field line touching the equator of the outer sphere. There, the induced electric currents have to cross the magnetic field lines in order to loop back to the inner sphere. This produces a Lorentz force, which accelerates the fluid. Hollerbach *et al.* (2007) showed that nonlinear terms shift the zone of super-rotation from the outer sphere to close to the inner sphere, as observed here. The excess of 20 % is in good agreement with the super-rotation measured in the *DTS* experiment for $f = 3$ Hz ($Re = 4.5 \times 10^5$) (Brito *et al.* 2011).

3. Spectra and modes

3.1. *Frequency spectra*

In order to compare the numerical results to the experimental measurements of the fluctuations, we perform a simulation over a long time-window (600 rotation periods) and record the magnetic field induced at the surface at selected latitudes. We then

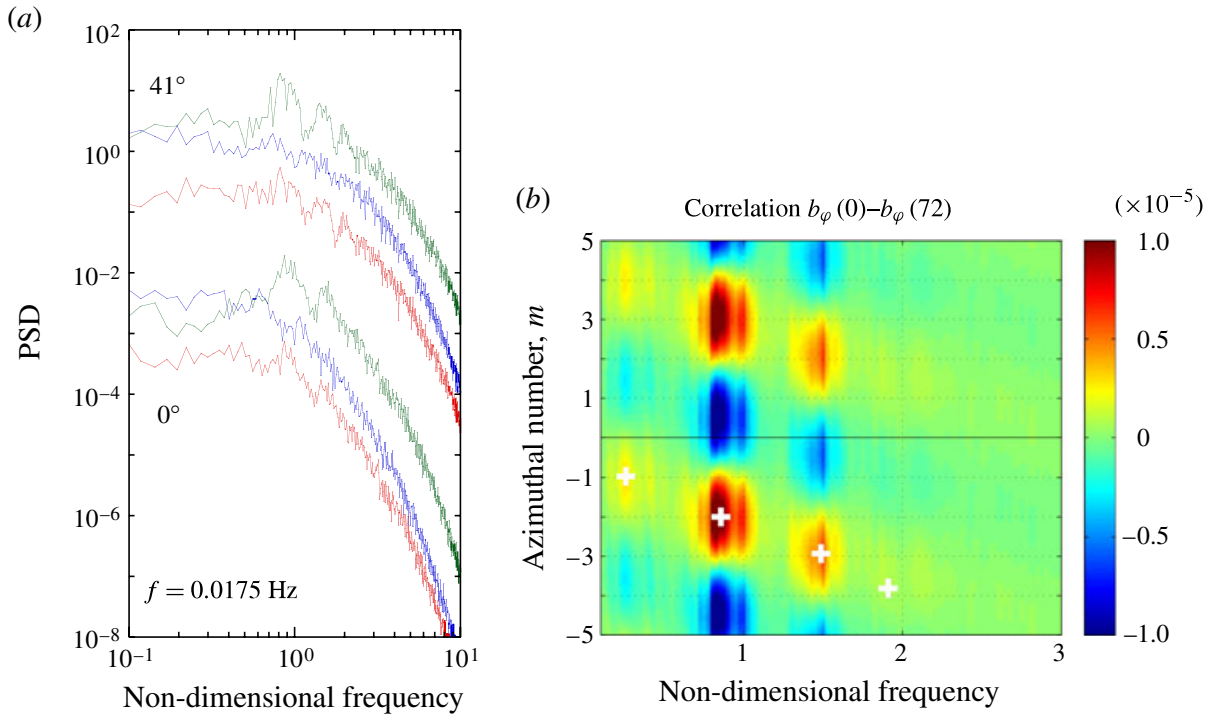

FIGURE 5. (Colour online) Spectral bumps in our reference numerical simulation ($Pm = 10^{-3}$, $Re = 2611$ and $\Lambda = 3.4 \times 10^{-2}$). (*a*) Frequency spectra of the three components of the magnetic field (b_r, b_θ, b_φ in this order, from bottom to top) recorded at two different latitudes (0 and 41° as indicated). Same non-dimensionalization and plotting conventions as in figure 1(*a*). The time window used lasts 540 turns. Note the spectral bumps and compare with figure 1(*a*). (*b*) m versus frequency plot for the same run, obtained from the covariance of two b_φ time-series recorded at points 72° apart in longitude (same latitude = 41°). The red positive patches (marked with a white '+') for negative m indicate that the successive spectral bumps have a well-defined mode number m, whose absolute value increases with frequency (compare with figure 1*b* where the relevant m are positive because the inner sphere spins in the negative direction).

compute the power spectra of these records as a function of frequency. Typical spectra are shown in figure 5(*a*). A sequence of bumps is clearly visible for both the radial and the azimuthal components of the magnetic field. The spectra do not display power-law behaviour.

We note that long time series (longer than 300 rotation periods) are needed for the spectral bumps to show up clearly. The bumps are not as pronounced as in figure 1(*a*), but we note that 4000 turns were used for those experimental spectra. It is also possible that the bumps are enhanced at higher Reynolds number.

3.2. *Azimuthal mode number*

Pursuing further the comparison with the experimental results, we examine whether the various spectral bumps correspond to specific azimuthal mode numbers. As in Schmitt *et al.* (2008), we correlate the signals computed at the same latitude (41°) but 72° apart in longitude. The signals are first narrow-band filtered, and we plot in figure 5(*b*) the amplitude of the covariance (colour scale) as a function of the peak frequency of the filter, for time-delays between the two, converted into azimuthal mode number m (y-axis). As in the experiments (see figure 1*b*), we find that each spectral bump corresponds to a single dominant (here negative by convention) azimuthal mode number m. The successive bumps have increasing azimuthal m (1, 2 and 3).

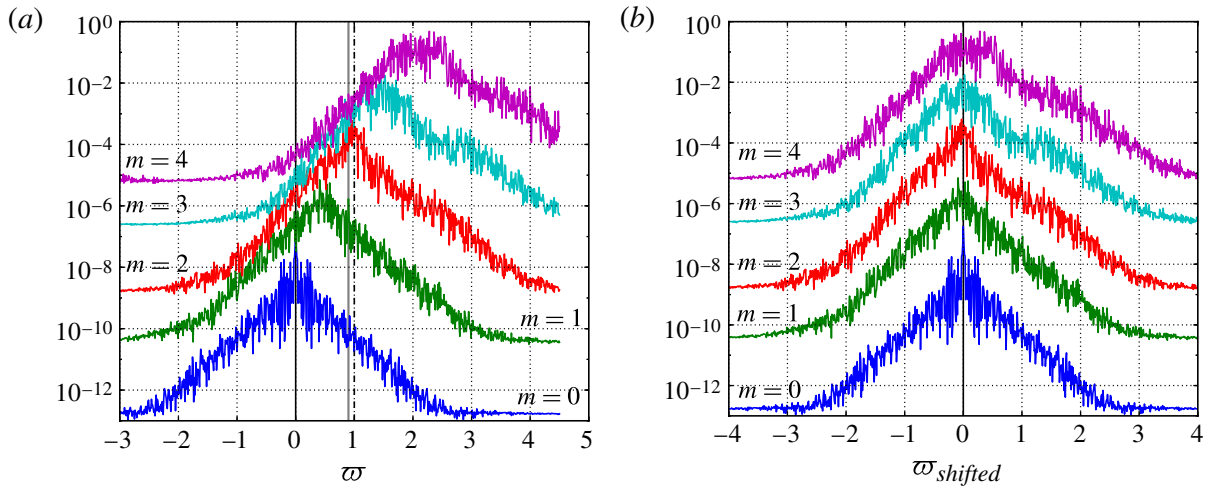

FIGURE 6. (Colour online) Partial energy frequency spectra $\mathscr{E}_m(\varpi)$ of the equatorially symmetric magnetic field at $r < 0.55$. Frequencies are normalized by f, the rotation frequency of the inner sphere. (*a*) Raw spectra for azimuthal mode numbers $m = 0$ to 4 (shifted vertically for clarity). The vertical grey solid line indicates the frequency ϖ^* at which we retrieve the $m = 2$ mode structure in figure 8. (*b*) Same as (*a*) except that frequencies are shifted according to: $\varpi_{shifted} = \varpi - mf_{fluid}$ (see text).

3.3. *Full Fourier transform*

In the numerical simulations, we can construct frequency spectra for each m. When the stationary regime is reached, we record 900 snapshots of the full fields, regularly spaced in time during 100 rotation periods: $\boldsymbol{F}(r, \theta, \varphi, t)$, where $\boldsymbol{F}$ can be either $\boldsymbol{u}$ or $\boldsymbol{B}$. A two-dimensional Fourier transform in the azimuthal and temporal directions φ and t gives us a collection of complex vectors $\boldsymbol{F}_m^{\varpi}$ representing the field for azimuthal number m and discrete frequency ϖ, such that

$$\boldsymbol{F}(r, \theta, \varphi, t) = \sum_m \sum_{\varpi} \boldsymbol{F}_m^{\varpi}(r, \theta) \mathrm{e}^{\mathrm{i}(m\varphi - \varpi t)}. \tag{3.1}$$

Note that the sign of the frequency has thus a precise meaning: positive (negative) frequencies correspond to prograde (retrograde) waves or modes.

This allows us to compute partial energy spectra

$$\mathscr{E}_m(\varpi) = \int_{r_1}^{r_2} \int_{\theta_1}^{\theta_2} \|\boldsymbol{F}_m^{\varpi}(r, \theta)\|^2 \, r \, \sin\theta \, \mathrm{d}\theta \, \mathrm{d}r. \tag{3.2}$$

Magnetic partial energy spectra $\mathscr{E}_m(\varpi)$ for the inner region ($0.35 < r < 0.55$, $0 < \theta < \pi$) are shown in figure 6(*a*) for $m = 0$–4. They are dominated by a single peak, which moves towards positive (prograde) frequencies as m increases. This can be interpreted as the advection of stationary or low-frequency structures by a prograde fluid velocity. We therefore shift the frequency of the spectra in figure 6(*b*), according to:

$$\varpi_{shifted} = \varpi - mf_{fluid} \tag{3.3}$$

where $f_{fluid} = 0.5$. We choose this value because it provides a good alignment of the spectral peaks and is compatible with the bulk fluid velocity in the outer region beneath the boundary layer (see figure 3*a*). This shift explains the linear evolution of the frequencies of the spectral bumps with m observed both in the *DTS* experiment

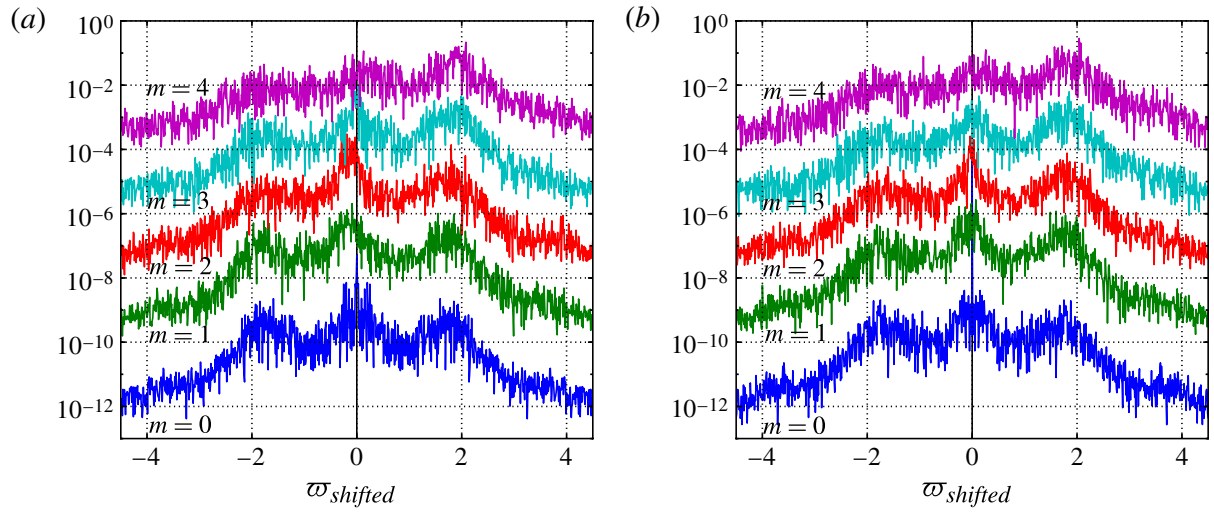

FIGURE 7. (Colour online) Partial energy frequency spectra $\mathscr{E}_m(\varpi)$ of the magnetic field at the outer surface ($1 < r < 1.024$, $0.35 < \sin\theta < 0.6$) for different m. (*a*) Equatorially symmetric part. (*b*) Equatorially antisymmetric part. Frequencies are normalized by f, the rotation frequency of the inner sphere, and are shifted according to (3.3). $Pm = 10^{-3}$, $Re = 2611$ and $\Lambda = 3.4 \times 10^{-2}$.

(figure 1*b*) and in the simulation (figure 5*b*). It means that the peaks are caused by the advection of periodic structures by the mean flow, or by a non-dispersive wave.

We now turn to the partial energy spectra of the magnetic field at high latitude ($0.35 < \sin\theta < 0.6$), at the surface of the sphere ($1 < r < 1.024$), displayed in figures 7(*a*) and 7(*b*) for the equatorially symmetric and antisymmetric parts, respectively. The frequencies are again shifted according to (3.3). This time, three peaks dominate the $m = 0$ spectra. The spectrum is symmetric with respect to $\varpi = 0$ since there cannot be prograde or retrograde propagation for $m = 0$: only latitudinal propagation or time-oscillations are permitted. The lateral peaks yield a frequency $\varpi^{\dagger} \simeq 1.8$. As m increases, the lateral peak becomes dominant in the prograde direction, while it vanishes in the retrograde direction. We note that the peaks are well aligned in these shifted representations, meaning that these secondary fluctuations are also advected at roughly the same angular velocity as the central peak. But both stationary and propagating waves are required to explain that this peak is not at zero frequency, and that it has both a prograde and a retrograde signature, and that the former dominates for $m \neq 0$.

Note that these secondary peaks do not show up in the regular frequency spectra or m-plots of point measurements (figure 5). This illustrates the interest and potential of the full Fourier transform method that we have developed.

3.4. *Mode structure*

Picking the frequency that yields the maximum spectral energy density for a given m, we derive the structure of the corresponding mode. One example for $m = 2$ is shown in figure 8, where we plot, for both u_r and B_r, the structure of the mode in a meridional plane and in map view at $r = 0.95$. We selected a mode for which B_r is symmetric with respect to the equator (and thus u_r is antisymmetric).

The meridional map for u_r reveals structures in the outer region, while B_r shows similar patterns that extend deeper down to the inner sphere. While the map view of u_r near the outer boundary displays short-wavelength structures, we find it remarkable

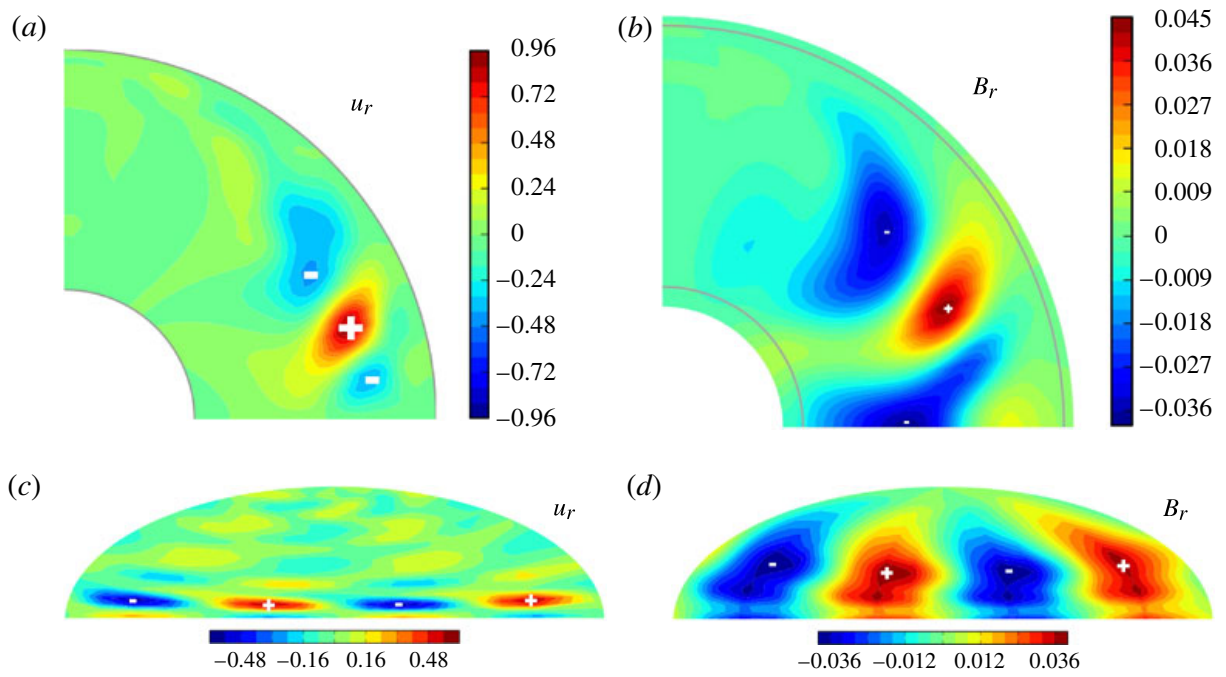

FIGURE 8. (Colour online) $m = 2$ mode structure given by the full Fourier transform method, for frequency $\varpi^* = 0.9$, which corresponds to the $m = 2$ peak in figure 6(*a*). $Pm = 10^{-3}$, $Re = 2611$ and $\Lambda = 3.4 \times 10^{-2}$. Energy densities are normalized by $E_K^0 = \rho\Omega^2 r_i^2/2$. (*a*), (*b*) Isovalues in the $\varphi = 0°$ meridional plane of the radial velocity and radial magnetic field, respectively. (*c*), (*d*) Map view of the isovalues at $r = 0.95$ of the radial velocity and radial magnetic field, respectively. Positive (negative) extrema are marked with a white '+' ('-') symbol, respectively.

that the structure of B_r is very smooth and very similar to those retrieved in the *DTS* experiment, and well-accounted for in the linear modal approach of Schmitt *et al.* (2013).

4. Fluctuations and instabilities

Having shown that our numerical simulations recover the essential features of the modes and spectra of the *DTS* experiment, even though their Reynolds number is much smaller, we now examine where and how the modes are excited. The first guide we use is the location of the largest fluctuations.

4.1. *Energy fluctuations*

We compute the kinetic energy density as $\delta E_K = \rho\langle(u - \langle u\rangle)^2\rangle/2$ and the magnetic energy density as $\delta E_M = \langle(b - \langle b\rangle)^2\rangle/2\mu_0$, where $\langle\rangle$ denotes time-averaging. We normalize both by a reference kinetic energy density $E_K^0 = \rho\Omega^2 r_i^2/2$, and we integrate over azimuth.

Figure 9 displays the resulting kinetic and magnetic energy densities of the fluctuations in a meridional plane for our reference simulation. We observe that the kinetic energy is maximum in the outer boundary layer, while the (much weaker) magnetic energy extends all the way to the inner sphere.

Figure 10 shows the radial profiles obtained after integration over the colatitude θ. It illustrates the effect of varying the Reynolds and the Hartmann numbers of the simulations. The fluctuations remain strongest in the outer boundary layer, but extend deeper inside the fluid with increasing Reynolds number. For the highest Reynolds

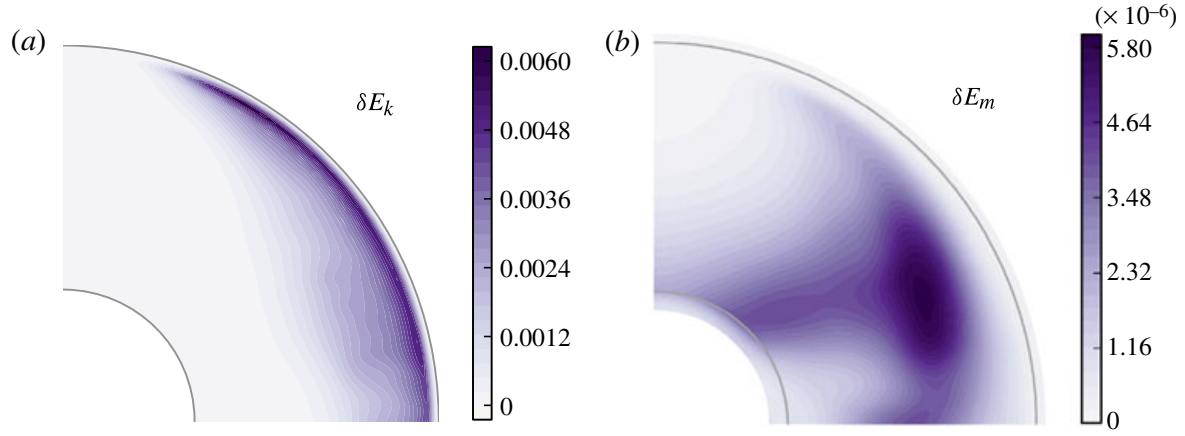

FIGURE 9. (Colour online) Time-and-azimuth-averaged meridional map of the energy density of the fluctuations. (*a*) Kinetic energy. (*b*) Magnetic energy. $Pm = 10^{-3}$, $Re = 2611$ and $\Lambda = 3.4 \times 10^{-2}$. The energy densities are normalized by E_K^0.

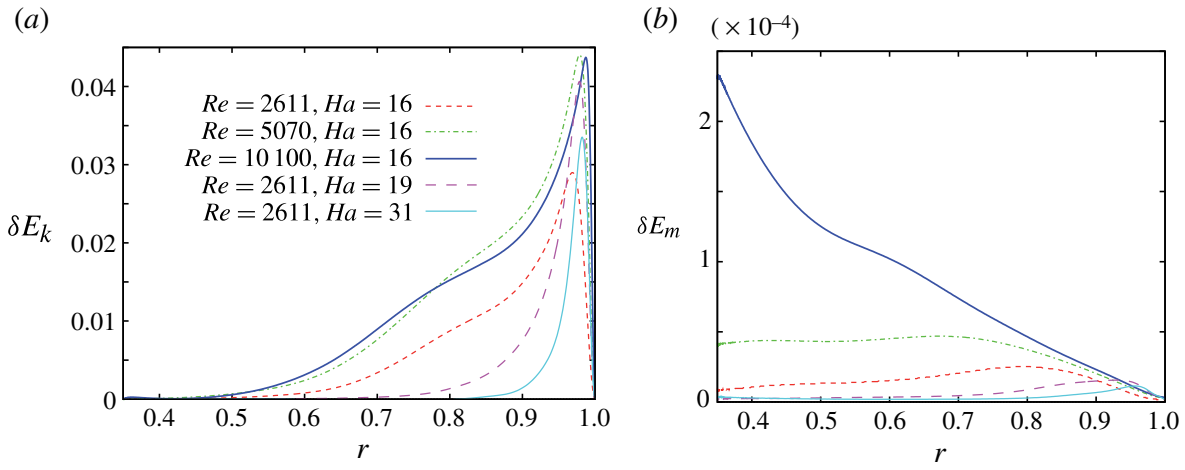

FIGURE 10. (Colour online) Time-and-colatitude-averaged energy density of the fluctuations as a function of radius r. (*a*) Kinetic energy. (*b*) Magnetic energy. The energy densities are normalized by E_K^0. The plots compare the fluctuations obtained for three simulations with the same Hartmann number ($Ha = 16$) and increasing Reynolds numbers ($Re = 2611$, 5070 and 10 100), and three simulations with the same Reynolds number ($Re = 2611$) and increasing Hartmann numbers ($Ha = 16$, 19 and 31). Other dimensionless numbers as in table 1. Note that the magnetic energy is smaller than the kinetic energy by three orders of magnitude, but increases strongly toward the inner sphere for the simulation with the highest Reynolds number.

number ($Re = 10\,100$), this causes the magnetic energy to strongly increase with depth, as the fluctuations interact with the larger imposed magnetic field near the inner sphere.

4.2. *Origin of the fluctuations*

It is beyond the scope of this paper to characterize the complete scenario by which instabilities develop in our geometry. However, we find it important to identify where the instabilities originate in order to understand the excitation of the modes we observe and extrapolate to other situations. The energy maps (figure 9) as well as movies of

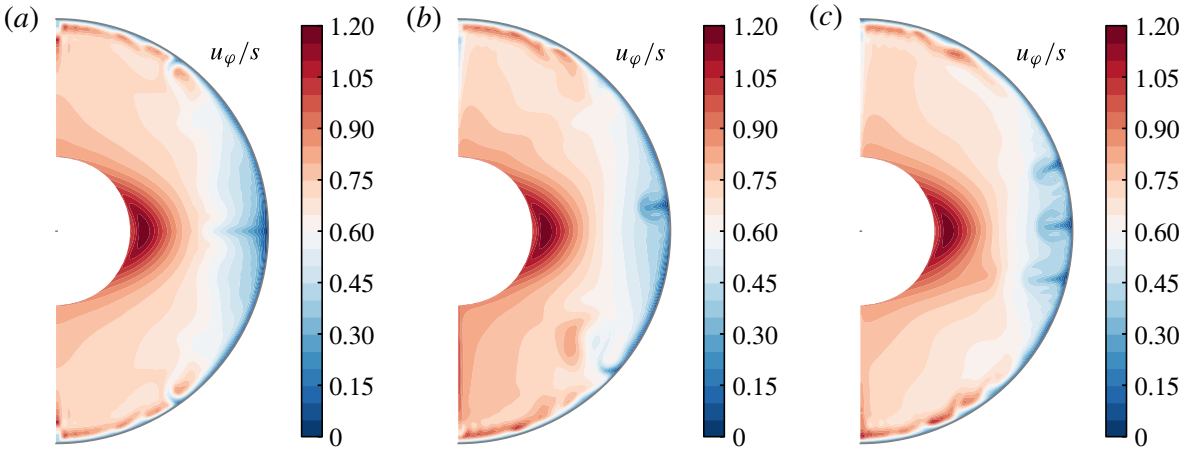

FIGURE 11. (Colour online) Meridional snap-shots of the angular velocity of the fluid at successive times t (given in number of turns of the inner sphere) in our reference simulation. $Pm = 10^{-3}$, $Re = 2611$ and $\Lambda = 3.4 \times 10^{-2}$. (*a*) $t = 17.5$; (*b*) $t = 93.8$; (*c*) $t = 675$.

the simulations (see online supplementary material available at journals.cambridge.org/flm) strongly suggest that fluctuations are initiated in the outer boundary layer. There is a large azimuthal velocity drop across the outer boundary layer, from the vigorously entrained fluid in the core flow to the outer container at rest.

A detailed inspection of the numerical simulations reveals two types of instabilities, which do not occur in the same region but appear to be coupled through the meridional circulation: (i) instability of a Bödewadt-type layer at high latitude; (ii) secondary instability of a centripetal jet at the equator. We use the meridional snap-shots of figure 11 to illustrate these two mechanisms.

4.2.1. *Bödewadt layer instability*

The flow that appears when a fluid rotates at constant angular velocity above a flat disk at rest has been studied by Bödewadt (1940) who has found the analytic expression of the boundary layer that develops at the surface of the disk. It is characterized by a large overshoot in the azimuthal velocity profile caused by the centripetal radial circulation. As shown by Lingwood (1997), this boundary layer is particularly unstable, and several teams have analysed the instabilities that take place (e.g. Savas 1987; Lingwood 1997; Gauthier, Gondret & Rabaud 1999; Schouveiler, Le Gal & Chauve 2001; Lopez *et al.* 2009). Two types of instability have been reported: axisymmetric rolls that propagate inwards (following the centripetal circulation of the boundary layer), and spiral rolls. A Bödewadt-type situation is encountered in our geometry at high latitude. Figure 3(*a*) shows a clear overshoot of the angular velocity at latitudes above $\sim 40°$, linked to a polewards meridional circulation. In this region, we observe polewards-propagating axisymmetric rolls in our simulations when the inner sphere is spun from rest. This is best seen in the movies provided as supplementary material online, but the signature of the rolls is clearly visible at high latitude in the three snap-shots of figure 11.

It also shows up in the spatio-temporal representations of the instabilities at $r = 0.95$, just beneath the outer boundary layer (figure 12). Figure 12(*a*) gives the axisymmetric part of u_θ as a function of time (x-axis) and latitude (y-axis) from $-\pi/2$ to $\pi/2$. The high-latitude rolls show up as successive inclined lines in this time–latitude plot.

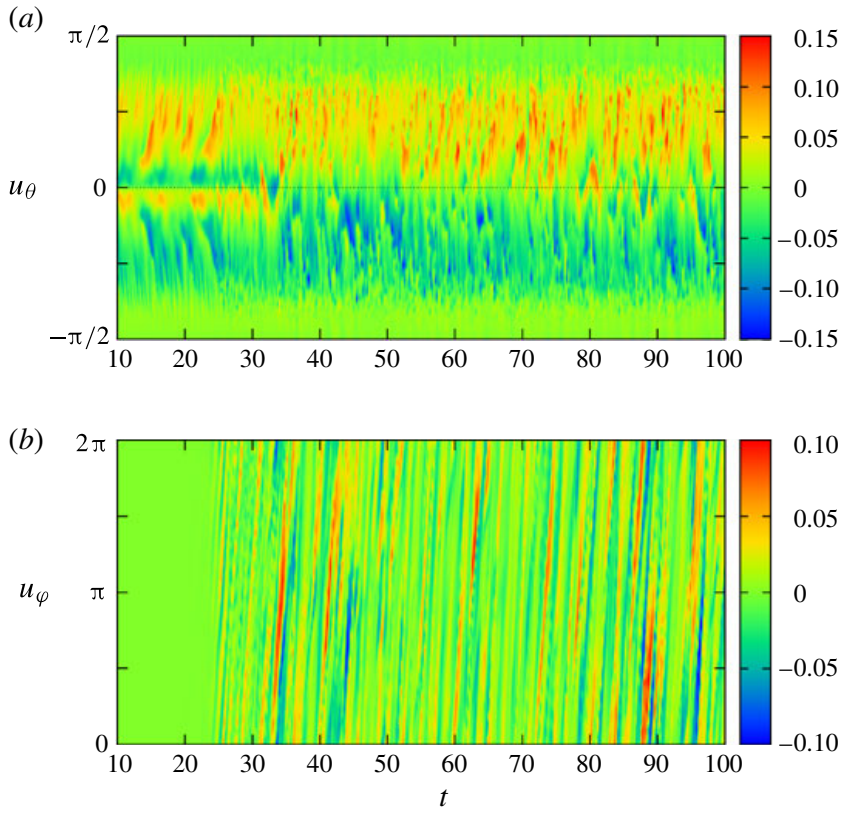

FIGURE 12. (Colour online) Spatio-temporal representation of the velocity fluctuations in the simulation at radius $r = 0.95$. $Pm = 10^{-3}$, $Re = 2611$ and $\Lambda = 3.4 \times 10^{-2}$. (*a*) u_θ isovalues of the axisymmetric flow ($m = 0$) in a latitude–time plot. (*b*) u_φ isovalues at 10° latitude in a longitude–time plot ($m = 0$ term removed). Velocities are normalized by the reference velocity Ωr_i. Time is given in rotation periods.

Note that similar high-latitude rolls have been reported in axisymmetric simulations of magnetized spherical Couette flow (Hollerbach *et al.* 2007; Brito *et al.* 2011).

4.2.2. *Equatorial centripetal jet instability*

A different kind of instability takes place at the equator. In figure 12(*a*), polewards-migrating rings yield a butterfly pattern, which also reveals that the equatorial downwelling instability creates a meridional circulation of opposite sign around the equator for $t < 30$ turns. Brito *et al.* (2011) report this equatorial counter-rotating cell for some parameters in their axisymmetric equatorially symmetric simulations. As shown in figure 11(*a*), it is associated with a sheet that draws fluid – and reduced angular momentum – from the outer boundary inside the sphere, in the equatorial plane. It can probably be described as a centrifugal Taylor–Görtler instability (Saric 1994), similar to those observed by Noir *et al.* (2009) in libration-induced flows in a sphere. As usually happens for these vortices, the nonlinear evolution of the instability leads to mushroom-type downwellings (figure 11*b,c* and online movies (supplementary material)).

At time $t \simeq 24$ turns, both the equatorial symmetry and the axisymmetry are broken by an $m = 3$ undulation, which rapidly disrupts the pattern of the fluctuations. Note however that axisymmetric bursts persist throughout, with amplitudes comparable to the initial ones. They propagate mostly polewards, but some occasionally cross the equator.

The $m = 3$ undulation is best observed in the spatio-temporal plot of figure 12(*b*), which displays the non-axisymmetric fluctuations of the azimuthal velocity at a latitude of 10°, as a function of time and longitude (y-axis) from 0 to 2π. Until $t \simeq 24$ turns, there is no non-axisymmetric fluctuation, but at $t \simeq 24$ turns an $m = 3$ mode appears (there are three maxima on a vertical line for a given t). After a few turns, this initial $m = 3$ undulation is replaced by chaotic fluctuations with dominant $m = 1$ and $m = 2$ contributions, which travel in the prograde direction with approximately the same velocity (given by the slope of the colour streaks in this figure).

The $m = 3$ secondary instability is similar to those observed in non-magnetic spherical Couette flow (Dumas 1991; Guervilly & Cardin 2010) or with an axial magnetic field (Hollerbach 2009). In these cases, it takes place on the centrifugal equatorial jet, which is a primary feature of these flows.

In our case note that, while the equatorial counter-rotating cell is essential for the centripetal jet to form, the time-averaged meridional circulation (shown in figure 3*b*) does not show this feature, as if the interplay of the developed instabilities had erased it.

4.2.3. *Threshold of instability*

Although we do not intend to decipher the complete scenario of instability, we have determined the threshold of instability, which is found at $Re_c = 1860$, with a critical azimuthal mode number of 2. Interestingly, it seems that the two (coupled) instabilities described above are present from this threshold. We can relate this threshold to the critical Reynolds number of the boundary layer. Following Lingwood (1997), we define the local Reynolds number $re = \omega^\star s^\star l/\nu$, where l is the thickness of the laminar boundary layer: $l = \sqrt{\nu/\omega^\star}$, with $\omega^\star$ the dimensional angular velocity of the fluid with respect to the wall at a position specified by its dimensional cylindrical radius $s^\star$. We can relate it to our global Reynolds number Re by:

$$re = \omega s \sqrt{\frac{r_o}{r_i}} \sqrt{Re}, \tag{4.1}$$

where the angular velocity ω just outside the boundary layer is non-dimensionalized by $2\pi f$ and the cylindrical radius s by r_o, as before. Picking $\omega \simeq 0.7$ at a latitude of 45° ($s \simeq 0.7$) from figure 4, we get $re_c \simeq 36$. This is somewhat larger than the critical value of 21.6 found by Lingwood (1997) for the absolute instability of a pure Bödewadt layer, for which she predicts a critical mode number $m_c = \beta_c re_c = -0.1174 \times 21.6 \simeq -2.5$, which is not incompatible with our observation of an initial $m = 2$ or $m = 3$ pattern. It is difficult to assess whether the higher threshold we get is due to a stabilizing effect of the magnetic field as in Moresco & Alboussière (2004), or to the spherical geometry.

In any case, all the experiments analysed by Schmitt *et al.* (2008, 2013) are far above this threshold. Our main conclusion at this stage is that the fluctuations we observe are initiated in the outer boundary layer, where the influence of the magnetic field is probably negligible. Because the fluid is in rapid rotation beneath the outer sphere at rest, the outer boundary is very unstable, and subject to non-geostrophic instabilities. We therefore expect a radically different behaviour when the outer sphere spins and the boundary layer is of Ekman type.

4.3. *Comparison with experimental results*

We cannot measure the total kinetic and magnetic energies of the fluctuations in the *DTS* experiment. However, we can make a quantitative assessment of the energy of the fluctuations as a function of radius, at given latitudes. The kinetic energy is

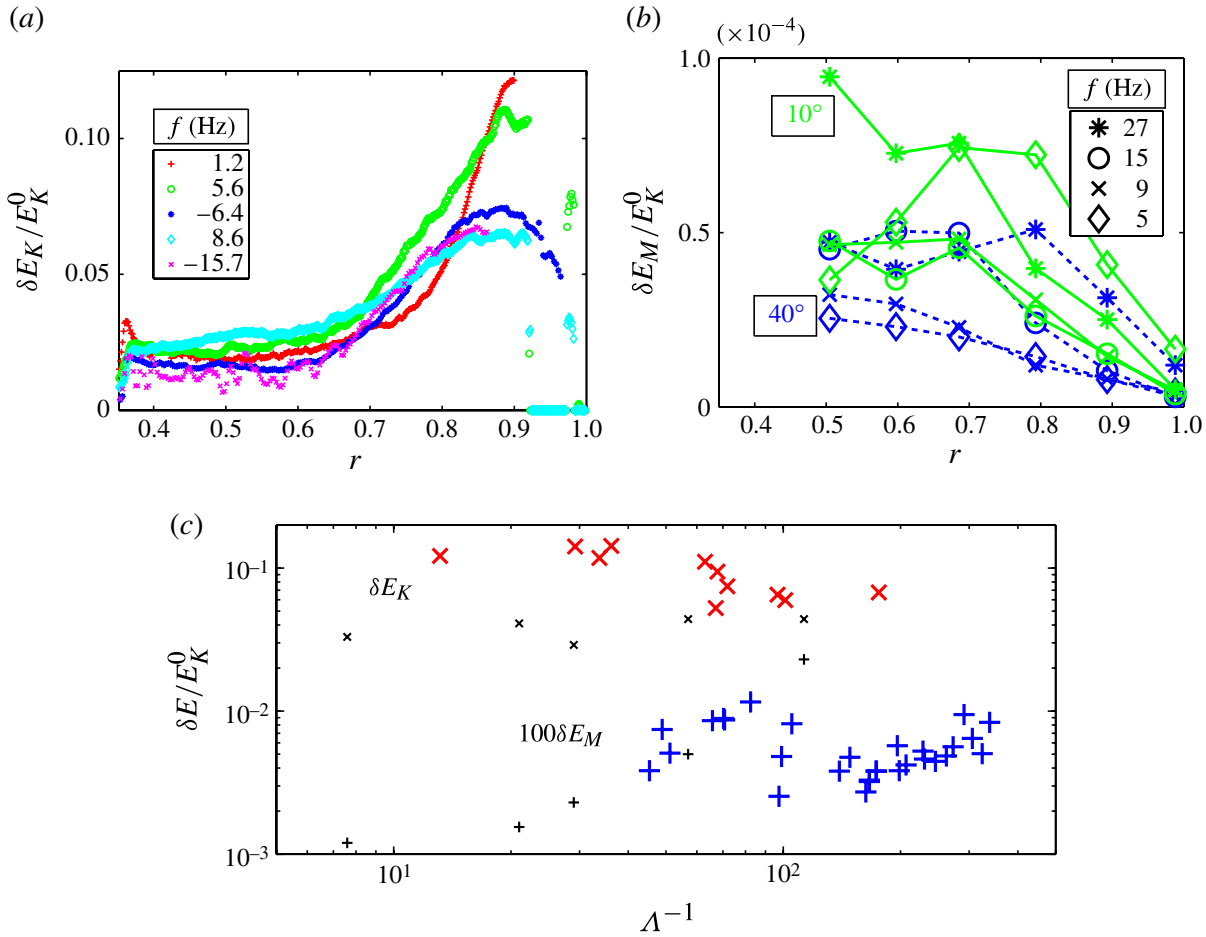

FIGURE 13. (Colour online) Energy of the fluctuations in the *DTS* experiment (all energy densities are normalized by $E_K^0 = \rho\Omega^2 r_i^2/2$). (*a*) Selected radial profiles of the kinetic energy of the fluctuations δE_K deduced from ultrasonic Doppler radial velocity measurements at latitude $-20°$. (*b*) Selected radial profiles of the magnetic energy of the fluctuations δE_M deduced from b_φ measurements in a sleeve at two different latitudes (10° – solid green – and 40° – dashed blue). The symbols correspond to different rotation rates f of the inner sphere, given in Hz in the legends. (*c*) Evolution of the kinetic ('×') and magnetic ('+') energies as a function of the inverse of the Elsasser number. The small black symbols are from the numerical simulations. The large coloured symbols are deduced from the maximum value of the experimental radial profiles of δE_K and δE_M at various latitudes and forcings f, using the same markers. Note that magnetic energies are multiplied by 100.

obtained from the fluctuations of the radial velocity measured by ultrasound Doppler velocimetry along a radial shot at a latitude of $-20°$. The magnetic energy is derived from the fluctuations of the azimuthal component of the magnetic field measured at three latitudes, 10°, 20° and 40°, and at six different radii, using Hall probes inserted in a sleeve, after removing a contribution at the rotation frequency f and harmonics, which is due to small heterogeneities of the imposed magnetic field. All energy densities are scaled with $E_K^0 = \rho\Omega^2 r_i^2/2$. As for the simulations, we integrate over azimuth by multiplying the measured r.m.s. by $2\pi r \sin\theta$ and convert to energy. In order to relate to the numerical results, we assume that fluctuations are isotropic. Additional measurements of the magnetic energy from radial and orthoradial probes partly support this hypothesis. Nevertheless, the comparison remains approximative.

The kinetic energy profiles (figure 13*a*) confirm that fluctuations are strongest near the outer surface. The maximum is deeper than in the numerical simulations (compare

with figure 10*a*), a consequence of the much higher Reynolds number. Note however that the thin viscous boundary layer cannot be resolved from the Doppler velocity profiles.

The magnetic energy profiles (figure 13*b*) clearly show that fluctuations are strongest near the inner sphere. Figure 10(*b*) shows that only the simulation with the highest Reynolds number displays this behaviour.

Figure 13(*c*) compares the kinetic and magnetic energies of the fluctuations obtained from both the simulations (small black crosses) and the experiments (large coloured crosses). Since we do not have the full latitudinal dependence in the experiments, we simply take the maximum of each profile as an estimate of the overall energy. The horizontal axis is Λ^{-1}, the inverse of the Elsasser number. It measures the ratio of the inertial force to the Lorentz force. The magnetic energy remains much smaller than the kinetic energy. It clearly increases with Λ^{-1} in the simulations: velocity fluctuations penetrate deeper into the fluid and induce larger magnetic fluctuations because the imposed magnetic field is stronger there. The experimental data follow the same trend for small forcing f, but there seems to be a strong drop near $\Lambda^{-1} = 100$, before it increases again. We have no explanation for this behaviour.

4.4. *The role of the Lorentz force*

Although magnetic energies are much smaller than kinetic energies, the Lorentz force plays a major role. The strong imposed dipolar magnetic field governs the dynamics of the mean flow in the *DTS* experiment. In particular, the very efficient entrainment of the fluid by the conductive inner sphere, and the zone of super-rotation next to it, are entirely due to the presence of the magnetic field.

In order to see the effect of the Lorentz force on the fluctuations, we have run a simulation in which the Lorentz force is nulled out except for $m = 0$. We find that the radial profile of angular velocity at the equator remains essentially the same, illustrating that nonlinear interactions of fluctuations with $m \neq 0$ barely contribute to the mean flow. Frequency spectra of the surface magnetic field (figure 14*a*) still display spectral bumps, but they are narrower and much more intense. Furthermore, the azimuthal mode number analysis (figure 14*b*) reveals that modes of a given m show up at several distinct frequencies.

The damping effect of the Lorentz force is best illustrated by plots of the radial profile of the energy of the fluctuations. Figure 15 displays the resulting radial profiles of the kinetic and magnetic energies, integrated over time and colatitude. While the kinetic energy of the fluctuations is negligible for $r < 0.6$ when the Lorentz force is present, fluctuations invade the complete fluid shell when it is suppressed. Fluctuations are largest beneath the outer shell where the magnetic field is weakest, but even there fluctuations are much weaker when the Lorentz force is active.

The magnetic energy of the fluctuations reaches only a thousandth of the kinetic energy in the *DTS* configuration. Not surprisingly, when the Lorentz force is suppressed, it jumps by a factor of 100 near the inner sphere, where the imposed magnetic field is strongest. This demonstrates how dangerous it can be to infer magnetic energy and dissipation from flow solutions computed without the feedback of the Lorentz force (see discussion between Glatzmaier 2008 and Liu, Goldreich & Stevenson 2008).

5. Discussion

We have obtained bumpy frequency spectra in numerical simulations of the magnetized spherical Couette flow (figure 5*a*). They compare very well with spectra

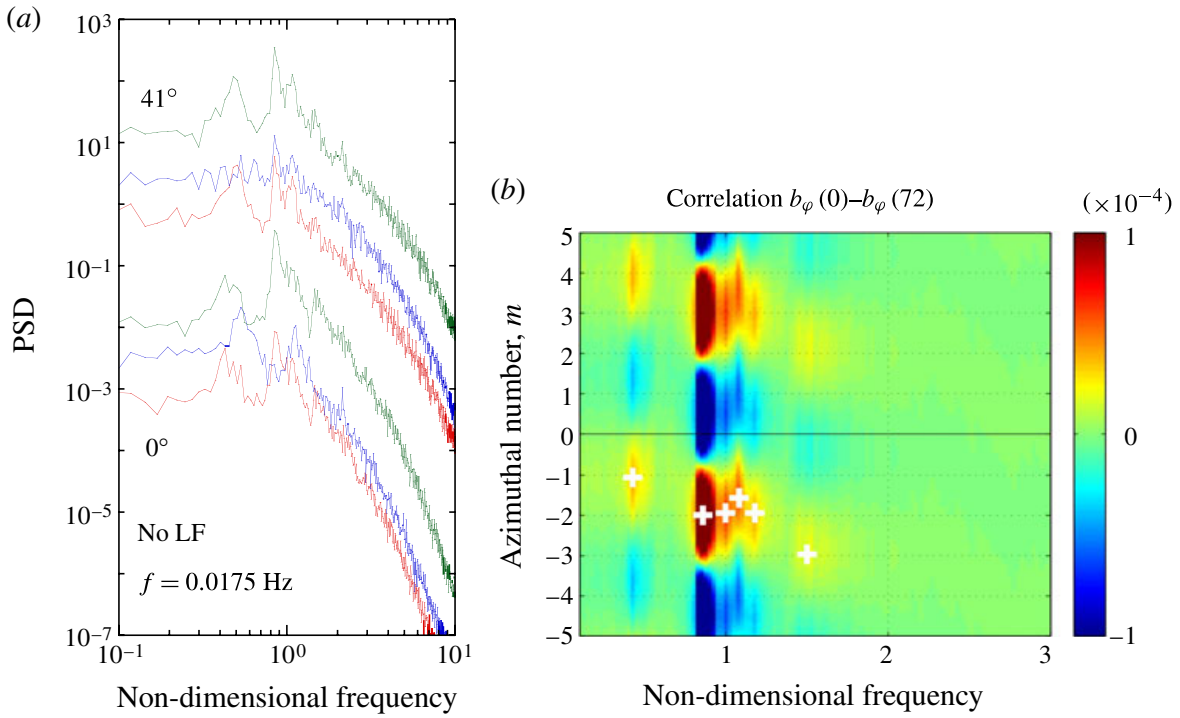

FIGURE 14. (Colour online) Same as figure 5 but for a simulation where the Lorentz force is nulled out for $m \neq 0$. Sharp spectral peaks are observed on all three components of the magnetic field. Neighbouring frequencies can have different azimuthal modenumber m.

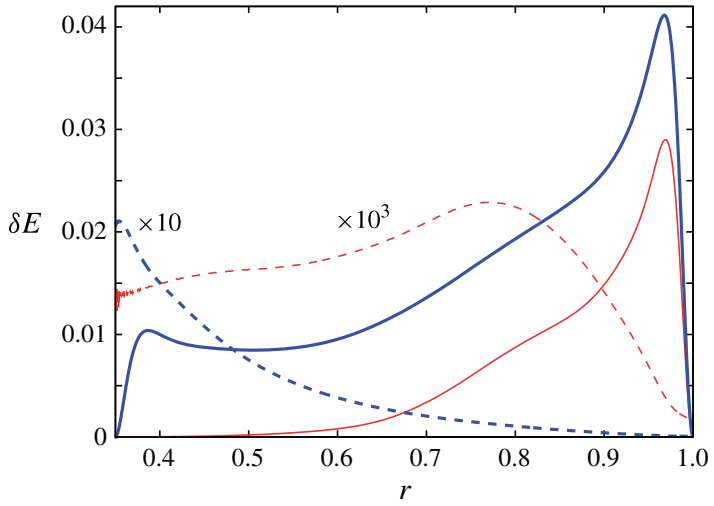

FIGURE 15. (Colour online) Time-and-colatitude-averaged energy density of the fluctuations as a function of radius r. This plot compares the kinetic (solid lines) and magnetic (dashed lines) energies of the reference simulation (thin red) with a simulation (thick blue) with the same parameters ($Pm = 10^{-3}$, $Re = 2611$ and $\Lambda = 3.4 \times 10^{-2}$), but in which the Lorentz force has been nulled out for $m \neq 0$. Note that the magnetic energy is two orders of magnitude larger in the latter case.

obtained in the *DTS* experiment from magnetic and electric time-records (Schmitt *et al.* 2008). As in the experiment, the dominant azimuthal mode number increases by 1 from one frequency bump to the next (figure 5*b*). Very large Reynolds numbers are not required for getting this behaviour, but one needs to accumulate long time-series (typically 300 turns of the inner sphere) for the peaks to show up clearly in the spectra. However, we note that bumps in the numerical spectra are not as pronounced as in the experiments.

We have developed a new method, which bridges the gap between the linear modal approach (Rieutord & Valdettaro 1997; Kelley *et al.* 2007; Schmitt *et al.* 2008) and full nonlinear simulations and experiments. By performing a time-domain Fourier transform of the full fields for each azimuthal number m, we recover the dominant frequencies (figures 6 and 7) and obtain the structure of the modes (figure 8), which can then be compared to linear solutions and to experimental observations. We think that this approach will help in identifying the mode selection mechanism in other experiments (Kelley *et al.* 2010).

Snap-shots (figure 11) and spatio-temporal plots (figure 12) reveal a rather different story, in which chaotic instabilities are swept by the flow. We could show that these two views are dual: since the instabilities circle around the sphere, the parts that are in phase between two successive passages are statistically enhanced. Since the spectral bumps are more pronounced in the experiments, this effect appears to be more efficient at large Reynolds number.

The maps of the kinetic energy of the fluctuations (figures 9*a*, 10*a* and 13*a*) indicate that they are initiated in the outer boundary layer, with only minor influence of the magnetic field. Instabilities appear above a critical Reynolds number $Re_c = 1860$. We identify two types of instability: (i) axisymmetric polewards-migrating rolls at high latitude; (ii) non-axisymmetric ($m = 2$ at the threshold) secondary instabilities of an equatorial centripetal jet. The first type is similar to the instabilities of a Bödewadt layer. The second type resembles the jet instability of the centrifugal equatorial sheet in non-magnetized spherical Couette flow. The two instabilities are coupled by the meridional circulation (they trigger one another), and the system quickly evolves towards a chaotic state in which outer boundary layer instabilities are swept around by the azimuthal and meridional large-scale flows.

Schmitt *et al.* (2008) observe that fluctuations in the DTS experiment are delayed and reduced when the outer sphere is spinning. We think that this is because the boundary layer is then closer to an Ekman-type, which is much more stable (Lingwood 1997), and that non-geostrophic instabilities are hampered.

The fluctuations of kinetic energy are much larger than those of magnetic energy (figure 13*c*), which are mostly slaves of the former. If we assume that the magnetic fluctuations scale as $b \simeq aRmB$, we obtain that the ratio of the magnetic to kinetic energy behaves as $\delta E_M/\delta E_K \simeq a^2 Lu^2$, where Lu is the Lundquist number defined in § 2.4. Since the Lundquist number is of order one in both the experiments and the simulations the a pre-factor must be rather small to explain the observed energy contrast. In fact, direct measurements of the mean induced azimuthal magnetic field yield $a \simeq 0.1$. Both the *DTS* measurements (figure 13*b*) and our largest Reynolds number numerical simulation (figure 10*b*) display a strong increase of the magnetic energy fluctuations when getting closer to the inner sphere. This appears to be essentially the consequence of the strong increase of the imposed dipolar field there. Indeed, the local Lundquist number increases from $Lu = 0.5$ at the equator of the outer sphere to $Lu = 12$ at the equator of the inner sphere.

At first order, we expect both energies to be proportional to the square of the imposed inner sphere velocity. However, we note that when scaled accordingly, the kinetic energy tends to decrease when the forcing is increased, while the scaled magnetic energy increases (figure 13*c*). Brito *et al.* (2011) showed that the energy of the mean flow behaves similarly, and proposed that this is a consequence of the increasing turbulent friction at the outer surface: as the friction increases, the core flow is slowed down, while the shear between the spinning inner sphere and the fluid increases, inducing a stronger magnetic field. We think that another effect explains

the trend observed for the energy fluctuations: as the forcing increases, the damping effect of the magnetic field decreases. Instabilities penetrate deeper into the fluid and produce larger magnetic fluctuations, even though their scaled kinetic energy is reduced because of the decreased velocity drop across the outer boundary layer. We note that for large forcing f the magnetic energy is smaller in the experiments than in the simulations, suggesting again the role of the strong turbulence.

Although the magnetic energy is very small, the Lorentz force plays a major role: it determines the very efficient entrainment of the fluid by the spinning inner sphere, but it also heavily damps the fluctuations in most of the fluid. When we remove the Lorentz force for $m \neq 0$, fluctuations invade the fluid (figure 15), and sharper and more numerous frequency peaks are observed in the spectra (figure 14). This gets closer to the observations of Kelley *et al.* (2007), where the imposed magnetic field was weak and only served as a marker of the flow.

Even though bumpy frequency spectra are observed in both situations (weak or strong magnetic field), they differ in several important aspects. In the *DTS* experiment, we observe broad peaks corresponding to azimuthal mode numbers up to $m = 10$ for all rotation rates f of the inner sphere, when the outer sphere is at rest. Both equatorially symmetric and antisymmetric modes are present (Schmitt *et al.* 2013). The fluid is efficiently entrained by the magnetic coupling with the spinning inner sphere, and the largest velocity gradients are located near the outer boundary. Modes and fluctuations are strongly damped by the imposed magnetic field.

In contrast, when the magnetic field is weak and the outer sphere is also spinning, as in Kelley *et al.* (2007) and Rieutord *et al.* (2012), the spectra are dominated by sharp peaks corresponding to inertial modes with selected azimuthal numbers m. Only equatorially antisymmetric modes appear to be excited (Rieutord *et al.* 2012). Most of the fluid rotates rigidly with the outer sphere, and velocity gradients are strong only in the Stewartson layer tangent to the inner sphere. Rieutord *et al.* (2012) show that this layer can behave as a critical layer, thereby exciting modes with a dominant azimuthal mode number $m = -4\hat{\omega}/Ro$, where $\hat{\omega}$ is the frequency of the mode. The Rossby number is defined as $Ro = f_i/f_o - 1$, where f_i and f_o are the rotation frequencies of the inner and outer spheres, respectively.

Because of these differences, we do not expect the mechanism proposed by Rieutord *et al.* (2012) to apply to the situation discussed in this article. However, it would be interesting to investigate whether the idea of critical layers can help in understanding the sort of statistical resonance we invoke to explain our observations.

Note that in our geometry, one could have expected instabilities to develop in the inner region near the equator, where the flow obeys Ferraro's law, and where a small velocity perturbation produces a large Lorentz force. This does not appear to be the case. In the present study, we have kept the Lundquist number small, as in the *DTS* experiment. Alfvén waves are therefore damped out rapidly. They might still contribute to shaping the modes near the inner sphere. It would be interesting to investigate the turbulent regime in the *DTS* geometry at larger Lundquist number.

Acknowledgements

We thank D. Jault for stimulating discussions. R. Hollerbach and three referees helped us improve our manuscript. We gratefully acknowledge the support of CNRS and Université de Grenoble through the collaborative program 'Turbulence, Magnetohydrodynamics and Dynamo'. Part of the numerical simulations were run at the Service Commun de Calcul Intensif de l'Observatoire de Grenoble (SCCI).

Supplementary movies

Supplementary movies are available at journals.cambridge.org/flm.

REFERENCES

BALBUS, S. A. & HAWLEY, J. F. 1991 A powerful local shear instability in weakly magnetized disks. 1. Linear analysis. *Astrophys. J.* **376** (1, Part 1), 214–222.

BERHANU, M., MONCHAUX, R., FAUVE, S., MORDANT, N., PÉTRÉLIS, F., CHIFFAUDEL, A., DAVIAUD, F., DUBRULLE, B., MARIÉ, L., RAVELET, F., BOURGOIN, M., ODIER, P., PINTON, J.-F. & VOLK, R. 2007 Magnetic field reversals in an experimental turbulent dynamo. *Europhys. Lett.* **77**, 59001.

BÖDEWADT, U. T. 1940 Die Drehstromung über festem Grund. *Z. Angew. Math. Mech.* **20**, 241–253.

BRITO, D., ALBOUSSIÈRE, T., CARDIN, P., GAGNIÈRE, N., JAULT, D., LA RIZZA, P., MASSON, J. P., NATAF, H. C. & SCHMITT, D. 2011 Zonal shear and super-rotation in a magnetized spherical Couette-flow experiment. *Phys. Rev.* E **83** (6, Part 2), 066310.

BUSSE, F. H. 1975 Model of geodynamo. *Geophys. J. R. Astron. Soc.* **42** (2), 437–459.

CARDIN, P., BRITO, D., JAULT, D., NATAF, H.-C. & MASSON, J.-P. 2002 Towards a rapidly rotating liquid sodium dynamo experiment. *Magnetohydrodynamics* **38**, 177–189.

DORMY, E., CARDIN, P. & JAULT, D. 1998 MHD flow in a slightly differentially rotating spherical shell, with conducting inner core, in a dipolar magnetic field. *Earth Planet. Sci. Lett.* **160**, 15–30.

DUMAS, G. 1991 Study of spherical Couette flow via 3-D spectral simulations: large and narrow-gap flows and their transitions. PhD thesis, California Institute of Technology, Pasadena, California (USA), 231pp.

ELSASSER, W. M. 1946 Induction effects in terrestrial magnetism part I. Theory. *Phys. Rev.* **69** (3–4), 106–116.

FERRARO, V. C. A. 1937 The non-uniform rotation of the sun and its magnetic field. *Mon. Not. R. Astron. Soc.* **97**, 458–472.

FRICK, P., NOSKOV, V., DENISOV, S. & STEPANOV, R. 2010 Direct measurement of effective magnetic diffusivity in turbulent flow of liquid sodium. *Phys. Rev. Lett.* **105** (18), 184502.

GAILITIS, A., LIELAUSIS, O., PLATACIS, E., DEMENT'EV, S., CIFERSONS, A., GERBETH, G., GUNDRUM, T., STEFANI, F., CHRISTEN, M. & WILL, G. 2001 Magnetic field saturation in the Riga dynamo experiment. *Phys. Rev. Lett.* **86**, 3024–3027.

GAUTHIER, G., GONDRET, P. & RABAUD, M. 1999 Axisymmetric propagating vortices in the flow between a stationary and a rotating disk enclosed by a cylinder. *J. Fluid Mech.* **386**, 105–126.

GISSINGER, C., JI, H. & GOODMAN, J. 2011 Instabilities in magnetized spherical Couette flow. *Phys. Rev.* E **84** (2, Part 2), 026308.

GLATZMAIER, G. A. 2008 A note on 'Constraints on deep-seated zonal winds inside Jupiter and Saturn'. *Icarus* **196**, 665–666.

GLATZMAIER, G. A. & ROBERTS, P. H 1995 A three-dimensional convective dynamo solution with rotating and finitely conducting inner-core and mantle. *Phys. Earth Planet. Inter.* **91** (1–3), 63–75.

GUERVILLY, C. & CARDIN, P. 2010 Numerical simulations of dynamos generated in spherical Couette flows. *Geophys. Astrophys. Fluid Dyn.* **104** (2), 221–248.

HOLLERBACH, R. 2009 Non-axisymmetric instabilities in magnetic spherical Couette flow. *Proc. R. Soc. Lond.* A **465** (2107), 2003–2013.

HOLLERBACH, R., CANET, E. & FOURNIER, A. 2007 Spherical Couette flow in a dipolar magnetic field. *Eur. J. Mech.* B **26**, 729–737.

HOLLERBACH, R & SKINNER, S 2001 Instabilities of magnetically induced shear layers and jets. *Proc. R. Soc. Lond.* A **457** (2008), 785–802.

JAULT, D. 2008 Axial invariance of rapidly varying diffusionless motions in the Earth's core interior. *Phys. Earth Planet. Inter.* **166**, 67–76.

KAPLAN, E. J., CLARK, M. M., NORNBERG, M. D., RAHBARNIA, K., RASMUS, A. M., TAYLOR, N. Z., FOREST, C. B. & SPENCE, E. J. 2011 Reducing global turbulent resistivity by eliminating large eddies in a spherical liquid-sodium experiment. *Phys. Rev. Lett.* **106** (25), 254502.

KELLEY, D. H., TRIANA, S. A., ZIMMERMAN, D. S. & LATHROP, D. P. 2010 Selection of inertial modes in spherical Couette flow. *Phys. Rev.* E **81** (2, Part 2), 026311.

KELLEY, D. H., TRIANA, S. A., ZIMMERMAN, D. S., TILGNER, A. & LATHROP, D. P. 2007 Inertial waves driven by differential rotation in a planetary geometry. *Geophys. Astrophys. Fluid Dyn.* **101** (5–6), 469–487.

LARMOR, J. 1919 How could a rotating body such as the Sun become a magnet? *Report of the British Association for the Advancement of Science 87th meeting*, pp. 159–160.

LATHROP, D. P. & FOREST, C. B. 2011 Magnetic dynamos in the lab. *Phys. Today* **64** (7), 40–45.

LE BARS, M., WIECZOREK, M. A., KARATEKIN, O., CEBRON, D. & LANEUVILLE, M. 2011 An impact-driven dynamo for the early Moon. *Nature* **479**, 215–218.

LINGWOOD, R. J. 1997 Absolute instability of the Ekman layer and related rotating flows. *J. Fluid Mech.* **331**, 405–428.

LIU, J., GOLDREICH, P. M. & STEVENSON, D. J. 2008 Constraints on deep-seated zonal winds inside Jupiter and Saturn. *Icarus* **196**, 653–664.

LOPEZ, J. M., MARQUES, F., RUBIO, A. M. & AVILA, M. 2009 Crossflow instability of finite Bödewadt flows: transients and spiral waves. *Phys. Fluids* **21** (11), 114107.

MATSUI, H., ADAMS, M., KELLEY, D., TRIANA, S. A., ZIMMERMAN, D., BUFFETT, B. A. & LATHROP, D. P. 2011 Numerical and experimental investigation of shear-driven inertial oscillations in an Earth-like geometry. *Phys. Earth Planet. Inter.* **188**, 194–202.

MONCHAUX, R., BERHANU, M., BOURGOIN, M., MOULIN, M., ODIER, P., PINTON, J.-F., VOLK, R., FAUVE, S., MORDANT, N., PÉTRÉLIS, F., CHIFFAUDEL, A., DAVIAUD, F., DUBRULLE, B., GASQUET, C., MARIÉ, L. & RAVELET, F. 2007 Generation of a magnetic field by dynamo action in a turbulent flow of liquid sodium. *Phys. Rev. Lett.* **98** (4), 044502.

MORESCO, P. & ALBOUSSIÈRE, T. 2004 Stability of Bödewadt–Hartmann layers. *Eur. J. Mech.* B/*Fluids* **23** (6), 851–859.

NATAF, H.-C., ALBOUSSIÈRE, T., BRITO, D., CARDIN, P., GAGNIÈRE, N., JAULT, D., MASSON, J.-P. & SCHMITT, D. 2006 Experimental study of super-rotation in a magnetostrophic spherical Couette flow. *Geophys. Astrophys. Fluid Dyn.* **100**, 281–298.

NATAF, H.-C., ALBOUSSIÈRE, T., BRITO, D., CARDIN, P., GAGNIÈRE, N., JAULT, D. & SCHMITT, D. 2008 Rapidly rotating spherical Couette flow in adipolar magnetic field: an experimental study of the mean axisymmetric flow. *Phys. Earth Planet. Inter.* **170**, 60–72.

NOIR, J., HEMMERLIN, F., WICHT, J., BACA, S. M. & AURNOU, J. M. 2009 An experimental and numerical study of librationally driven flow in planetary cores and subsurface oceans. *Phys. Earth Planet. Inter.* **173** (1–2), 141–152.

NORNBERG, M. D., JI, H., SCHARTMAN, E., ROACH, A. & GOODMAN, J. 2010 Observation of magnetocoriolis waves in a liquid metal Taylor–Couette experiment. *Phys. Rev. Lett.* **104** (7), 074501.

RIEUTORD, M., TRIANA, S. A., ZIMMERMAN, D. S. & LATHROP, D. P. 2012 Excitation of inertial modes in an experimental spherical Couette flow. *Phys. Rev.* E **86** (2, Part 2), 026304.

RIEUTORD, M. & VALDETTARO, L. 1997 Inertial waves in a rotating spherical shell. *J. Fluid Mech.* **341**, 77–99.

ROACH, A. H., SPENCE, E. J., GISSINGER, C., EDLUND, E. M., SLOBODA, P., GOODMAN, J. & JI, H. 2012 Observation of a free-Shercliff-layer instability in cylindrical geometry. *Phys. Rev. Lett.* **108** (15), 154502.

SARIC, W. S. 1994 Görtler vortices. *Annu. Rev. Fluid Mech.* **26**, 379–409.

SAVAS, Ö. M. 1987 Stability of Bödewadt flow. *J. Fluid Mech.* **183**, 77–94.

SCHAEFFER, N. 2012 Efficient spherical harmonic transforms aimed at pseudo-spectral numerical simulations. ArXiv e-prints 1202.6522.

SCHMITT, D., ALBOUSSIÈRE, T., BRITO, D., CARDIN, P., GAGNIÈRE, N., JAULT, D. & NATAF, H.-C. 2008 Rotating spherical Couette flow in a dipolar magnetic field: experimental study of magneto-inertial waves. *J. Fluid Mech.* **604**, 175–197.

SCHMITT, D., CARDIN, P., LA RIZZA, P. & NATAF, H.-C. 2013 Magneto-Coriolis waves in a spherical Couette flow experiment. *Eur. J. Mech.* B/*Fluids* **37**, 10–22.

SCHOUVEILER, L., LE GAL, P. & CHAUVE, MP 2001 Instabilities of the flow between a rotating and a stationary disk. *J. Fluid Mech.* **443**, 329–350.

SISAN, D. R., MUJICA, N., TILLOTSON, W. A., HUANG, Y.-M., DORLAND, W., HASSAM, A. B., ANTONSEN, T. M. & LATHROP, D. P. 2004 Experimental observation and characterization of the magnetorotational instability. *Phys. Rev. Lett.* **93** (11), 114502.

STARCHENKO, S. V. 1997 Magnetohydrodynamics of a viscous spherical shell in a strong potential field. *J. Expl Theor. Phys.* **85** (6), 1125–1137.

STIEGLITZ, R. & MÜLLER, U. 2001 Experimental demonstration of a homogeneous two-scale dynamo. *Phys. Fluids* **13**, 561–564.

Turbulence Reduces Magnetic Diffusivity in a Liquid Sodium Experiment

Simon Cabanes, Nathanaël Schaeffer, and Henri-Claude Nataf*
Univ. Grenoble Alpes, ISTerre, F-38000 Grenoble, France and
CNRS, ISTerre, F-38000 Grenoble, France
(Dated: October 5, 2015 – published in *Phys. Rev. Lett.* **113**, 184501 (2014))

The contribution of small scale turbulent fluctuations to the induction of mean magnetic field is investigated in our liquid sodium spherical Couette experiment with an imposed magnetic field. An inversion technique is applied to a large number of measurements at $Rm \approx 100$ to obtain radial profiles of the α and β effects and maps of the mean flow. It appears that the small scale turbulent fluctuations can be modeled as a strong contribution to the magnetic diffusivity that is negative in the interior region and positive close to the outer shell. Direct numerical simulations of our experiment support these results. The lowering of the effective magnetic diffusivity by small scale fluctuations implies that turbulence can actually help to achieve self-generation of large scale magnetic fields.

The Earth, the Sun and many other astrophysical bodies produce their own magnetic field by dynamo action, where the induction of a magnetic field by fluid motion overcomes the Joule dissipation. In all astrophysical bodies, the conducting fluid undergoes turbulent motions, which can also significantly affect the induction of a large-scale magnetic field by either enhancing it or weakening it. It is therefore of primary interest to quantify the role of these fluctuations in the dynamo problem.

The induction equation for the mean magnetic field $\langle \mathbf{B} \rangle$ reads:

$$\frac{\partial \langle \mathbf{B} \rangle}{\partial t} = \nabla \times (\langle \mathbf{U} \rangle \times \langle \mathbf{B} \rangle + \mathcal{E}) + \eta \Delta \langle \mathbf{B} \rangle \qquad (1)$$

where $\langle U \rangle$ is the mean velocity field, $\eta = (\mu_0 \sigma)^{-1}$ is the magnetic diffusivity (involving the magnetic permeability μ_0 and the conductivity of the fluid σ), and $\mathcal{E} = \langle \tilde{\mathbf{u}} \times \tilde{\mathbf{b}} \rangle$ is the mean electromotive force (emf) due to small scale fluctuating magnetic $\tilde{\mathbf{b}}$ and velocity $\tilde{\mathbf{u}}$ fields. The relative strength between the inductive and dissipative effects is given by the magnetic Reynolds number $Rm = UL/\eta$ (U and L are characteristic velocity and the characteristic length-scale). When there is a scale separation between the turbulent fluctuations and the mean flow, we can follow the mean-field theory and expand the emf in terms of mean magnetic quantities: $\mathcal{E} = \alpha \langle \mathbf{B} \rangle - \beta \nabla \times \langle \mathbf{B} \rangle$. For homogeneous isotropic turbulence, α and β are scalar quantities. α is related to the flow helicity and results in an electrical current aligned with the mean magnetic field, whereas β can be interpreted as a turbulent diffusivity effectively increasing ($\beta > 0$) or decreasing ($\beta < 0$) electrical currents. The effective magnetic diffusivity $\eta_{eff} = \eta + \beta$ can have tremendous effects on energy dissipation and on dynamo action by reducing or increasing the effective magnetic Reynolds number $Rm_{eff} = UL/\eta_{eff}$.

However, direct determination of these small-scale contributions remains a challenging issue for experimental studies and numerical simulations.

The first generation of dynamo experiments were designed to show that turbulent flows with strong geometrically-imposed helicity could self-generate their own magnetic fields. Since the success of Riga [1] and Karlsruhe [2] dynamos, several other liquid metal experiments have sought to overcome the effects of magnetohydrodynamic turbulence in less constrained, more geophysically relevant flow geometries. Unfortunately, dynamo action remains elusive, and the effective contribution of small-scale motions to large-scale magnetic fields remains poorly understood, though the small-scale motions seem to work against dynamo action [3, 4].

In the Perm torus-shaped liquid sodium experiment, the effective magnetic diffusivity was inferred from phase shift measurements of an alternating magnetic signal, indicating turbulent increases in magnetic diffusivity of up to $\approx 30\%$ [4]. The Madison experiment, a sphere containing two counter-rotating helical vortices, found that an externally applied magnetic field was weakened by about 20% at $Rm = 130$, which they interpreted as a negative global α-effect [3]. The installation of an equatorial baffle was found to reduce the amplitude of the largest-scale turbulent eddies and hence the α-effect [5]. In the same set-up, Rahbarnia *et al.* [6] measured the local emf directly, finding contributions from both α and β, but with a dominant β-effect. They reported an increase in magnetic diffusivity of about 30%. The Von Karman Sodium experiment, a cylinder containing another two-vortex liquid sodium flow, reported a magnetic diffusivity increase of about 100% [7].

We analyze data from the Derviche Tourneur Sodium experiment (DTS), a magnetized spherical Couette flow experiment sketched in Figure 1. Forty liters of liquid sodium are enclosed between an inner sphere (radius $r_i =$ 74mm) and a concentric outer stainless steel shell (inner radius $r_o = 210$mm). The inner sphere can rotate around the vertical axis at rates up to $f = 30$Hz, yielding a maximal value of 94 for the magnetic Reynolds number defined as $Rm = 2\pi f r_o^2/\eta$. The inner sphere consists of a copper shell containing a strong permanent magnet,

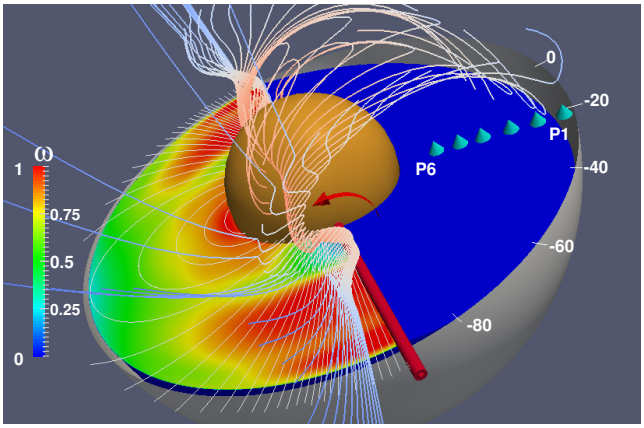

FIG. 1. Sketch of the DTS experiment with its liquid sodium contained between an outer stainless steel shell (grey, with latitude labels in degrees) and an inner copper sphere (orange), which spins as indicated by the red arrow around the vertical rotation axis (here tilted for clarity). *left half of the sphere*: the field lines of the dipolar magnetic field imposed by the central magnet are drawn on top of the contour map of the fluid angular velocity ω (normalized by that of the inner sphere) inverted from data measured for $Rm = 94$. *right half of the sphere*: field lines of the total reconstructed magnetic field. The field lines are strongly distorted by the flow (ω-effect). The blue cones mark the radial positions of the 6 magnetometers $P1$ ($r = radius/r_o = 0.99$) to $P6$ ($r = 0.50$), which measure the azimuthal magnetic field. They can be placed at 4 different latitudes (here $-20°$).

which produces a, mostly dipolar, magnetic field pointing upwards along the rotation axis. The intensity of the magnetic field decreases from $B_i \simeq 180$mT at the equator of the inner sphere to $B_o \simeq 7.1$mT at the equator of the outer shell. More details are given in [8].

In a recent study [9], we developed a new strategy to determine the mean velocity and induced magnetic fields. Following earlier works [8, 10], we collect ultrasound Doppler velocity profiles, electric potential measurements, global torque data, and measurements of the induced magnetic field inside the sodium layer, to reconstruct meridional maps of the mean flow and magnetic field at a given Rm, taking into account the link established by the induction equation. But we further constrain these fields by analyzing the response of the fluid shell to a time-periodic magnetic field, as in Frick *et al.* [4]. In our case, the time-periodic signal simply results from the rotation of our central magnet, whose small deviations from axisymmetry produce a field varying at the rotation frequency and its harmonics. We have expanded the complete magnetic potential of the magnet in spherical harmonics up to degree 11 and order 6, which we then use to compute the solution of the time-dependent induction equation. The predictions for a given mean velocity field are compared to actual magnetic measurements inside the sodium shell at 4 latitudes and at 6 radii, as depicted in Figure 1. We construct a non-linear inversion scheme of the induction equation to retrieve the mean axisymmetric (and equatorially-symmetric) toroidal and poloidal velocity fields that minimize the difference between the predictions and all measurements at a given rotation rate f of the inner sphere. Cabanes *et al.* [9] discuss in detail the solutions and fits for $Rm = 28$.

TABLE I. For each inner sphere rotation rate f, we list the corresponding Rm, the total number Np of free parameters we invert for, the total number Nd of data points including mean measurements and time-varying magnetic data, and the associated global normalized misfit χ (the error-weighted rms difference between observations and predictions). The number of data points is much smaller at high Rm as ultrasound Doppler velocimetry is not operational. Values in brackets are the numbers obtained when we do not invert for α and β.

f (Hz)	Rm	Np	Nd	χ
-9	28	108 (96)	1130	1.5 (1.8)
-15	47	108 (96)	440	2.5 (3.3)
-23	72	60 (48)	230	2.5 (4.9)
-30	94	60 (48)	230	2.9 (5.9)

In the present study, we extend the analysis to the largest available $Rm = 47$, 72 and 94 (see Table I for details). Figure 1 displays a meridional map of the angular velocity inverted for $Rm = 94$, and the field lines of the predicted magnetic field. They confirm that, near the equator of the inner sphere where the magnetic field is strong, the angular velocity stays nearly constant along magnetic field lines (Ferraro law [11]). That region displays super-rotation, while the flow becomes more geostrophic further away from the inner sphere.

However, the mean velocity field alone does not fully account for the measured mean magnetic field. Figueroa *et al.* [12] point out that velocity fluctuations invade the interior of the shell in DTS as the rotation rate f increases, and that magnetic fluctuations always get larger towards the inner sphere because of the strong imposed magnetic field there. We therefore extend our previous approach [9] to take into account the contribution of turbulent fluctuations to the mean magnetic field. Following earlier attempts [3, 4, 6], we choose to invert for α and β, but since we expect that fluctuations will strongly depend upon the intensity of the mean magnetic field, we allow them to vary with radius. Note that time-varying magnetic signals are particularly sensitive to the effective magnetic diffusivity, hence to β [4, 13].

We thus simultaneously invert for the mean axisymmetric toroidal velocity field $U_T(r, \theta)$ and for radial profiles $\alpha(r)$ and $\beta(r)$. U_T is decomposed in spherical harmonics up to $l_{max} = 8$ (m=0) and in Chebychev polynomials in radius up to $n_{max} = 11$. $\alpha(r)$ and $\beta(r)$ are projected on Chebychev polynomials up to $k_{max} = 5$,

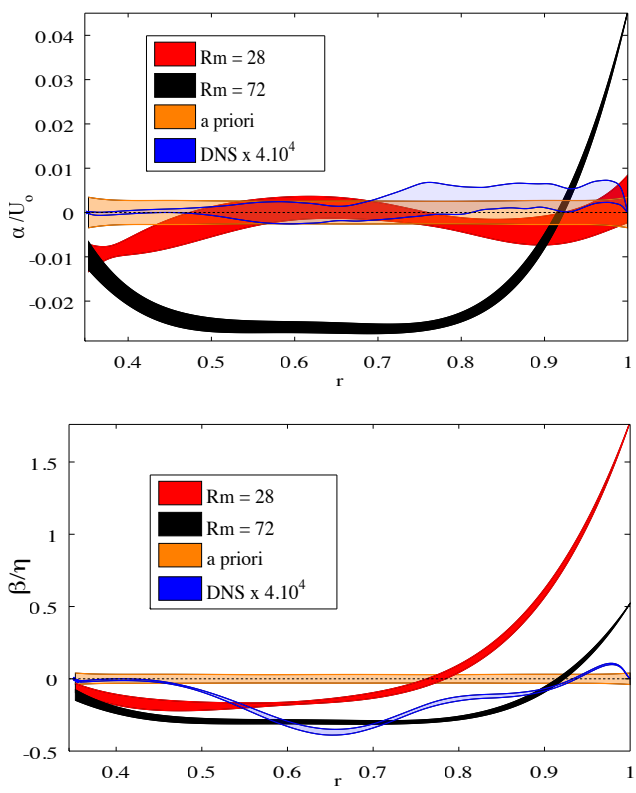

FIG. 2. Radial profiles of the α-effect (a) and β-effect (b) with their error bars, obtained by the inversion of DTS data for two magnetic Reynolds number: $Rm = 28$ and 72. The *a priori* null profile, along with its error bar, is also drawn. The blue curve shows the $\alpha(r)$ and $\beta(r)$ profiles retrieved from a numerical simulation of the DTS experiment at $Rm = 29$ and $Re = 2.9 \times 10^4$, blown up by a factor 4×10^4.

leading to:

$$\mathcal{E}(r) = \sum_{k=0}^{5} T_k(r) \left(\alpha_k \langle \mathbf{B} \rangle - \beta_k \nabla \times \langle \mathbf{B} \rangle\right), \qquad (2)$$

where T_k is the degree k Chebychev polynomial of the first kind and $\langle \mathbf{B} \rangle$ is the total mean magnetic field, solution of equation (1). Since the inversion is slightly non-linear, we use the linearized least-square Bayesian method of Tarantola and Valette [14], taking the *a posteriori* velocity model from a lower Rm, upscaled to the new Rm, as the *a priori* velocity model. We choose a zero value as the *a priori* model for all α_k and β_k. The poloidal velocity field is at least one order of magnitude smaller than the toroidal one. We do not invert for it at $Rm = 72$ and 94 but we include in the direct model a meridional flow up-scaled from the solution obtained at $Rm = 47$ [9]. We find that solving for the emf, which adds only 12 degrees of freedom, reduces the global normalized misfit significantly (see Table I).

Figure 2 shows the radial profiles of α and β (with their

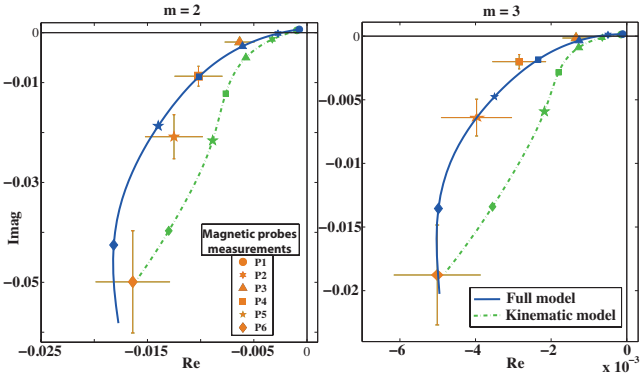

FIG. 3. Measurements and model fits for an example of time-varying magnetic signals measured at $2f$ (m=2) and $3f$ (m=3) frequencies, for a rotation rate of the inner sphere $f = -23$Hz ($Rm = 72$). See text for explanations.

a posteriori model errors) produced by the inversion of data at $Rm = 28$ and 72. The profiles for $Rm = 94$ (not shown) are almost the same as for $Rm = 72$. α is normalized by $U_0 = 2\pi f r_o$, and β by η. For the lower Rm value, we observe practically no α-effect, while the $\beta(r)$ profile indicates that the β-effect increases strongly when going from the Lorentz-force-dominated inner region to the Coriolis-force-dominated outer region. It reaches values of 1.7η near the outer boundary, where velocity fluctuations are strongest [12]. For the higher Rm, some α-effect is required to match the data over most of the fluid domain. The $\beta(r)$ profile displays strongly negative values (down to -0.3η) over almost the complete fluid shell, but rises sharply to positive values near the outer boundary.

The introduction of the α- and β-effects clearly improves the fit to the measurements. We illustrate this in Figure 3, which compares the prediction of our model, with and without the α and β terms, to the measurements of the time-varying signals for $f = -23$Hz ($Rm = 72$), at a given latitude ($-20°$). There, a sleeve intrudes into the sodium volume and records the azimuthal component of the magnetic field at 6 different radii labeled P1 to P6 (as drawn in Figure 1). When the inner sphere spins, small deviations of its magnetic field from axisymmetry produce a magnetic signal that oscillates at the rotation frequency f and its overtones. Here we focus on the $2f$ and $3f$ overtones caused by the $m = 2$ and $m = 3$ heterogeneities of the magnet. We measure the phase and amplitude of the time-varying magnetic signals at all 6 radii and plot them (with their error bars) in the complex plane, normalized by B_0 (the intensity of the imposed magnetic field at the equator of the outer shell). When the inner sphere is at rest, we record only the magnet's potential field weakening with increasing distance. Advection and diffusion completely distort this pattern when the inner sphere spins. The blue solid line displays the prediction from our full model of these mag-

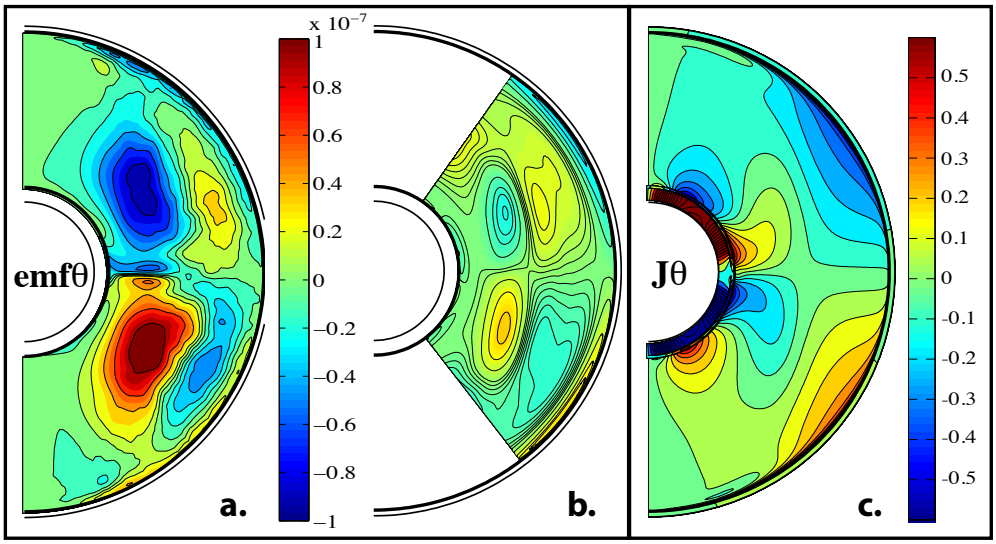

FIG. 4. Meridional cross section contour maps showing orthoradial component (θ) of emf $\mathcal{E}$ and of electrical current $\langle \mathbf{J} \rangle$. (a) Averaged emf $\mathcal{E}_t$ obtained from DNS. (b) Reconstructed emf $\mathcal{E}_{\alpha\beta}$ from inverted α and β profiles. High latitudes (white area) are excluded from the least-square fit. (c) Mean electrical current from DNS.

netic signals from the largest values at the inner sphere boundary ($r = r_i$) to small values at the outer sphere ($r = r_o$). Symbols mark the radial positions of the P6 to P1 magnetometers. The green dashed line is the trajectory predicted by our model when we remove the α and β terms. This altered model fails to produce the observations, indicating that the β-effect that we retrieve contributes significantly to the measured signals.

In addition to the inversion of experimental measurements, we perform direct numerical simulations (DNS) of the experiment. Our code, based on spherical harmonic expansion [15] and finite differences in radius, has already been used to simulate the experiment. We restarted the most turbulent computation of Figueroa *et al.* [12] with a new imposed magnetic field containing the additional non-axisymmetric and non-dipolar terms. This simulation reaches $Re = 2\pi f r_o^2/\nu = 2.9 \times 10^4$ (ν is the kinematic viscosity), $Rm = 29$ and a magnetostrophic regime close to that of the experiment [8]. Turbulence is generated by the destabilization of the outer boundary layer, yielding plumes that penetrate inward to regions of stronger magnetic fields. There, the velocity fluctuations are damped, but the associated magnetic fluctuations are stronger [12]. Six snapshots of the fields are saved every five turns. After we have reached a statistically steady regime, we average the fields over 162 turns of the inner sphere to obtain $\langle \mathbf{B} \rangle$ and $\langle \mathbf{U} \rangle$. It is then straightforward to compute the mean emf $\mathcal{E} = \langle \tilde{\mathbf{u}} \times \tilde{\mathbf{b}} \rangle$ where fluctuating fields are obtained from the difference between a snapshot and the time- and longitude-averaged field.

Meridional maps of the mean emf $\mathcal{E}_t$ are obtained and the latitudinal component is displayed in Figure 4a. The α and β profiles that best explain this mean emf (least-square solution of equation 2 excluding high latitudes) are shown in Figure 2. We estimate the error bar on the profiles as the standard deviation of emfs computed from 5 subsamples of 40 snapshots. One component of the emf $\mathcal{E}_{\alpha\beta}$ computed with these α and β profiles is shown in Fig. 4b, and can be compared to the actual emf $\mathcal{E}_t$ (Fig. 4a). Although the α and β profiles do not explain all of the mean emf, most features are recovered. Other components exhibit a similar behavior (not shown).

The parity (symmetry with respect to the equatorial plane) of the emf and of $\langle \mathbf{J} \rangle$ are clearly even (Fig. 4c), while $\langle \mathbf{B} \rangle$ is odd. This is in line with the fact that the DNS, just like the experiments at the lowest Rm, predicts no α-effect (see Fig. 2a). This might seem surprising given that the mean flow displays helicity. However, if we split the velocity fluctuations into even ($\tilde{\mathbf{u}}^+$) and odd ($\tilde{\mathbf{u}}^-$) parity, we see that their interaction with the mean odd magnetic field generates odd ($\tilde{\mathbf{b}}^-$) and even ($\tilde{\mathbf{b}}^+$) magnetic fluctuations, respectively. The resulting emf $\mathcal{E} = \tilde{\mathbf{u}} \times \tilde{\mathbf{b}}$ is therefore always even, if the odd and even velocity fluctuations are uncorrelated. This is likely true in the low Rm regime. The fact that the higher Rm-experiments require a non-zero α-effect (Fig. 2a) reveals that the velocity fluctuations are interacting with an already-distorted larger-scale magnetic field, or that correlations between the two parities become non-zero.

The dipolar component of the induced magnetic field predicted by our full model is small but non-zero at the surface of the outer shell, even when the α-effect is negligible. Spence *et al.* [3] have shown that an axisymmetric flow interacting with an axisymmetric magnetic field cannot produce an external dipole. This remains true if fluctuations only result in a homogeneous β-effect. Even

with a radially-varying β-effect as we obtain here, an external dipole can be produced only if a meridional flow is present.

The most striking feature of the $\beta(r)$ profiles we retrieve is the strong negative values (down to -0.3η) that span a large portion of the liquid sodium shell, especially at large Rm (see Fig. 2). The DNS supports this result, showing that it is not an artifact of considering only a radial dependence for α and β. The much lower amplitude of β in the DNS is due to a Reynolds number 300 times smaller than that in the experiment, suggesting that β may scale with Re^2 (but see the Erratum below). Although negative β values, and hence reduced magnetic diffusivity, are not unexpected [16–19], it is the first time that they are observed in experiment. Our DTS experiment combines a strong imposed magnetic field and strong rotation. These could be the ingredients that lead to this behavior. Were β to become even more negative, it might promote dynamo action.

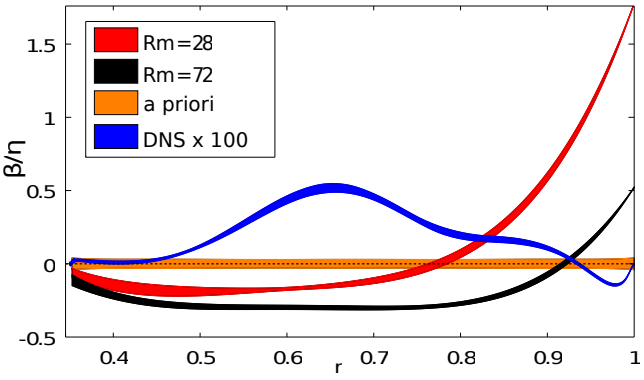

FIG. 5. (color online) Radial profiles of the β-effect with their error bars (the line thickness), obtained by the inversion of DTS data for two magnetic Reynolds number: $Rm = 28$ and 72. The *a priori* null profile, along with its error bar, is also drawn. β is normalized by the molecular magnetic diffusivity η. The blue curve shows the $\beta(r)$ profile retrieved from a numerical simulation of the DTS experiment at $Rm = 29$ and $Re = 2.9 \times 10^4$, blown up by a factor 100.

ERRATUM

In our original letter [20], there was an inconsistency in the sign convention used for β. The typos have been corrected in the present document and did not affect the profiles inverted from our experimental data. Unfortunately the wrong sign for β was used when analyzing the results of the numerical simulations. In addition, a mistake in the normalization of the EMF computed from the simulations makes it appear 561 times smaller than it actually is. The much lower amplitude of β in the DNS was interpreted as a suggestion for β scaling as Re^2 (the square of the Reynolds number). Instead, the correct amplitude is actually in line with a β effect increasing proportionally to the Reynolds number: $\beta \sim Re$.

Figure 5 replaces the original Fig. 2b found in our letter. After making the corrections, the numerical simulations are no more in good agreement with the β-effect found in the experiment, as they now have more or less opposite signs.

We acknowledge that our numerical simulations, performed at much lower Reynolds number, do not show the same behavior as the experimental data. These data remain however best explained by a reduced effective magnetic diffusivity due to turbulent fluctuations.

ACKNOWLEDGMENTS

This work was supported by the National Program of Planetology of CNRS-INSU under contract number AO2013-799128, and by the University of Grenoble. Most computations were performed on the Froggy platform of CIMENT (`https://ciment.ujf-grenoble.fr`), supported by the Rhône-Alpes region (CPER07_13 CIRA), OSUG@2020 LabEx (ANR10 LABX56) and Equip@Meso (ANR10 EQPX-29-01). We thank two anonymous referees and Elliot Kaplan for useful suggestions.

We wish to thank Johann Hérault and Frank Stefani for pointing out the inconsistency of the sign of β in our original letter. We also thank Elliot Kaplan for spotting the normalization issue in the numerical simulation post-processing code.

* henri-claude.nataf@ujf-grenoble.fr

[1] A. Gailitis, O. Lielausis, E. Platacis, S. Dement'ev, A. Cifersons, G. Gerbeth, T. Gundrum, F. Stefani, M. Christen, and G. Will, Phys. Rev. Lett. **86**, 3024 (2001).
[2] R. Stieglitz and U. Müller, Phys. Fluids **13**, 561 (2001).
[3] E. Spence, M. Nornberg, C. Jacobson, R. Kendrick, and C. Forest, Phys. Rev. Lett. **96**, 055002 (2006).
[4] P. Frick, V. Noskov, S. Denisov, and R. Stepanov, Phys. Rev. Lett. **105**, 184502 (2010).
[5] E. J. Kaplan, M. M. Clark, M. D. Nornberg, K. Rahbarnia, A. M. Rasmus, N. Z. Taylor, C. B. Forest, and E. J. Spence, Phys. Rev. Lett. **106**, 254502 (2011).
[6] K. Rahbarnia, B. P. Brown, M. M. Clark, E. J. Kaplan, M. D. Nornberg, A. M. Rasmus, N. Zane Taylor, C. B. Forest, F. Jenko, A. Limone, J.-F. Pinton, N. Plihon, and G. Verhille, Astrophys. J. **759**, 80 (2012).
[7] F. Ravelet, B. Dubrulle, F. Daviaud, and P.-A. Ratie,

Phys. Rev. Lett. **109**, 024503 (2012).
[8] D. Brito, T. Alboussiere, P. Cardin, N. Gagnière, D. Jault, P. La Rizza, J.-P. Masson, H.-C. Nataf, and D. Schmitt, Phys. Rev. E **83**, 066310 (2011).
[9] S. Cabanes, N. Schaeffer, and H.-C. Nataf, Phys. Rev. E **90**, 043018 (2014), arXiv:1407.2703.
[10] H.-C. Nataf, Comptes Rendus Physique **14**, 248 (2013).
[11] V. Ferraro, Mon. Not. Roy. Astron. Soc. **97**, 458 (1937).
[12] A. Figueroa, N. Schaeffer, H.-C. Nataf, and D. Schmitt, J. Fluid Mech. **716**, 445 (2013).
[13] S. M. Tobias and F. Cattaneo, J. Fluid Mech. **717**, 347 (2013).
[14] A. Tarantola and B. Valette, Reviews of Geophysics **20**, 219 (1982).
[15] N. Schaeffer, Geochem. Geophys. Geosys. **14**, 751 (2013).
[16] V. Zheligovsky and O. Podvigina, Geophys. Astrophys. Fluid Dyn. **97**, 225 (2003).
[17] A. Brandenburg, K.-H. Rädler, and M. Schrinner, Astronomy and Astrophysics **482**, 739 (2008).
[18] A. Giesecke, F. Stefani, and G. Gerbeth, New Journal of Physics **16**, 073034 (2014).
[19] A. Lanotte, A. Noullez, M. Vergassola, and A. Wirth, Geophysical & Astrophysical Fluid Dynamics **91**, 131 (1999).
[20] S. Cabanes, N. Schaeffer, and H.-C. Nataf, Phys. Rev. Lett. **113**, 184501 (2014).

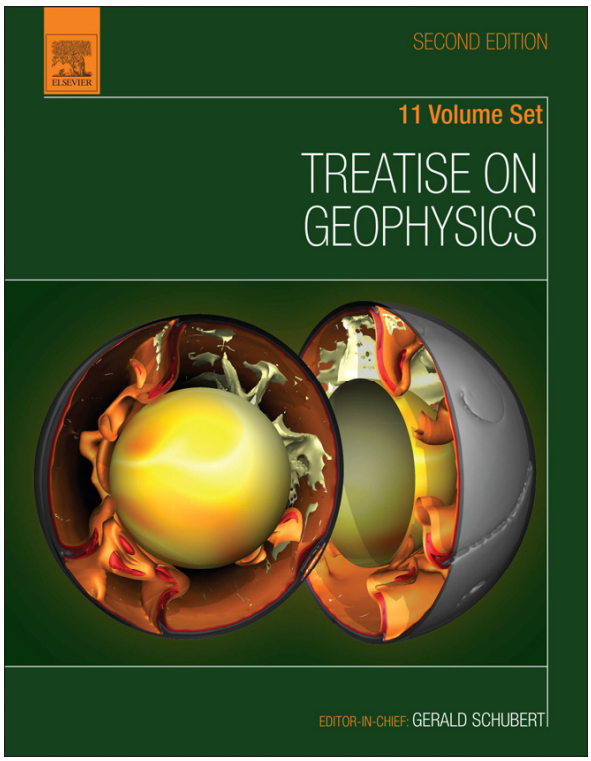

Nataf H.-C., and Schaeffer N Turbulence in the Core. In: Gerald Schubert (editor-in-chief) Treatise on Geophysics, 2nd edition, Vol 8. Oxford: Elsevier; 2015. p. 161-181.

8.06 Turbulence in the Core

H-C Nataf and N Schaeffer, University Grenoble Alpes / CNRS, Grenoble, France

*Treatise on Geophysics, 2nd edition, (*2015), vol. 8, pp. 161-181

8.06.1 Introduction

In this chapter, we have the difficult task of describing the invisible part of the core: turbulent structures that we cannot detect but have to be there. Indeed, nonlinear interactions in the liquid core lead to the formation of velocity, temperature, and magnetic structures on a large range of scales. Their roles are important: they transfer energy between large and small length scales, and in the end, they control the dissipation of the geodynamo. Turbulence is at work everywhere and has been studied for decades. Our first step is to define turbulence and show why one should care about turbulence in the core. Then, we review a few fundamental features of hydrodynamic turbulence. Many tools are needed to decipher turbulence: we present key results obtained from numerical simulations, laboratory experiments, and observations of natural systems. Unfortunately, no observations of the internal geomagnetic field are possible at small scales, mostly because of the crustal field that overprints the small-scale core field. Observations of turbulence in other systems are thus welcome to gain insight in what could happen in the Earth's core. We also devote one section to the parameterization of turbulence in numerical simulations.

The last two sections focus on the core. Turbulence implies a range of timescales and length scales. We define dimensionless numbers depending on the length scale ℓ. They measure the relative weight of the various terms in the governing equations. Using the known properties of the core and its large-scale velocity and magnetic field, we evaluate these various numbers. We introduce τ–ℓ-diagrams that help us identify the scales at which turbulent regimes change. Step by step, we explore the suite of plausible turbulent regimes for the core, introducing successively the effects of rotation and magnetic field. Our analysis emphasizes the crucial role of rotation in limiting the dissipation of the geodynamo and points out the need for dedicated studies.

8.06.1.1 What Is Turbulence?

8.06.1.1.1 An attempt to define turbulence

Turbulence is difficult to define precisely, but we can list a few elements that characterize turbulent motion. The most prominent feature of turbulence is that the motion of the fluid involves a wide range of spatial and temporal scales. These scales cannot be treated independently and there is no scale separation between small and large scales, although different regimes can be identified.

In order for the various scales to interact, the nonlinear terms of the evolution equation must be important. In the case of pure hydrodynamic turbulence, this is ensured by a large Reynolds number $Re = UL/\nu \gg 1$, ratio of the diffusive time L^2/ν to the advection time L/U (L is a characteristic length, U a typical velocity, and ν the kinematic viscosity of the fluid). However, in a self-magnetized conducting fluid driven by thermochemical convection, there are other nonlinear terms that allow interaction of different scales.

A flow executing turbulent motion often exhibits eddies of various scales, but this may not be the case when a strong magnetic field and background rotation are present, as it is the case for the Earth's core. Turbulence is not chaos, but all turbulent flows exhibit fluctuations that call for a statistical description, rather than a deterministic one. If the precise details of the flow are controlled by initial conditions or small perturbations that we cannot measure, global quantities such as the energy dissipation rate, the average velocity field, and the amplitude of fluctuations are of great interest and are expected to be well defined and measurable.

As opposed to laminar motion, where the fluid particles follow a pattern controlled by the viscosity, with little change from one fluid particle to its neighbor, a turbulent motion involves complex time dependence and spatial dependence.

8.06.1.1.2 Is the earth's core turbulent?

Due to the low viscosity of molten iron, the Reynolds number is certainly very large – $Re \sim 10^8$ – meaning that the viscous term (which is the only isotropic dissipation term) acts mainly at small scale. Furthermore, the nonlinear terms associated with the Lorentz force are in fact much larger than the inertial term at large scale, leading to a ratio of nonlinear to viscous force of about 10^{12}.

However, the importance of the magnetic field and the global rotation rate make the turbulence rather peculiar. It is sometimes advocated that the flow variations along the rotation axis or magnetic field lines are inhibited, leading to sheet-like (laminar) motion that cannot be turbulent anymore (because velocity is now mostly perpendicular to its gradient). These are a lot of constraints for an incompressible vector field that has only two degrees of freedom.

We shall see in the following sections that not all these constraints have the same strength. In an attempt to describe the dynamics of the system, we will discuss how it can organize itself on a broad range of timescales and length scales in several different regimes.

8.06.1.2 Why Care?

Turbulent small-scale fields within the core will not be observed. So, why care? They can have a collective or average effect that has a direct measurable consequence on the large-scale flow and magnetic field, which we investigate. They also control the dissipation, which we need to assess in order to know how much power is needed to drive the dynamo.

8.06.1.2.1 Small scales contribute to secular variation

Much of what we know about flow and magnetic field within the core is deduced from the analysis of the secular variation of the magnetic field observed at the surface of the Earth (see Chapter 8.04). The magnetic field at the core–mantle boundary is determined only up to degree 13 of the spherical harmonics (corresponding to a wavelength of about $2\pi \times 3500/13 = 1700$ km at the top of the core). Its time derivative is known up to degree 10 for the most recent epoch. One aims at reconstructing the large-scale velocity $\mathbf{u}$ by inverting the frozen flux induction equation of the radial component of the magnetic field B_r at the core–mantle boundary:

$$\partial_t B_r + \nabla_H \cdot (\mathbf{u} B_r) = 0 \qquad [1]$$

where ∇_H is the horizontal part of the divergence operator (see Chapter 8.04). The problem is that unresolved small-scale motions can interact with unresolved small-scale magnetic field to contribute to the large-scale induction term of this

equation. Eymin and Hulot (2005) showed that realistic amplitudes of these two unresolved fields produce representation errors that largely exceed the observational errors. Better models are obtained when these representation errors are taken into account in core flow inversions (Pais and Jault, 2008). It is therefore of interest to get some constraints on the evolution of the velocity and magnetic field with harmonic degree beyond what can be inferred from the observations.

8.06.1.2.2 Small scales and dynamo action

Mean-field dynamo theories developed in the 1960s (Moffatt, 1961; Steenbeck et al., 1966) have demonstrated that the interaction of the small scales of a turbulent flow in a conducting fluid with the small scales of the magnetic field they induce can produce a large-scale magnetic field (see Moffatt, 1978, for a review). This mechanism is nicely illustrated by the success of the two-scale dynamo experiment in Karlsruhe (Stieglitz and Müller, 2001). Liquid sodium was forced to flow up and down in helicoid motions in an array of pipes set up to mimic the two-dimensional periodic paving of the G. O. Roberts dynamo (Roberts, 1972). Induction was clearly taking place at the scale of each of the 52 individual 0.21 m diameter pipes. Nevertheless, a large-scale magnetic field was produced at the scale of the complete 1.7 m diameter assembly.

The simplest forms of mean-field dynamo theory predict that isotropic homogeneous turbulent motions in a conducting fluid produce a large-scale electromotive force $\varepsilon = \boldsymbol{\alpha} : \langle \boldsymbol{B} \rangle + \boldsymbol{\beta} : \boldsymbol{\nabla} \times \langle \boldsymbol{B} \rangle$, where $\langle \boldsymbol{B} \rangle$ is the large-scale magnetic field; $\boldsymbol{\alpha}$ and $\boldsymbol{\beta}$ are two tensors, which depend upon the turbulent characteristics of the flow; and ':' is the tensorial dot product. In this view, the α-effect is crucial for enabling the large-scale magnetic field to grow, while the β-effect can increase or decrease the magnetic diffusivity. Parameterized numerical dynamo models relying on these ideas have had a crucial role in explaining the solar cycle, and they are still very useful (see Charbonneau, 2005, for a review). However, the lack of scale separation and the expected deviations from isotropy and homogeneity can strongly impact the relevance of this theory for the geodynamo.

8.06.1.2.3 Dissipation and efficiency

In the so-called inertial range of classical turbulence, energy is transferred from the large scales to the small scales, with almost no energy loss. The dissipation of energy occurs at the smallest scales, where velocity gradients become large enough for viscous forces to balance nonlinear inertial terms. The smaller this scale, the higher the dissipation. We examine several alternative scenarios for turbulence in **Section 8.06.6** and show that they yield extremely diverse dissipation rates. The efficiency of convective motions for producing a dynamo therefore strongly depends on the organization of the turbulent velocity and magnetic fields.

8.06.1.2.4 Mixing

Turbulence affects the mixing of fluid parcels and of what they transport. It has therefore received considerable attention in atmospheric and oceanic sciences, where the transport of pollutants or nutrients has an important socioeconomic impact. This question has not yet been tackled in studies of core dynamics. However, seismology reveals that layers at the bottom and at the top of the liquid core may have a slightly different composition. How much mixing takes place between these layers and the rest of the core has important geodynamic implications (Alboussière et al., 2010). The observation of the atmospheres of Jupiter and Saturn reveals that zonal bands with alternating wind directions are able to maintain a strikingly different chemical signature, yielding contrasting colors, despite a very active turbulence. We should keep this in mind when considering the fluid inside the cylinder tangent to the inner core.

8.06.2 Fundamentals of Turbulence

Identified by Feynman as 'the most important unsolved problem of classical physics,' turbulence has been the subject of numerous studies over a large part of the twentieth century. Unsolved fundamental issues remain, but an impressive corpus of results and models has been acquired (see Frisch, 1995, for a review and more). We give here a simple overview of some fundamental aspects of hydrodynamic turbulence (i.e., in the absence of global rotation and magnetic field).

8.06.2.1 Energy Density Spectra and Energy Cascade

While all turbulent fields undergo large fluctuations in time and space, it has been found that energy density spectra of the flows are robust and universal in hydrodynamic turbulence. In addition, these spectra nicely summarize the scaling properties of the flow and the energy transfer that takes place. Defining k as the (scalar) wave number of the flow in the Fourier space, the energy density $E(k)$ is defined by

$$\widetilde{E} = \frac{1}{2}\langle u^2 \rangle = \int_0^\infty E(k)\,\mathrm{d}k \qquad [2]$$

where $\widetilde{E}$ is the energy of the fluctuations per unit mass. The theory of 'universal turbulence' was established by Kolmogorov (1941a). The basic idea is that there should be a wave number k_0 above which turbulence does not depend upon how energy is fed to the flow. The only thing that counts is the mean power per unit mass ε it provides and that is also dissipated in the stationary regime. In this idealized view, universal turbulence should thus be isotropic and homogeneous, and it should have a self-similar character.

The smaller length scale at which dissipation operates is called Kolmogorov's scale, with wave number k_D. It depends upon ε and the kinematic viscosity ν. Viscous dissipation per unit mass can be written as $\nu(\boldsymbol{\nabla u})^2$, which we express as $\nu k_\mathrm{D}^2 (u(k_\mathrm{D}))^2$ at the k_D wave number. The typical velocity $u(k_\mathrm{D})$ is obtained by stating that the Reynolds number at this scale should be about 1 for dissipation to occur, yielding $u(k_\mathrm{D}) \sim \nu k_\mathrm{D}$. We thus obtain

$$k_\mathrm{D} = \left(\frac{\varepsilon}{\nu^3}\right)^{1/4} \qquad [3]$$

The main assumption of Kolmogorov is then that, in the wave number range between the injection scale and the dissipation scale ($k_0 \ll k \ll k_\mathrm{D}$), all statistically averaged quantities at wave number k are a function of k and ε only. Dimensional analysis then commands

$$E(k) = C_K \varepsilon^{2/3} k^{-5/3} \quad [4]$$

which is the famous $k^{-5/3}$ law derived by Obukhov (1941), where C_K is a dimensionless constant called 'Kolmogorov's constant.' It has been found that a wide class of actual turbulent flows follow this law, sometimes over many decades in wave number, and C_K has been measured to lie between 1.5 and 2.

The k power-law dependence of $E(k)$ is a signature of self-similarity in this wavenumber range, called the inertial range, along which energy cascades from the injection length scale down to the dissipation scale. Self-similarity extends to higher-order 'structure functions' $S_p(\ell)$, which are defined as $S_p(\ell) = \langle \delta u^p(\ell) \rangle$, where $\langle\rangle$ denotes a statistical average and $\delta u(\ell)$ is the velocity difference measured between two points separated by a distance ℓ. Longitudinal velocity differences are usually considered (i.e., difference in the projection of velocity on the line that links the two points). The measurements yield

$$S_p(\ell) \sim \ell^{\zeta_p} \quad [5]$$

where the exponents ζ_p appear to be universal. $E(k)$ is directly related to $S_2(\ell)$, so that $\zeta_2 = 2/3$ for Kolmogorov's $E(k)$ spectra. In fact, under Kolmogorov's hypotheses, one gets $\zeta_p = p/3$ for all p. The measurements indicate that the actual ζ_p exponents clearly deviate from this prediction as p increases (Anselmet et al., 1984). The high-order structure functions are related to the tails of the probability distribution function of velocity differences. For small separation distances ℓ, these distributions strongly deviate from normal distributions, showing a larger influence of intermittent 'rare' events.

8.06.2.2 Structures

The apparition of flow structures is an unavoidable consequence of the break of symmetry that characterizes the instabilities at the origin of turbulence. Anyone who has looked at turbulent flows in a river or in the air will retrieve the image – nicely illustrated by Leonardo da Vinci – that vortices or eddies are the building bricks of hydrodynamic turbulence. Eddies come in a large range of sizes. They are usually longer than wide and can even stretch into vorticity filaments. The core of an eddy has a strong but relatively homogeneous vorticity $\boldsymbol{\omega} = \nabla \times \boldsymbol{u}$, while the opposite holds on its edges. There, the shear between eddies nucleates smaller eddies. Long filaments can also break into shorter filaments. In this way, energy cascades down to small scales, where dissipation occurs.

With this in mind, it does not seem obvious that, even if vortices can take all sizes and orientations, the embedding of essentially one-dimensional structures (vorticity filaments) into three-dimensional space will have no influence on the statistically averaged quantities at wave number k, as originally assumed by Kolmogorov. This idea is the starting point of She and Leveque (1994). They showed that vorticity filaments dissipate the available surrounding energy very efficiently by forcing the lower-intensity eddies into an essentially bidimensional flow around them. Vorticity filaments are relatively rare, as they correspond to eddies that have had the opportunity to stretch and get stronger. To illustrate this phenomenon, Kaneda and Morishita (2013) reported that 33% of the energy dissipation occurs in 5% of the volume in one of the highest Reynolds number direct numerical simulation (DNS) performed to date. One consequence is that the average moments of the energy dissipation $\langle \varepsilon^p(\ell) \rangle$ within a sphere of radius ℓ depends upon the scale ℓ. Self-similarity implies

$$\langle \varepsilon^p(\ell) \rangle \sim \ell^{\tau_p} \quad [6]$$

where the exponents τ_p should again be universal. Kolmogorov's hypothesis that all statistically averaged quantities only depend upon scale and mean dissipation ε implies $\langle \varepsilon^p(\ell) \rangle = \varepsilon^p$, independent of ℓ (i.e., $\tau_p = 0, \forall_p$). If this hypothesis is relaxed to take into account intermittency, the 'refined similarity hypothesis' derived by Kolmogorov (1962) yields a relation between the ζ_p and τ_p exponents:

$$\zeta_p = p/3 + \tau_{p/3} \quad [7]$$

She and Leveque (1994) derived expressions for τ_p and hence for ζ_p that are in excellent agreement with the measurements:

$$\zeta_p = p/9 + 2\left[1 - \left(\frac{2}{3}\right)^{p/3}\right] \quad [8]$$

Note that the –5/3 exponent of k in the expression for $E(k)$ is hardly modified by this extension and that the ζ_3 exponent is always 1, as it can be derived with no adjustable parameter from the Navier–Stokes equation in some conditions (see Frisch, 1995; Kaneda and Morishita, 2013; Kolmogorov, 1941b), yielding Kolmogorov's equation (also called the four-fifths law):

$$S_3(\ell) = -\frac{4}{5}\varepsilon\ell \quad [9]$$

Turbulence can be strongly modified by the presence of global rotation and/or magnetic field. Although we are still lacking a thorough description of turbulence under such conditions, we will unravel and discuss some of its known or inferred properties in **Section 8.06.6** and try to get closer to a description that applies to the Earth's core.

8.06.3 Tools for Turbulence

8.06.3.1 Direct Numerical Simulations

DNSs consist in fully solving the equations of the problem, namely, the Navier–Stokes equation together with the induction and the codensity equations (see **Section 8.06.5.1**). The best Navier–Stokes simulations reach an impressive resolution of 4096^3 (Kaneda and Morishita, 2013). The size of the resulting discrete problem for the Earth's core is such that we cannot hope a DNS at the real parameters anytime soon: from the core size to the Ekman layer thickness, six orders of magnitude in length scale and timescale must be resolved.

The problem is made even worse by the need to take into account the spherical geometry and the coupling with the induction equation. Nevertheless, DNS of the geodynamo have proved very useful, as exposed in **Chapter 8.10**. They clearly demonstrate the role of rotation in the generation of a large-scale magnetic field, dominated by a dipole aligned with the axis of rotation. Furthermore, scaling relationships derived

from these simulations seem to indicate that their output is independent of the precise values of the diffusion coefficients (Christensen and Aubert, 2006), giving hope that relevant asymptotic regimes are attained even though diffusivities are far larger than the values expected for the core.

Some DNS have tackled the question of small-scale turbulence in core situations. Following the theoretical work of Braginsky and Meytlis (1990), StPierre (1996) performed DNS of turbulence in the presence of both rotation and magnetic field. He found that buoyant patches rapidly break up into platelike structures elongated in the directions of the rotation axis and of the prevailing magnetic field. Giesecke (2007) found similar results. However, it is not clear how a turbulent cascade of energy can build upon such structures. Besides, these simulations do not take into account the fact that rotation and magnetic field characteristic times are several orders of magnitude apart in the core (see **Section 8.06.6**).

MHD turbulence is very difficult to model. The magnetic field imposes a strong anisotropy, which can be used to reduce the full MHD equations. Energy spectra for 'weak' and 'strong' MHD turbulence have been obtained this way (see Tobias et al., 2013, for a review).

Even though DNSs are not able to simulate the core, they can offer some insight in the dynamics and, in particular, give hints to support the scenarios that we elaborate based on various studies in different dynamical regimes. **Figures 1** and **2** display a snapshot of a full geodynamo DNS computed for fairly extreme parameters that get closer to core values. It shows thinner elongated coherent structures in the velocity field than in simulations at milder Ekman numbers. It strongly supports the large-scale, high magnetic Reynolds number (Rm; see **Table 2**) picture, where the Coriolis force dominates.

8.06.3.2 Laboratory Experiments

The exploration of highly turbulent flows is possible in laboratory experiments. Very long time series are easily obtained. The main problem is often to access the quantities that best document turbulent behavior. Laboratory experiments have played and are still playing an important role in the exploration of the dynamics of geophysical and astrophysical fluids. A review of the experimental results that shed light on core dynamics is given in **Chapter 8.13**.

Early experiments used local intrusive probes and provided key measurements on several features of turbulence. For example, Anselmet et al. (1984) determined the structure exponents ζ_p in a turbulent jet up to $p=10$, providing a strong motivation for theoretical improvements (Frisch, 1995). The first experimental wavenumber energy density spectra for MHD turbulence in an applied magnetic field were measured by Alemany et al. (1979) using velocity probes attached to a grid moving in a column of mercury placed within a solenoid. They found a kinetic energy spectrum $E_u(k) \sim k^{-3}$ demonstrating the strong damping of fluctuations by the applied magnetic field in the low magnetic Reynolds number regime.

Recent experiments rely on optical methods based on particle image velocimetry (PIV), which have evolved into very efficient tools (see Westerweel et al., 2013, for a recent review) and brought new constraints on turbulence in transparent fluids, such as air and water. Let us cite, as an example, the determination of the structure coefficients of Lagrangian velocity increments in a von Kármán flow (Xu et al., 2006) and the structure coefficients of velocity increments in shallow layer rotating turbulence (Baroud et al., 2003). These methods have also been very useful for establishing the idea that the mixing

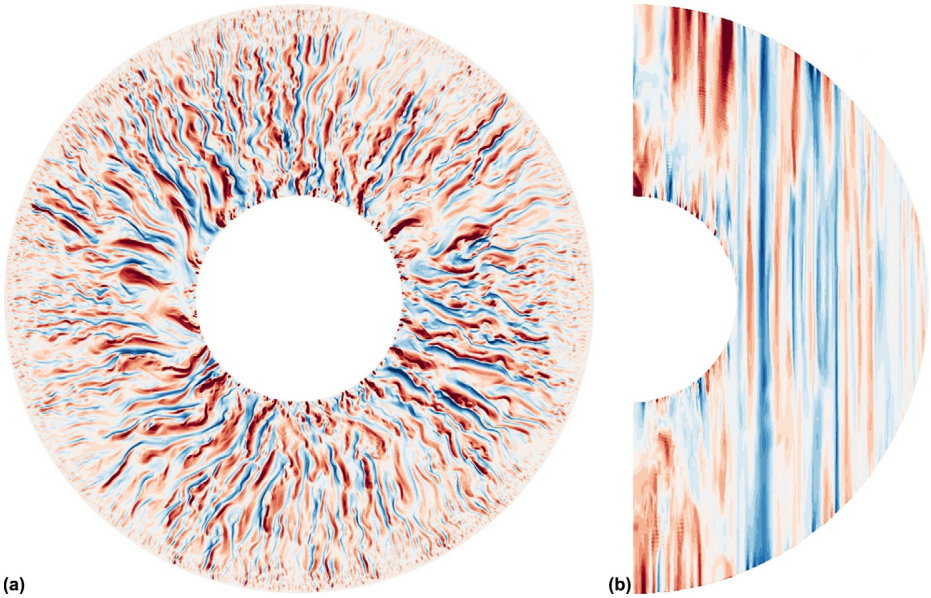

Figure 1 Cylindrical radial velocity component u_s in the equatorial plane (a) and a meridional plane (b). Snapshots from a dynamo DNS at $E=10^{-7}$, $Pm=0.1$, $Pr=1$, and $Ra=2.4\times10^{13}$ (see **Table 2** for the definition of these numbers using ℓ as the radial distance between the inner shell and outer shell), using spherical harmonic expansion up to degree 893 and 1024 radial shells.

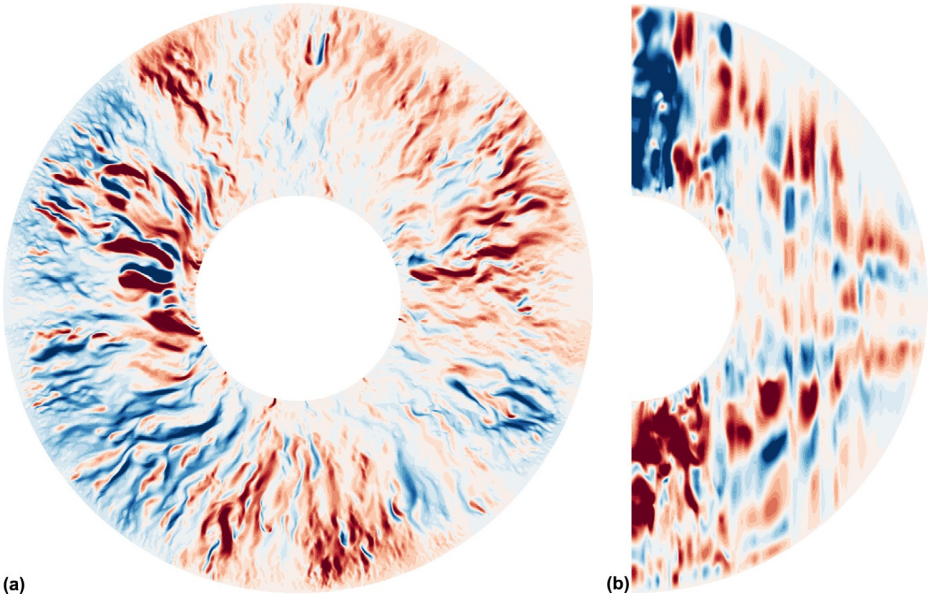

Figure 2 Cylindrical radial magnetic field component B_s in the equatorial plane (a) and a meridional plane (b). Snapshots from a dynamo DNS at $E=10^{-7}$, $Pm=0.1$, $Pr=1$, and $Ra=2.4\times10^{13}$ (see **Table 2** for the definition of these numbers using ℓ as the radial distance between the inner shell and outer shell), using spherical harmonic expansion up to degree 893 and 1024 radial shells.

of potential vorticity (PV) plays a major role in shaping zonal flows in rotating fluids (Aubert et al., 2002). Recently, using a transparent electrolyte and a superconducting magnet, Andreev et al. (2013) demonstrated that PIV methods can be used in MHD experiments.

Advances in handling helium gas at low temperatures have opened a new way for exploring thermal convection at very high Rayleigh numbers. As we will see in **Section 8.06.6.2**, the Rayleigh number measures the vigor of convection. Niemela et al. (2000) reported heat transfer measurements for an amazing range of 11 decades in Rayleigh number from 10^6 to 10^{17}, displaying a very simple power-law dependence of the Nusselt number $Nu=0.124Ra^{0.309}$ over the full range (the Nusselt number measures the convective heat transfer efficiency). They also provide nice evidence for a Kolmogorov $f^{-5/3}$ frequency power spectrum of temperature fluctuations at $Ra=6\times10^{11}$.

For experiments with liquid metals, which are essential for investigating magnetohydrodynamic turbulence, acoustic Doppler velocimetry has proved very useful (Brito et al., 2001, 2011; Stefani et al., 2009). Interestingly, in such experiments, induced magnetic fields resulting from the interaction of the flow with a weak imposed magnetic field, which can be measured outside the experiment, provide an information on the hydrodynamic flow that would be difficult to retrieve otherwise. For example, Kelley et al. (2007) discovered that specific inertial modes were excited in a rotating spherical Couette flow experiment using liquid sodium as a working fluid. These modes appear to be excited by critical layers attached to the Stewartson layer that accommodates the angular velocity jump between the inner sphere and the outer sphere when both rotate (Rieutord et al., 2012).

When a strong dipolar magnetic field is applied in the same Couette geometry, as in the DTS experiment (see Brito et al., 2011), modes are also observed (Schmitt et al., 2008, 2013), but the modes are strongly affected by the Lorentz force. The DTS experiment also demonstrates that turbulence is strongly hampered under the action of both global rotation and a strong magnetic field (Nataf et al., 2008; Nataf and Gagnière, 2008).

The pioneer dynamo experiments of Riga (Gailitis et al., 2001) and Karlsruhe (Stieglitz and Müller, 2001) have not only demonstrated the self-sustained dynamo process in the Lab but also opened the way to using liquid sodium as a working fluid in MHD and dynamo experiments. Several teams across the world have followed their example and set up sodium experiments in which the mean flow is accompanied by fluctuations of a similar amplitude (see Lathrop and Forest, 2011; Verhille et al., 2010, for recent reviews). Spontaneous generation of a magnetic field has thus been observed in the VKS experiment in Cadarache (Monchaux et al., 2007), but only when the impellers are ferromagnetic. A variety of different dynamical regimes have been observed in this device, including spectacular chaotic reversals of the magnetic field (Berhanu et al., 2007). One of the main lessons from these studies is that turbulent fluctuations appear to hinder the dynamo action that the mean flow should produce if it were alone. Besides, ohmic dissipation remains high in these experiments, and Alfvén waves are too damped to play a dynamical role, except when the device is placed in a very strong magnetic field (Alboussiere et al., 2011). Using plasma as a working fluid opens new possibilities, which are under investigation (Spence et al., 2009).

8.06.3.3 Observations

Unfortunately, no observations of the internal geomagnetic field are possible at small scales, mostly because of the crustal field that overprints the small-scale core field. Observations of

turbulence in other systems are thus required to gain insight in what happens in the Earth's core.

Characterization of turbulence in the Earth's atmospheric boundary layer was probably the first target of detailed analyses of turbulence. The first measurements of turbulent fluxes were performed in Australia by the eddy correlation technique (Swinbank, 1951; see Hogstrom, 1996, for a review). All these observations shed light on the universal behavior of turbulence in natural environments, showing, for example, that the von Kármán constant $K=u_*/(z\partial_z u_H)$, relating the amplitude of turbulent fluctuations u_* to the vertical gradient of mean horizontal velocity $\partial_z u_H$ in the inertial sublayer, is constant and equal to its laboratory value of 0.4, irrespective of the roughness of the ground, as expected from the scale-invariant properties of universal turbulence (Lo et al., 2005).

Later on, compilations of data from commercial aircraft flights demonstrated that winds and temperature follow Kolmogorov's $k^{-5/3}$ law for wavelengths from a few kilometers up to 400 km, steepening to a k^{-3} law at larger scales (Nastrom and Gage, 1985). Coupling these observations with simulations from general circulation models opens the way to determining the actual energy fluxes responsible for this behavior (Augier and Lindborg, 2013).

Space exploration of the solar system has revealed the fantastic dynamics of the atmospheres of Jupiter and Saturn and opened the way for detailed analyses of their turbulent behavior. The long-term stability of the strong and numerous zonal jets they display remains a strong driver for modeling turbulence on a rotating sphere (see Vasavada and Showman, 2005, for a review).

Combining observations and high-performance numerical modeling, the reanalysis of ocean circulation nicely illustrates the role of quasi-geostrophic mesoscale eddies in the dynamics of the ocean. In particular, zonal motions resulting from the interaction of turbulent eddies have recently been detected (Maximenko et al., 2005).

The solar wind is a great laboratory for MHD turbulence, as reviewed by Bruno and Carbone (2005). Even though it is a collisionless plasma, MHD turbulence is expected for frequencies below 0.1 Hz. Two types of solar winds must be distinguished. The fast wind originates from polar regions of the Sun and has mean velocities about twice as fast as the slow wind coming from equatorial regions. The temporal fluctuations in the solar wind have been measured by several probes starting in the 1960s. The measurements show three regimes in the temporal energy spectrum $E(f)\sim f^{\alpha}$: The lowest frequencies have $\alpha\simeq -1$ for period about a day or longer, while higher frequencies follow $\alpha\simeq -3/2$ for the fast wind and $\alpha\simeq -5/3$ for the slow wind. Finally, at periods around a few seconds, $\alpha\simeq -2$ is found. The transition between the first two regimes is rather sharp and is located around 10–16 hours, depending on the distance from the Sun. The fluctuations are found to be anisotropic, with much weaker fluctuations along the local magnetic field. A strong correlation exists between the velocity and the magnetic fluctuations, especially for the fast wind, showing the predominance of (incompressible) Alfvén waves in solar wind turbulence. At a large distance from the Sun, magnetic field fluctuations are twice more energetic than velocity fluctuations. This observation remains puzzling, although it is also observed in some dynamo simulations.

8.06.3.4 Shell Models

Shell models of turbulence originated in the 1970s, as a tool for accessing the statistical properties of universal turbulence. In these models, structures are ignored, as all fields are projected on a suite of shells of wave number k_n in the spectral domain. The sequence of wave numbers k_n is chosen to be geometric, thus enabling a wide range of length scales to be covered with a limited number of grid points. One takes into account the symmetries and conservation laws that pertain to the type of turbulence under study (2-D or 3-D hydrodynamic turbulence, magnetohydrodynamic turbulence, etc.). The game is then to choose the rules that govern the transfer between shells, which mimic the nonlinear interactions between the various fields of the various shells. The phenomenon of intermittency described earlier in the text can be recovered in shell models.

Shell models have received a lot of attention in the past decade, and extensions to MHD and rotating turbulence have been worked out (see Plunian et al., 2013, for a thorough review). Shell models are particularly appealing for exploring MHD turbulence in fluids with a very small (or very large) magnetic Prandtl number, for which DNSs are hopeless because of the large range of scales to be resolved. The magnetic Prandtl number $Pm=\nu/\eta$ is the ratio of kinematic viscosity over magnetic diffusivity. It is of the order of 10^{-5} for liquid iron in the core. As an example, Plunian and Stepanov (2010) explored how the ratio of magnetic to viscous dissipation varies with the magnetic Prandtl number. They found that, under model assumptions, magnetic dissipation is at least ten times larger than viscous dissipation for core values.

8.06.3.5 Plume Model

In contrast with the approach we just described, David Loper and others focused on buoyant plumes envisioned as the elementary structure at the origin of turbulent motions in the core. The analysis of the dynamics of such plumes in core conditions led David Loper to infer that rising plumes would have dimensions in the range 10–1000 m, typical relative density anomalies between 10^{-10} and 10^{-8}, and upwelling velocities from 10^{-3} to $10^{-1}\,\mathrm{m\,s^{-1}}$, depending on actual core properties. At the base of the convecting outer core, plumes would occupy a fraction of the surface between 10^{-5} and 10^{-1}. The reader is referred to David Loper's chapter (Loper, 2007) in the first edition of the Treatise on Geophysics for a complete description of the plume model.

8.06.4 Parameterization of Turbulence

Numerical simulations are limited by the available memory of the computer and its computing power. The more turbulent the flow, the larger the scale range. Therefore, DNSs that resolve all the spatial scales down to the viscous dissipation scale (the limit of turbulent small scales) cannot reach strongly turbulent regimes. If one could capture the (statistical) effect of turbulent small scales on the larger scales and properly predict the turbulent small-scale state corresponding to the large scales that produce it, we could in principle parameterize the effect of small-scale turbulence.

If several parameterizations for purely hydrodynamic, homogeneous, isotropic turbulence are available and used in hydrodynamic simulations or in the MHD regime at low Rm and low interaction parameter (e.g., Ponty et al., 2005), we should at least question their use for modeling the Earth's core.

On one hand, if we target the dynamics to the small scales inside the Earth's core, we will see that the turbulence inside the Earth's core may never reach the parameter-space region where simple hydrodynamic turbulence takes place (see Section 8.06.6). Thus, we are left with a challenging task: finding a necessarily anisotropic parameterization that depends on the local magnetic field and on the global rotation.

On the other hand, the current numerical geodynamo models do not seem to operate in such a regime, and hydrodynamic turbulence may indeed be important for the small scales in these models. Indeed, even with a magnetic field and a large magnetic diffusivity, part of the flow that is aligned with the magnetic field will not produce electric current and dissipation. Viscosity is the only isotropic dissipation in such systems. Furthermore, the smaller the scale, the smaller the influence of the magnetic field (interaction parameter); hence, the smallest scales may only rely on hydrodynamic turbulence for the energy to reach the viscous dissipation scale.

Here, we wish not to provide a detailed theoretical framework for subgrid-scale modeling, but rather list a few approaches that have been used to perform numerical simulation of the Earth's core. With the previously mentioned limitations in mind, we describe two approaches.

8.06.4.1 Hyperdiffusivities or Eddy Diffusivities

Hyperdiffusivity is the simplest form of parameterization of small-scale turbulence, where the effect of unresolved small scales is expressed as an enhanced diffusivity on the resolved scales. In hydrodynamic turbulence, where the interactions are mostly local (which means that a given scale is mostly influenced by its neighboring scales), such enhanced diffusivity can arguably be restricted to the smallest resolved scales. Although there is no physical justification for the use of hyperdiffusivity, there is a practical one: with increased viscosity at small scales, a numerical simulation is able to dissipate more energy, which would have been the main effect of smaller unresolved scales.

The first geodynamo simulation by Glatzmaier and Roberts (1995) made use of hyperdiffusivity at all scales, which is arguably both a concern and not really a small-scale parameterization, but it allowed to run a full geodynamo model on the computers of the early 1990s. A more reasonable approach is to restrict the use of hyperdiffusivity only at the smaller scales. Following the pioneers, many authors use a hyperdiffusivity of the type $\nu(l)=\nu_0(1+a(l-l_0)^n)$ for $l>l_0$ and $\nu(l)=\nu_0$ for $l\le l_0$, where l is the spherical harmonic degree (angular wave number) and a, l_0, and n are adjustable parameters. It must be emphasized that this is still an isotropic viscosity but its value depends only on l and not on the radial spatial size (for practical reasons). This (historical) formula may seem overly complicated, with three adjustable parameters. A simpler, more elegant form for hyperdiffusivity with self-similarity properties would be

$$\nu(l)=\begin{cases}\nu_0 & \text{for } l\le l_0\\ \nu_0 q^{l-l_0} & \text{for } l\le l_0\end{cases} \quad [10]$$

which has only two independent parameters l_0 and q.

Finally, we want to emphasize that such an approach must be used with care, as it has been shown to have significant effect on the dynamics (Grote et al., 2000).

8.06.4.2 Large Eddy Simulations

Attempts have been made to apply models of hydrodynamic turbulence to model the subgrid scales of the peculiar turbulence occurring inside the Earth's core. A rather successful model is the large eddy simulations (LESs) using a similarity model, where the energy transfer due to the interaction with smaller, unresolved scales is estimated by the transfer that actually occurs between the small but resolved scales of the simulation (e.g., Lesieur, 2008). This has the huge advantage over the eddy-diffusivity technique that it can capture the anisotropic nature of transfer between scales. Although the idea seems interesting, these LES models are still in an early development stage. Indeed, they are constantly compared with higher-resolution DNS, and there are many important tunable parameters (e.g., Buffett, 2003; Chen and Jones, 2008; Matsui and Buffett, 2012). Furthermore, the DNS that they are compared with are far from the dynamical regime expected in the Earth. The presence of boundaries, where turbulence is no more homogeneous, is also a difficulty for LES models.

Currently, LES can be useful to run simulations over a long time period, where the corresponding DNS is feasible but slower. By comparing with a short-term DNS and tuning the subgrid-scale model to reproduce it, we can then trust the LES model for the long-term simulation.

A greater challenge for these models is to actually predict rather than reproduce, which would be a major breakthrough, but it is not clear whether or not they will ever succeed. A key to success might be to ensure that the smallest resolved scales are actually in the low Rm regime, where the self-similar hypothesis is more likely to hold.

8.06.5 Equations, Timescales, and Length Scales

8.06.5.1 Equations

The velocity field $\boldsymbol{u}$ describing the flow of the Earth's liquid core of density ρ is governed by the Navier–Stokes equation including the Coriolis force (due to the rotation rate Ω of the planet), the Lorentz force, and the buoyancy force. It is supplemented with the mass-conservation equation, simplified in the anelastic framework (Gilman and Glatzmaier, 1981; see Chapter 8.03):

$$\partial_t\boldsymbol{u}+(\boldsymbol{u}\cdot\boldsymbol{\nabla})\boldsymbol{u}+2\boldsymbol{\Omega}\times\boldsymbol{u}=-\boldsymbol{\nabla}\Pi+C\boldsymbol{g}+(\boldsymbol{B}\cdot\boldsymbol{\nabla})\boldsymbol{B}/\rho\mu_0+\nu\nabla^2\boldsymbol{u} \quad [11]$$

$$\boldsymbol{\nabla}\cdot(\rho\boldsymbol{u})=0 \quad [12]$$

where Π is a reduced pressure including other potential forces (such as the centrifugal force and magnetic pressure). The evolution of the divergence-free magnetic field $\boldsymbol{B}$ in this liquid metal is governed by the induction equation:

$$\partial_t \boldsymbol{B} + (\boldsymbol{u}\cdot\boldsymbol{\nabla})\boldsymbol{B} = (\boldsymbol{B}\cdot\boldsymbol{\nabla})\boldsymbol{u} + \eta\nabla^2\boldsymbol{B} \quad [13]$$

$$\boldsymbol{\nabla}\cdot\boldsymbol{B} = 0 \quad [14]$$

The evolution of the buoyancy is less well known, as it originates from both chemical and thermal variations, which have different diffusivities. As we are not focusing on the energy injection mechanism details, we can use a single codensity C, with a specified volumetric source term S:

$$\partial_t C + (\boldsymbol{u}\cdot\boldsymbol{\nabla})C = \kappa\nabla^2 C - S \quad [15]$$

There are assumptions behind these equations that we would like to make explicit. For simplicity, the diffusive terms are written as a simple Laplace operator, which implies a homogeneous diffusivity. As the diffusivities are very small, these terms are important only at small scales, while we expect the variations of the diffusivity coefficient to be moderate over the depth of the core. The codensity formulation hides the difference between thermal and chemical diffusivities.

These equations must be completed by boundary conditions. Boundary conditions are important and can control the dynamical state of the system (see, e.g., Sakuraba and Roberts, 2009), but they are thought to have only an indirect effect on the small-scale turbulence.

8.06.5.2 Ordering of Forces in the Earth's Core

For the Earth's core, the order of magnitude of the different terms can be evaluated. We will focus on the scale dependence of this ordering that may help to understand the dynamics of the small scales. From the inversion of the geomagnetic secular variations (see Chapter 8.04), we have an estimate of the large-scale velocity field at the core surface: $U \sim 15$ km year$^{-1} \sim 5\times10^{-4}$ m s^{-1}. More recently, the observation of torsional oscillations by Gillet et al. (2010) has given us an estimate of the magnetic field strength deep inside the core ($B_0 \sim 3\times10^{-3}$ T). The buoyancy force drives the system, but it is hard to assess its strength and compare it to other forces. Indeed, convection tends to smooth the codensity through mixing. We will rather focus on the velocity and magnetic fields as a result from this buoyancy and try to understand how they organize at various scales.

For doing so, we build ℓ-scale dimensionless numbers, which compare the weight of the various terms of the equations at a typical length scale ℓ. This length scale can be related to the wave number k in a Fourier decomposition by $\ell = 2\pi/k$. We find it convenient to express these numbers as ratios of characteristic times, which are functions of ℓ. For example, diffusive phenomena will have timescale τ and length scale ℓ related by

$$\tau_\nu(\ell) = \ell^2/\nu \quad [16]$$

where we have picked here the diffusion of momentum, governed by the kinematic viscosity ν. We can thus define an ℓ-scale *Reynolds number*

$$Re(\ell) = \frac{u(\ell)\ell}{\nu} = \frac{\tau_\nu(\ell)}{\tau_u(\ell)}$$

which compares advection to diffusion of momentum at the ℓ-scale. Other relevant times are listed in Table 1 and will be introduced in the coming sections, while ℓ-scale dimensionless numbers are listed in Table 2.

Table 1 Characteristic times at length scale ℓ

Notation	*Expression*	*Description*
$\tau_\nu(\ell)$	ν^2/ν	Viscous time
$\tau_\eta(\ell)$	ℓ^2/η	Magnetic diffusion time
$\tau_\kappa(\ell)$	ℓ^2/κ	Thermal diffusion time
$\tau_D(\ell)$	ℓ^2/D	Compositional diffusion time
$\tau_\rho(\ell)$	$\sqrt{\frac{\ell}{g}\frac{\rho}{\lvert\Delta\rho\rvert}}$	Buoyancy time
t_Ω	$1/\Omega$	Rotation time (independent of ℓ)
$\tau_{\text{Rossby}}(\ell)$	$r_o/\Omega\ell$	Rossby wave propagation time/ bidimensionalization time
$\tau_{\text{Alfvén}}(\ell)$	$\ell\sqrt{\rho\mu_0}/B_0$	Alfvén wave propagation time (large-scale magnetic field)
$\tau_u(\ell)$	$\ell/u(\ell)$	Eddy turnover time, regime-dependent
$\tau_b(\ell)$	$\ell\sqrt{\rho\mu_0}/b(\ell)$	Alfvén wave collision time, regime-dependent

Symbols and properties as defined in Chapter 8.01 – ρ, ν, k, D, and η (noted λ in Chapter 8.01) – are, respectively, the density, kinematic viscosity, thermal diffusivity, compositional diffusivity, and magnetic diffusivity of liquid iron at core conditions. r_o is the radius of the outer core, g is the gravity, Ω is the angular velocity of the Earth, and B_0 is the intensity of the large-scale magnetic field inside the core. $u(\ell)$ and $b(\ell)$ are the eddy turnover time and magnetic field intensity at length scale ℓ, respectively, which we try to determine for various turbulence scenarios.

8.06.5.2.1 Coriolis force

The ℓ-scale *Ekman number*

$$E(\ell) = \frac{\nu}{\ell^2\Omega} = \frac{t_\Omega}{\tau_\nu(\ell)}$$

compares viscous forces to the Coriolis force. It is the ratio of the rotation time t_Ω over the viscous diffusion time $\tau_\nu(\ell)$. This number is tiny at large scales and reaches unity for scales comparable to the laminar Ekman layer thickness, estimated to be less than a meter in the Earth's core. It is unlikely that turbulence reaches such small scales, because dissipation would be too large (see Section 8.06.6). This means that the Coriolis force is important at every scale, including the dissipative scales.

The ℓ-scale *Rossby number*

$$Ro(\ell) = \frac{u(\ell)}{\ell\Omega} = \frac{t_\Omega}{\tau_u(\ell)}$$

compares eddy entrainment force to the Coriolis force. It is also the ratio of the rotation time over the eddy turnover time at length scale ℓ. For the scale of the whole core, we have $Ro_0 \sim 10^{-6}$, a small value showing the predominance of the Coriolis force at large scales, which will eventually decrease toward smaller scales (if we assume that $u(\ell)/\ell$ increases as ℓ decreases). Depending upon the evolution of the typical velocity $u(\ell)$ with scale ℓ, it may or may not reach values of the order of one or more, which would mark a transition from rotation-dominated turbulence to 3-D turbulence.

Table 2 ℓ-*scale* dimensionless numbers

Notation	*Expression*	*Time ratio*	*Description*
$Re(\ell)$	$\frac{u(\ell)\ell}{\nu}$	$\frac{\tau_\nu(\ell)}{\tau_u(\ell)}$	Reynolds number
$E(\ell)$	$\frac{\nu}{\ell^2\Omega}$	$\frac{t_\Omega}{\tau_\nu(\ell)}$	Ekman number
$Ro(\ell)$	$\frac{u(\ell)}{\Omega\ell}$	$\frac{t_\Omega}{\tau_u(\ell)}$	Rossby number
$Rm(\ell)$	$\frac{u(\ell)\ell}{\eta}$	$\frac{\tau_\eta(\ell)}{\tau_u(\ell)}$	Magnetic Reynolds number
$n(\ell)$	$\frac{b^2(\ell)}{\rho\mu_0 u^2(\ell)}$	$\frac{\tau_u^2(\ell)}{\tau_b^2(\ell)}$	Interaction parameter (small-scale magnetic field)
$N(\ell)$	$\frac{B_0 b(\ell)}{\rho\mu_0 u^2(\ell)}$	$\frac{\tau_u^2(\ell)}{\tau_{\text{Alfven}}(\ell)\tau_b(\ell)}$	Interaction parameter (large-scale magnetic field)
$\Lambda(\ell)$	$\frac{b(\ell)B_0}{\rho\mu_0 u(\ell)\Omega\ell}$	$\frac{\tau_u(\ell)t_\Omega}{\tau_b(\ell)\tau_{\text{Alfven}}(\ell)}$	Elsasser number
$Lu(\ell)$	$\frac{\ell B_0}{\eta\sqrt{\rho\mu_0}}$	$\frac{\tau_\eta(\ell)}{\tau_{\text{Alfven}}(\ell)}$	Lundquist number
$\lambda(\ell)$	$\frac{B_0}{\sqrt{\rho\mu_0}\Omega\ell}$	$\frac{t_\Omega}{\tau_{\text{Alfven}}(\ell)}$	Lehnert (or magnetic Rossby) number
$Ra(\ell)$	$\frac{(-\Delta\rho/\rho)g\ell^3}{\kappa\nu}$	$\frac{\tau_\kappa(\ell)\tau_\nu(\ell)}{\tau_\rho^2(\ell)}$	Rayleigh number
Pr	ν/κ		Prandtl number (independent of ℓ)
Pm	ν/η		Magnetic Prandtl number (independent of ℓ)

One recovers the classical expression of these numbers at the integral scale r_o by setting $\ell = r_o$. These numbers are also expressed as ratios of characteristic ℓ – scale times, which are defined in **Table 1**.

8.06.5.2.2 Magnetic induction

The ℓ-scale *magnetic Reynolds number*

$$Rm(\ell) = \frac{u(\ell)\ell}{\eta} = \frac{\tau_\eta(\ell)}{\tau_u(\ell)}$$

compares magnetic induction to magnetic diffusion in the induction equation. Evaluated at the largest scale, we have $Rm_0 \sim 10^3$, meaning that a dynamo could take place in the Earth's core. At such scales, the magnetic field has a dynamics of its own and is not a slave of the velocity field. $Rm(\ell)$ decreases with decreasing scale, and when it drops below unity, the magnetic field evolution will be mostly dissipative.

The ℓ-scale *interaction parameter*

$$n(\ell) = \frac{b^2(\ell)}{\rho\mu_0 u^2(\ell)} = \frac{\tau_u^2(\ell)}{\tau_b^2(\ell)}$$

is the ratio of the Lorentz force to the inertial force. When there is a dominant large-scale magnetic field B_0, one can define another interaction parameter:

$$N(\ell) = \frac{B_0 b(\ell)}{\rho\mu_0 u^2(\ell)} = \frac{\tau_u^2(\ell)}{\tau_{\text{Alfven}}(\ell)\tau_b(\ell)}$$

At the largest scale, the ratio of magnetic energy to kinetic energy $N_0 = n_0 \sim 10^4$, which means that the inertial forces are negligible compared with the Lorentz force at large scales.

In small Rm MHD turbulence, the magnetic field is a slave of the velocity field, and the Lorentz force is a linear term. When the magnetic Reynolds number is large, the magnetic field is not a slave of the velocity field and has its own dynamics. Then, the Lorentz force is truly a nonlinear term of the system, and the nonlinear transfer of energy between scales can happen through the Lorentz force. When both the interaction parameters $N(\ell)$ and $Rm(\ell)$ are large, we argue that the nonlinear transfer of energy between scales is dominated by the Lorentz force, while the inertial force plays a negligible role.

At length scales ℓ where $Rm(\ell)$ is small, the induction equation provides an estimate of $b(\ell) \sim u(\ell)B_0\ell/\eta$, where B_0 is the large-scale magnetic field. One can thus build a small-scale interaction parameter $N(\ell \to 0) \sim \ell B_0^2/\eta\rho\mu_0 u(\ell)$. If $Rm(\ell) < 1$, we also have $u(\ell) < \eta/\ell$, so that $N(\ell \to 0) > \ell^2 B_0^2/\eta^2\rho\mu_0 \sim \tau_\eta^2(\ell)/\tau_{\text{Alfvén}}^2(\ell)$. Applying these relations to the Earth's core, we find that $N > 1$ for $\ell > 30$ m. The transition from nonlinear energy transfer dominated by the Lorentz force to an energy transfer dominated by advection may occur at a larger scale than this conservative estimate, but we can safely advocate that most of the nonlinearity of the core dynamics is due to the Lorentz force.

8.06.5.2.3 Lorentz versus Coriolis

We can also compare the Coriolis and Lorentz forces, forming the *Elsasser number*:

$$\Lambda(\ell) = \frac{b(\ell)B_0}{\rho\mu_0 u(\ell)\Omega\ell} = \frac{\tau_u(\ell)t_\Omega}{\tau_b(\ell)\tau_{\text{Alfven}}(\ell)}$$

The large-scale estimate of this ratio gives $\Lambda_0 \sim 0.01$. At scales sufficiently small where $Rm(\ell) < 1$, the low Rm estimate of $b(\ell)$ gives an Elsasser number independent of the length scale: $\Lambda(\ell \to 0) = B_0^2/\rho\mu_0\eta\Omega \sim 10$. This means that the Coriolis force clearly dominates at large scales but progressively yields to the Lorentz force at small scales.

Using the small Rm expression of $\Lambda(\ell)$ in a dynamo regime is inappropriate and results in wrong estimates of the importance of Lorentz and Coriolis forces (Soderlund et al., 2012).

8.06.5.3 Waves and Transients

A thorough description of waves that can propagate in the Earth's core is given in Chapter 8.09. If we leave aside sound waves (or seismic waves), there are several other waves that can propagate in our system. First of all, the strong influence of global rotation Ω allows *inertial waves* to exist. They are anisotropic and dispersive, and their group velocity $V_\Omega \sim \Omega\ell$ depends on the length scale ℓ measured in a plane perpendicular to the rotation axis. The propagation of energy by inertial waves occurs mainly along the rotation axis (Davidson et al., 2006), leading to the formation of structures elongated along the rotation axis. The Rossby number, which we have already introduced, also measures the ratio of fluid velocity to inertial wave group velocity.

The presence of the magnetic field allows *Alfvén waves*. Discovered theoretically by Alfvén (1942), these waves couple the velocity field and the magnetic field (see Chapter 8.09). Following the analysis of Tobias et al. (2013), we consider a region at rest with a uniform and constant magnetic field $\boldsymbol{B}_0$. Introducing the Elsasser variables $z^{\pm} = \boldsymbol{u} \pm \boldsymbol{b}/\sqrt{\rho\mu_0}$, where $\boldsymbol{u}$ and $\boldsymbol{b}$ are the velocity and magnetic fluctuations, respectively, the Navier–Stokes and induction equations can be combined to yield

$$(\partial_t \mp \boldsymbol{V}_A \cdot \boldsymbol{\nabla}) z^{\pm} + (z^{\mp} \cdot \boldsymbol{\nabla}) z^{\pm} = -\boldsymbol{\nabla} P + \frac{1}{2}(\nu + \eta)\nabla^2 z^{\pm} + \frac{1}{2}(\nu - \eta)\nabla^2 z^{\mp} \quad [17]$$

In the absence of dissipation ($\nu = \eta = 0$), eqn [17] describes wave-type motions, which propagate in either directions along the $\boldsymbol{B}_0$ field lines, with the Alfvén wave velocity $\boldsymbol{V}_A = \boldsymbol{B}_0/\sqrt{\rho\mu_0}$. In a uniform magnetic field, these waves are nondispersive so that wave packets of any shape propagate without distortion.

These waves are damped by diffusive phenomena, whose importance is measured by the *Lundquist number*:

$$Lu(\ell) = \frac{B_0 \ell}{\sqrt{\rho\mu_0}(\eta + \nu)} = \frac{\tau_{\eta+\nu}}{\tau_{\text{Alfven}}}$$

which compares the diffusive time to the Alfvén propagation time. In liquid metals, where $\eta \gg \nu$, it reduces to $Lu(\ell) = V_A \ell/\eta = \tau_\eta(\ell)/\tau_{\text{Alfvén}}(\ell)$. When $Lu(\ell) < 1$, Alfvén waves are damped and do not exist anymore. In the Earth's core, we have $Lu_0 \sim 10^5$.

The *Alfvén number*

$$A(\ell) = \frac{u(\ell)\sqrt{\rho\mu_0}}{B_0} = \frac{\tau_{\text{Alfven}}(\ell)}{\tau_u(\ell)}$$

measures the ratio of fluid velocity to Alfvén wave speed. It is always small in the core ($A(\ell) < 0.01$), meaning that these waves are dynamically important, at least in the directions perpendicular to the rotation axis.

The ratio of Alfvén to inertial wave speed has been called the *Lehnert number* by Jault (2008) and is also called the magnetic Rossby number in Chapter 8.03:

$$\lambda(\ell) = \frac{B_0}{\sqrt{\rho\mu_0}\Omega\ell} = \frac{t_\Omega}{\tau_{\text{Alfven}}(\ell)}$$

At large scale, $\lambda_0 \sim 10^{-4}$ means that the Taylor columns can form very rapidly (an effect of inertial wave propagation) before the magnetic field can act on the flow (Gillet et al., 2011; Jault, 2008). Once a Taylor column is formed, it can slowly evolve, driven by buoyancy and/or the Lorentz force. At smaller scale, the time to build the Taylor column increases and the columns start to wither. Stationary flow can also escape this Taylor constraint, forming thermal or magnetic winds.

8.06.5.4 What Should Be Considered a Small Scale?

In view of the previous evaluations, there seems to be two main regimes in the core: the high Rm at large scales and the low Rm at small scales. Based on $Rm(\ell)$, the transition happens at a length scale $\ell \sim 10$ km or larger, depending on how $u(\ell)$ evolves with ℓ.

In the high Rm regime, the Coriolis force dominates and balances buoyancy, leading to strongly anisotropic dynamics, with predominance of tall coherent structures elongated along the direction of the rotation axis. The kinetic energy is efficiently converted to magnetic energy, and the transfer between scales is ensured by both the Lorentz force and the induction equation.

In the low Rm regime, the Lorentz force dominates the Coriolis force, which still remains important. The dynamical structures are anisotropic, strongly influenced by the direction of the local magnetic field. A significant part of the kinetic energy is dissipated through Joule heating, but motion along the magnetic field remains almost dissipationless. The interaction parameter is still large so the inertial terms are unlikely to be important for the energy transfer between scales, which happens mainly through the Lorentz force. This regime is probably well described by low Rm rotating MHD turbulence at high interaction parameter.

In this picture, the buoyancy is merely a shadow that provides the driving force. However, the injection of kinetic energy by buoyancy, which happens presumably at small scales, is of particular interest for this problem. In particular, it means that the large scale is possibly the result of a nonlinear cascade of energy due to the Lorentz force, from small scales to large scales.

The next section will detail the mechanisms and try to paint a broad picture of turbulence in the core from large to small scales.

8.06.6 Turbulent Regimes for the Core

The previous section has shown that the relative importance of the various forces depends upon the length scale considered. In this section, we try to infer the actual turbulent regimes that should take place in the Earth's core. We consider as given the various diffusivities and the size and rotation rate of the core. We further assume that the large-scale flow velocity is known, from secular variation inversions (see Chapter 8.04), and that the magnetic field has a dominant large-scale component, whose typical intensity in the core is also known, from the observed velocity of torsional oscillations (Gillet et al., 2010). The actual values we use are listed in Table 3. The questions we address are the following: At what length scale and timescale is the turbulence regime dominated by rotation? By the magnetic field? Can we infer the evolution of flow velocity and small-scale magnetic field in these different regimes? How much energy is dissipated? What is the balance between viscous dissipation and ohmic dissipation? Which waves can propagate?

We perform this exercise step by step, introducing the various ingredients that affect turbulence.

8.06.6.1 τ–ℓ Regime Diagrams

We introduce a τ–ℓ regime diagram that helps retrieve important properties of turbulence and that we will use as a guide when we investigate the effects of rotation and magnetic field on turbulence. It consists in plotting the timescale τ of the relevant physical phenomena as a function of their length scale ℓ.

Figure 3 shows $\tau(\ell)$ versus ℓ for classical hydrodynamic Kolmogorov turbulence, in a log-log plot. For the sake of

illustration, we have assumed that energy is injected at the integral scale ($\ell = r_o$) at a typical timescale $t_{SV} = 300$ years for flow in the core at this length scale. Let us draw the relevant $\tau_u(\ell)$ turnover time of an eddy of radius ℓ. In Kolmogorov's universal turbulence with its $E(k) \simeq \varepsilon^{2/3} k^{-5/3}$ energy density spectrum, the typical eddy turnover time is given by

Table 3 Properties of the core with their numerical values used to draw the figures, as gathered by Peter Olson Chapter 8.01

Property	*Value*	*Unit*	*Description*
κ	5×10^{-6}	$m^2\ s^{-1}$	Thermal diffusivity
D	10^{-9}	$m^2\ s^{-1}$	Chemical diffusivity
ν	10^{-6}	$m^2\ s^{-1}$	Kinematic viscosity
η	1	$m^2\ s^{-1}$	Magnetic diffusivity
r_o	3.48×10^6	m	Radius of the core
M_o	1.835×10^{24}	kg	Mass of the outer core
t_Ω	1.38×10^4	s	Rotation time of the Earth (i.e., $1/2\pi$ day)
t_{SV}	9×10^9	s	r_o-scale core flow time from secular variation inversion (i.e., $\simeq$300 years)
$t_{Alfvén}$	1.4×10^8	s	r_o-scale torsional Alfvén wave time (i.e., $\simeq$4 years)
P	$<10^{13}$	W	Power dissipated in the core

Note that some properties have large uncertainties (see Chapter 8.01). We also define the spin-up time $t_{spin\text{-}up} = r_o/\sqrt{\nu\Omega} \simeq 13000$ years.

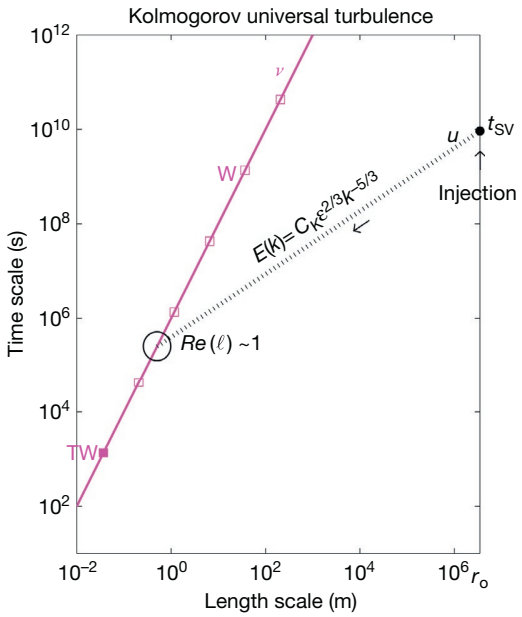

Figure 3 τ–ℓ regime diagram for Kolmogorov's universal hydrodynamic turbulence. Energy cascades from the injection scale (taken here as the integral scale $\ell = r_o$ with timescale $t_{SV} = 300$ years) following Kolmogorov's universal law $\tau_u(\ell) \sim \ell^{2/3} \varepsilon^{-1/3}$ down to the dissipation scale when it intersects the viscous line $\tau_\nu(\ell)$, yielding $Re(\ell) \sim 1$. Viscous dissipation can be read at this intersection point, using values graduated along the $\tau_\nu(\ell)$ line.

$$\tau_u(\ell) \simeq \ell^{2/3} \varepsilon^{-1/3} \qquad [18]$$

since $E(k)k \simeq u^2(\ell)$ and (Note that in this chapter, we will occasionally drop 2π factors and other prefactors for simplicity, since we are mainly dealing with orders of magnitude $k \sim 1/\ell$).

When eddy turnover times are shorter than viscous diffusion time at the same ℓ, fluid motions follow Kolmogorov's cascade downscale until the $\tau_u(\ell)$ line intersects the viscous time line. Intersection points in τ–ℓ regime diagrams correspond to scales at which the regime changes. This intersection corresponds to $Re(\ell) = u(\ell)\ell/\nu \sim 1$, where $Re(\ell)$ is the ℓ-scale Reynolds number, hence the scale at which the regime changes from the inertial range to the diffusive range.

The energy dissipation per unit mass ε is simply deduced from the ratio of the kinetic energy (per unit mass) at this scale divided by the corresponding timescale, yielding $\varepsilon = \ell^2/\tau_\nu^3(\ell) = \nu/\tau_\nu^2(\ell)$. Multiplying by the mass of the liquid outer core $M_o = 1.835 \times 10^{24}$ kg, we obtain the total viscous dissipation, which we have indicated by squares along the $\tau_\nu(\ell)$ viscous line. The squares are a factor of 10^3 apart, and the TW square ($1\ TW = 10^{12}$ W) is filled for reference.

8.06.6.2 Turbulent Convection

Convective motions appear in a fluid layer heated at the bottom and cooled at the top when the temperature gradient is large enough.

8.06.6.2.1 The Rayleigh number

Lord Rayleigh established that the onset of convection is attained when the Rayleigh number Ra_0 reaches a critical value Ra_c, where the Rayleigh number (at the integral scale) is defined as

$$Ra_0 = \frac{(-\Delta\rho/\rho) g r_o^3}{\kappa\nu} \qquad [19]$$

with r_o the thickness of the fluid layer, g the acceleration due to gravity, κ the thermal diffusivity of the fluid, and ν its kinematic viscosity. The $-\Delta\rho/\rho$ term determines the relative density ratio across the layer. It is equal to $\alpha\Delta T$ when the density variations are due to temperature alone, where α is thermal expansivity and ΔT the temperature variation.

It is not so easy to estimate the Rayleigh number in the liquid core, because most of the temperature contrast between the top of the core and its base is due to compression via the equation of state (see Chapter 8.01). This part defines the adiabatic (or isentropic) temperature profile, and only the density variations in excess of it should be included in the $\Delta\rho$ term in the expression of the Rayleigh number. Since heat conducted along the adiabat is large, it is possible that the Rayleigh number is subcritical in part of the core. However, as soon as the density profile departs from the adiabat, the Rayleigh number can get very large.

We will use the τ–ℓ regime diagram of Figure 4 to illustrate this point. One can define a ℓ-scale *Rayleigh number* $Ra(\ell)$ as a thermal diffusion time $\tau_\kappa(\ell)$ times a viscous diffusion time $\tau_\nu(\ell)$ divided by the square of a 'buoyancy time' $\tau_\rho(\ell)$ (which is analogous to the inverse of the buoyancy frequency used in stratified fluids):

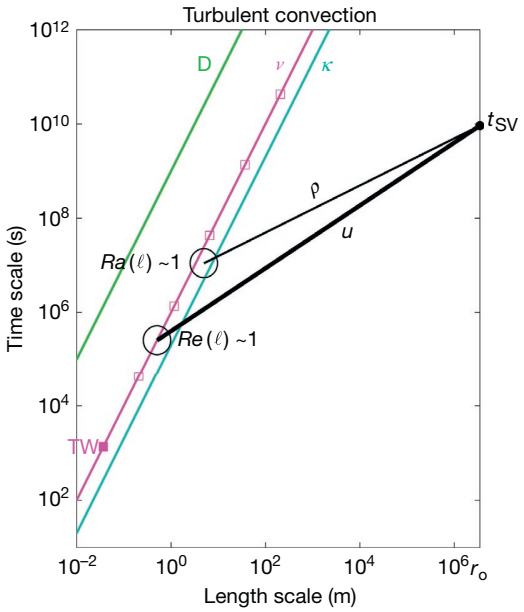

Figure 4 τ–ℓ regime diagram for turbulent thermal convection. The intersection of the 'buoyancy' line $\tau_\rho(\ell)$ with a line at middistance between the viscous line $\tau_\nu(\ell)$ and the thermal diffusion line $\tau_\kappa(\ell)$ defines $Ra(\ell) \sim 1$, where the regime changes from convective at larger scales to diffusive at smaller scales. The $\tau_u(\ell)$ line gives the evolution of the eddy turnover time as a function of ℓ and is here assumed to follow Kolmogorov's law from the integral scale ($\tau_u(r_o) = t_{SV}$) down to the diffusion scale, where the $\tau_u(\ell)$ line intersects the $\tau_\nu(\ell)$ line, yielding $Re(\ell) \sim 1$.

$$Ra(\ell) = \frac{\tau_\kappa(\ell)\tau_\nu(\ell)}{\tau_\rho^2(\ell)} \qquad [20]$$

where $\tau_\rho(\ell) = \sqrt{\frac{\ell}{g}\frac{\rho}{|\Delta\rho|}}$, $\tau_\kappa(\ell) = \ell^2/\kappa$ and $\tau_\nu(\ell) = \ell^2/\nu$.

Using the diffusivities listed in Chapter 8.01 and given again in Table 3, we trace the lines defined by $\tau_\kappa(\ell)$ and $\tau_\nu(\ell)$ in Figure 4.

8.06.6.2.2 Density perturbation

All we know from observations about density perturbations $\Delta\rho/\rho$ is that they are too small to be detected. We pick here a value $\Delta\rho/\rho \simeq 10^{-15}$, which we will justify in the succeeding text, to trace $\tau_\rho(\ell)$. Where $\tau_\rho(\ell)$ is halfway between $\tau_\kappa(\ell)$ and $\tau_\nu(\ell)$ defines the length scale ℓ and corresponding timescale at which $Ra(\ell) \sim 1$. Buoyant fluid parcels with dimensions larger than a few meters will rise with typical rise time of several months. We have also drawn the line $\tau_D(\ell)$ that corresponds to chemical diffusion. We see that chemical (or compositional) convection would start for smaller fluid parcels.

We will see later, when we introduce the role of rotation, that a better value for $\Delta\rho/\rho$ is probably about 10^{-9}. The present value was chosen to be consistent with the hypothesis that large-scale core motions were due to thermal convection, in the absence of rotation and magnetic field. One may then relate the large-scale time t_{SV} to the integral Rayleigh number Ra_0 and thus deduce $\Delta\rho/\rho$. The scaling law for convective large-scale velocity U is not that well known. An ad hoc scaling such as $U \simeq Ra_0^{1/2}\sqrt{\kappa\nu}/r_o$ is not unreasonable in our range of Prandtl and Rayleigh numbers (see Ahlers et al. (2009) for a review) and simply yields $\Delta\rho/\rho \simeq r_o/gt_{SV}^2 \sim 10^{-15}$ and $Ra_0 \simeq \tau_\kappa(r_0)\tau_\nu(r_0)/t_{SV}^2 \sim 10^{17}$.

8.06.6.2.3 Injection and dissipation scales

One could think that the scale ℓ at which $Ra(\ell) \sim 1$ should be the injection scale, in the language of hydrodynamic turbulence. This is not the case in nonrotating convection. Instead, the size of the container appears to be the relevant injection scale, from which energy cascades down to the dissipation scale. More precisely, the classical $k^{-5/3}$ law is retrieved below what is called the Bolgiano scale (after Bolgiano, 1959). The Bolgiano scale appears to be the height of the container in incompressible fluids (Boffetta et al., 2012; Niemela et al., 2000) and the so-called scale height in compressible fluids when the Rayleigh number Ra_0 is larger than 10^{11} (Rieutord and Rincon, 2010). The scale height $H = C_p/\alpha g$ is the height over which density has changed by a factor e under the effect of pressure. In the core, $H \simeq 8900$ km, which is larger than the radius of the core. Therefore, the Bolgiano scale should simply be the radius of the core.

We can then estimate what would be the energy spectrum in the core, if the Earth was not rotating and nonmagnetic. In the τ–ℓ regime diagram of Figure 4, we start from the observed large-scale flow t_{SV} at $\ell = r_o$ and cascade following Kolmogorov's law down to the dissipation scale when the $\tau_u(\ell)$ line intersects the viscous line $\tau_\nu(\ell)$. This happens at a Kolmogorov length scale of about 1 m. We deduce the dissipation per unit mass $\varepsilon = \ell^2/\tau_\nu^3(\ell) = \nu/\tau_\nu^2(\ell) \sim 10^{-17}$ W kg^{-1}, which yields a total viscous dissipation of about 30 MW only.

The idea that buoyancy, which is the driving force of the geodynamo, is available to produce turbulent motions within the core without impeding a specific scale is important to keep in mind.

8.06.6.3 Turbulence in a Rotating Sphere

We have seen in previous chapters that global rotation imposes strong constraints upon flow structures. The Taylor–Proudman theorem implies that the axes of the turbulent eddies are essentially aligned with the axis of rotation of the rotating container. This has led to the idea that turbulence in rotating fluids is essentially two-dimensional. Enabling high-resolution numerical simulations (e.g., Legras et al., 1988) and powerful statistical mechanics approaches (Robert and Sommeria, 1991), 2-D turbulence has been intensively studied early on (Kraichnan and Montgomery, 1980). In the absence of dissipation and forcing, two-dimensionality results in the conservation of the total enstrophy (the integral of the squared vorticity $\int \omega^2$), thereby modifying the classical Kolmogorov cascade into a double cascade: an inverse cascade of energy from the injection scale up to larger length scales with a spectral energy density spectrum $E(k) \sim k^{-5/3}$ and a direct cascade of enstrophy from the injection scale down to smaller length scales with $E(k) \sim k^{-3}$.

However, in a layer at the surface of a rotating sphere, such as the atmosphere, there is an essential difference: strong zonal motions can appear, which are fed by the eddies. Indeed, vortices that move away from the axis of rotation experience a reduction of the Coriolis force, which vanishes at the equator.

This limits the extent of eddies in a latitudinal direction and leads to quasi-geostrophic vortices. On the contrary, azimuthal velocities, which follow geostrophic contours, encounter no resistance, except for viscous friction in the Ekman layers that form at the boundary. These phenomena are nicely displayed in the atmosphere of giant planets, such as Jupiter and Saturn, where strong alternating azimuthal jets circle the planet, entraining and shearing quasi-geostrophic vortices.

Similarly, in a thick layer such as the liquid outer core, columnar vortices that move away from the axis of rotation impinge on the bounding spherical shell. There, the non-penetration condition implies that the velocity component aligned with the cylindrical radius coordinate must convert into a velocity component aligned with the rotation axis, plunging toward the equator from both sides. Such a flow violates the Taylor–Proudman theorem and is therefore inhibited, while azimuthal (zonal) flows are not affected.

Let us examine the τ–ℓ regime diagram of Figure 5 to get a sense of the modifications brought up by rotation in the context of core turbulence. One new timescale stands out: the rotation time of the Earth t_Ω (i.e., $1/2\pi$ day). The intersection of the $\tau_\nu(\ell)$ viscous line with t_Ω defines the thickness of the Ekman layer $\delta_E = \sqrt{\nu/\Omega}$, where Ω is the angular velocity of the Earth. The Ekman layer is about 0.1 m thick. We also introduce the spin-up time $t_{\text{spin-up}} = r_o/\sqrt{\nu\Omega} \simeq 13\,000$ years and draw it in Figure 5. The spin-up time is the time it takes for the core to adjust to a change in the angular velocity of the mantle through viscous coupling, that is, the time it takes for the whole fluid to circulate through the Ekman layer.

8.06.6.3.1 Bidimensionalization and Rossby waves

Inertial waves have periods longer than half a day. They are responsible for implementing the Taylor–Proudman constraint on the flows. Flows at timescales shorter than half a day will not be bidimensionalized. In fact, a blob of vorticity of size ℓ grows into a bidimensional column at a speed equal to $\Omega\ell$ (Davidson, 2013). This means that it takes only a few days for such a blob to convert into an elongated vorticity column, say, ten times longer than wide, whatever the value of ℓ. In a thin layer such as the atmosphere or the ocean, the columns rapidly extend across the entire layer.

However, it is important to realize that in a thick layer such as the liquid outer core, the time required for such a column to reach the core–mantle boundary is given by $\tau_{\text{Rossby}}(\ell) = r_o/\Omega\ell$. The corresponding line is drawn in Figure 5. We have labeled it as the Rossby line, because it also roughly corresponds to the time it takes for a Rossby wave of azimuthal wavelength ℓ to propagate one wavelength. Indeed, the expression of the pulsation of a Rossby wave, as recalled in Chapter 8.09, reads

$$w_{\text{Rossby}} = -2\Omega\frac{\beta k_\varphi}{k^2}$$

with $\beta = \alpha/H_c$, where α is the slope of the spherical shell and H_c the height of the quasi-geostrophic column and k is the wave number of the Rossby wave. Approximating $\alpha \sim 1$ and $H_c \sim r_o$ at midlatitudes and $k \sim k_\varphi$, we retrieve $\tau_{\text{Rossby}}(\ell) \sim r_o/\Omega\ell$.

Above the Rossby line, columns extend across the entire core: motions are quasi-geostrophic (QG). Assuming that ℓ now defines the diameter of the columnar eddies in the equatorial plane, the viscous line $\tau_\nu(\ell)$ is unchanged. However, viscous friction is also present at the ends of the column. There, the velocity drops to zero at the rigid core–mantle boundary. The velocity drop takes place across an Ekman layer of thickness δ_E, thin enough for viscous forces to balance the Coriolis force. The dissipation per unit mass due to viscous friction at the ends of the columns can be written

$$\varepsilon_{QG} = \frac{\ell^2}{\tau_u^2(\ell)\, t_{\text{spin-up}}} \qquad [21]$$

The intersection of the viscous line $\tau_\nu(\ell)$ with the spin-up time marks the length scale at which friction on the walls of a column equals friction at its ends. It occurs for a length $\ell = r_o E_0^{1/4}$, where $E_0 = \nu/\Omega r_o$ is the Ekman number at the integral scale.

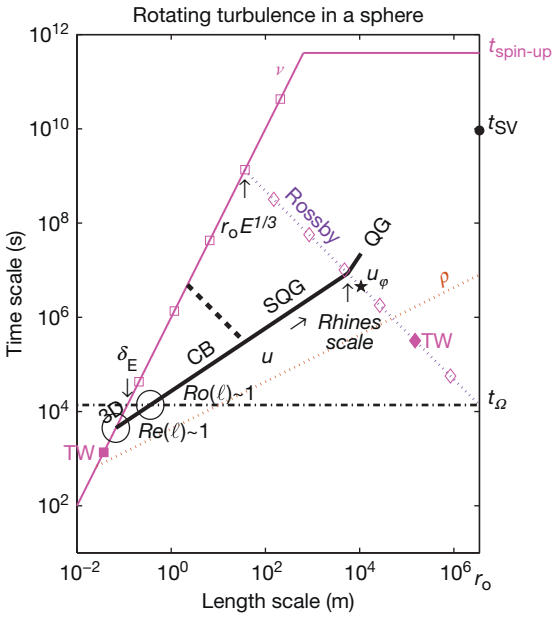

Figure 5 τ–ℓ regime diagram for rotating turbulence in a spherical shell. Rotation yields a specific timescale: t_Ω (dash-dot horizontal line). Its intersection with the viscous line (magenta) yields the Ekman boundary layer thickness δ_E. We also draw a horizontal line for the spin-up time $t_{\text{spin-up}} = r_o/\sqrt{\nu\Omega}$. The dotted line labeled 'Rossby' represents the time $\tau_{\text{Rossby}}(\ell)$ it takes for a Rossby wave to propagate one wavelength ℓ. Its intersection with the viscous line occurs for $\ell = r_o E^{1/3}$, which is the width of convective columns at the onset of convection. The brown dotted line labeled ρ represents the buoyancy line $\tau_\rho(\ell)$. The u_φ star on the Rossby line marks the width (Rhines scale) and velocity of the zonal jets that would make a turn round the Earth in time t_{SV}. The black solid line is the eddy turnover time $\tau_u(\ell)$ line of nonzonal eddies that we infer, starting from the Rhines scale in the quasi-geostrophic (QG) regime. It becomes semi-quasi-geostrophic (SQG) and follows Kolmogorov's slope after crossing the Rossby line and might enter critical balance (CB) at scales smaller than the injection scale (here taken as $r_o E^{1/3}$). The intersection with t_Ω defines $Ro(\ell) \sim 1$. Turbulence becomes three-dimensional (3-D) below the t_Ω line. The intersection with the viscous line defines $Re(\ell) \sim 1$ and provides the amount of viscous dissipation. Viscous dissipation of the zonal and quasi-geostrophic flows occurs in the Ekman layers and is read on the Rossby line, where diamonds are a factor of 10^3 apart, and the terawatt diamond is filled for reference.

We expect that turbulent motions whose timescale and length scale fall in the triangle bounded by the three lines $t_\Omega - \tau_\nu - \tau_{\text{Rossby}}$ will be strongly influenced by rotation with elongated eddies aligned with the rotation axis (z-axis). Those above the $\tau_{\text{Rossby}}(\ell)$ line will be quasi-geostrophic (QG) columnar vortices extending all the way across the liquid core. We find it logical to evaluate on the Rossby line the viscous dissipation due to quasi-geostrophic and zonal motions since below this line, columns will not necessarily reach the surface Ekman layers. QG and zonal flow viscous dissipation $M_o \varepsilon_{QG}$ is thus graduated with diamonds on the Rossby line. The diamonds are a factor of 10^3 apart, and the TW diamond ($1\ \text{TW} = 10^{12}$ W) is filled for reference.

8.06.6.3.2 Zonal flows and potential vorticity

We have seen that truly geostrophic motions (i.e., zonal (or azimuthal) motions in a sphere or a spheroid) behave in a specific way. In contrast to nonaxisymmetric motions, they get organized in winds or jets of a given width. Their lifetime can be extremely long, and they often carry the largest part of the kinetic energy of the flow. Clearly, these bands will limit the maximum size that QG columns can achieve, since they are separated by what appears to be strong barriers. There has been much debate on the origin and characteristics of these bands. One idea has become quite successful, which assesses that bands are the expression of the mixing of potential vorticity (PV) in a staircase fashion (Dritschel and McIntyre, 2008). PV q defined by $q = (w_z + 2\Omega)/H_c$ is an important quantity in rotating fluids because it is conserved when advected by a columnar flow (w_z being the z-component of the vorticity in the rotating frame and H_c the height of the column), when viscous effects are ignored. In a stratified medium with linear density profile, mixing produces a stack of layers in which the density is fairly homogeneous. These layers remain isolated from each other because the sharp density jump across their borders acts as a barrier for small density fluctuations (Phillips, 1972). It is believed that something very similar happens for PV in a rotating fluid in a sphere.

The conservation of PV is also at the origin of Rossby waves. As a column of fluid at rest (outside the cylinder tangent to the inner core) moves away toward the mantle, its height decreases. In order to conserve PV, the column acquires a negative vorticity (in the rotating frame). The opposite holds for a column moving toward high latitude. Both contribute to a prograde, that is, eastward, motion. This wave motion is called a Rossby wave. Note that in shallow layers such as the ocean or atmosphere at the surface of a rotating planet, Rossby waves propagate westward because the planetary vorticity gradient has the opposite sign. The velocity of Rossby waves increases when their wave number decreases. We have drawn the line $\tau_{\text{Rossby}} = r_o/\Omega\ell$ as representing the timescale versus length scale signature of Rossby waves in the τ–ℓ regime diagram of Figure 5.

The intersection of the Rossby line $\tau_{\text{Rossby}}(\ell)$ with the eddy turnover time $\tau_u(\ell)$ defines a Rhines length scale ℓ_{Rhines} while its intersection with the viscous line $\tau_\nu(\ell)$ provides the length scale of thermal Rossby waves $r_o E_0^{1/3}$, which appear at the threshold of convection (Busse, 1970; Jones et al., 2000). The Rhines scale describes how the sphericity of the core stops the inverse cascade of energy from small-scale vortices.

8.06.6.3.3 Possible turbulent regimes

Let us now try to infer what would be the different turbulent regimes encountered in the core if it was nonmagnetic but rotating. Starting from the 'observed' timescale t_{SV} at the largest length scale r_o, we run into a problem: there should be no motion at this scale, since the maximum diameter of columnar eddies is set by the width of zonal bands. We should therefore reinterpret t_{SV} as the typical time a zonal jet takes to circle once around the core. This sets its velocity $u_\varphi = 2\pi r_o/t_{SV}$, which enters the definition of the Rhines scale: $\ell_{\text{Rhines}} \sim \sqrt{u_\varphi r_o/\Omega}$ (Dritschel and McIntyre, 2008). We assume that this defines the width of the zonal jets. The corresponding viscous dissipation can be read on the Rossby line. Guided by observations of the atmosphere of Jupiter, we further assume that the velocity of the eddies at the same scale (their maximum size) will be five times smaller, thus defining the starting point of the turbulent regime diagram we want to construct. Note that actual large-scale zonal velocities are similar to nonzonal velocities in the Earth's core (Hulot et al., 2002; Pais and Jault, 2008) (see the Chapter 8.04).

Above the Rossby line, these eddies are columns extending all the way across the core. The dissipation of these QG vortices can be read at the intersection of the $\tau_u(\ell)$ line with the Rossby line. It is always smaller than that of the zonal jets (because we have assumed eddies have smaller velocities than jets). The inverse energy cascade yields a Kolmogorov-like law for $\tau_u(\ell)$ in that regime. Below the Rossby line, vortices are still very much elongated in the z-direction, but they do not necessarily extend all the way across the core. We label this regime SQG for semi-quasi-geostrophic. In 2-D turbulence, the conservation of enstrophy modifies the turbulent cascade: energy cascades from the injection scale upscale to the largest possible scale (the inverse energy cascade), while enstrophy cascades downscale.

8.06.6.3.4 Below the injection scale

What is the injection scale in our case? Near the onset of convection, it would be the length scale of thermal Rossby waves $r_o E_0^{1/3}$ (Busse, 1970). However, when strong zonal winds are present, they certainly inject energy and enstrophy at their (larger) scale. 2-D turbulence scenarios and quasi-geostrophic numerical models predict a strong decrease of energy for scales below the injection scale. The thick dashed line in Figure 5 displays what would be the τ_u line in the case of an energy spectrum $E(k) \sim k^{-5}$. However, we have seen that rotating turbulence was not strictly 2-D in this regime (below the Rossby line). It has been recently proposed by Nazarenko and Schekochihin (2011) that the flow reaches a 'critical balance' (CB) in this regime that sees the columns progressively shrink in length until 3-D turbulence is reached at $Ro(\ell) \sim 1$ (at the intersection of the $\tau_u(\ell)$ and t_Ω lines). This is what we have drawn in Figure 5, keeping Kolmogorov's slope all the way down to the dissipation scale ($Re(\ell) \sim 1$), where the remaining viscous dissipation can be read.

Note that in our scenario, the $\tau_u(\ell)$ line barely gets below t_Ω, meaning that turbulence remains influenced by rotation almost down to the dissipation scale. Also, note that the total viscous dissipation (zonal and QG plus SQG) is now of the order of 100 GW, compared with 30 MW in the absence of

rotation. As rotation inhibits convection, a larger energy input and larger buoyancy forces are needed to provide the velocities we observe. The $\Delta\rho/\rho$ term can be estimated here by assuming a balance between the buoyancy and the Coriolis forces yielding $\Delta\rho/\rho \simeq 2\Omega r_o/g t_{SV} \sim 10^{-9}$, some six orders of magnitude larger than in the nonrotating case, hence the position of the $\tau_\rho(\ell)$ line in Figure 5.

8.06.6.4 MHD Turbulence

Let us pursue our exercise by building a plausible scenario of turbulence if the core had the magnetic field we observe at large scales but was not rotating.

8.06.6.4.1 Mechanisms of MHD turbulence

Turbulence in the presence of a strong imposed magnetic field is quite different from classical hydrodynamic turbulence. While eddies are the building bricks of hydrodynamic turbulence, it is believed that Alfvén waves are those of magnetohydrodynamic turbulence (Tobias et al., 2013), at least as long as fluid velocities are smaller than the Alfvén speed ($u(\ell) < V_A$) and the Lundquist number is large $Lu(\ell) \gg 1$. In a uniform magnetic field, these waves are nondispersive so that wave packets of any shape propagate without distortion. However, the collision of counterpropagating Alfvén waves does produce some distortion as the waves then propagate along modified field lines. These collisions produce smaller scales to which energy cascades down without dissipation, just like in classical hydrodynamic turbulence, until the dissipation scale is reached. Indeed, the half-sum and half-difference of the energies E^+ and E^- of the Elsasser variables correspond, respectively, to the total energy and cross helicity $\int u \cdot b$, which are both conserved in ideal incompressible MHD.

Two regimes have been identified: weak turbulence, in which the linear term $(V_A \cdot \nabla) z^\pm$ of eqn [17] dominates over the nonlinear term $(z^\mp \cdot \nabla)\, z^\pm$, and strong turbulence when the opposite holds. In weak turbulence, it takes several collisions of wave packets for energy to cascade to smaller scales and the energy spectral density is inferred to scale as $E(k) \sim k^{-2}$, while nonlinear collisions in strong turbulence are more efficient in that respect, yielding $E(k) \sim k^{-3/2}$. The transition occurs when the Alfvén wave collision time $\tau_b(\ell)$ is of the same order as the large-scale Alfvén wave time $t_{Alfvén}$. Turbulence always gets strong at short length scales. Note that in both cases, one expects an equipartition of energy between the velocity and magnetic fluctuations since Alfvén waves are in equipartition. It is also important to realize that the cascade is for length scales perpendicular to the direction of the guide field $\boldsymbol{B}_0$: the wave packets retain their along-field shape. As a consequence, the wave packets become more and more elongated in the guide field direction, somewhat like vortices are elongated along the rotation axis in rotating turbulence, except that the effect gets larger as the length scale gets smaller, in contrast to the rotating case.

8.06.6.4.2 Two scenarios of MHD turbulence

Let us try to sketch the turbulent regimes a magnetized nonrotating Earth would experience. We will discuss two alternative scenarios and use the τ–ℓ regime diagrams of Figures 6 and 7 as a guide. We again consider that we know the values of the diffusivities and draw a new line for magnetic diffusion as $\tau_\eta(\ell) = \ell^2/\eta$. The large-scale starting point for the velocity field is the same as before, deduced from secular variation core flow inversion. We also assume that we know the intensity of the large-scale magnetic field. Indeed, the recent discovery of torsional waves in the Earth's core (Gillet et al., 2010) provides a profile of the *rms* intensity of the *s*-component of the magnetic field as a function of *s*, where *s* is the cylindrical radius.

We infer a typical intensity of $B_0 = 3$ mT, which translates into a large-scale Alfvén wave velocity $V_A = B_0/\sqrt{\rho\mu_0} \simeq 25$ mms^{-1}. Note that, in fact, the velocity of torsional oscillations depends upon the integral of B_s^2 over azimuth and *z*, so that the contribution of small scales is included in our estimate of B_0. We plot the line $\tau_{Alfvén} = V_A \ell$ in the τ–ℓ regime diagram of Figure 6. At the largest scale ($\ell = r_o$), the corresponding time is about 10^8 s, that is, a few years, some two orders of magnitude smaller that the characteristic time of secular variation. This is just an expression of the fact that magnetic energy is about four orders of magnitude larger than kinetic energy in the Earth's core. Indeed, when expressed in Alfvén velocity, the magnetic field intensity directly compares to flow velocity. The intersection of the $\tau_\eta(\ell)$ and $\tau_{Alfvén}(\ell)$ lines defines the minimum wavelength ℓ Alfvén waves can achieve without being completely dissipated. It corresponds to an ℓ-scale Lundquist number $Lu(\ell) = \tau_\eta(\ell)/\tau_{Alfvén}(\ell) \sim 1$.

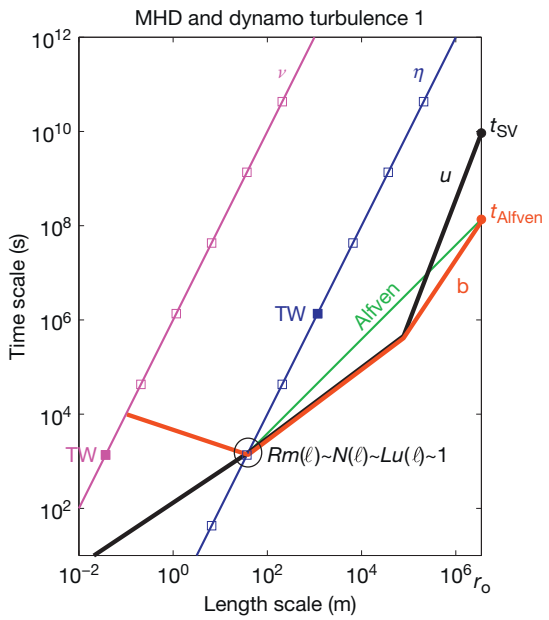

Figure 6 A highly dissipative scenario for magnetohydrodynamic and dynamo turbulence. The timescale of the large-scale magnetic field is $t_{Alfvén}$, deduced from the velocity V_A of torsional oscillations. The green line $\tau_{Alfvén}(\ell)$ gives the time it takes for an Alfvén wave to travel a distance ℓ at this velocity V_A. The red line $\tau_b(\ell)$ measures the strength of the magnetic field at length scale ℓ: it is the characteristic collision time of Alfvén waves. The blue line $\tau_\eta(\ell)$ is the magnetic diffusion line. Ohmic dissipation is graduated with squares along that line. The squares are a factor of 10^3 apart, and the terawatt square is filled. Here, we assume that the τ_u, τ_b, and $\tau_{Alfvén}$ lines all intersect the τ_η line at the same point, where $Rm(\ell) \sim N(\ell) \sim Lu(\ell) \sim 1$, yielding unrealistic ohmic dissipation of millions of TW. The eddy turnover time τ_u continues downscale and intersects the τ_ν line at very small scales, yielding again unrealistic viscous dissipation. This scenario is discarded because it would imply super-Alfvénic velocities.

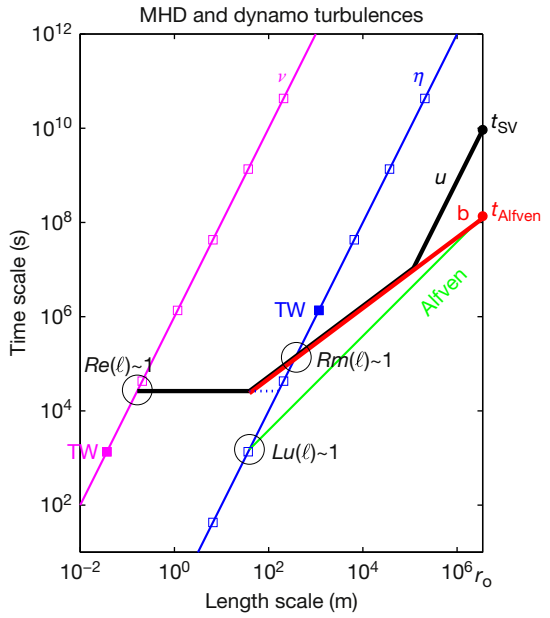

Figure 7 A more realistic scenario for magnetohydrodynamic and dynamo turbulence. In this scenario, we relax the hypothesis that the induction–diffusion balance is achieved at $Rm \sim 1$. Instead, we consider that Alfvén waves can propagate down to a scale ℓ where $Lu(\ell) \sim 1$, that is, at the intersection of the $\tau_\eta(\ell)$ line (blue) with the $\tau_{\text{Alfvén}}(\ell)$ line (green). We assume that the strong turbulence MHD cascade begins at the largest scale r_o. The interaction parameter $N(\ell)$ remains large at all scales, and the flow at small scale is strongly damped by the large-scale magnetic field. Projecting along the blue dashed line yields an ohmic dissipation of about a thousand terawatts, as read on the $\tau_\eta(\ell)$ line.

Where should we plot the lines for the typical velocity field $\tau_u(\ell)$ and for the typical magnetic field $\tau_b(\ell)$ (expressed in Alfvén wave time)? We apply the principles of the MHD turbulence cascade we just described. Assuming equipartition down to the magnetic diffusion scale implies that both the $\tau_u(\ell)$ and $\tau_b(\ell)$ lines should intersect the $\tau_\eta(\ell)$ magnetic diffusion line at the same place in the diagram, which will thus correspond to $Rm(\ell) \sim 1$.

8.06.6.4.3 A highly dissipative scenario

It is then tempting to infer that smaller scales will be in a regime where the small-scale magnetic field results from the diffusion of the magnetic field induced by the interaction of the small-scale velocity field with the large-scale magnetic field. In this diffusive regime, one has $(\boldsymbol{B}_0 \cdot \boldsymbol{\nabla})\boldsymbol{u} \sim \eta \nabla^2 \boldsymbol{b}$, yielding $b \sim uB_0\ell/\eta$, which translates into $\tau_b(\ell) = \tau_{\text{Alfvén}}(\ell)\tau_u(\ell)/\tau_\eta(\ell)$. Since we defined the intersection point by $\tau_u(\ell) = \tau_b(\ell) = \tau_\eta(\ell)$, the intersection should take place where the $\tau_\eta(\ell)$ and $\tau_{\text{Alfvén}}(\ell)$ lines intersect. This intersection thus simultaneously correspond to $Lu(\ell) \sim 1$, $Rm(\ell) \sim 1$, and $N(\ell) \sim 1$, where $N(\ell)$ is the ℓ-scale interaction parameter that measures the effect of the large-scale magnetic field on the velocity field.

At this intersection point, magnetic diffusion takes over and we read the ohmic dissipation $(=M_o\eta/\tau_\eta^2(\ell))$ on the $\tau_\eta(\ell)$ line. It reaches a million terawatts, a value that is clearly unacceptable since no core flux can be larger than our estimate of a total flux from the mantle to the core of 13 TW (see Table 3). The velocity field is probably reduced at this intersection, but what remains should still cascade downscale (Plunian et al., 2013). One can easily check that the interaction parameter decreases as the length scale decreases in this regime, so that hydrodynamic turbulence is recovered with its classical Kolmogorov cascade, as drawn. Figure 6 shows that we finally reach the viscous line $\tau_\nu(\ell)$ for length scales below a millimeter and read a viscous dissipation of a million terawatts again!

There is one problem with this scenario. MHD turbulence above the intersection point at $Rm(\ell) \sim 1$ would be in the strong turbulence regime, for which the energy spectrum is found to be $E(k) \sim k^{-3/2}$ (Tobias et al., 2013), yielding $\tau \sim \ell^{3/4}$, as drawn in Figure 6. This means that the $\tau_u(\ell)$ line is *below* the $\tau_{\text{Alfvén}}(\ell)$ line over a large range of scales, implying that the fluid velocity is larger than the Alfvén speed, which contradicts the hypotheses of Alfvén wave turbulence.

8.06.6.4.4 A more realistic scenario

We thus take into account the latter constraint and require that τ_u and τ_b remain above the Alfvén line. The new scenario we build is drawn in Figure 7. We let the MHD strong turbulence cascade start from the largest scale r_o at time $t_{\text{Alfvén}}$ and assume it goes all the way down to the length scale $\ell \sim \eta\sqrt{\rho\mu_0}/B_0$ for which $Lu(\ell) \sim 1$, at the intersection of the $\tau_\eta(\ell)$ and $\tau_{\text{Alfvén}}(\ell)$ lines. Equipartition is still required, implying that $\tau_u(\ell)$ gets down to times much shorter than t_{SV} to join the $\tau_b(\ell)$ line. We have assumed here a spectrum $E_u(k) \sim k$ for this part, meaning that there is more kinetic energy at small scale than at the integral scale. In contrast with the previous scenario, the interaction parameter $N(\ell) = \tau_u^2(\ell)/\tau_{\text{Alfvén}}(\ell)\tau_b(\ell)$ remains large at all scales, meaning that the large-scale magnetic field strongly influences the flow. Turbulence in the magnetic diffusive regime with a strong applied magnetic field has been explored in laboratory experiments (Alemany et al., 1979). The small scales of the flow are severely damped by the applied magnetic field: the kinetic energy spectrum is $E_u(k) \sim k^{-3}$, which translates into a constant $\tau_u(\ell)$, as drawn in Figure 7. The magnetic energy spectrum is even steeper (not drawn), obeying the induction–diffusion balance. We read an ohmic dissipation of more than a thousand terawatts, which could be much lower though if the strong MHD turbulence spectrum was steeper than $k^{-3/2}$.

Assuming that equipartition at small scale down to the magnetic diffusion scale has a drastic influence on the kinetic and magnetic energy spectra. It is difficult to build scenarios that do not require an unrealistic ohmic dissipation. We will see that rotation can help us recover a more viable scenario.

8.06.6.5 Turbulence in Planetary Cores

The Earth is rotating rather fast. On periods longer than a day, rotation inhibits Alfvén waves (Braginsky, 1970; Jault, 2008). Only geostrophic Alfvén waves, that is, torsional oscillations, are not inhibited. They have indeed been detected in the core (Gillet et al., 2010), and we have used their observed velocity to set our magnetic time $t_{\text{Alfvén}}$ at the integral scale r_o. Quasi-geostrophic Alfvén waves are also possible. But in both cases, the constraint of rotation prevents Alfvén wave collision to be the mechanism by which the magnetic energy cascades down to dissipation.

Using the τ–ℓ regime diagram of Figure 8, let us try to infer what turbulence could look like in the core, taking into account the Earth's rotation and the presence of a strong large-scale magnetic field. The main difference with the previous scenarios is that we do not impose equipartition at small scales. We let the eddy turnover time $\tau_u(\ell)$ decrease with length scale ℓ, assuming a spectrum $E_u(k) \sim k^{-5/3}$ in the dynamo regime. The intersection of the $\tau_u(\ell)$ line with $\tau_\eta(\ell)$ defines the length scale where $Rm(\ell) \sim 1$, below which the flow cannot generate a magnetic field. Below this scale, if the large-scale magnetic field B_0 is dominant, the small-scale magnetic field is obtained by the balance between induction and diffusion and obeys $\tau_b(\ell) = \tau_{\text{Alfvén}}(\ell)\tau_u(\ell)/\tau_\eta(\ell)$. This time, flow velocities remain much lower than Alfvénic speeds. Since $\tau_u(\ell) = \tau_\eta(\ell)$ for $Rm(\ell) \sim 1$, the small-scale magnetic field at $Rm(\ell) \sim 1$ must lie on the Alfvén line. For simplicity, we have thus drawn the $\tau_b(\ell)$ line following the Alfvén line in the dynamo regime.

The interaction parameter $N(\ell) = \tau_u^2(\ell)/\tau_{\text{Alfvén}}(\ell)\tau_b(\ell)$ is very large at all scales, meaning that the large-scale magnetic field strongly influences the flow. Below the scale for which $Rm(\ell) \sim 1$, we thus enter a diffusive regime with a strong applied magnetic field, where Alfvén waves are inhibited by rotation. Following Alemany et al. (1979), we assume a kinetic energy spectrum $E_u(k) \sim k^{-3}$, which translates into a constant $\tau_u(\ell)$, as drawn in Figure 8. The magnetic energy spectrum is even steeper, obeying the induction–diffusion balance.

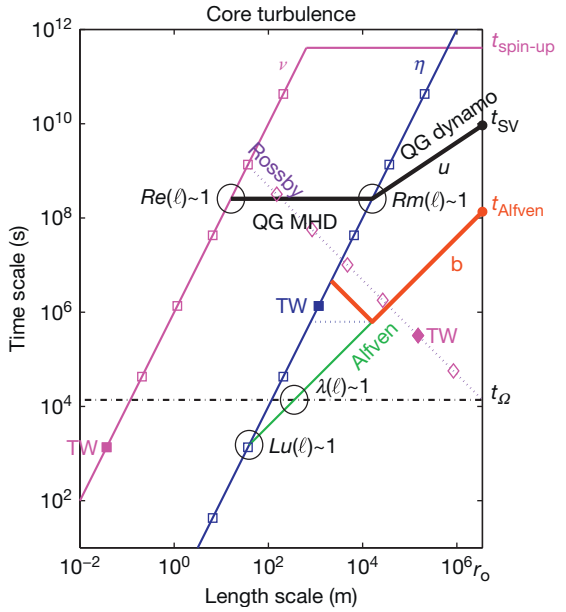

Figure 8 τ–ℓ regime diagram for turbulence in the Earth's core. Both rotation and the magnetic field are taken into account, combining the lines already defined in Figures 5–7. We assume that the kinetic energy density follows a $k^{-5/3}$ law in the quasi-geostrophic dynamo regime. The intersection of the $\tau_u(\ell)$ and $\tau_\eta(\ell)$ lines defines $Rm(\ell) \sim 1$, which marks the transition from the dynamo to the diffusive regime. Quasi-geostrophic (QG) and semi-quasi-geostrophic (SQG) diffusive MHDs govern the following part, with a kinetic energy density spectrum in k^{-3} (yielding a flat $\tau_u(\ell)$ line) and a magnetic energy density spectrum in k^{-5}. Viscous dissipations of the QG (read on the Rossby line) and of the SQG (read on the $\tau_\nu(\ell)$ line) MHD flows amount to a few kilowatts only. Ohmic dissipation is maximum at the length scale ℓ where $Rm(\ell) \sim 1$. Projecting along the blue dashed line yields an ohmic dissipation of a few terawatt, as read on the $\tau_\eta(\ell)$ line. Alfvén waves can be excited and propagate for scales falling on the Alfvén green line between its intersection with t_Ω (which defines $\lambda(\ell) \sim 1$) and that with the magnetic diffusion line (which defines $Lu(\ell) \sim 1$).

Note that in our scenario, the flow is above the Rossby line in the dynamo regime, hence quasi-geostrophic. Most of the nondynamo MHD regime lies above the Rossby line, hence being also quasi-geostrophic (QG). Viscous dissipation can be read along the $\tau_{\text{Rossby}}(\ell)$ line for the quasi-geostrophic MHD flow and on the $\tau_\nu(\ell)$ line for the semi-quasi-geostrophic MHD motions. Both are very small, below the kilowatt range. Ohmic dissipation dominates and mostly occurs at the ℓ-scale where $Rm(\ell) \sim 1$. It can be read along the $\tau_\eta(\ell)$ line, where the dashed blue line intersects, amounting to a few terawatts for the present scenario.

Behind this scenario is the idea that turbulence is very much hindered under the combined constraints of strong magnetic field and fast rotation. The rotating magnetized spherical Couette flow (DTS) experiment provides evidence for this behavior (Nataf and Gagnière, 2008). We end up with a very sluggish core, where the smallest eddies are ten meters in diameter and have turnover times of several years!

Note that the Alfvén line intersects the $\tau_\eta(\ell)$ line below the t_Ω line. This intersection defines $Lu(\ell) \sim 1$, while the intersection of the Alfvén line with the t_Ω line defines $\lambda(\ell) \sim 1$. In that region of the τ–ℓ diagram, it is possible for Alfvén waves to propagate without being hindered by the Earth's rotation (because $\lambda(\ell) > 1$) and without being damped by magnetic diffusion (because $Lu(\ell) > 1$). However, such waves will not be involved in the cascade of energy from large to small scales. Similarly, fluid motions could be excited at timescales shorter than a day (e.g., by tides), but they are not part of the energy cascade.

8.06.7 Summary and Perspectives

Early numerical simulations of the geodynamo have demonstrated the crucial role of rotation in the *generation* of the magnetic field. One of our main messages here is that rotation could also play a key role in limiting the *dissipation* of the magnetic field.

Indeed, the classical scenario of MHD turbulence in the absence of rotation, based on the collision of Alfvén waves, predicts dissipation rates far too large for the core. The constraints brought by rotation prevent Alfvén waves to be the carriers of turbulence. Instead, turbulence gets organized in quasi-geostrophic eddies, strongly elongated along the rotation axis, and strongly damped by the large-scale magnetic field. We end up with a very sluggish core, in which the smallest eddies are ten meters in diameter and have turnover times of several years. The smallest magnetic field structures are even larger, in the kilometer range, but their lifetime might be much shorter (of the order of months). In this scenario, viscous dissipation is negligible, while ohmic dissipation is in the terawatt range. However, one should keep in mind that slightly different scenarios would lead to largely different dissipations.

We note that a planet like Venus, which rotates much more slowly than the Earth (rotation period of 243 days), would not

be in this regime and would not be able to sustain a magnetic field as large as that of the Earth.

The τ–ℓ regime diagram that we introduced is a useful tool for determining the various regimes that can be encountered when going from the large scales down to the dissipative scales. We hope it can guide the construction of appropriate parameterizations of turbulence in LES.

In exploring the various turbulent scenarios, we have noted that key elements were still missing, calling for more experimental and numerical studies. For example, we do not know how to relate quasi-geostrophic and zonal velocities in a convecting sphere. What is the relevant injection scale in these systems? Furthermore, some fundamental differences between the case of the atmosphere of giant planets and that of the core might have been overlooked. Our observation that the time required for a Taylor column to grow and extend across the core is comparable with the propagation time of a Rossby wave questions the validity of quasi-geostrophic modeling of small scales.

MHD and rotating turbulence are even more uncertain. The scenarios we have built are very speculative and await experimental and numerical backing.

What is the prospect of detecting turbulent structures in the core? We have seen that the expected relative density variations are extremely small ($\sim 10^{-9}$), far too small to affect the propagation of seismic waves or the gravity field. However, the velocity of seismic waves can also be modified by rotation, flow velocity, and magnetic field. How important are these effects? Our τ–ℓ diagrams can guide us again. Seismic waves in the core have velocities of about 9 km s^{-1}, yielding a characteristic time of about 400 s at the integral scale r_o. Scattering of seismic waves by turbulent structures roughly scales as their time ratio: strong effects occur when times are comparable. In Figure 8, we see that the time that gets closest to the seismic time is t_Ω: indeed, it is well known that seismic normal modes of the Earth are split by the Coriolis force. The next relevant time is the magnetic Alfvén wave time, but it is already 3 orders of magnitude further away from seismic times, leaving little hope for detection.

Acknowledgments

We thank Dan Lathrop for a fruitful review and Jérôme Noir for spotting an error in an earlier version of our manuscript.

References

Ahlers G, Grossmann S, and Lohse D (2009) Heat transfer and large scale dynamics in turbulent Rayleigh–Benard convection. *Reviews of Modern Physics* 81: 503–537. http://dx.doi.org/10.1103/RevModPhys.81.503.

Alboussière T, Cardin P, Debray F, et al. (2011) Experimental evidence of Alfvén wave propagation in a gallium alloy. *Physics of Fluids* 23: 096601. http://dx.doi.org/10.1063/1.3633090.

Alboussière T, Deguen R, and Melzani M (2010) Melting-induced stratification above the Earth's inner core due to convective translation. *Nature* 466: 744–747. http://dx.doi.org/10.1038/nature09257.

Alemany A, Moreau R, Sulem P, and Frisch U (1979) Influence of an external magnetic field on homogeneous MHD turbulence. *Journal de Mécanique* 18: 277–313.

Alfvén H (1942) Existence of electromagnetic–hydrodynamic waves. *Nature* 150: 405–406. http://dx.doi.org/10.1038/150405d0.

Andreev O, Kolesnikov Y, and Thess A (2013) Visualization of the Ludford column. *Journal of Fluid Mechanics* 721: 438–453. http://dx.doi.org/10.1017/jfm.2013.76.

Anselmet F, Gagne Y, Hopfinger EJ, and Antonia RA (1984) High-order velocity structure functions in turbulent shear flows. *Journal of Fluid Mechanics* 140: 63–89. http://dx.doi.org/10.1017/S0022112084000513.

Aubert J, Jung S, and Swinney HL (2002) Observations of zonal flow created by potential vorticity mixing in a rotating fluid. *Geophysical Research Letters* 29. http://dx.doi.org/10.1029/2002GL015422.

Augier P and Lindborg E (2013) A new formulation of the spectral energy budget of the atmosphere, with application to two high-resolution general circulation models. *Journal of the Atmospheric Sciences* 70: 2293–2308. http://dx.doi.org/10.1175/JAS-D-12-0281.1.

Baroud CN, Plapp BB, Swinney HL, and She ZS (2003) Scaling in three-dimensional and quasi-two-dimensional rotating turbulent flows. *Physics of Fluids* 15: 2091–2104. http://dx.doi.org/10.1063/1.1577120.

Berhanu M, Monchaux R, Fauve S, et al. (2007) Magnetic field reversals in an experimental turbulent dynamo. *Europhysics Letters* 77: 59001. http://dx.doi.org/10.1209/0295-5075/77/59001.

Boffetta G, De Lillo F, Mazzino A, and Musacchio S (2012) Bolgiano scale in confined Rayleigh–Taylor turbulence. *Journal of Fluid Mechanics* 690: 426–440. http://dx.doi.org/10.1017/jfm.2011.446.

Bolgiano R Jr. (1959) Turbulent spectra in a stably stratified atmosphere. *Journal of Geophysical Research* 64: 2226–2229. http://dx.doi.org/10.1029/JZ064i012p02226.

Braginsky SI (1970) Spectrum of oscillations of the Earth's hydro-magnetic dynamo. *Geomagnetism and Aeronomy* 10: 221–233.

Braginsky SI and Meytlis VP (1990) Local turbulence in the Earth's core. *Geophysical and Astrophysical Fluid Dynamics* 55: 71–87. http://dx.doi.org/10.1080/03091929008203556.

Brito D, Alboussière T, Cardin P, et al. (2011) Zonal shear and super-rotation in a magnetized spherical Couette-flow experiment. *Physical Review E* 83: 066310. http://dx.doi.org/10.1103/PhysRevE.83.066310.

Brito D, Nataf HC, Cardin P, Aubert J, and Masson J (2001) Ultrasonic Doppler velocimetry in liquid gallium. *Experiments in Fluids* 31: 653–663. http://dx.doi.org/10.1007/s003480100312.

Bruno R and Carbone V (2005) The solar wind as a turbulence laboratory. *Living Reviews in Solar Physics* 2. http://www.livingreviews.org/lrsp-2005-4.

Buffett BA (2003) A comparison of subgrid-scale models for large-eddy simulations of convection in the Earth's core. *Geophysical Journal International* 153: 753–765. http://dx.doi.org/10.1046/j.1365-246X.2003.01930.x.

Busse FH (1970) Thermal instabilities in rapidly rotating systems. *Journal of Fluid Mechanics* 44: 441–460. http://dx.doi.org/10.1017/S0022112070001921.

Charbonneau P (2005) Dynamo models of the solar cycle. *Living Reviews in Solar Physics* 2. http://www.livingreviews.org/lrsp-2005-2 [on line article] cited [october 2, 2012].

Chen Q and Jones CA (2008) Similarity and dynamic similarity models for large-eddy simulations of a rotating convection-driven dynamo. *Geophysical Journal International* 172: 103–114. http://dx.doi.org/10.1111/j.1365-246X.2007.03621.x.

Christensen UR and Aubert J (2006) Scaling properties of convection-driven dynamos in rotating spherical shells and application to planetary magnetic fields. *Geophysical Journal International* 166: 97–114. http://dx.doi.org/10.1111/j.1365-246X.2006.03009.x.

Davidson PA (2013) Rapidly-rotating turbulence: An experimental perspective. In: Davidson PA, Kaneda Y, and Sreenivasan KR (eds.) *Ten Chapters in Turbulence*, pp. 318–350. Cambridge: Cambridge University Press. http://dx.doi.org/10.1017/CBO9781139032810.009.

Davidson PA, Staplehurst PJ, and Dalziel SB (2006) On the evolution of eddies in a rapidly rotating system. *Journal of Fluid Mechanics* 557: 135–144. http://dx.doi.org/10.1017/S0022112006009827.

Dritschel DG and McIntyre ME (2008) Multiple jets as PV staircases: The Phillips effect and the resilience of eddy-transport barriers. *Journal of the Atmospheric Sciences* 65: 855–874. http://dx.doi.org/10.1175/2007JAS2227.1.

Eymin C and Hulot G (2005) On core surface flows inferred from satellite magnetic data. *Physics of the Earth and Planetary Interiors* 152: 200–220. http://dx.doi.org/10.1016/j.pepi.2005.06.009.

Frisch U (1995) *Turbulence: The Legacy of A.N. Kolmogorov*. Cambridge: Cambridge University Press.

Gailitis A, Lielausis O, Platacis E, et al. (2001) Magnetic field saturation in the Riga dynamo experiment. *Physical Reviews Letters* 86: 3024–3027. http://dx.doi.org/10.1103/PhysRevLett.86.3024.

Giesecke A (2007) Anisotropic turbulence in weakly stratified rotating magnetoconvection. *Geophysical Journal International* 171: 1017–1028. http://dx.doi.org/10.1111/j.1365-246X.2007.03567.x.

Gillet N, Jault D, Canet E, and Fournier A (2010) Fast torsional waves and strong magnetic field within the Earth's core. *Nature* 465: 74–77. http://dx.doi.org/10.1038/nature09010.

Gillet N, Schaeffer N, and Jault D (2011) Rationale and geophysical evidence for quasi-geostrophic rapid dynamics within the Earth's outer core. *Physics of the Earth and Planetary Interiors* 187: 380–390. http://dx.doi.org/10.1016/j.pepi.2012.03.006.

Gilman PA and Glatzmaier GA (1981) Compressible convection in a rotating spherical shell. I – Anelastic equations. II – A linear anelastic model. III – Analytic model for compressible vorticity waves. *The Astrophysical Journal Supplement Series* 45: 335–388. http://dx.doi.org/10.1086/190714.

Glatzmaier GA and Roberts PH (1995) A three-dimensional self-consistent computer simulation of a geomagnetic field reversal. *Nature* 377: 203–209. http://dx.doi.org/10.1038/377203a0.

Grote E, Busse FH, and Tilgner A (2000) Effects of hyperdiffusivities on dynamo simulations. *Geophysical Research Letters* 27: 2001–2004. http://dx.doi.org/10.1029/1999GL011155.

Högström U (1996) Review of some basic characteristics of the atmospheric surface layer. *Boundary-Layer Meteorology* 78: 215–246. http://dx.doi.org/10.1007/BF00120937.

Hulot G, Eymin C, Langlais B, et al. (2002) Small-scale structure of the geodynamo inferred from Oersted and Magsat satellite data. *Nature* 416: 620–623. http://dx.doi.org/10.1038/416620a.

Jault D (2008) Axial invariance of rapidly varying diffusionless motions in the Earth's core interior. *Physics of the Earth and Planetary Interiors* 166: 67–76. http://dx.doi.org/10.1016/j.pepi.2007.11.001.

Jones CA, Soward AM, and Mussa AI (2000) The onset of thermal convection in a rapidly rotating sphere. *Journal of Fluid Mechanics* 405: 157–179. http://dx.doi.org/10.1017/S0022112099007235.

Kaneda Y and Morishita K (2013) Small-scale statistics and structure of turbulence in the light of high resolution direct numerical simulation. In: Davidson PA, Kaneda Y, and Sreenivasan KR (eds.) *Ten Chapters in Turbulence*, pp. 1–42. Cambridge: Cambridge University Press. http://dx.doi.org/10.1017/CBO9781139032810.002.

Kelley DH, Triana SA, Zimmerman DS, Tilgner A, and Lathrop DP (2007) Inertial waves driven by differential rotation in a planetary geometry. *Geophysical and Astrophysical Fluid Dynamics* 101: 469–487. http://dx.doi.org/10.1080/03091920701561907.

Kolmogorov AN (1941a) The local structure of turbulence in incompressible viscous fluid for very large Reynolds number. *Doklady Akademii Nauk SSSR* 30: 299–303.

Kolmogorov AN (1941b) Dissipation of energy in the locally isotropic turbulence. *Doklady Akademii Nauk SSSR* 32: 16–18.

Kolmogorov AN (1962) A refinement of previous hypotheses concerning the local structure of turbulence in a viscous incompressible fluid at high Reynolds number. *Journal of Fluid Mechanics* 13: 82–85. http://dx.doi.org/10.1017/S0022112062000518.

Kraichnan RH and Montgomery D (1980) Two-dimensional turbulence. *Reports on Progress in Physics* 43: 547–619. http://dx.doi.org/10.1088/0034-4885/43/5/001.

Lathrop DP and Forest CB (2011) Magnetic dynamos in the lab. *Physics Today* 64: 40–45. http://dx.doi.org/10.1063/PT.3.1166.

Legras B, Santangelo P, and Benzi R (1988) High-resolution numerical experiments for forced two-dimensional turbulence. *Europhysics Letters* 5: 37–42. http://dx.doi.org/10.1209/0295-5075/5/1/007.

Lesieur M (2008) *Turbulence in Fluids*. Fourth Edition: Springer.

Lo TS, L'vov VS, Pomyalov A, and Procaccia I (2005) Estimating von Karman's constant from homogeneous turbulence. *Europhysics Letters* 72: 943–949. http://dx.doi.org/10.1209/epl/i2005-10323-8.

Matsui H and Buffett BA (2012) Large-eddy simulations of convection-driven dynamos using a dynamic scale-similarity model. *Geophysical and Astrophysical Fluid Dynamics* 106: 250–276. http://dx.doi.org/10.1080/03091929.2011.590806.

Maximenko NA, Bang B, and Sasaki H (2005) Observational evidence of alternating zonal jets in the world ocean. *Geophysical Research Letters* 32. http://dx.doi.org/10.1029/2005GL022728.

Moffatt HK (1961) The amplification of a weak applied magnetic field by turbulence in fluids of moderate conductivity. *Journal of Fluid Mechanics* 11: 625–635. http://dx.doi.org/10.1017/S0022112061000779.

Moffatt HK (1978) *Magnetic Field Generation in Electrically Conducting Fluids*. Cambridge: Cambridge University Press.

Monchaux R, Berhanu M, Bourgoin M, et al. (2007) Generation of a magnetic field by dynamo action in a turbulent flow of liquid sodium. *Physical Review Letters* 98: 044502. http://dx.doi.org/10.1103/PhysRevLett.98.044502.

Nastrom GD and Gage KS (1985) A climatology of atmospheric wavenumber spectra of wind and temperature observed by commercial aircraft. *Journal of the Atmospheric Sciences* 42: 950–960. http://dx.doi.org/10.1175/1520-0469(1985)042<0950:ACOAWS>2.0.CO;2.

Nataf HC, Alboussière T, Brito D, et al. (2008) Rapidly rotating spherical Couette flow in a dipolar magnetic field: An experimental study of the mean axisymmetric flow. *Physics of the Earth and Planetary Interiors* 170: 60–72. http://dx.doi.org/10.1016/j.pepi.2008.07.034.

Nataf HC and Gagnière N (2008) On the peculiar nature of turbulence in planetary dynamos. *Comptes Rendus Physique* 9: 702–710. http://dx.doi.org/10.1016/j.crhy.2008.07.009.

Nazarenko SV and Schekochihin AA (2011) Critical balance in magnetohydrodynamic, rotating and stratified turbulence: Towards a universal scaling conjecture. *Journal of Fluid Mechanics* 677: 134–153. http://dx.doi.org/10.1017/S002211201100067X.

Niemela JJ, Skrbek L, Sreenivasan KR, and Donnelly RJ (2000) Turbulent convection at very high Rayleigh numbers. *Nature* 404: 837–840. http://dx.doi.org/10.1038/35009036.

Obukhov A (1941) Spectral energy distribution in a turbulent spectral energy distribution in a turbulent flow. *Doklady Akademii Nauk SSSR* 32: 22–24.

Pais MA and Jault D (2008) Quasi-geostrophic flows responsible for the secular variation of the Earth's magnetic field. *Geophysical Journal International* 173: 421–443. http://dx.doi.org/10.1111/j.1365-246X.2008.03741.x.

Phillips OM (1972) Turbulence in a strongly stratified fluid—Is it unstable? *Deep Sea Research and Oceanographic Abstracts* 19: 79–81. http://dx.doi.org/10.1016/0011-7471(72)90074-5.

Plunian F and Stepanov R (2010) Cascades and dissipation ratio in rotating magnetohydrodynamic turbulence at low magnetic Prandtl number. *Physical Review E* 82. http://dx.doi.org/10.1103/PhysRevE.82.046311.

Plunian F, Stepanov R, and Frick P (2013) Shell models of magnetohydrodynamic turbulence. *Physics Reports* 523: 1–60. http://dx.doi.org/10.1016/j.physrep.2012.09.001.

Ponty Y, Mininni PD, Montgomery DC, Pinton JF, Politano H, and Pouquet A (2005) Numerical study of dynamo action at low magnetic Prandtl numbers. *Physical Review Letters* 94: 164502. http://dx.doi.org/10.1103/PhysRevLett.94.164502.

Rieutord M and Rincon F (2010) The Sun's supergranulation. *Living Reviews in Solar Physics* 7. http://www.livingreviews.org/lrsp-2010-2 [Online Article]: cited [October 2, 2012].

Rieutord M, Triana SA, Zimmerman DS, and Lathrop DP (2012) Excitation of inertial modes in an experimental spherical Couette flow. *Physical Review E* 86. http://dx.doi.org/10.1103/PhysRevE.86.026304.

Robert R and Sommeria J (1991) Statistical equilibrium states for two-dimensional flows. *Journal of Fluid Mechanics* 229: 291–310. http://dx.doi.org/10.1017/S0022112091003038.

Roberts GO (1972) Dynamo action of fluid motions with two-dimensional periodicity. *Philosophical Transactions of the Royal Society of London, Series A* 271: 411–454. http://dx.doi.org/10.1098/rsta.1972.0015.

Sakuraba A and Roberts PH (2009) Generation of a strong magnetic field using uniform heat flux at the surface of the core. *Nature Geoscience* 2: 802–805. http://dx.doi.org/10.1038/ngeo643.

Schmitt D, Alboussière T, Brito D, et al. (2008) Rotating spherical Couette flow in a dipolar magnetic field: Experimental study of magneto-inertial waves. *Journal of Fluid Mechanics* 604: 175–197. http://dx.doi.org/10.1017/S0022112008001298.

Schmitt D, Cardin P, La Rizza P, and Nataf HC (2013) Magneto-Coriolis waves in a spherical Couette flow experiment. *European Journal of Mechanics B/Fluids* 37: 10–22. http://dx.doi.org/10.1016/j.euromechflu.2012.09.001.

She ZS and Leveque E (1994) Universal scaling laws in fully-developed turbulence. *Physical Reviews Letters* 72: 336–339. http://dx.doi.org/10.1103/PhysRevLett.72.336.

Soderlund KM, King EM, and Aurnou JM (2012) The influence of magnetic fields in planetary dynamo models. *Earth and Planetary Science Letters* 333–334: 9–20. http://dx.doi.org/10.1016/j.epsl.2012.03.038.

Spence EJ, Reuter K, and Forest CB (2009) A spherical plasma dynamo experiment. *Astrophysical Journal* 700: 470–478. http://dx.doi.org/10.1088/0004-637X/700/1/470.

Steenbeck M, Krause F, and Rädler KH (1966) A calculation of the mean electromotive force in an electrically conducting fluid in turbulent motion, under the influence of Coriolis forces. *Zeitschrift für Naturforschung* A21: 369–376.

Stefani F, Gerbeth G, Gundrum T, et al. (2009) Helical magnetorotational instability in a Taylor–Couette flow with strongly reduced Ekman pumping. *Physical Review E* 80: 066303. http://dx.doi.org/10.1103/PhysRevE.80.066303.

Stieglitz R and Müller U (2001) Experimental demonstration of a homogeneous two-scale dynamo. *Physics of Fluids* 13: 561–564. http://dx.doi.org/10.1063/1.1331315.

StPierre MG (1996) On the local nature of turbulence in Earth's outer core. *Geophysical and Astrophysical Fluid Dynamics* 83: 293–306. http://dx.doi.org/10.1080/03091929608208969.

Swinbank WC (1951) The measurement of vertical transfer of heat and water vapour by eddies in the lower atmosphere. *Journal of Meteorology* 8: 135–145. http://dx.doi.org/10.1175/1520-0469(1951)008%3C0135:TMOVTO%3E2.0.CO;2.

Tobias S, Cattaneo F, and Boldyrev S (2013) MHD dynamos and turbulence. In: Davidson PA, Kaneda Y, and Sreenivasan KR (eds.) *Ten Chapters in Turbulence*, pp. 351–404. Cambridge: Cambridge University Press. http://dx.doi.org/10.1017/CBO9781139032810.010.

Vasavada AR and Showman AP (2005) Jovian atmospheric dynamics: An update after Galileo and Cassini. *Reports on Progress in Physics* 68: 1935–1996. http://dx.doi.org/10.1088/0034-4885/68/8/R06.

Verhille G, Plihon N, Bourgoin M, Odier P, and Pinton JF (2010) Laboratory dynamo experiments. *Space Science Reviews* 152: 543–564. http://dx.doi.org/10.1007/s11214-009-9546-1.

Westerweel J, Elsinga GE, and Adrian RJ (2013) Particle image velocimetry for complex and turbulent flows. *Annual Review of Fluid Mechanics* 45: 409–436. http://dx.doi.org/10.1146/annurev-fluid-120710-101204.

Xu H, Bourgoin M, Ouellette NT, and Bodenschatz E (2006) High order Lagrangian velocity statistics in turbulence. *Physical Reviews Letters* 96. http://dx.doi.org/10.1103/PhysRevLett.96.024503.

Can Core Flows inferred from Geomagnetic Field Models explain the Earth's Dynamo?

N. Schaeffer[1], E. Lora Silva[2*], M. A. Pais[2,3]

[1] ISTerre, University of Grenoble 1, CNRS, *F-38041* Grenoble, France
[2] CITEUC, Geophysical and Astronomical Observatory, University of Coimbra, *3040-004* Coimbra, Portugal
[3] Physics Department, University of Coimbra, *3004-516* Coimbra, Portugal
[*] present address: Department of Chemistry, University of Bath, Claverton Down, Bath BA2 7AY, United Kingdom

December 8, 2015

Abstract

We test the ability of large scale velocity fields inferred from geomagnetic secular variation data to produce the global magnetic field of the Earth. Our kinematic dynamo calculations use quasi-geostrophic (QG) flows inverted from geomagnetic field models which, as such, incorporate flow structures that are Earth-like and may be important for the geodynamo. Furthermore, the QG hypothesis allows straightforward prolongation of the flow from the core surface to the bulk. As expected from previous studies, we check that a simple QG flow is not able to sustain the magnetic field against ohmic decay. Additional complexity is then introduced in the flow, inspired by the action of the Lorentz force. Indeed, on centenial time-scales, the Lorentz force can balance the Coriolis force and strict quasi-geostrophy may not be the best ansatz. When our columnar flow is modified to account for the action of the Lorentz force, magnetic field is generated for Elsasser numbers larger than 0.25 and magnetic Reynolds numbers larger than 100. This suggests that our large scale flow captures the relevant features for the generation of the Earth's magnetic field and that the invisible small scale flow may not be directly involved in this process. Near the threshold, the resulting magnetic field is dominated by an axial dipole, with some reversed flux patches. Time-dependence is also considered, derived from principal component analysis applied to the inverted flows. We find that time periods from 120 to 50 years do not affect the mean growth rate of the kinematic dynamos. Finally we notice the footprint of the inner-core in the magnetic field generated deep in the bulk of the shell, although we did not include one in our computations.

1 Introduction

The main Earth's magnetic field and its temporal variations are generated by the motions of liquid metal in the core. Provided some assumptions are made, it is possible to infer the large scales of the flow at the top of the Earth's core, from observations of the geomagnetic field and its variations with time, which are commonly referred to as Secular Variation (SV). Because the crustal magnetic field dominates at small spatial scales, the core field is known only for the largest scales (up to spherical harmonic degree 13). Similarly, because of time varying

currents in the magnetosphere and in the ionosphere, the SV produced by core processes can be isolated only up to harmonic degree 12 to 14 [e.g. Olsen et al., 2014]. Unfortunately, this inherently also limits to relatively large scales the flow we can reconstruct at the top of the core.

Direct numerical simulations of the geodynamo, pioneered by Glatzmaier and Roberts [1995] can be tuned to produce magnetic fields that resemble closely the one of the Earth [e.g. Christensen et al., 2010, Christensen, 2011, Aubert et al., 2013]. However, the mechanism by which the magnetic field is actually generated in the Earth's core is not clear. Indeed, the parameter range in which those simulations operate is arguably very far from the one expected in the Earth, and when extrapolating them to realistic Earth parameters, we obtain a picture where the convective flow is important down to small scales of 0.1 to 10 km wide. Is this hidden small scale flow (both from numerics and from inversions) important for the generation of the magnetic field? Or is the large scale flow alone responsible for the induction? To help answer these difficult questions, the modest goal of this paper is to test the capability for dynamo action of the large scale flows inferred from geomagnetic field models.

The importance of the Coriolis force in the core arguably leads to flows that are mainly invariant along the rotation axis, which are referred to as quasi-geostrophic (QG) or columnar flows. These columnar flows are thought to be relevant at large spatial scales and short time-scales [Jault, 2008, Gillet et al., 2011]. At smaller spatial scales or more importantly at longer time scales, the columns are expected to wither: at such scales the Lorentz and buoyancy forces should arguably be both taken into account. The effect of the Lorentz force is of particular interest as Sreenivasan and Jones [2011] have shown that the induced magnetic pumping significantly enhances the dynamo action of the flow.

In this study, we use a columnar flow assumption to infer the flow at the core surface. The reconstruction of the flow inside the whole core is thus straightforward. We then use this reconstructed flow in a kinematic dynamo code to explore its dynamo capability. Despite being a much simpler approach than solving the full dynamical system, solving only the induction equation has already proven to be useful [e.g. Gubbins, 2008, Tobias and Cattaneo, 2013, Cabanes et al., 2014]. Although care must be taken when applying anti-dynamo theorems to bounded flows [see e.g. Bachtiar et al., 2006, Li et al., 2010], the quasi-two dimensionality of our columnar flows does not *a priori* help dynamo action [Jones, 2008]. Despite this fact, columnar flows have already proven to be capable of dynamo action in the presence of large-scale zonal shears [Schaeffer and Cardin, 2006, Guervilly, 2010]. In addition to the large-scale shears, both studies stress the importance of time-variability of the flow for the dynamo action. As for inverted core flows, they never exhibit dominant large scale shears. To try to boost the dynamo efficiency of columnar flows, we introduce a time-dependence matching inferred core flows and perturbate the flow with the magnetic pumping described by Sreenivasan and Jones [2011]. As we will show, only the latter actually leads to dynamo action.

Even though our flow explains an important part of the observed SV, we do not expect the growing dynamo field to match any particular feature of the secular variation as, e.g., the dipole moment decay rate. The reasons are inherent to the kinematic dynamo problem and are detailed in section 5. The point we wish to highlight in the present study is that our flow model, obtained through a geomagnetic field model inversion, and including a physically relevant magnetic pumping that does not change the surface flow, is efficient to maintain the magnetic field of the Earth, without the need for contributions from smaller scales.

The paper is organized as follow: in the next section the method for obtaining the core

flows is described and discussed. Then we describe the procedure we follow to compute kinematic dynamos from the core flows, and introduce the relevant parameters. The results are first described in section 4, and then discussed in section 5. We end the paper with concluding remarks.

2 Inverted core flows

2.1 Columnar flows

Columnar flow can be seen as the outcome of competing mechanisms that propagate information inside the core: Alfvén waves due to the magnetic tension in the medium and inertial waves due to the restoring effect of Coriolis force. On short time-scales and large length-scales, these latter waves are quicker in propagating perturbations axially (along planetary vorticity lines) inside the liquid core, as expressed by a small Lehnert number, i.e. the ratio between Alfvén wave and inertial wave speeds [Jault, 2008, Gillet et al., 2011, Nataf and Schaeffer, 2015].

Schaeffer and Pais [2011] pointed out that equatorially anti-symmetric (AS) features can be present inside a spherical rotating container as a result of some anti-symmetric excitation. When looking for this symmetry in core flows inverted from geomagnetic field models, they further noticed that the AS component tends to prevail for small scale flows [see also Gillet et al., 2011], which can be understood in terms of a lengthscale-dependent Lehnert number, $\lambda_\ell = B/\ell\Omega\sqrt{\rho\mu_0}$, larger for small-scale structures.

In a recent work, Pais et al. [2015] applied Principal Component Analysis tools to the streamfunction ξ of the QG flow inverted from geomagnetic field models. The 'data', which consisted in the values of streamfunction ξ on a regular spatial grid at the core surface, were decomposed into a mean flow plus a linear combination of a small number of spatial patterns multiplied by time-varying coefficients. This approach is particularly useful in the present context, by providing the means to describe the time-varying flow derived from geomagnetic field model *gufm1* over a 150 year time period with a small number of parameters (see section 3.3.1).

Since allowing for an AS component in inverted core flows improved variation of Length-of-Day (ΔLOD) estimations, Schaeffer and Pais [2011] argued in favor of considering both flow symmetries in the inversion.

2.2 Obtaining the core flow

The geomagnetic field model *gufm1* has been inverted for a large-scale columnar flow and an AS component, providing for a flow solution for each epoch in the 1840-1990 period (one independent flow snapshot each year). The inversion accounts for a separation of QG and AS flows as in Schaeffer and Pais [2011].

The columnar flow verifies the following kinematic condition at the core-mantle boundary (CMB):

$$\nabla_H \cdot \mathbf{u}^+ = \frac{2\tan\theta}{r_c} u_\theta^+ \tag{1}$$

with r_c the Earth's core radius, whereas the AS component satisfies

$$\nabla_H \cdot \mathbf{u}^- = 0 \qquad . \tag{2}$$

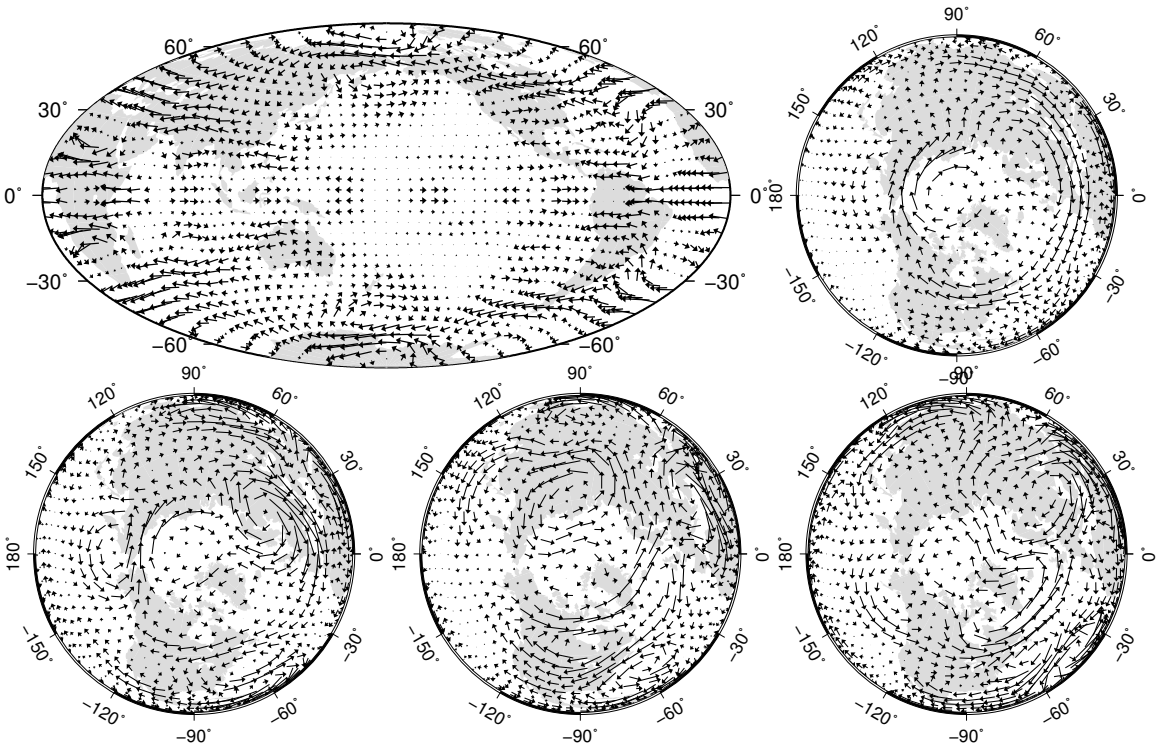

Figure 1: On the top row, the mean flow using a Hammer projection centered at the 180° meridian (left) and an ortographic projection as seen from the North pole (right). On the bottom row, the three spatial structures or Empirical Orthogonal Functions characterizing the first three modes from the PC analysis. The EOFs are normalised and the scale is arbitrary.

These are the surface constraints of a flow that in the bulk of the core has a QG component, equatorially symmetric (upper index '+'), and an AS component (upper index '-').

In Schaeffer and Pais [2011], the AS component $\mathbf{u}^-$ had no particular kinematical constraint imposed. By using (2) instead, the AS surface flow component can be completely retrieved from a toroidal scalar $\mathcal{T}$, in the same way as the QG surface flow component can be retrieved from a streamfunction scalar ξ [see e.g. Pais and Jault, 2008, Pais et al., 2015].

$$\mathbf{u}^+ = \frac{1}{\cos\theta}\nabla_H \wedge \xi(\theta,\phi)\,\hat{r} + \frac{\sin\theta}{r_c\cos^2\theta}\,\xi(\theta,\phi)\,\hat{\phi} \tag{3}$$

$$\mathbf{u}^- = \nabla_H \wedge \mathcal{T}(\theta,\phi)\,\hat{r} \tag{4}$$

where ξ and $\mathcal{T}$ are given in rad/yr. In this study, where we test the ability of QG flows to increase the energy of magnetic field modes that have a similar morphology to the Earth's field, we extracted $\mathbf{u}^+$ from the inverted flows and did not further consider the AS component $\mathbf{u}^-$.

Besides the two conditions (1) and (2) imposed on the surface flow through quadratic forms on the flow coefficients multiplied by relatively high regularization parameters, two further regularizations are used: a penalization of the azimuthal gradients, $\int_{CMB}[(1/\sin\theta)\,(\partial\mathbf{u}/\partial\phi)^2]dS$ as in Schaeffer and Pais [2011], supporting the observation of structures developed preferably along parallels in natural rotating flow systems; a penalization of radial vorticity and horizontal divergence, $\int_{CMB}[(\hat{r}\cdot\nabla_H\wedge\mathbf{u})^2+(\nabla_H\cdot\mathbf{u})^2]dS$, corresponding to the ℓ^3 norm used in Gillet et al. [2009] and favoring a large scale flow.

Following Pais et al. [2015], the streamfunction ξ obtained for the QG flow is analyzed into a linear combination of a small number of spatial patterns multiplied by time-varying coefficients, using Principal Component Analysis (PCA). Five modes are retained, which explain more than 95% of the time variability of the flow. The reduced streamfunction model reconstructed from these main modes is given by

$$\xi(r_c,\theta,\phi,t) = \xi^0(r_c,\theta,\phi) + \sum_{k=1}^{5} PC_k(t)\,\xi^k_{EOF}(r_c,\theta,\phi) \tag{5}$$

where ξ^0 is the mean flow, obtained by averaging the flow coefficients over the time-period 1840 - 1990, ξ^k_{EOF} is the Empirical Orthogonal Function (EOF) of order k depending on spatial coordinates, and $PC_k(t)$ is a function of time, the Principal Component (PC) of order k. The product $PC_k(t)\,\xi^k_{EOF}(r_c,\theta,\phi)$ is the kth PCA mode, and explains a percentage of the time variability found in data. The different modes are uncorrelated in time during the 1840-1990 interval and in space over the whole CMB. Figure 1 shows the flow at the CMB captured by ξ^0 and the first three EOFs. Figure 2 shows plots of the five first PCs that enter expression 5. Note the resemblance between this flow and those in Schaeffer and Pais [2011] and Pais et al. [2015]. In all cases, the mean flow shows strong azimuthal currents at high latitudes centered at -145° longitude and at low latitudes centered at 0°. The three large vortices at medium/high latitudes described in Pais et al. [2015] are also present.

The polar anticyclone lying inside the tangent cylinder cannot be conveniently retrieved with conventional QG flow regularization [e.g. Pais and Jault, 2008]. It is nonetheless an important feature of core flows which has already been discussed in both observations [e.g. Olson and Aurnou, 1999], and geodynamo simulations [e.g. Aubert, 2005].

3 A kinematic dynamo problem

3.1 Induction equation

The evolution of the magnetic field within an electrically conducting fluid is given by the induction equation

$$\frac{\partial \mathbf{B}}{\partial t} = \nabla \times (\mathbf{v} \times \mathbf{B}) + \eta \nabla^2 \mathbf{B}. \tag{6}$$

where $\eta = (\mu_0 \sigma)^{-1}$ is the magnetic diffusivity, μ_0 is the magnetic permeability of empty space, and σ is the electrical conductivity of the fluid that we assume to be homogeneous. Here, $\mathbf{v}$ denotes the entire three-dimensional flow in the bulk, while $\mathbf{u}$ is the flow at the core surface.

The key parameter for dynamo action is the magnetic Reynolds number

$$Rm = V_0 r_c / \eta = V_0 r_c \mu_0 \sigma$$

which compares the magnitude of the induction term to the ohmic dissipation. We use as characteristic speed V_0 the maximum value of the velocity of the flow field $\mathbf{v}$, and as length scale the radius r_c of the core. The core flows in this study have $V_0 \sim 15$ km/yr, leading to $Rm \sim 800$ to 3000 for the Earth's core, depending on the estimated electrical conductivity [Pozzo et al., 2012].

Dynamo action, which is the spontaneous growth of a magnetic field from the motion of a conducting fluid, happens when the induction overcomes ohmic dissipation, which occurs for $Rm > Rm_c$. Numerical computations are generally needed to determine the critical magnetic Reynolds number Rm_c, because it depends on the precise details of the flow. Efficient flows in spheres have $Rm_c \sim 10$ to 100 [e.g. Dudley and James, 1989, Jones, 2008]. Note however, that not all flow fields can ultimately trigger dynamo action, in which case Rm_c is not defined. Finding Rm_c and the fastest growing magnetic field $\mathbf{B}$ when the flow $\mathbf{v}$ is prescribed is referred to as the kinematic dynamo problem.

In the context of geomagnetism, Gubbins [2008] and Sarson [2003] studied the kinematic dynamo problem for minimalistic flows that captured some expected features of core flows. Here, the prescribed velocity field $\mathbf{v}$ and its time evolution are expected to be more Earth-like, since they are derived from the core flow $\mathbf{u}^+$ inverted from geomagnetic field observations as described in section 2. This will be detailed below.

3.2 Numerical procedure

In order to determine Rm_c for a given flow $\mathbf{v}$, we compute the time-evolution of $\mathbf{B}$ as given by the induction equation (6), for several values of the magnetic diffusivity η.

We time-step the induction equation (6) numerically, using the XSHELLS code [Gillet et al., 2011, Monteux et al., 2012, Cabanes et al., 2014], which is available as free software, and has been adapted for this study [see Schaeffer et al., 2015]. It uses the spherical harmonic transform library SHTns [Schaeffer, 2013] and finite differences in radius. The integration scheme is second order in time with the diffusion terms treated by a Crank-Nicolson scheme, whereas an Adams-Bashforth one is used for the induction term.

Both the prescribed flow $\mathbf{v}$ and the magnetic field $\mathbf{B}$ occupy the full sphere: we have no solid inner-core in our computations to avoid the issues arising when trying to reconstruct a columnar flow compatible with a solid inner-core. Note that the XSHELLS code has been benchmarked to full-sphere solutions [Marti et al., 2014] and used in a previous study involving

full-spheres [Monteux et al., 2012]. The mantle is assumed electrically insulating, so that the magnetic field in the liquid sphere matches a potential field outside the conducting domain.

The magnetic energy is monitored, its growth rate indicating if the flow leads to dynamo action. However, when starting from a random magnetic seed, transient decay and growth may be observed before the average growth-rate converges to a constant value. The time needed to obtain a well converged mean growth-rate is typically a fraction of the magnetic diffusion time $T_\eta = r_c^2/\eta$. All our simulations have been running at least for one fifth of T_η but often one half of T_η and, in a few cases, up to $2T_\eta$.

A typical run is set up with $N_r = 300$ radial levels, and spherical harmonic expansions truncated at degree $\ell_{max} = 149$ and order $m_{max} = 85$. For the most demanding cases (largest Rm) and to check numerical convergence, we pushed resolution up to $(N_r, \ell_{max}, m_{max}) = (320, 250, 150)$. The computations are always fully dealiased using the appropriate numbers of grid points in latitudinal ($N_\theta > 3\ell_{max}/2$) and longitudinal ($N_\phi > 3m_{max}$) directions.

3.3 Prescribed flow models

3.3.1 Time dependence through PC

It has been shown that the time-dependence can be important for dynamo action [Willis and Gubbins, 2004, Schaeffer and Cardin, 2006, Tilgner, 2008]. We thus also use flows varying in time in our kinematic dynamo study, as captured by geomagnetic observations. The prescribed velocity field $\mathbf{u}$ is computed from equation (3), with $\xi(t)$ given by equation (5). In order to assess if a flow is capable of sustaining a magnetic field against ohmic dissipation, we need to integrate the induction equation (6) for times comparable to the magnetic diffusion time. Because the magnetic diffusion time in the Earth is much longer than the time-period for which the core flow $\mathbf{u}$ is computed, we cannot reconstruct the flow for a time long enough for a simulation to run. To overcome this, we fitted each of the first five principal components $PC_k(t)$ (see eq. 5) with one sine function $\widetilde{PC}_k(t) = A_k \sin(\omega_k t + \alpha_k)$, as represented in figure 2. This allows us to compute a flow $\mathbf{u}$ at any time, by extrapolating from decade time scales at which observations take place to much larger diffusive ones at which dynamo action may occur.

The prescribed bulk flow $\mathbf{v}(t)$ is then reconstructed from the symmetric surface flow $\mathbf{u}^+(t)$ using the approach we now describe.

3.3.2 Purely columnar flow

The simplest way to reconstruct the flow at any depth in the core, is to assume a columnar flow. The cylindrical components (s,ϕ,z) of the bulk flow $\mathbf{v}$ are related to the spherical components (θ,ϕ) of the surface flow $\mathbf{u}^+$ by

$$\begin{aligned} v_s(s,\phi) &= \frac{H(s)}{r_c} u_\theta^+(\theta,\phi) \\ v_\phi(s,\phi) &= u_\phi^+(\theta,\phi) \\ v_z(s,\phi,z) &= -\frac{sz}{r_c H(s)}\, u_\theta^+(\theta,\phi) \end{aligned} \tag{7}$$

with $s = r_c \sin\theta$ the cylindrical radial coordinate and $H(s) = \sqrt{r_c^2 - s^2}$ the half height of a fluid column. Because $\mathbf{u}^+$ derives from a pseudo-streamfunction (see eq. 3), mass conservation

Figure 2: The main five PCs (used to reconstruct the flow using eq. 5) and their fitted sine functions, each defined by an amplitude, a time period and a phase shift.

is ensured and we always have $\nabla.\mathbf{v} = 0$ [see also Amit and Pais, 2013]. Remember also that in this study, we ignore the AS component $\mathbf{u}^-$.

3.3.3 Magnetic pumping

Helicity is another important ingredient for dynamo action as it leads to the so-called alpha-effect [e.g. Jones, 2008] whereby poloidal magnetic field is produced from toroidal field. Ekman pumping in columnar vortices produces helicity [Busse, 1975], but it vanishes at small enough Ekman numbers [e.g. Schaeffer and Cardin, 2006].

On centenial time-scales the influence of the Lorentz force on the flow should be taken into account. Indeed, when a magnetic field permeates columnar vortices, Sreenivasan and Jones [2011] have put forward an effect coined magnetic pumping, which produces an axial flow in phase with axial vorticity, that significantly enhances the mean helicity of the flow and consequent dynamo action. Because fields of dipolar symmetry have a more efficient magnetic pumping, they argued that this effect could explain the preference of dipole-dominated magnetic fields in their simulations.

The magnetic pumping is proportional to the local vorticity and to the square of the magnetic field. Sreenivasan and Jones [2011] have computed magnetic pumping solutions for a simple toroidal field

$$B_\phi = B_0 \frac{s}{r_c} \frac{z(H(s)^2 - z^2)}{H(s)^3} \tag{8}$$

of dipolar symmetry.

Because in our kinematic dynamo approach the flow is prescribed by the streamfunction ξ (eq. 3 and 5), we cannot take into account the retroaction of the dynamic magnetic field. Instead, we assume the Earth permeated by a simple toroidal field of dipolar symmetry, and follow Sreenivasan and Jones [2011]. As no explicit expression of the magnetic pumping is available, we choose to model the corresponding axial velocity v_z^{mp} with the following parametrization that closely mimics the magnetic pumping computed by Sreenivasan and Jones [2011] (see their equation 3.9 and their figure 1b). Using a Fourier decomposition $\xi(s,\phi) = \sum_m \xi_m(s) e^{im\phi}$, we prescribe, for all azimuthal wavenumber m:

$$v_z^{mp} = \Lambda\, V_0\, f(z/H(s))\, b(s)\, m^2 \xi_m(s) \tag{9}$$

where $f(x) = -\frac{7}{2}x(1-x)^2(1+x)^2$ captures vertical variations due to the above magnetic field geometry B_ϕ, and $b(s) = 4s(r_c - s)/r_c^2$ takes into account additional magnetic field variations with s. The profiles $f(x)$ and $b(s)$ are represented in Figure 3, and the assumed toroidal field in Figure 4 (left).

The Elsasser number

$$\Lambda = \frac{B_0^2}{\mu_0 \rho \Omega \eta} \tag{10}$$

controls the strength of the magnetic pumping, where B_0 is the maximum of the amplitude of the large scale magnetic field, ρ is the fluid density and Ω the rotation rate of the Earth.

Note also that we have approximated the local vorticity by $m^2\xi_m$, neglecting the contribution of the radial derivative of $\xi(s,\phi)$. This approximation allows us to conveniently satisfy the mass-conservation by adding a contribution v_ϕ^{mp} to the azimuthal flow:

$$v_\phi^{mp} = \Lambda V_0\, ism\, \xi_m(s)\, b(s)\, \frac{1}{H(s)} f'(z/H(s)) \tag{11}$$

Our magnetic pumping flow correction defined by equations (9) and (11) enhances the helicity of the flow while satisfying the mass conservation as well as the impenetrable boundary condition at the core-mantle boundary. It is also noteworthy that the magnetic pumping does not alter the surface flow.

Although we could have parameterized the small correction due to buoyancy forces in a similar manner, Sreenivasan and Jones [2011] mention that it has a much smaller effect on helicity. Therefore, and to keep our study simple, we ignore the small deformation of columns induced by buoyancy effects.

4 Results

We have computed kinematic dynamos with a combination of the two parameters Λ and Rm. Using only the mean flow $\mathbf{u}^+$ averaged in time and a purely columnar velocity field $\mathbf{v}$ given by equations 7, we found no dynamo for any tested value of Rm up to $Rm = 2600$. This is not unexpected as Schaeffer and Cardin [2006] also did not find dynamo action with stationary columnar flows.

In addition, adding the time dependence prescribed by our principal component analysis did not help, and no dynamo was found up to $Rm = 2600$. Moreover, we checked that the average growth rate is exactly the same as for the mean flow only. Willis and Gubbins [2004] showed that adding low frequency perturbations to a mean flow did not change the growth

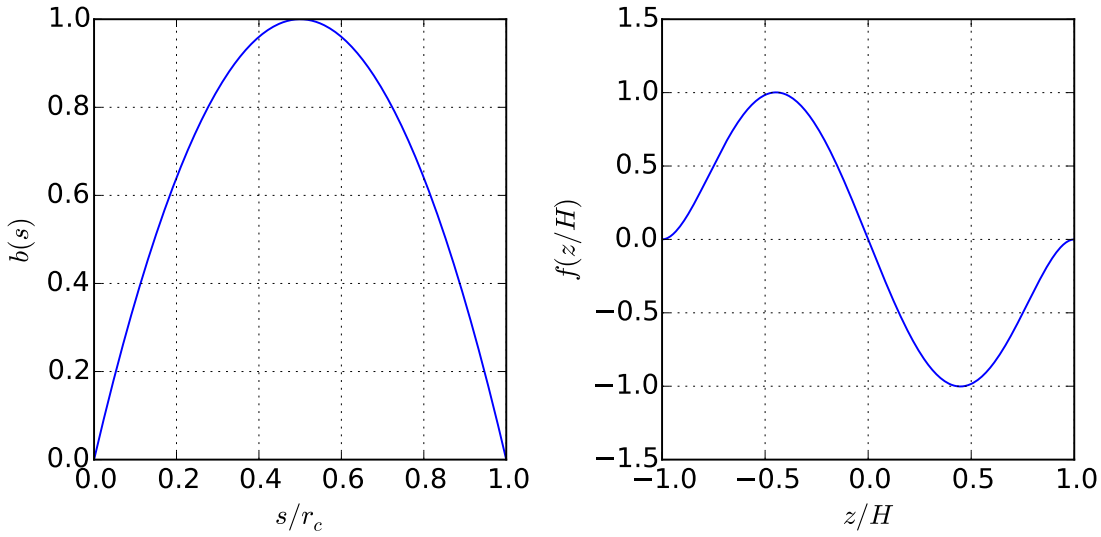

Figure 3: Radial (left) and vertical (right) profiles of our parametrized magnetic pumping. They were chosen to capture the dependence with s and z corresponding to a simple field of dipolar symmetry [see figure 1b of Sreenivasan and Jones, 2011].

rate, while higher frequency often enhanced dynamo action. Since our principal components have periods larger than 60 years, it does not exclude that lower period motions can participate in the dynamo process.

Nevertheless, as an auspicious result, adding magnetic pumping (eq. 9 and 11) to our core flows allowed them to produce growing magnetic fields: the larger the Elsasser number Λ, the lower the critical magnetic Reynolds number, down to $Rm_c \sim 250$. Below $\Lambda = 0.5$, we could not find a dynamo for Rm up to 1700. These computations are summarized in table 1 and figure 5, showing a regime diagram for dynamo action with magnetic pumping. We note that the time-dependence has still no effect on the average growth rate, even in the presence of magnetic pumping.

Since our flow $\mathbf{v}$ is symmetric with respect to the equatorial plane, the magnetic field eigen modes of the kinematic dynamo problem also have a definite symmetry (either symmetric or anti-symmetric). It turns out that the fastest growing magnetic field is anti-symmetric with a large dipolar component (see figure 6), which is consistent with the assumption used to model the magnetic pumping (see section 3.3.3).

Because the growing magnetic field is likely different from the simple assumed toroidal field responsible for the magnetic pumping in our framework, the resulting kinematic dynamos are not *a priori* dynamically self-consistent. As an *a posteriori* consistency check, we can compare the growing axisymmetric toroidal magnetic field to the one we have used to compute the magnetic pumping in equations 9 and 11. As shown in Fig. 4, they are in fair agreement, although more complexity can be seen in the growing magnetic field. In particular they are both equatorially antisymmetric.

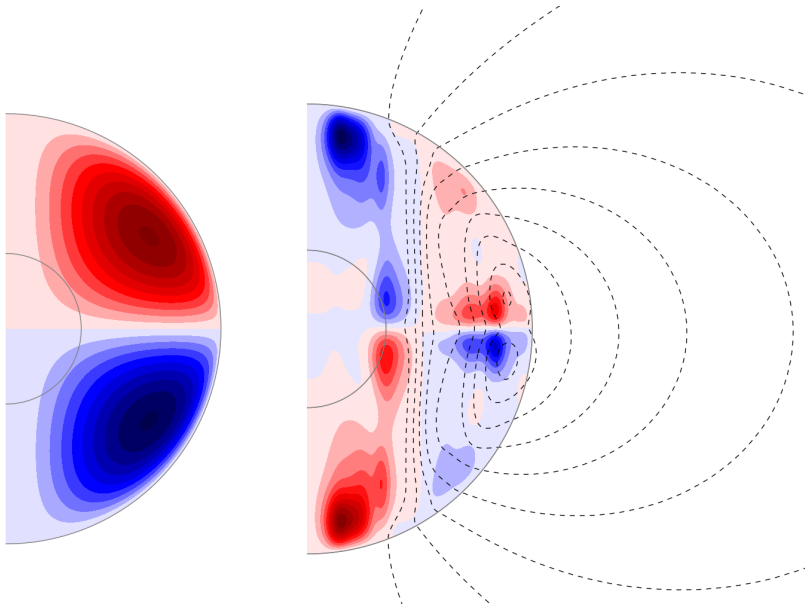

Figure 4: Left: the simple magnetic field used in eqs. 9 and 11 to model the magnetic pumping. Right: axisymmetric part of the growing magnetic field for $Rm = 978$ and $\Lambda = 0.9$. The colormap shows the azimuthal (toroidal) component and the black contours show the meridional (poloidal) field lines. The small gray circle marks the size of Earth's inner-core, although we have none in our study.

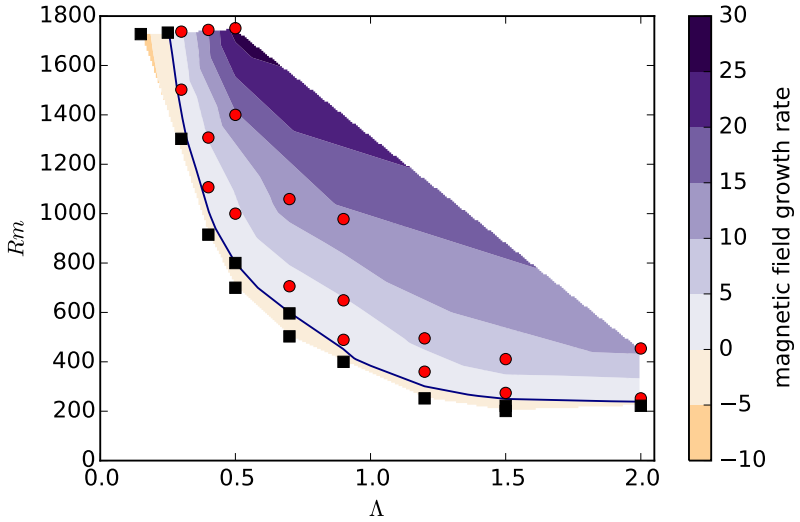

Figure 5: Growth rate as a function of the magnetic Reynolds number Rm and the Elsasser number Λ controlling the magnetic pumping. Black squares are failed dynamos (for which the magnetic field decays) while red circles are dynamos (exhibiting growing magnetic field). The contour lines are interpolated using the shown data points. The growth rate has been normalized using the magnetic diffusion time. The data is given in table 1.

Λ	Rm	Rm^*	γ	B_{rms}/B_{dip}
0.15	1727	600	-7.6	
0.25	1733	602	-0.4	
0.3	1303	453	-1.28	
0.3	1502	522	1.15	18.1
0.3	1737	604	4.44	17.2
0.4	915	318	-1.5	
0.4	1107	385	1.5	13.6
0.4	1308	455	5.3	12.9
0.4	1744	606	14.9	14.7
0.5	800	279	-0.01	
0.5	700	244	-1.7	
0.5	1000	348	4	11.2
0.5	1400	488	14.5	12.1
0.5	1751	610	27	14.0
0.7	503	176	-2	
0.7	596	209	-0.08	
0.7	706	247	2.55	8.4
0.7	1059	371	12.7	10.1
0.9	400	142	-1	
0.9	489	173	0.74	6.5
0.9	649	230	4.66	7.4
0.9	978	346	14	9.2
1.2	252	91.2	-1.9	
1.2	360	130	2.3	5.5
1.2	495	179	6.4	6.4
1.5	201	74.7	-2.9	
1.5	222	82.5	-1.6	
1.5	274	102	1.4	5.1
1.5	411	153	8	6.2
2	222	80.7	-1.1	
2	252	92	0.9	5.2
2	454	165	11	6.9

Table 1: Kinematic dynamo runs using the mean core flow and our magnetic pumping parameterization. The magnetic Reynolds number is computed using the maximum velocity (Rm) or the rms velocity (Rm^*). γ is the growth rate in magnetic diffusion time units, computed from the temporal evolution of the magnetic energy $E_B(t)$ as $\gamma = (2E_B)^{-1}\,\partial_t E_B$. For the growing magnetic field cases ($\gamma > 0$), the amplitude ratio between the root-mean-square field in the bulk and the dipole at the surface is given by B_{rms}/B_{dip}.

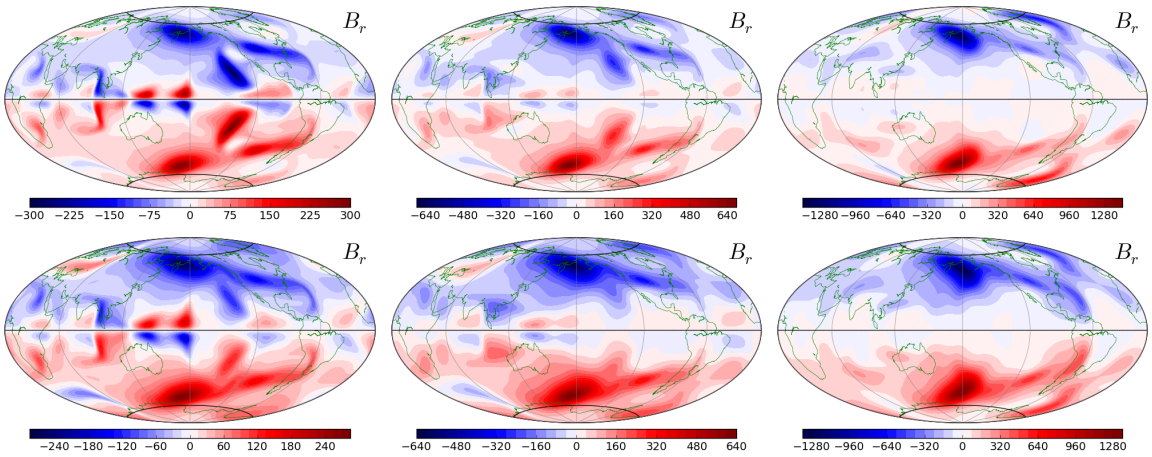

Figure 6: Growing radial magnetic field shown at the top of the core (Aitoff projection). It has been rescaled to match the assumed Elsasser number $\Lambda = 0.5$ (left), $\Lambda = 0.9$ (middle), $\Lambda = 2$ (right). For each Λ, the top row is the largest Rm whereas the bottom row is the smallest Rm leading to a growing field (see table 1 for precise values). The units are μT

5 Discussion

While Guervilly et al. [2012] used a forcing at the surface to produce a dynamic bulk flow compatible with the observed zonal jets of giant planets, here we decided to entirely prescribe the flow, as the core flow is more complex and time dependent.

We have observed growing magnetic fields in columnar flows with magnetic pumping, for magnetic Reynolds number $Rm = V_0 r_c/\eta$ as low as 252 (for Elsasser number $\Lambda = 2$). If we use the root-mean-square velocity in the bulk instead of the maximum velocity V_0, it translates to $Rm^* = 92$. This rather low value of Rm^* indicates that magnetic pumping in columnar flows is a rather efficient mechanism for dynamo action.

Our flow is a model of the large scale flow in the Earth's core where, because the operating dynamo is saturated, the Lorentz force backreacts on the flow to prevent further exponential growth of the magnetic field. Flows from such saturated dynamos have been found to still be efficient kinematic dynamos [Cattaneo and Tobias, 2009, Tilgner and Brandenburg, 2008]. If our flow is mainly responsible for the saturated geodynamo, then according to Cattaneo and Tobias [2009] it is also a kinematic dynamo for a growing magnetic field not everywhere proportional to the geomagnetic field and not backreacting on the flow (a passive field). Our kinematic dynamo calculations thus exhibit the property of velocity fields arising from a saturated dynamo to lead to exponential growth of a passive magnetic field.

Furthermore, in a kinematic dynamo, the obtained field is an eigenmode, growing or decaying at the same rate everywhere, effectively enslaving the time variation of the surface field to the time variation in the bulk. It may be worth emphasizing that because of vanishing radial velocities at the core surface, the magnetic field there is connected to the bulk field only through magnetic diffusion. As a result, in a regime of exponentially growing field, the dipole moment is also expected to grow. In contrast, the present geomagnetic field is expectedly in a saturated regime, where Lorentz forces play an important role back-reacting on the flow, although diffusion has probably also a non negligible effect. In particular, the observed

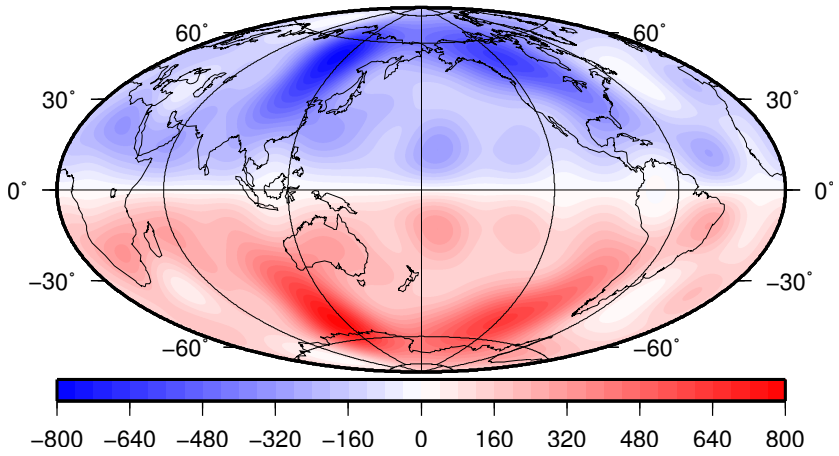

Figure 7: Anti-symmetric part of the radial magnetic field of *gufm1*, averaged from 1840 to 1990 (Hammer projection). Units are in μT.

rapid dipole moment decrease has been ascribed to either growth of reverse geomagnetic flux patches in the Southern Hemisphere [e.g. Gubbins et al., 2006], or advection of normal flux to the equator and of reversed flux to the poles [e.g. Olson and Amit, 2006]. Hence, particular features of the observed SV are much dependent on the particular geodynamo regime and cannot be considered here. In particular, we cannot compare the growth rate obtained for our passive field with the current decay rate of the geomagnetic (saturated) field strength. In fact, the present decay of the zonal dipole magnetic field energy which is being observed for the last 170 years, could in principle fit into the time variability observed in saturated geodynamos [see e.g. Christensen, 2011, Fig. 6].

Cattaneo and Tobias [2009] have also shown that, in spite of their differences, the growing passive field and the self-consistent saturated field have similar spatial structures. It may thus be interesting to compare the spatial structure of the growing magnetic field that emerges from our kinematic dynamos to the Earth's internal magnetic field observed nowadays. To ease this comparison, the mean anti-symmetric magnetic field of *gufm1* is shown in figure 7. The morphology of the growing field does not vary too much within the portion of the parameter space we have explored (see Fig. 6). It is always of dipolar symmetry, consistent with the simple toroidal field assumed to compute the magnetic pumping (eq 9). As a general trend, larger Rm have more pronounced small-scale features, and large Λ lead to fewer but stronger intense flux patches, and also lower amplitude reverse flux patches near the equator. A noticeable feature is the strong flux patch located right under the Bering Strait, which is associated with a large vortex in the mean flow, as can be seen in figure 8.

We want to emphasize that a perfect match with the Earth's magnetic field is not expected. Indeed, our mean flow computed over 150 years is unlikely to be an accurate estimate of the mean flow over a magnetic diffusion time (about 10^5 yrs). Hence, the strong magnetic flux patch under the Bering Strait, clearly associated with an intense vortex in the mean flow as seen in figure 8 and having no corresponding feature in the present Earth's field, may indicate that this very vortex is not part of the long-term mean flow. However, the presence of symmetric flux patches in the Earth's field not far from this location (with northern hemisphere signatures under North America and Eastern Russia, Fig. 7), may also suggest

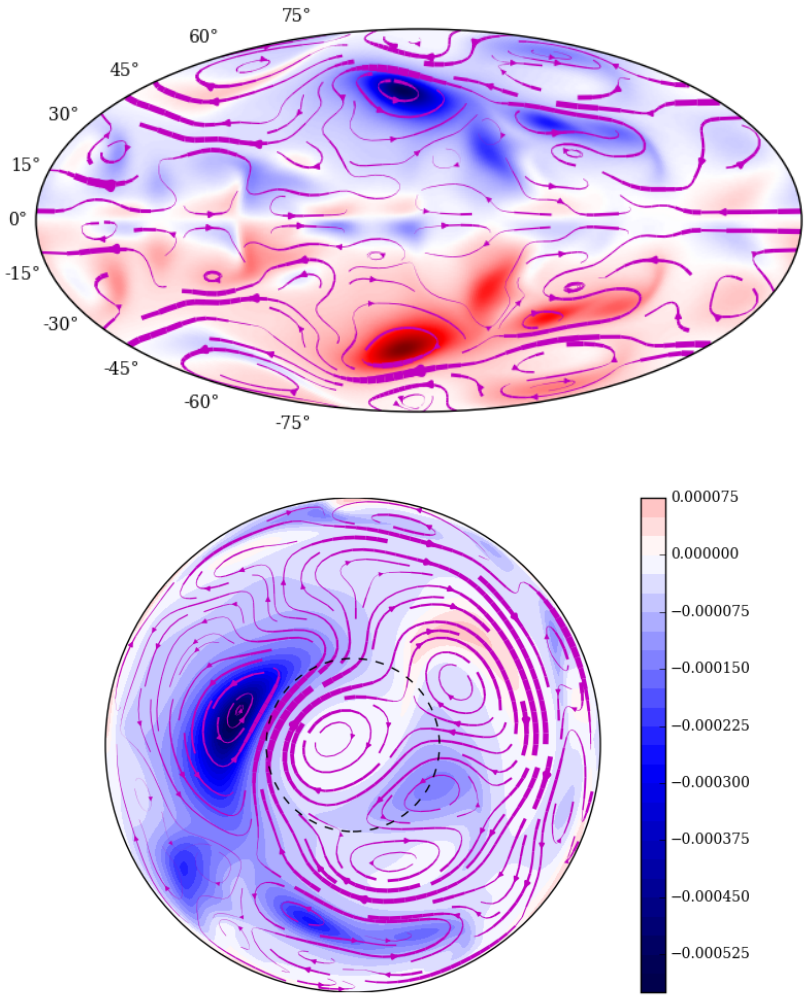

Figure 8: Growing radial magnetic field (colormap) and streamlines of the surface mean flow for $Rm = 978$ and $\Lambda = 0.9$. Top: Aitoff projection at the core surface centered on the pacific; bottom: north-pole view projected onto the equatorial plane (the Greenwich meridian is on the right, as in Fig. 1). The thickness of the streamlines is proportional to the velocity. The dashed circle marks the boundary of the Earth's inner-core.

that the whirl structure has suffered some displacement around its present position, over very long time periods. The fact that this vortex is also present in the first EOF (see figure 1) supports our hypothesis.

It is also satisfying that, when rescaling the magnetic field to match the imposed Λ, the radial field at the top of the core has the same order of magnitude as the Earth's field. Furthermore, the amplitude ratio between the root-mean-square field in the bulk and the dipolar field at the surface is around ~ 10 (see table 1), in agreement with numerical geodynamo models [Christensen, 2011] and torsional oscillations of ~ 6 yrs periodicity retrieved from geomagnetic field models [Gillet et al., 2010].

Another striking result is the footprint of the inner-core in the magnetic field generated deep inside the sphere, in spite of no inner core being present in our numerical computations. This display of the inner core presence is manifest in the change of sign of the magnetic field near the (virtual) tangent cylinder (see figure 4). This is related to the visible dichotomy in the prescribed flows (see figures 1 and 8).

The mechanism of dynamo generation that is considered in this study involves helicity. Here, an enhancement of helicity is prescribed in the bulk, which propagates no footprint whatsoever up to the core surface. It is, accordingly, contrasting with the scenario considered by Amit and Olson [2004] where the in-phase occurrence of vorticity and flow shear in the volume is assumed to manifest on the core surface in the form of correlated horizontal divergence and radial vorticity.

For $\Lambda = 0.25$ and below, no dynamos were found for $Rm \leq 1700$, as shown in figure 5. It appears that below some magnetic field strength, dynamo action due to the magnetic-pumping is lost, meaning that a strong magnetic field is needed for this mechanism to work. This is known as a subcritical behaviour [Sreenivasan and Jones, 2011, Morin and Dormy, 2009]. Our findings thus suggest that today, a subcritical dynamo may actually produce the magnetic field of our planet. If this is the case, a sudden change in our planet's field may occur when in the distant future the magnetic field bulk intensity drops below some threshold.

The magnetic-pumping model used in this study is admittedly crude. A more realistic model, which would dynamically adjust the magnetic-pumping to the actual magnetic field, would allow more realistic kinematic dynamos, with dynamic adjustment of the pumping flow to the growing magnetic field. It may also be possible to improve the quasi-geostrophic dynamos of Schaeffer and Cardin [2006] and Guervilly [2010] towards non-linear quasi-geostrophic geodynamo models.

6 Conclusion

We have shown that magnetic pumping in columnar core flows, leads to dynamo action. The distinctive feature of our study is to use a prescribed velocity field and its time evolution, derived from current geomagnetic field observations. This expectedly gives them an Earth-like nature, exhibiting features with specific geographical location and vorticity distribution that are most relevant to test their dynamo action. Note also that our kinematic dynamo approach allows us to reach realistic values of the electrical conductivity.

Furthermore, we show that relaxing the strict axial invariance with a magnetic-pumping is enough for large scale core flows to produce a dipolar field that resembles the one of the Earth, without the contribution of small scales. As an additional consistency check, the magnetic field in the bulk is about 10 times larger than at the surface (see table 1), in agreement with

the study of Gillet et al. [2010]. Magnetic pumping is arguably an important mechanism for the geodynamo.

In our computations, the magnetic field generation takes place in the bulk of the core where the flow is perturbated, and the surface magnetic field is connected to the bulk field only by diffusion. In the Earth's core, in a saturated but fluctuating regime, it is still unclear how much magnetic diffusion can contribute to the SV. Studies bridging numerical dynamo simulations and geomagnetic field inversions may help to shed more light on the subject, by providing estimates of the radial diffusion at the core surface.

For about fifty years, time-dependent geomagnetic field models have been used to infer the geometry and intensity of large scale flows in the core responsible for secular variation. Are these flow features expected to be present at diffusive timescales, much larger than the time window where we can constrain them with observations? The answer depends also on their ability for dynamo action. Our present results, together with previous studies proposing a possible dynamical mechanism for the main mean flow features such as the large eccentric jet [see Aubert et al., 2013], suggest indeed that they could be present for a very long time.

Acknowledgments

The authors thank A. Jackson, R. Holme and an anonymous reviewer for their useful comments. E. Lora Silva and M. A. Pais were supported by FCT (PTDC/CTE-GIX/119967/2010) through the project COMPETE (FCOMP-01-0124-FEDER-019978). M. A. Pais is grateful to the Grenoble University for funding her stay as an invited professor for two months. ISTerre is part of Labex OSUG@2020 (ANR10 LABX56). Most of the computations were performed using the Froggy platform of the CIMENT infrastructure (`https://ciment.ujf-grenoble.fr`), supported by the Rhône-Alpes region (GRANT CPER07_13 CIRA), the OSUG@2020 labex (reference ANR10 LABX56) and the Equip@Meso project (reference ANR-10-EQPX-29-01). The colorful figures were plotted using matplotlib (`http://matplotlib.org/`).

References

H. Amit and P. Olson. Helical core flow from geomagnetic secular variation. *Physics of the Earth and Planetary Interiors*, 147:1–25, October 2004. doi:10.1016/j.pepi.2004.02.006.

H. Amit and M. A. Pais. Differences between tangential geostrophy and columnar flow. *Geophys. J. Int.*, 194:145–157, July 2013. doi:10.1093/gji/ggt077.

Julien Aubert. Steady zonal flows in spherical shell dynamos. *Journal of Fluid Mechanics*, 542:53–67, 2005.

Julien Aubert, Christopher C. Finlay, and Alexandre Fournier. Bottom-up control of geomagnetic secular variation by the Earth's inner core. *Nature*, 502(7470):219–223, October 2013. ISSN 0028-0836. doi:10.1038/nature12574. URL `http://dx.doi.org/10.1038/nature12574`.

A. A. Bachtiar, D. J. Ivers, and R. W. James. Planar velocity dynamos in a sphere. *Proceedings of the Royal Society of London A: Mathematical, Physical and Engineering Sciences*, 462 (2072):2439–2456, August 2006. ISSN 1471-2946. doi:10.1098/rspa.2006.1671. URL `http://dx.doi.org/10.1098/rspa.2006.1671`.

F. H. Busse. A model of the geodynamo. *Geophysical Journal of the Royal Astronomical Society*, 42(2):437–459., April 1975. ISSN 0016-8009. doi:10.1111/j.1365-246X.1975.tb05871.x. URL http://dx.doi.org/10.1111/j.1365-246X.1975.tb05871.x.

Simon Cabanes, Nathanaël Schaeffer, and Henri-Claude Nataf. Turbulence reduces magnetic diffusivity in a liquid sodium experiment. *Physical Review Letters*, 113:184501, 2014. doi:10.1103/PhysRevLett.113.184501. URL https://hal.archives-ouvertes.fr/hal-01086279.

Fausto Cattaneo and Steven M. Tobias. Dynamo properties of the turbulent velocity field of a saturated dynamo. *Journal of Fluid Mechanics*, 621:205–214, February 2009. ISSN 1469-7645. doi:10.1017/s0022112008004990. URL http://dx.doi.org/10.1017/s0022112008004990.

Ulrich R. Christensen. Geodynamo models: Tools for understanding properties of earth's magnetic field. *Physics of the Earth and Planetary Interiors*, 187(3-4):157–169, August 2011. ISSN 00319201. doi:10.1016/j.pepi.2011.03.012. URL http://dx.doi.org/10.1016/j.pepi.2011.03.012.

Ulrich R. Christensen, Julien Aubert, and Gauthier Hulot. Conditions for earth-like geodynamo models. *Earth and Planetary Science Letters*, 296(3-4):487–496, August 2010. ISSN 0012821X. doi:10.1016/j.epsl.2010.06.009. URL http://dx.doi.org/10.1016/j.epsl.2010.06.009.

M. Dudley and R. James. Time-dependent kinematic dynamos with stationary flows. *Proc. Roy. Soc. Lond. A*, 425:407–429, 1989.

N. Gillet, M. A. Pais, and D. Jault. Ensemble inversion of time-dependent core flow models. *Geochemistry, Geophysics, Geosystems*, 10:Q06004, June 2009. doi:10.1029/2008GC002290.

N. Gillet, D. Jault, E. Canet, and A. Fournier. Fast torsional waves and strong magnetic field within the Earth's core. *Nature*, 465:74–77, May 2010. doi:10.1038/nature09010.

N. Gillet, N. Schaeffer, and D. Jault. Rationale and geophysical evidence for quasi-geostrophic rapid dynamics within the earth's outer core. *Physics of the Earth and Planetary Interiors*, 187:380–390, 2011. doi:10.1016/j.pepi.2011.01.005.

G. Glatzmaier and P. Roberts. A three-dimensional self-consistent computer simulation of a geomagnetic field reversal. *Nature*, 377, 1995.

D. Gubbins, A. L. Jones, and C. C. Finlay. Fall in Earth's Magnetic Field Is Erratic. *Science*, 312:900–902, May 2006. doi:10.1126/science.1124855.

David Gubbins. Implication of kinematic dynamo studies for the geodynamo. *Geophysical Journal International*, 173(1):79–91, 2008. doi:10.1111/j.1365-246X.2007.03707.x. URL http://gji.oxfordjournals.org/content/173/1/79.abstract.

Céline Guervilly. *Numerical study of planetary dynamos generated by surface shear or internal heating*. Theses, Université Joseph-Fourier - Grenoble I, October 2010. URL https://tel.archives-ouvertes.fr/tel-00576177.

Céline Guervilly, Philippe Cardin, and Nathanaël Schaeffer. A dynamo driven by zonal jets at the upper surface: Applications to giant planets. *Icarus*, 218(1):100 – 114, 2012. ISSN 0019-1035. doi:http://dx.doi.org/10.1016/j.icarus.2011.11.014. URL `http://www.sciencedirect.com/science/article/pii/S0019103511004416`.

Dominique Jault. Axial invariance of rapidly varying diffusionless motions in the earth's core interior. *Physics of the Earth and Planetary Interiors*, 166:67–76, 2008. doi:10.1016/j.pepi.2007.11.001.

Chris A. Jones. Course 2 dynamo theory. In Ph. Cardin and L.F. Cugliandolo, editors, *Dynamos*, volume 88 of *Les Houches*, pages 45 – 135. Elsevier, 2008. doi:http://dx.doi.org/10.1016/S0924-8099(08)80006-6. URL `http://www.sciencedirect.com/science/article/pii/S0924809908800066`.

Kuan Li, Philip W. Livermore, and Andrew Jackson. An optimal galerkin scheme to solve the kinematic dynamo eigenvalue problem in a full sphere. *Journal of Computational Physics*, 229(23):8666–8683, November 2010. ISSN 00219991. doi:10.1016/j.jcp.2010.07.039. URL `http://dx.doi.org/10.1016/j.jcp.2010.07.039`.

P. Marti, N. Schaeffer, R. Hollerbach, D. Cebron, C. Nore, F. Luddens, J. L. Guermond, J. Aubert, S. Takehiro, Y. Sasaki, Y. Y. Hayashi, R. Simitev, F. Busse, S. Vantieghem, and A. Jackson. Full sphere hydrodynamic and dynamo benchmarks. *Geophys. J. Int.*, 197(1):119–134, January 2014. ISSN 1365-246X. doi:10.1093/gji/ggt518. URL `http://dx.doi.org/10.1093/gji/ggt518`.

Julien Monteux, Nathanaël Schaeffer, Hagay Amit, and Philippe Cardin. Can a sinking metallic diapir generate a dynamo? *J. Geophys. Res.*, 117(E10):E10005+, October 2012. ISSN 0148-0227. doi:10.1029/2012je004075. URL `http://dx.doi.org/10.1029/2012je004075`.

Vincent Morin and Emmanuel Dormy. The dynamo bifurcation in rotating spherical shells. *International Journal of Modern Physics B*, 23(28n29):5467–5482, 2009.

H.-C. Nataf and N. Schaeffer. 8.06 - turbulence in the core. In Gerald Schubert, editor, *Treatise on Geophysics (Second Edition)*, pages 161 – 181. Elsevier, Oxford, second edition edition, 2015. ISBN 978-0-444-53803-1. doi:10.1016/B978-0-444-53802-4.00142-1. URL `http://www.sciencedirect.com/science/article/pii/B9780444538024001421`.

N. Olsen, H. Lühr, C. C. Finlay, T. J. Sabaka, I. Michaelis, J. Rauberg, and L. Tøffner-Clausen. The CHAOS-4 geomagnetic field model. *Geophysical Journal International*, 197: 815–827, May 2014. doi:10.1093/gji/ggu033.

P. Olson and H. Amit. Changes in earth's dipole. *Naturwissenschaften*, 93:519–542, November 2006. doi:10.1007/s00114-006-0138-6.

Peter Olson and Jonathan Aurnou. A polar vortex in the earth's core. *Nature*, 402(6758): 170–173, 1999.

M. A. Pais and D. Jault. Quasi-geostrophic flows responsible for the secular variation of the earth's magnetic field. *Geophys. J. Int.*, 173:421–443, 2008. doi:10.1111/j.1365-246X.2008.03741.x.

M. A. Pais, A. L. Morozova, and N. Schaeffer. Variability modes in core flows inverted from geomagnetic field models. *Geophys. J. Int.*, 200(1):402–420, 2015. doi:10.1093/gji/ggu403. URL http://gji.oxfordjournals.org/content/200/1/402.abstract.

Monica Pozzo, Chris Davies, David Gubbins, and Dario Alfè. Thermal and electrical conductivity of iron at earth's core conditions. *Nature*, 485(7398):355–358, April 2012. ISSN 0028-0836. doi:10.1038/nature11031. URL http://dx.doi.org/10.1038/nature11031.

Graeme R. Sarson. Kinematic dynamos driven by thermal-wind flows. *Proceedings of the Royal Society of London A: Mathematical, Physical and Engineering Sciences*, 459(2033): 1241–1259, 2003. ISSN 1364-5021. doi:10.1098/rspa.2002.1073.

N. Schaeffer and M. A. Pais. On symmetry and anisotropy of Earth-core flows. *Geophys. Res. Lett.*, 38:L10309, May 2011. doi:10.1029/2011GL046888.

Nathanaël Schaeffer. Efficient spherical harmonic transforms aimed at pseudospectral numerical simulations. *Geochem. Geophys. Geosyst.*, 14(3):751–758, March 2013. doi:10.1002/ggge.20071. URL http://arxiv.org/abs/1202.6522.

Nathanael Schaeffer and Philippe Cardin. Quasi-geostrophic kinematic dynamos at low magnetic prandtl number. *Earth and Planetary Science Letters*, 245(3-4):595–604, May 2006. doi:10.1016/j.epsl.2006.03.024. URL http://dx.doi.org/10.1016/j.epsl.2006.03.024.

Nathanael Schaeffer, Estelina Lora Silva, and Maria Alexandra Pais. xshells code for core flow dynamos. *figshare*, page doi:10.6084/m9.figshare.1439333, 06 2015. doi:10.6084/m9.figshare.1439333. URL http://dx.doi.org/10.6084/m9.figshare.1439333.

Binod Sreenivasan and Chris A. Jones. Helicity generation and subcritical behaviour in rapidly rotating dynamos. *Journal of Fluid Mechanics*, 688:5–30, 2011. doi:10.1017/jfm.2011.233. URL http://dx.doi.org/10.1017/jfm.2011.233.

A. Tilgner. Dynamo action with wave motion. *Phys. Rev. Lett.*, 100:128501, Mar 2008. doi:10.1103/PhysRevLett.100.128501. URL http://link.aps.org/doi/10.1103/PhysRevLett.100.128501.

Andreas Tilgner and Axel Brandenburg. A growing dynamo from a saturated roberts flow dynamo. *Monthly Notices of the Royal Astronomical Society*, 391(3):1477–1481, December 2008. ISSN 1365-2966. doi:10.1111/j.1365-2966.2008.14006.x. URL http://dx.doi.org/10.1111/j.1365-2966.2008.14006.x.

SM Tobias and F Cattaneo. Shear-driven dynamo waves at high magnetic reynolds number. *Nature*, 497(7450):463–465, 2013.

Ashley P Willis and David Gubbins. Kinematic dynamo action in a sphere: effects of periodic time-dependent flows on solutions with axial dipole symmetry. *Geophysical & Astrophysical Fluid Dynamics*, 98(6):537–554, 2004.

Appendix C

The XSHELLS code

C.1 Description

XSHELLS is yet another code simulating incompressible fluids in a spherical cavity. In addition to the Navier-Stokes equation with an optional Coriolis force, it can also time-step the coupled induction equation for MHD (with imposed magnetic field or in a dynamo regime), as well as the temperature (or codensity) equation in the Boussineq framework.

XSHELLS uses finite differences (second order) in the radial direction and spherical harmonic decomposition (pseudo-spectral). The time-stepping uses semi-implicit Crank-Nicolson scheme for the diffusive terms, while the non-linear terms can be handled either by an Adams-Bashforth or a Predictor-Corrector scheme (both second order in time).

XSHELLS is written in C++ and designed for speed. It uses the blazingly fast spherical harmonic transform library SHTns, as well as hybrid parallelization using OpenMP and/or MPI. This allows it to run efficiently on your laptop or on parallel supercomputers. A post-processing program is provided to extract useful data and export fields to matlab/octave, python/matplotlib or paraview.

XSHELLS passes the full-sphere benchmarks (Marti et al., 2014) as well as case 0 and 1 of the geodynamo benchmarks (Christensen, Aubert, Cardin, et al., 2001).

XSHELLS is free software, distributed under the CeCILL Licence (compatible with GNU GPL): everybody is free to use, modify and contribute to the code[1].

[1]Public code repository: `https://bitbucket.org/nschaeff/xshells`

C.2 Framework

To solve numerically the induction equation and the Navier-Stokes equation, spherical harmonic expansion is used together with finite differences in the radial direction. Spherical harmonics are very convenient for expressing the Laplace operator :

$$\Delta f = \frac{1}{r}\partial^2_{rr}(rf) - \frac{1}{r^2}\ell(\ell+1)f = \partial^2_{rr}f + \frac{2}{r}\partial_r f - \frac{1}{r^2}\ell(\ell+1)f \tag{C.1}$$

where ℓ is the harmonic degree.

Poloidal/Toroidal expansion is used, and any vector field $\mathbf{v}$ can be written as :

$$\mathbf{v} = \begin{pmatrix} 0 & + & \frac{1}{r}\ell(\ell+1)P_v \\ \frac{1}{\sin\theta}\partial_\phi T_v & + & \partial_\theta S_v \\ -\partial_\theta T_v & + & \frac{1}{\sin\theta}\partial_\phi S_v \end{pmatrix} \tag{C.2}$$

Where T_v is the toroidal scalar. When the vector is divergence free $\nabla.\mathbf{v} = 0$, the spheroidal component S_v is related to the poloidal P_v :

$$S = \frac{1}{r}\partial_r(rP_v) = \partial_r P_v + \frac{P_v}{r} \tag{C.3}$$

In this document we will consider only these types of solenoidal vectors.

C.3 Boundary conditions

C.3.1 Central condition at $r = 0$

At the center of the sphere, special conditions apply, which are independent of the physical nature of the field.

For a scalar field S to be consistent, only one value is allowed at the center, which implies $S = 0$ for $\ell > 0$.

For a vector field $\mathbf{v}$ to be consistent, only one vector is allowed at the center. This can be ensured by choosing a Cartesian projection v_x, v_y, v_z and transforming it to spherical components. This gives $P_v = 0$ and $T_v = 0$ for every ℓ, but $S_v = 0$ only for $\ell \neq 1$. More precisely, we have:

$$\mathbf{v}|_{r=0} = \begin{pmatrix} S_v \\ \partial_\theta S_v \\ \frac{1}{\sin\theta}\partial_\phi S_v \end{pmatrix} \tag{C.4}$$

with

$$S_v(r=0) = \begin{cases} 2\partial_r P_v|_{r=0} & \text{for } \ell = 1 \\ 0 & \text{for } \ell \neq 1 \end{cases} \tag{C.5}$$

C.3.2 Magnetic field

Electric insulator

In the insulator, we have no electrical currents $\mathbf{j} = \nabla \times \mathbf{b} = 0$ which means $\Delta P_b = 0$ and $T_b = 0$. Hence one has, for a given spherical harmonic degree ℓ :

$$\Delta P = \frac{1}{r}\partial^2_{rr}(rP) - \frac{\ell(\ell+1)}{r^2}P = 0 \tag{C.6}$$

which has solutions of the form

$$P = C_o\, r^{\ell} + C_i\, r^{-(\ell+1)} \tag{C.7}$$

Here $C_i = 0$ (resp. $C_o = 0$) if there are no internal (resp. external) sources of magnetic field.

Without other sources of magnetic field, the normal current at the boundary $\mathbf{j}.\mathbf{n}$ is continuous and so is T_b. In addition, the magnetic field $\mathbf{b}$ is continuous too, implying the continuity of P_b and $\partial_r P_b$. Hence, at the boundary, depending on whether the field is computed outside or inside the boundary, equation C.7 leads to

$$T = 0 \tag{C.8}$$

$$\partial_r P = \ell P/r \qquad \text{for the inner boundary} \tag{C.9}$$

$$\partial_r P = -(\ell+1)P/r \qquad \text{for the outer boundary} \tag{C.10}$$

Of course this is only valid if there are no external sources of magnetic fields.

With an applied magnetic field coming from a source not included in our system, both C_i and C_o are non-zero. However, at the boundary with an insulator, one still has the continuity of the magnetic field's poloidal scalar P and its derivative $\partial_r P$.

The total magnetic field produced by different sources is the sum of the magnetic field produced by individual sources, so that $P = P_{self} + P_{out}$. The field P_{self} originating from our system can thus be deduced from the total field P because the magnetic field imposed from outside is known at the boundary as $P_{out} = C_o\, r^{\ell}$. Hence the derivative of eq. C.7 reads :

$$\partial_r P = \ell/r\, P_{out} - (\ell+1)/r\, (P - P_{out})$$

Similarly, the magnetic field imposed from inside the inner shell is known at the boundary as $P_{in} = C_i\, r^{-(\ell+1)}$. Hence the derivative of eq. C.7 reads :

$$\partial_r P = \ell/r\,(P - P_{in}) - (\ell+1)/r\,P_{in}$$

And finally the general boundary conditions for the poloidal and toroidal scalar of the magnetic field at an insulating boundary reads :

$$T = 0 \tag{C.11}$$
$$\partial_r P = \ell P/r \quad -(2\ell+1)/r\,P_{in} \quad \text{for the inner boundary} \tag{C.12}$$
$$\partial_r P = -(\ell+1)P/r \quad +(2\ell+1)/r\,P_{out} \quad \text{for the outer boundary} \tag{C.13}$$

Finite-difference formulation. At the boundary, ΔP is approximated with only two points thanks to the previous boundary conditions. Accurate to second order in ϵ, the Taylor expansion gives :

$$P(r+\epsilon) = P(r) + \epsilon\partial_r P + \frac{\epsilon^2}{2}\partial^2_{rr} P$$

and using the BC :

$$P(r+\epsilon) = P(r) + \epsilon\left(\alpha\frac{P(r)}{r} + \beta\frac{P_0}{r}\right) + \frac{\epsilon^2}{2}\partial^2_{rr} P$$

with $\alpha = \ell$, $\beta = -(2\ell+1)$ for the inner boundary and $\alpha = -(\ell+1)$, $\beta = 2\ell+1$ for the outer boundary, and P_0 the poloidal scalar at the boundary of the imposed field. Finally

$$\partial^2_{rr} P = -\left(\frac{2}{\epsilon^2} + \frac{2\alpha}{r\epsilon}\right) P(r) \;+\; \frac{2}{\epsilon^2} P(r+\epsilon) \;-\; \frac{2\beta}{r\epsilon} P_0 \tag{C.14}$$

From which we write the discrete Laplace operator :

$$\Delta P = \frac{2\alpha}{r^2}P - \left(\frac{2}{\epsilon^2} + \frac{2\alpha}{r\epsilon}\right)P - \frac{\ell(\ell+1)}{r^2}P \tag{C.15}$$
$$+ \frac{2}{\epsilon^2}P(r+\epsilon) \tag{C.16}$$
$$+ 2\beta P_0\left(\frac{1}{r^2} - \frac{1}{r\epsilon}\right) \tag{C.17}$$

In XSHELLS, an additional shell containing $(2\ell+1)P_0$ is stored, so that an arbitrary potential field can be imposed from outside the conductive domain.

C.3.3 Temperature field

Imposed temperature

The temperature T at the boundary is imposed. For example the crystallization of the inner-core happens at fixed temperature (at a given pressure).

$$T = T_{\text{boundary}} \tag{C.18}$$

There is no need to compute the Laplacian here, as the temperature is imposed. This boundary condition is straightforward to impose.

Imposed thermal flux

The flux at the boundary is imposed, that is $\partial_r T = (\partial_r T)_{\text{boundary}}$. For example, the heat flux extracted from the core by the mantle is supposed to be imposed by the mantle.

Finite-difference formulation. From the taylor expansion, one gets

$$\partial^2_{rr} T = \frac{2}{\epsilon^2} T(r+\epsilon) \; - \; \frac{2}{\epsilon^2} T(r) \; - \; \frac{2}{\epsilon} (\partial_r T)_0 \tag{C.19}$$

which leads to the Laplacian of T at the boundary, with $(\partial_r T)_0$ imposed :

$$\begin{aligned} \Delta T(r_0) &= \frac{2}{\epsilon^2} \, T(r_0+\epsilon) && \text{(C.20)} \\ &- \left(\frac{2}{\epsilon^2} + \frac{\ell(\ell+1)}{r^2} \right) T(r_0) && \text{(C.21)} \\ &+ \left(\frac{2}{r} - \frac{2}{\epsilon} \right) (\partial_r T)_0 && \text{(C.22)} \end{aligned}$$

In XSHELLS, an additional shell containing $(\partial_r T)_0$ is stored, so that an arbitrary flux can be imposed at the boundary.

Stationary solution without motion for $\ell = 0$

The temperature equation reads (constant thermal diffusivity):

$$\partial_t T = \Delta T + Q \tag{C.23}$$

where Q is a constant accounting for internal heating. The stationary solution for $\ell = 0$ is then:

$$T_0(r) = -\frac{Q r^2}{6} + \frac{A}{r} + B \tag{C.24}$$

where A and B are constants defined by the boundary conditions. In particular, if the domain extends to $r = 0$ (full sphere), $A = 0$ and the profile is fixed besides a temperature shift (B). If the domain excludes $r = 0$, one must provide two boundary conditions, either the flux or the temperature at each boundary.

Central condition

For a full sphere, the temperature is free at $r = 0$, but only for $\ell = 0$ (see C.3.1). For $\ell > 1$, there is no problem, as the temperature field at the centre is fixed to 0.

For $\ell = 0$ we have $\partial_r T = 0$ because ∇T must be defined at $r = 0$ (implying $\partial_r T = 0$ for $\ell \neq 1$). To summarize, we have:

$$T = 0 \quad \text{for } \ell > 0 \tag{C.25}$$
$$\partial_r T = 0 \quad \text{for } \ell \neq 1 \tag{C.26}$$
$$\Delta T = 0 \quad \text{for } \ell > 0 \tag{C.27}$$

Finite-difference formulation for $l = 0$. Accurate to second order in ϵ, the Taylor expansion gives :

$$T(\epsilon) = T(0) + \epsilon \partial_r T|_0 + \frac{\epsilon^2}{2} \partial^2_{rr} T_0$$

and using the BC $\partial_r T = 0$:

$$T(\epsilon) = T(0) + \frac{\epsilon^2}{2} \partial^2_{rr} T_0$$

Finally

$$\partial^2_{rr} T = \frac{2}{\epsilon^2} \left(T(\epsilon) - T(0) \right) \tag{C.28}$$

This implies $T \sim Cr^2 + B$, so that we can compute

$$\frac{1}{r} \partial_r T = 2C = \partial_{rr} T \tag{C.29}$$

from which we can estimate the Laplacian:

$$\Delta T = -\frac{6}{\epsilon^2} T(0) \tag{C.30}$$
$$+ \frac{6}{\epsilon^2} T(\epsilon) \tag{C.31}$$

C.3.4 Velocity field

No-slip velocity

This is the most realistic boundary condition for a viscous fluid : the fluid follows the boundary.

$$\mathbf{u} = \mathbf{u}_{\text{boundary}} \tag{C.32}$$

which translates into

$$\begin{aligned} T &= T_{\text{boundary}} && \text{(C.33)}\\ P &= P_{\text{boundary}} && \text{(C.34)}\\ S &= S_{\text{boundary}} \qquad \Rightarrow\ \partial_r P = (\partial_r P)_{\text{boundary}} && \text{(C.35)}\\ & && \text{(C.36)} \end{aligned}$$

For an arbitrary boundary velocity, we thus need to prescribe T, P and $\partial_r P$ at the boundary. This allows also to compute the flow in a spherical sinking bubble.

Finite-difference formulation. From the taylor expansion, one gets

$$\partial^2_{rr} P = -\frac{2}{\epsilon^2} P_0 \ + \ \frac{2}{\epsilon^2} P(r+\epsilon) \ - \ \frac{2}{\epsilon}(\partial_r P)_0 \tag{C.37}$$

which leads to the Laplacian of P at the boundary, with P_0 and $(\partial_r P)_0$ imposed :

$$\begin{aligned} \Delta P &= \frac{2}{\epsilon^2}\, P(r+\epsilon) && \text{(C.38)}\\ &- \left(\frac{2}{\epsilon^2} + \frac{\ell(\ell+1)}{r^2}\right) P_0 && \text{(C.39)}\\ &+ \left(\frac{2}{r} - \frac{2}{\epsilon}\right) (\partial_r P)_0 && \text{(C.40)} \end{aligned}$$

In xshells, we add an additional *ghost* shell which contains $(\partial_r P)_0$, so that the boundary can have an arbitrary velocity.

Stress-free velocity

In order to neglect the thin viscous boundary layers that may form in the no-slip case, we can alternatively choose to let the fluid freely slip over the boundaries, that is to impose that the tangential constraint vanishes :

$$r\partial_r \frac{u_\theta}{r} + \frac{1}{r}\partial_\theta u_r = 0 \tag{C.41}$$

$$r\partial_r \frac{u_\phi}{r} + \frac{1}{r\sin\theta}\partial_\phi u_r = 0 \tag{C.42}$$

Assuming $u_r = 0$ and combining equations C.41 and C.42, one finds :

$$P = 0, \quad \partial_r \frac{T}{r} = 0, \quad \partial_r \frac{S}{r} = 0$$

which can be rewritten as :

$$P = 0 \tag{C.43}$$
$$\partial_r T = T/r \tag{C.44}$$
$$\partial^2_{rr} P = 0 \tag{C.45}$$

With an arbitrary imposed u_r and combining equations C.41 and C.42, without assuming $u_r = 0$, one finds :

$$\partial_r \frac{T}{r} = 0 \quad \text{for any } u_r \tag{C.46}$$
$$\partial_r \frac{S}{r} = -\frac{u_r}{r^2} \tag{C.47}$$

which can be rewritten as :

$$\partial_r T = T/r \tag{C.48}$$
$$\partial^2_{rr} P = \frac{2 - \ell(\ell+1)}{r^2} P \tag{C.49}$$

One need to add a condition which constrains u_r so that $P = P_0$ is known at the boundary.

We can notice here, that the result obtained by assuming $u_r = 0$ leads to a different matrix than the case of arbitrary u_r, possibly leading to a different numerical behaviour.

Finite-difference formulation. ΔT is handled like the electric insulator BC (sec. C.3.2), but with $\alpha = 1$ (and $\beta = 0$) :

$$\Delta T = \frac{2}{r^2} T - \left(\frac{2}{\epsilon^2} + \frac{2}{r\epsilon} \right) T - \frac{\ell(\ell+1)}{r^2} T \tag{C.50}$$
$$+ \frac{2}{\epsilon^2} T(r+\epsilon) \tag{C.51}$$

At the boundary, ΔP is approximated with only two points thanks to the previous boundary conditions. Accurate to second order in ϵ, the Taylor expansion gives :

$$P(r+\epsilon) = P_0 + \epsilon \partial_r P + \frac{\epsilon^2}{2} \partial^2_{rr} P$$

and using the BC :

$$P(r+\epsilon) = P_0 + \epsilon\partial_r P + \frac{\epsilon^2}{2}\frac{2-\ell(\ell+1)}{r^2}P_0$$

and finally

$$(\partial_r P)_0 = \left(-\frac{1}{\epsilon} + \epsilon\frac{\ell(\ell+1)-2}{2r^2}\right)P_0 \; + \; \frac{1}{\epsilon}P(r+\epsilon) \tag{C.52}$$

From which we write the discrete Laplace operator :

$$\Delta P = \left(\epsilon\frac{\ell(\ell+1)-2}{r^3} + \frac{2-2\ell(\ell+1)}{r^2} - \frac{2}{r\epsilon}\right)P_0 \tag{C.53}$$

$$+ \; \frac{2}{r\epsilon}P(r+\epsilon) \tag{C.54}$$

Central condition

Section C.3.1 gives geometrical constraints on the Poloidal/Toroidal decomposition at $r = 0$. For $\ell \neq 1$, we have enough constraints on the field: $T = 0$, $P = 0$, $\partial_r P = 0$.

For $\ell = 1$, the same regularity conditions for the vorticity field adds $\Delta P = 0$ (toroidal scalar of vorticity) at $r = 0$. Expanding $P(r \to 0) = ar + br^2 + cr^3$ gives for the laplace operator:

$$\Delta P|_{r\to 0}^{\ell=1} = 4b = 0$$

which translates into $\partial^2_{rr} P = 0$ for $\ell = 1$.

To summarize, we have:

$$T = 0, \quad P = 0, \quad \partial_r P = 0 \quad \text{for } \ell > 1 \tag{C.55}$$

$$T = 0, \quad P = 0, \quad \partial^2_{rr} P = 0 \quad \text{for } \ell = 1 \tag{C.56}$$

C.4 Time-stepping scheme

XSHELLS uses a variable step-size Crank-Nicolson Adams-Bashforth scheme (VSCNAB), as described by Wang and Ruuth (2008), their equation 2.9. They show in particular that there are no restriction on the time-step changes for VSCNAB to be stable as $dt \to 0$ (zero-stability).

Below we derive the variable step-size Adams-Bashforth part.

C.4.1 Adams-Bashforth with variable time-step

The following Taylor expansion allows us to relate $f(t+dt)$ which we want to evaluate, to the derivatives at time t:

$$f(t+dt) = f(t) + dtf'(t) + \frac{dt^2}{2}f''(t) + \frac{dt^3}{6}f'''(t) + O(dt^4)$$

The idea is now to evaluate $f''(t)$ from $f'(t)$ and $f'(t-dt_o)$, using another Taylor expansion:

$$f'(t-dt_o) = f'(t) - dt_o f''(t) + \frac{dt_o^2}{2}f'''(t) + O(dt_o^3)$$

leading to

$$f''(t) = \frac{f'(t) - f'(t-dt_o)}{dt_o} + \frac{dt_o}{2}f'''(t) + O(dt_o^2)$$

which we can now substitute into the first expansion:

$$f(t+dt) = f(t) + dt\left[f'(t)\left(1 + \frac{dt}{2dt_o}\right) - \frac{dt}{2dt_o}f'(t-dt_o)\right] \tag{C.57}$$

$$+ dt^3\left(\frac{dt_o}{4dt} + \frac{1}{6}\right)f'''(t) + O(dt^4) + O(dt^2\,dt_o^2) \tag{C.58}$$

When $dt_o = dt$, we find the classical second-order accurate Adams-Bashforth scheme:

$$f(t+dt) = f(t) + dt\left(\frac{3}{2}f'(t) - \frac{1}{2}f'(t-dt_o)\right) + \frac{5}{12}dt^3 f'''(t) + O(dt^4)$$

C.5 Implementation of variable conductivity

C.5.1 Induction equation

The induction equation reads :

$$\partial_t \mathbf{b} = \nabla \times (\mathbf{u} \times \mathbf{b} - \eta \nabla \times \mathbf{b}) \tag{C.59}$$

C.5.2 Continous variation with radius r

When $\eta \equiv \eta(r)$ we can expand the induction equation:

$$\partial_t \mathbf{b} = \nabla \times (\mathbf{u} \times \mathbf{b}) + \eta(r)\Delta\mathbf{b} + (\nabla \times \mathbf{b}) \times \nabla\eta(r) \tag{C.60}$$

Poloidal part

We introduce the electrical current $\mathbf{j} = \nabla \times \mathbf{b}$. The term involving $\nabla\eta$ has no radial component

$$\mathbf{r}.[\mathbf{j} \times \nabla\eta(r)] = 0 \tag{C.61}$$

implying **the poloidal part of the induction equation is unaltered**

$$\partial_t P_b = \eta(r)\Delta P_b + \mathrm{NL}_P \tag{C.62}$$

Toroidal part

The toroidal part is obtained by taking the radial component of the curl of the induction equation:

$$\mathbf{r}.\partial_t\mathbf{j} = \mathbf{r}.\nabla \times \nabla \times (\mathbf{u} \times \mathbf{b}) + \mathbf{r}.\nabla \times (\eta(r)\Delta\mathbf{b}) + \mathbf{r}.\nabla \times (\mathbf{j} \times \nabla\eta(r)) \tag{C.63}$$

The second term on the right hand side can be developed:

$$\begin{aligned} \mathbf{r}.\nabla \times (\eta(r)\Delta\mathbf{b}) &= \mathbf{r}.(\nabla\eta \times \Delta\mathbf{b} + \eta(r)\Delta\mathbf{j}) && \text{(C.64)} \\ &= \eta(r)\,\mathbf{r}.\Delta\mathbf{j} && \text{(C.65)} \\ &= \eta(r)\,\ell(\ell+1)\Delta T_b && \text{(C.66)} \end{aligned}$$

because, again, the term involving $\nabla\eta$ has no radial component.

The last term expands to:

$$\mathbf{r}.\nabla \times [\mathbf{j} \times \nabla\eta(r)] = r\partial_r\eta \left(-\frac{1}{r\sin\theta}\partial_\theta(\sin\theta j_\theta) - \frac{1}{r\sin\theta}\partial_\phi j_\phi\right) \tag{C.67}$$

using the definition of the vector components

$$\begin{aligned} j_\theta &= \frac{1}{\sin\theta}\partial_\phi T_j + \partial_\theta S_j && \text{(C.68)} \\ j_\phi &= \frac{1}{\sin\theta}\partial_\phi S_j - \partial_\theta T_j && \text{(C.69)} \end{aligned}$$

we find after some simplification:

$$\mathbf{r}.\nabla \times [(\nabla \times \mathbf{b}) \times \nabla\eta(r)] = \partial_r\eta\,\ell(\ell+1)S_j \tag{C.70}$$

Since $S_j = \frac{1}{r}\partial_r(rT_b)$, we finally obtain the **toroidal induction equation**:

$$\partial_t T_b = \eta(r)\Delta T_b + (\partial_r\eta)\,\frac{1}{r}\partial_r(rT_b) + \mathrm{NL}_T \tag{C.71}$$

where NL_T is the toroidal contribution of the non-linear terms. This is readily included into the tri-banded matrix of the Laplacian and can be solved at no additional computational cost.

Interestingly, equation C.71 can be rewritten as

$$\partial_t T_b = \frac{1}{r}\frac{\partial}{\partial r}\left(\eta\frac{\partial\, rT_b}{\partial r}\right) - \frac{\ell(\ell+1)}{r^2}T_b + \mathrm{NL}_T \tag{C.72}$$

C.5.3 Radial discontinuities of the conductivity

For discontinuous conductivities (ie a solid boundary with a different conductivity), the first jump conditions is that $\mathbf{B}$ is continuous across the interface. Hence P_b, $\partial_r P_b$ and T_b are continuous. The second jump condition, is $(j \times \mathbf{n})/\sigma$ continuous across the interface, from which we have the continuity of $\eta \partial_r (r T_b)$ and $\eta \Delta P_b$ (assuming the magnetic permeability μ is the same everywhere).

Since η is constant everywhere but at the discontinuity, the governing equation is

$$\partial_t \mathbf{b} = \nabla \times (\mathbf{u} \times \mathbf{b}) + \eta \Delta \mathbf{b} \tag{C.73}$$

In order to derive the finite difference approximation, we write the Taylor expansions left and right of the discontinuity located at r_0:

$$f_\pm = f_{0\pm} \pm dr (\partial_r f)_{0\pm} + \frac{dr^2}{2} (\partial_{rr} f)_{0\pm} \tag{C.74}$$

where $f_\pm = f(r_0 \pm dr)$, and $f_{0\pm}$ is the limit $f(r_0 \pm \varepsilon)$ when $\varepsilon \to 0^+$. This is the start for a finite difference formulation, with equidistant points around the discontinuity.

We can isolate $\partial_{rr} f$

$$2\frac{f_\pm - f_{0\pm}}{dr^2} \mp \frac{2}{dr} (\partial_r f)_{0\pm} = (\partial_{rr} f)_{0\pm} \tag{C.75}$$

and add the angular part to have an evaluation of $\Delta(f/r)$ at each side of the discontinuity:

$$2\frac{f_\pm - f_{0\pm}}{dr^2} \mp \frac{2}{dr} (\partial_r f)_{0\pm} - \frac{\ell(\ell+1)}{r_0^2} f_{0\pm} = (r\Delta(f/r))_{0\pm} \tag{C.76}$$

Poloidal part

Here, we take $f = rP$ in the previous finite difference formulation. In this case, f_0 and $(\partial_r f)_0$ are uniquely defined (by continuity). Multiplying equation C.76 by $\eta_+ \eta_-$ gives:

$$2\eta_+\eta_- \left(\frac{f_\pm - f_0}{dr^2} - \frac{\ell(\ell+1)}{2r_0^2} f_0 \right) = \pm \eta_+ \eta_- \frac{2}{dr} (\partial_r f)_0 + \eta_+ \eta_- (r\Delta P)_{0\pm} \tag{C.77}$$

By taking the sum of these equations, we eliminate $(\partial_r f)_0$:

$$2\eta_+\eta_- \left(\frac{f_+ + f_- - 2f_0}{dr^2} - \frac{\ell(\ell+1)}{r_0^2} f_0 \right) = (\eta_+ + \eta_-) r_0 K \tag{C.78}$$

with $K = \eta_+(\Delta P)_+ = \eta_-(\Delta P)_-$. We finally obtain the finite difference approximation of $\eta\Delta P$:

$$(\eta\Delta P)_0 = \frac{2\eta_+\eta_-}{\eta_+ + \eta_-}\left(\frac{r_+P_+ + r_-P_- - 2r_0P_0}{r_0dr^2} - \frac{\ell(\ell+1)}{r_0^2}\right) \tag{C.79}$$

Meaning that, for the finite difference formulation, η must simply be replaced by its harmonic mean at the interface. Or equivalently σ be replaced by its mean.

Toroidal part

Here, we take $f = rT$ in the finite difference formulation of equations C.74. In this case, f_0 is uniquely defined (by continuity) and $\eta_+(\partial_r f)_{0+} = \eta_-(\partial_r f)_{0-}$. Multiplying equation C.76 by $\eta_\pm$ gives:

$$2\eta_\pm\left(\frac{f_\pm - f_0}{dr^2} - \frac{\ell(\ell+1)}{2r_0^2}f_0\right) = \pm\eta_\pm\frac{2}{dr}(\partial_r f)_{0\pm} + \eta_\pm(r\Delta T)_{0\pm} \tag{C.80}$$

By taking the sum of these equations, we eliminate $\eta_\pm(\partial_r f)_{0\pm}$:

$$2\frac{\eta_+f_+ + \eta_-f_- - (\eta_+ + \eta_-)f_0}{dr^2} - (\eta_+ + \eta_-)\frac{\ell(\ell+1)}{r_0^2}f_0 = 2r_0K \tag{C.81}$$

with $K = \eta_+(\Delta T)_+ = \eta_-(\Delta T)_-$. We finally obtain the finite difference approximation of $\eta\Delta T$:

$$(\eta\Delta T)_0 = \frac{\eta_+r_+T_+ + \eta_-r_-T_- - (\eta_+ + \eta_-)r_0T_0}{r_0dr^2} - \frac{\eta_+ + \eta_-}{2}\frac{\ell(\ell+1)}{r_0^2}T_0 \tag{C.82}$$

Note that we do not have to take into account the derivative of η as in C.71, because η is constant before and after the jump.

alternate method:

Interestingly, starting from the formulation for variable conductivity C.72 we can set $F = \eta\partial_r(rT)$ which is continuous and can be approximated at the points $r_0 \pm dr/2$ by first order finite difference:

$$F(r_0 \pm dr/2) = \pm\eta_\pm\frac{r_\pm T_\pm - r_0T_0}{dr} \tag{C.83}$$

We can write the order one Taylor expansions for $F_\pm = F(r_0 \pm dr/2)$:

$$F_\pm = F_0 \pm \frac{dr}{2}(\partial_r F)_{0\pm} + ... \tag{C.84}$$

We multiply by $\pm 2/dr$ and subtract $\eta_\pm \ell(\ell+1)T_0/r_0$:

$$\pm 2\frac{F_\pm - F_0}{dr} - \eta_\pm \frac{\ell(\ell+1)}{r_0} T_0 = r_0 K \tag{C.85}$$

where $K = (1/r_0)(\partial_r F)_{0\pm} - \eta_\pm \ell(\ell+1)T_0/r_0^2$ is the diffusion operator of equation C.72 (which must be continuous because T is). By adding equations C.85, one obtains

$$2\frac{F_+ - F_-}{dr} - (\eta_+ + \eta_-)\frac{\ell(\ell+1)}{r_0} T_0 = 2r_0 K \tag{C.86}$$

and by substituting $F_\pm$ by its first order approximation C.83, we find for K:

$$K = \frac{\eta_+ r_+ T_+ + \eta_- r_- T_- - (\eta_+ + \eta_-) r_0 T_0}{r_0 dr^2} - \frac{\eta_+ + \eta_-}{2}\frac{\ell(\ell+1)}{r_0^2} T_0 \tag{C.87}$$

which is the same expression as in equation C.82. This alternate method of derivation appears less rigorous as it involves two order one Taylor expansion, instead of one order two expansion. It is however interesting as they show the coherency between continuous variation and discontinuity.

C.6 Optimization and parallelization

C.6.1 hybrid MPI/OpenMP parallelization

The following guidelines were used to implement the hybrid parallelization of XSHELLS:

Ensure Data Locality: by working shell by shell (e.g. without computing the whole spatial fields at once) we strongly reduce the memory requirement and increase the speed, because the data is more likely to be in cache memory (close to the computing core and very quick to access compared to main memory). This also implies that entire shells are distributed to MPI processes. XSHELLS can work with as many processes as radial shells.

Avoid transposition: since the different radial shells are distributed among MPI processes, operations involving coupling of radial shells require communications. The finite-difference formulation involves only local communications (with 1 or 2 nearest neighbors). Hence, instead of using the expensive `MPI_Alltoall()`, XSHELLS communicates with nearest neighbor only.

C.6.2 blocked LU-solver

The Crank-Nicolson scheme used by XSHELLS for the linear terms requires to invert a matrix or solve the system

$$Ax = b.$$

In fact, in the simple formulation where A involves only the Laplace operator, all spherical harmonics decouple and we have to solve a large number of independent systems, one for each (ℓ, m) pair:

$$A_{\ell,m} x_{\ell,m} = b_{\ell,m}$$

The straightforward way to solve this system is then to decompose $A = LU$, where L and U are respectively lower and upper triangular matrices. Then perform two cheap triangular solves, the forward substitution

$$y_{\ell,m} = L^{-1}_{\ell,m} b_{\ell,m}$$

and the backward substitution

$$x_{\ell,m} = U^{-1}_{\ell,m} y_{\ell,m}$$

which involve treating all shells sequentially.

A custom parallel LU-solver is implemented in XSHELLS for this task, which also handles the communications between processes. Instead of solving each (ℓ, m) sequentially which involves large wait times (a process must wait for previous ones to finish bofore starting to compute), XSHELLS takes advantage of the fact that all (ℓ, m) systems are independent so that we do not need to finish one before starting to solve the other. This means performing the forward substitution

$$y_{\ell,m} = L^{-1}_{\ell,m} b_{\ell,m}$$

for a small block of (ℓ, m), before passing the result to the next process which can start to compute without waiting that all (ℓ, m) are finished. Then, when all blocks are computed and transmitted, the backward substitution is done in the same way:

$$x_{\ell,m} = U^{-1}_{\ell,m} y_{\ell,m}$$

This is illustrated in Figure C.1.

There is an optimal block size. Indeed, if the block size is too large, the processes will wait idle before they can start computing. Conversely, if the block size is too small, the increasing number of communications to perform will slow down the process.

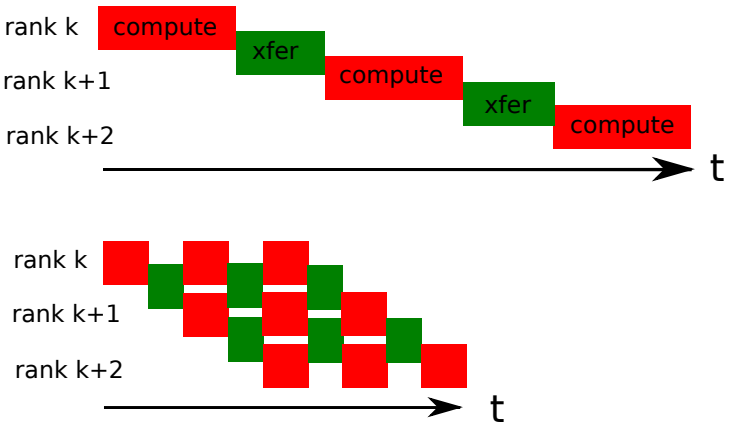

Figure C.1: Top: standard forward substitution, the processes (ranks) wait idle until the previous one has finished, leading to a low efficiency. Bottom: the blocked solver of XSHELLS reduces the wait time by solving a smaller number of systems (a block) before transmitting and solving the next block.

To find this optimal block size (which depends on the system details, the size of the problem, and the repartition of shells between processes), XSHELLS measures the performance of various block sizes at startup and chooses the best one. On an IBM Blue Gene/Q machine (Turing), this leads to a solve time divided by as much as 30.

Appendix D

A gallery of turbulent geodynamo simulations

D.1 Overview

In this appendix, we present a collection of preliminary results of geodynamo simulations at strongly-driven convection and low viscosity. The XSHELLS code (see appendix C) is used to solve equations 1.1 to 1.5. At both inner and outer boundaries, the heat flux is fixed, the velocity is zero (no-slip), and the magnetic field is matched to a potential field outside the fluid domain (insulating mantle and inner-core). The non-convective codensity profile $C_0(r)$ (see equation 1.3) is obtained using the thermochemical model of Aubert, Labrosse, and Poitou (2009), which accounts for a fraction $f_i = 0.75$ of buoyancy due to light element release at the inner-core boundary:

$$C_0(r) = \frac{a}{6} r^2 + \frac{b}{r} \tag{D.1}$$

with

$$a = -3\,\frac{1 - 2f_i}{r_o^3 - r_i^3}, \tag{D.2}$$

$$b = \frac{r_o^3 f_i - r_i^3 (1 - f_i)}{r_o^3 - r_i^3}. \tag{D.3}$$

	definition	initial	jump 1	jump 2	Earth's core
time span	$t/\mu_0\sigma D^2$	0.02	0.15	0.015	
Ek	$\nu/D^2\Omega$	10^{-5}	10^{-6}	10^{-7}	$3\,10^{-15}$
Ra	$\beta\alpha g D^4/\kappa\nu$	$6.34\,10^9$	$1.27\,10^{11}$	$2.54\,10^{12}$	10^{30} ?
Pm	$\nu\mu_0\sigma$	**0.4**	**0.2**	**0.1**	$3\,10^{-5}$
Pr	ν/κ	1	1	1	0.1 - 10
Rm	UD/η	**700**	**650**	**600**	2000
A	$\sqrt{\mu\rho}U/B$	**1.5**	**0.6**	**0.45**	0.01
Re	UD/ν	1770	3240	5960	$2\,10^8$
Ro	$U/D\Omega$	0.018	$3.2\,10^{-3}$	$6\,10^{-4}$	$3\,10^{-6}$
Le	$B/\sqrt{\mu\rho}D\Omega$	0.012	$5\,10^{-3}$	$1.3\,10^{-3}$	10^{-4}
Λ	$B^2/\eta\Omega$	5.8	5.7	1.7	1 - 10
F_ν	$D_\nu/(D_\eta + D_\nu)$	47%	24%	**17%**	?
F_η	$D_\eta/(D_\eta + D_\nu)$	53%	76%	**83%**	?
Nu		30.7	47.0	60.7	> 1
Ra/Ra_c		4800	4500	4200	> 1
N_r		224	512	1024	
L_{max}		191	479	893	
$dt.\Omega$		10^{-3}	$6.25\,10^{-3}$	10^{-2}	
time steps		$5\,10^6$	$4.8\,10^6$	10^6	
cores.hours		$3\,10^4$	$7.3\,10^5$	$1.7\,10^6$	

Table D.1: Various input and output parameters of our simulations, where D is the shell thickness, U the rms velocity and B the rms magnetic field. F_ν and F_η are the fraction of viscous and ohmic dissipation respectively. The Rayleigh number of the onset of convection Ra_c is bracketed numerically for case "initial" ($E = 10^{-5}$) and then extrapolated for jump 1 and jump 2 using the scaling $Ra_c \sim E^{-4/3}$.

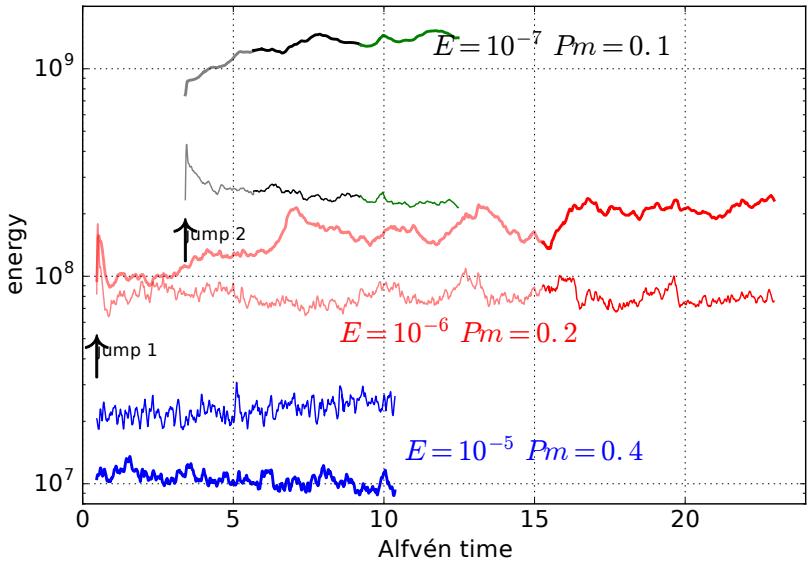

Figure D.1: Energy vs time for our 3 simulations. The time has been normalized with the Alfvén time-scale.

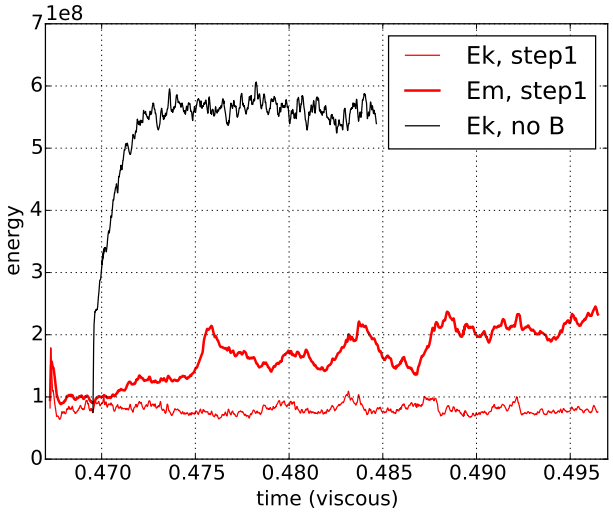

Figure D.2: Kinetic and magnetic energies as a function of time (normalized by the viscous diffusion time) for case jump 1 ($E = 10^{-6}$) and for the same parameters as jump 1, but with no magnetic field. It shows the strong influence of the magnetic field on the flow.

D.2 Instant fields

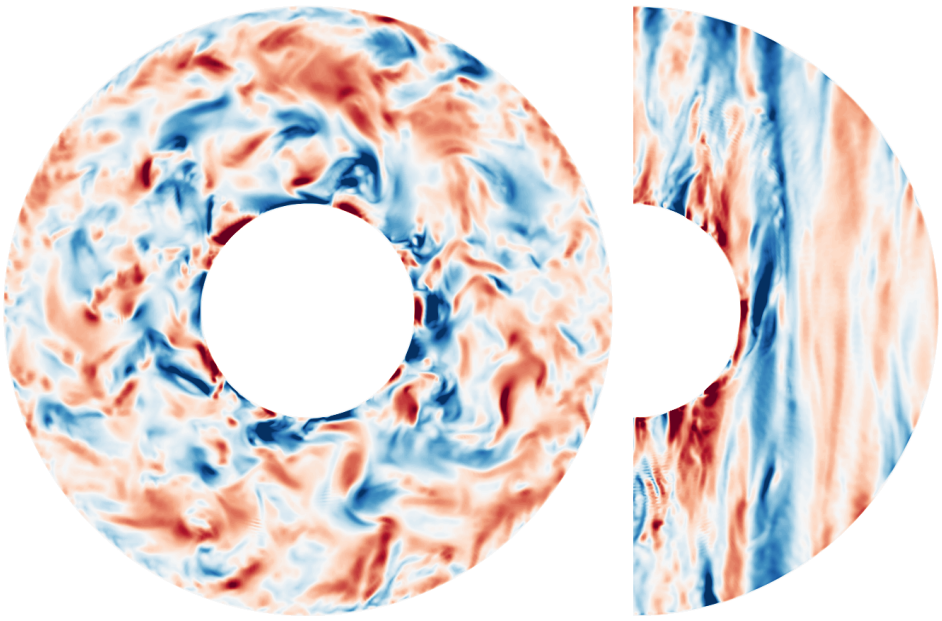

Figure D.3: Azimuthal velocity U_ϕ in equatorial (left) and meridional (right) planes, for case intial ($E = 10^{-5}$, $Pm = 0.4$, $A = 1.5$).

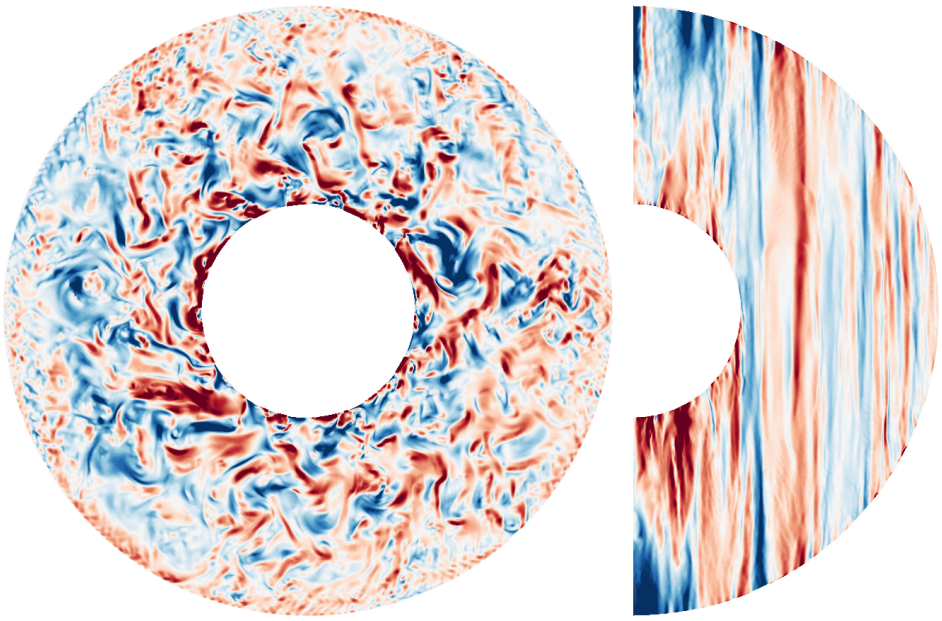

Figure D.4: Azimuthal velocity U_ϕ in equatorial (left) and meridional (right) planes, for case jump 1 ($E = 10^{-6}$, $Pm = 0.2$, $A = 0.6$).

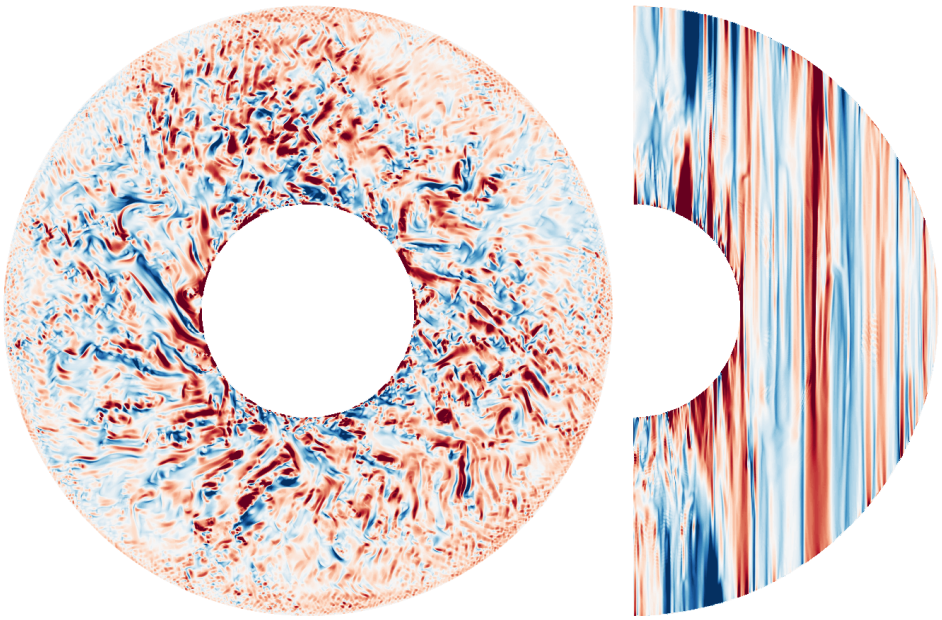

Figure D.5: Azimuthal velocity U_ϕ in equatorial (left) and meridional (right) planes, for case jump 2 ($E = 10^{-7}$, $Pm = 0.1$, $A = 0.45$).

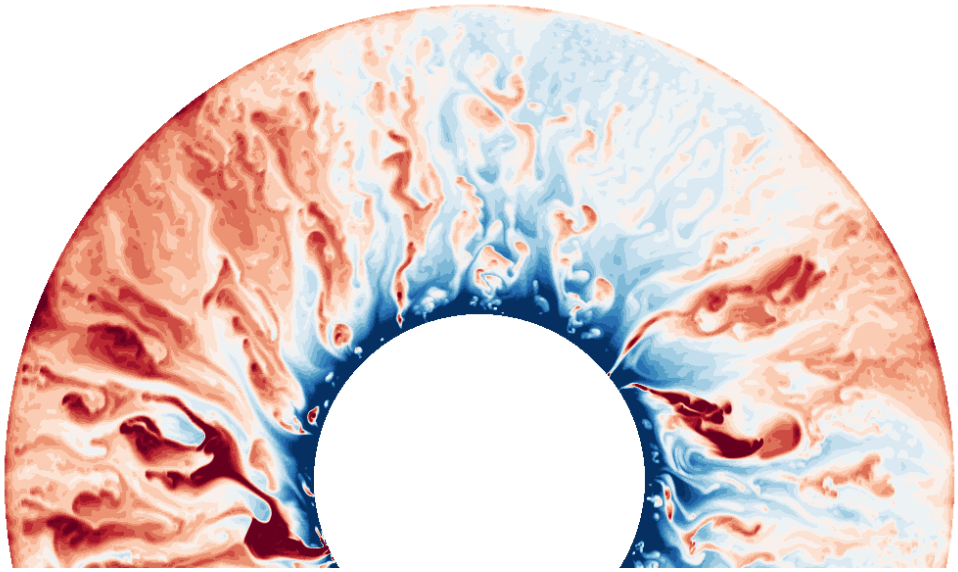

Figure D.6: Temperature field in the equatorial plane for jump 2. The mean temperature of each shell has been removed.

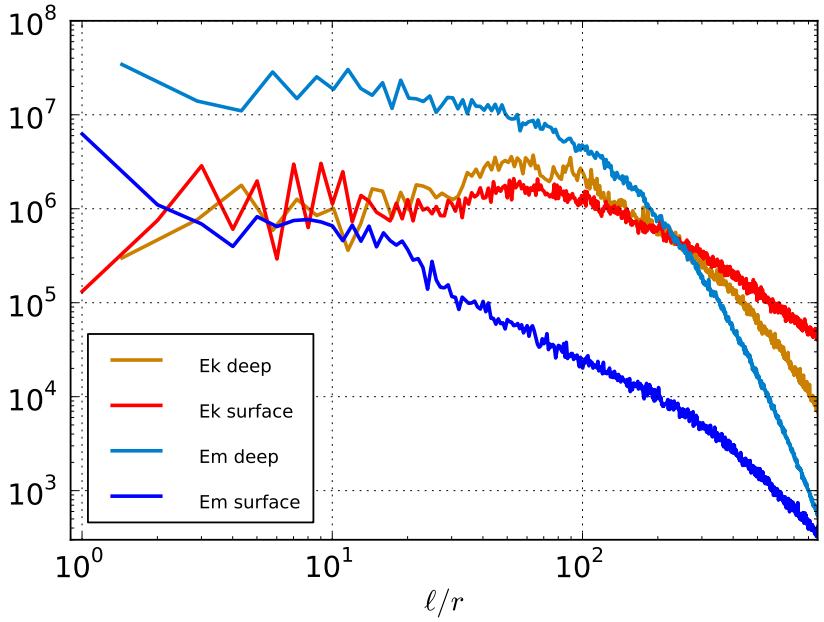

Figure D.7: Instantaneous spherical Harmonic spectra for jump 2, at two different depths. "Deep" refers to a spherical shell at mid-depth, while "surface" refers to a shell just below the Ekman boundary layer. "Ek" and "Em" refer to kinetic and magnetic energy spectra respectively.

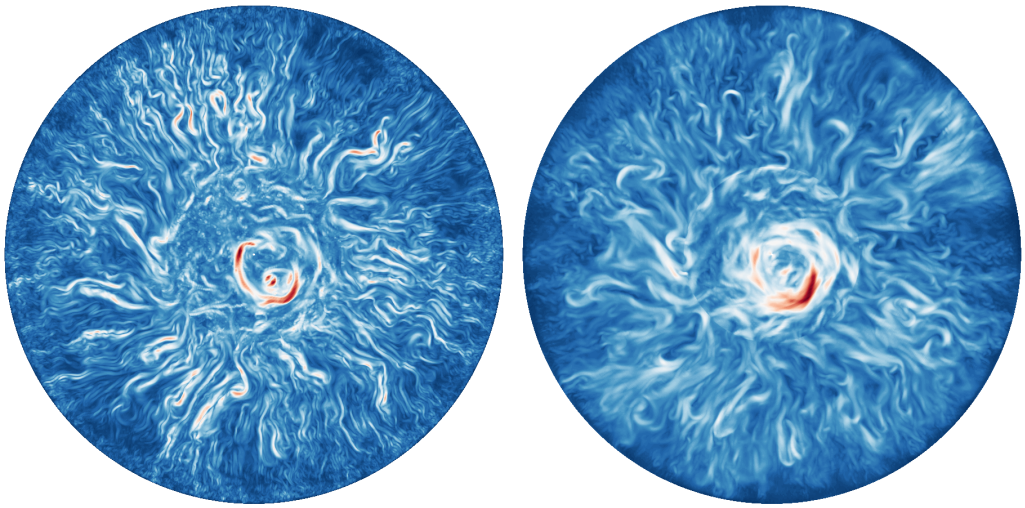

Figure D.8: Instantaneous z-averaged rms amplitude of equatorial flow (left) and magnetic field (right) for jump 2 simulation ($E = 10^{-7}, Pm = 0.1, Rm = 600, A \sim 0.45$.). The quantity showed is defined as $\left\langle F_s^2 + F_\phi^2 \right\rangle^{1/2}$, where F is the field (either u or b) and $\langle . \rangle$ denotes averaging along the z axis. Within the tangent cylinder, the average covers one hemisphere only.

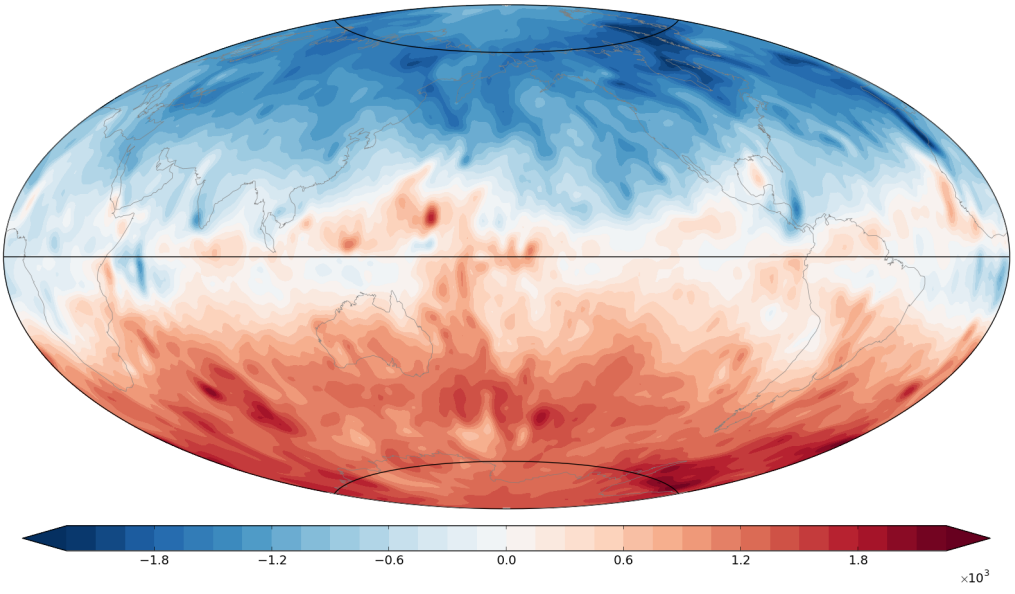

Figure D.9: Instantaneous radial magnetic field at the surface of simulation jump 1 ($E = 10^{-6}, Pm = 0.2$).

D.3 Time averaged fields

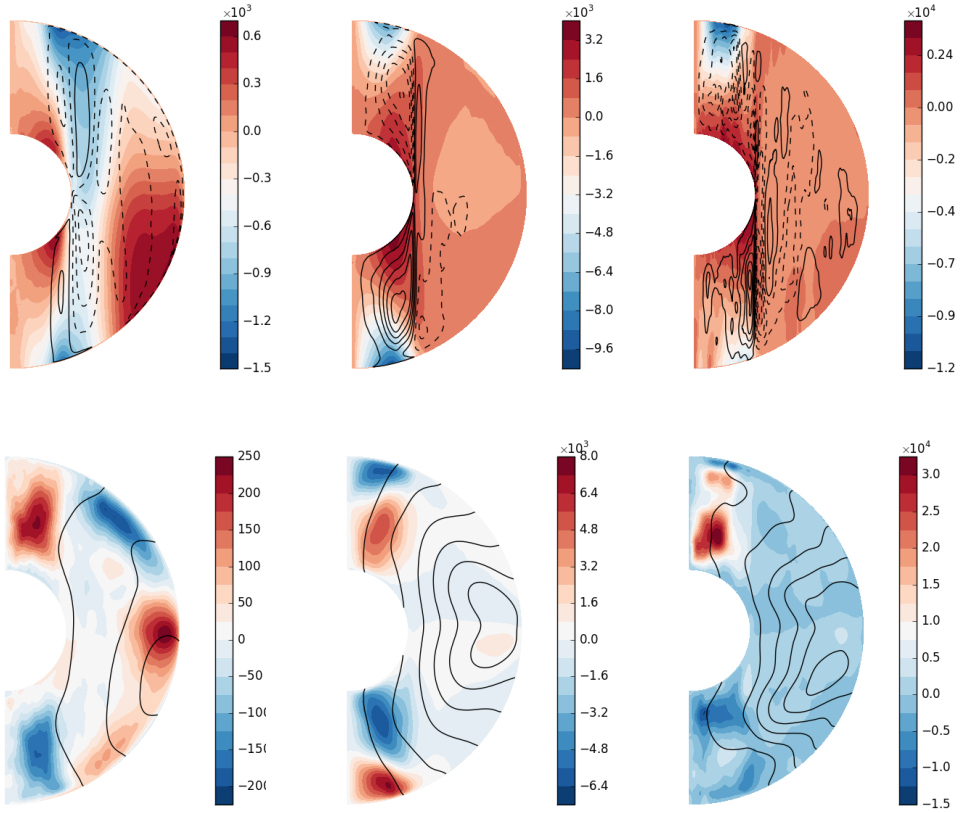

Figure D.10: Time and ϕ-averaged fields for our three simulations: initial (left), jump 1 (middle), jump 2 (right). Top line represents the averaged velocity field and bottom line the averaged magnetic field. Colors map the azimuthal components, while the meridional field-lines are materialized by black contour lines.

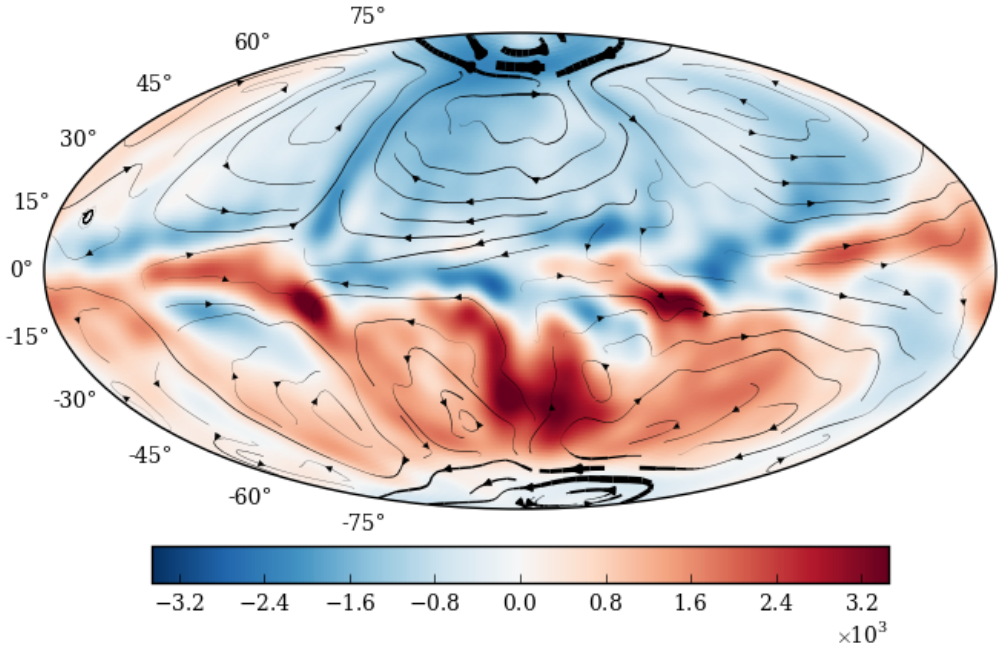

Figure D.11: Averaged fields at the top of the core for jump 2. The radial magnetic field is truncated at harmonic degree $\ell = 13$ (color map); the flow is truncated at $\ell = 26$ (streamlines). It shows the emergence of a large-scale flow.

Bibliography

Alfvén, H., (1942). "Existence of Electromagnetic-Hydrodynamic Waves". In: *Nature* 150, pp. 405–406 (cit. on pp. 9, 18).

Aubert, J., (2005). "Steady zonal flows in spherical shell dynamos". In: *Journal of Fluid Mechanics* 542, pp. 53–67 (cit. on pp. 26, 38).

Aubert, J., Finlay, C. C., Fournier, A., (2013). "Bottom-up control of geomagnetic secular variation by the Earth/'s inner core". In: *Nature* 502.7470, pp. 219–223 (cit. on pp. 5, 31).

Aubert, J., Gillet, N., Cardin, P., (2003). "Quasigeostrophic models of convection in rotating spherical shells". In: *Geochemistry, Geophysics, Geosystems* 4.7, n/a (cit. on p. 25).

Aubert, J., Labrosse, S., Poitou, C., (2009). "Modelling the palaeo-evolution of the geodynamo". In: *Geophysical Journal International* 179.3, pp. 1414–1428 (cit. on pp. 31, 39, 40, 178).

Braginsky, S. I., (1970). "Torsional magnetohydrodynamic vibrations in the Earth's core and variations in day length". In: *Geomag. Aeron.* 10, pp. 1–8 (cit. on pp. 9, 18).

Breuer, M., Manglik, A., Wicht, J., Trümper, T., Harder, H., Hansen, U., (2010). "Thermochemically driven convection in a rotating spherical shell". In: *Geophysical Journal International* 183.1, pp. 150–162 (cit. on p. 7).

Brito, D., Alboussière, T., Cardin, P., Gagniére, N., Jault, D., La Rizza, P., Masson, J.-P., Nataf, H.-C., Schmitt, D., (2011). "Zonal shear and superrotation in a magnetized spherical Couette-flow experiment". In: *Physical Review E* 83.6, Part 2 (cit. on p. 15).

Busse, F. H., (1970). "Thermal instabilities in rapidly rotating systems". In: *J. Fluid Mech.* 44, pp. 441–460 (cit. on pp. 7, 25).

— (2002). "Is low Rayleigh number convection possible in the Earth's core?" In: *Geophys. Res. Lett.* 29.7 (cit. on pp. 7, 40).

Cabanes, S., (2014). "Contributions des fluctuations turbulentes au champ magnétique induit dans une expérience en sodium liquide". PhD thesis. Université de Grenoble, France (cit. on p. 15).

Cabanes, S., **Schaeffer, N.**, Nataf, H.-C., (2014a). "Magnetic induction and diffusion mechanisms in a liquid sodium spherical Couette experiment". In: *Physical Review E* 90.4, p. 043018 (cit. on pp. 1, 15).
— (2014b). "Turbulence Reduces Magnetic Diffusivity in a Liquid Sodium Experiment". In: *Physical Review Letters* 113, p. 184501 (cit. on pp. 1, 15, 17, 41, 42).
— (2015). "Erratum: Turbulence Reduces Magnetic Diffusivity in a Liquid Sodium Experiment [Phys. Rev. Lett. 113 , 184501 (2014)]". In: *Phys. Rev. Lett.* 115.18 (cit. on p. 17).
Calkins, M. A., Aurnou, J. M., Eldredge, J. D., Julien, K., (2012). "The influence of fluid properties on the morphology of core turbulence and the geomagnetic field". In: *Earth and Planetary Science Letters* 359-360, pp. 55–60 (cit. on p. 25).
Canet, E., Finlay, C. C., Fournier, A., (2014). "Hydromagnetic quasi-geostrophic modes in rapidly rotating planetary cores". In: *Physics of the Earth and Planetary Interiors* 229, pp. 1–15 (cit. on p. 29).
Cardin, P., Olson, P., (1994). "Chaotic thermal convection in a rapidly rotating spherical shell: consequences for flow in the outer core." In: *Phys. Earth Planet. Inter.* 82 (cit. on p. 25).
Chacón, L., (2008). "An optimal, parallel, fully implicit Newton–Krylov solver for three-dimensional viscoresistive magnetohydrodynamicsa". In: *Physics of Plasmas (1994-present)* 15.5, pp. 056103+ (cit. on p. 44).
Christensen, U. R., Aubert, J., (2006). "Scaling properties of convection-driven dynamos in rotating spherical shells and application to planetary magnetic fields". In: *Geophysical Journal International* 166.1, pp. 97–114 (cit. on pp. 5, 8, 39).
Christensen, U. R., Aubert, J., Cardin, P., Dormy, E., Gibbons, S., Glatzmaier, G. A., Grote, E., Honkura, Y., Jones, C., Kono, M., Matsushima, M., Sakuraba, A., Takahashi, F., Tilgner, A., Wicht, J., Zhang, K., (2001). "A numerical dynamo benchmark". In: *Physics of The Earth and Planetary Interiors* 128.1-4, pp. 25–34 (cit. on pp. 11, 162).
Christensen, U. R., (2011). "Geodynamo models: Tools for understanding properties of Earth's magnetic field". In: *Physics of the Earth and Planetary Interiors* 187.3-4, pp. 157–169 (cit. on p. 31).
Christensen, U. R., Aubert, J., Hulot, G., (2010). "Conditions for Earth-like geodynamo models". In: *Earth and Planetary Science Letters* 296.3-4, pp. 487–496 (cit. on p. 31).
Christensen, U., Wicht, J., (2015). "8.10 - Numerical Dynamo Simulations". In: *Treatise on Geophysics (Second Edition)*. Ed. by G. Schubert. Second Edition. Oxford: Elsevier, pp. 245–277 (cit. on p. 11).

Clenshaw, C., Curtis, A., (1960). "A method for numerical integration on an automatic computer". In: *Numerische Mathematik* 2.1, pp. 197–205 (cit. on p. 12).
Davidson, P. A., (2013). "Scaling laws for planetary dynamos". In: *Geophysical Journal International* 195.1, pp. 67–74 (cit. on p. 8).
Dormy, E., (1997). "Modélisation numérique de la dynamo terrestre". PhD thesis. IPGP (cit. on p. 13).
Dormy, E., Soward, A., Jones, C., Jault, D., Cardin, P., (2004). "The onset of thermal convection in rotating spherical shells". In: *J. Fluid Mech.* 501, pp. 43–70 (cit. on pp. 7, 26).
Driscoll, J., Healy, D. M., (1994). "Computing Fourier Transforms and Convolutions on the 2-Sphere". In: *Advances in Applied Mathematics* 15.2, pp. 202–250 (cit. on p. 12).
Dziewonski, A. M., Anderson, D. L., (1981). "Preliminary reference Earth model". In: *Physics of the earth and planetary interiors* 25.4, pp. 297–356 (cit. on p. 4).
Favier, B., Grannan, A. M., Le Bars, M., Aurnou, J. M., (2015). "Generation and maintenance of bulk turbulence by libration-driven elliptical instability". In: *Physics of Fluids (1994-present)* 27.6, pp. 066601+ (cit. on p. 43).
Figueroa, A., **Schaeffer, N.**, Nataf, H. C., Schmitt, D., (2013). "Modes and instabilities in magnetized spherical Couette flow". In: *Journal of Fluid Mechanics* 716, pp. 445–469 (cit. on pp. 1, 15, 36).
Galtier, S., (2014). "Weak turbulence theory for rotating magnetohydrodynamics and planetary flows". In: *Journal of Fluid Mechanics* 757, pp. 114–154 (cit. on p. 29).
Gillet, N., Brito, D., Jault, D., Nataf, H. C., (2007a). "Experimental and numerical studies of convection in a rapidly rotating spherical shell". In: *Journal of Fluid Mechanics* 580, pp. 83–121 (cit. on p. 25).
— (2007b). "Experimental and numerical studies of magnetoconvection in a rapidly rotating spherical shell". In: *Journal of Fluid Mechanics* 580, pp. 123–143 (cit. on p. 25).
Gillet, N., Jault, D., Canet, E., Fournier, A., (2010). "Fast torsional waves and strong magnetic field within the Earth's core". In: *Nature* 465.7294, pp. 74–77 (cit. on pp. 18, 27, 29, 30).
Gillet, N., **Schaeffer, N.**, Jault, D., (2011). "Rationale and geophysical evidence for quasi-geostrophic rapid dynamics within the Earth's outer core". In: *Physics of the Earth and Planetary Interiors* (cit. on pp. 1, 9, 13, 25–30).

Glatzmaier, G., Roberts, P., (1995). "A three-dimensional self-consistent computer simulation of a geomagnetic field reversal". In: *Nature* 377 (cit. on p. 31).

Glatzmaier, G. A., Roberts, P. H., (1996). "An anelastic evolutionary geodynamo simulation driven by compositional and thermal convection". In: *Physica D: Nonlinear Phenomena* 97.1-3, pp. 81–94 (cit. on p. 40).

Greenspan, H. P., (1968). *The theory of rotating fluids*. Cambridge University Press (cit. on pp. 24, 44).

Guervilly, C., (2010). "Numerical study of planetary dynamos generated by surface shear or internal heating". Theses. Université Joseph-Fourier - Grenoble I (cit. on p. 42).

Healy Jr, D. M., Kostelec, P., Rockmore, D., (2004). "Towards safe and effective high-order Legendre transforms with applications to FFTs for the 2-sphere". In: *Advances in Computational Mathematics* 21.1-2, pp. 59–105 (cit. on p. 12).

Healy, D. M., Rockmore, D. N., Kostelec, P. J., Moore, S., (2003). "FFTs for the 2-Sphere-Improvements and Variations". In: *Journal of Fourier Analysis and Applications* 9.4, pp. 341–385 (cit. on p. 12).

Hernandez, V., Roman, J. E., Vidal, V., (2005). "SLEPc : A Scalable and Flexible Toolkit for the Solution of Eigenvalue Problems". In: *ACM Trans. Math. Software* 31.3, pp. 351–362 (cit. on p. 43).

Ivers, D., Phillips, C., (2001). "Dynamo problems in spherical and nearly spherical geometries". In: *Dynamo and Dynamics, a Mathematical Challenge*. Springer, pp. 207–215 (cit. on p. 43).

Jault, D., (2008). "Axial invariance of rapidly varying diffusionless motions in the Earth's core interior". In: *Phys. Earth Planet. Int.* 166, pp. 67–76 (cit. on pp. 9, 28–30).

Jault, D., Finlay, C., (2015). "8.09 - Waves in the Core and Mechanical Core–Mantle Interactions". In: *Treatise on Geophysics (Second Edition)*. Ed. by G. Schubert. Second Edition. Oxford: Elsevier, pp. 225–244 (cit. on p. 9).

Jault, D., Légaut, G., (2005). "Alfvén waves within the Earth's core". In: *Fluid Dynamics and Dynamos in Astrophysics and Geophysics*. Ed. by A. M. Soward, C. A. Jones, D. W. Hughes, & N. O. Weiss, pp. 277–+ (cit. on p. 9).

Jault, D., (2015). "Illuminating the electrical conductivity of the lowermost mantle from below". In: *Geophysical Journal International* 202.1, pp. 482–496 (cit. on p. 45).

Jones, C., (2015). "8.05 - Thermal and Compositional Convection in the Outer Core". In: *Treatise on Geophysics (Second Edition)*. Ed. by G. Schubert. Second Edition. Oxford: Elsevier, pp. 115–159 (cit. on p. 7).

Jones, C. A., (2011). "Planetary magnetic fields and fluid dynamos". In: *Annual Review of Fluid Mechanics* 43, pp. 583–614 (cit. on pp. 5, 9).
Jones, C. A., Soward, A. M., Mussa, A. I., (2000). "The onset of thermal convection in a rapidly rotating sphere". In: *Journal of Fluid Mechanics* 405, pp. 157–179 (cit. on p. 26).
Kageyama, A., Miyagoshi, T., Sato, T., (2008). "Formation of current coils in geodynamo simulations". In: *Nature* 454.7208, pp. 1106–1109 (cit. on p. 31).
Kopal, Z., (1980). "Clairaut coordinates and the vibrational stability of distorted stars". In: 70.2, pp. 407–424 (cit. on p. 43).
Laneuville, M., Wieczorek, M. A., Breuer, D., Aubert, J., Morard, G., Rückriemen, T., (2014). "A long-lived lunar dynamo powered by core crystallization". In: *Earth and Planetary Science Letters* 401, pp. 251–260 (cit. on p. 39).
Lesur, V., Gubbins, D., (1999). "Evaluation of fast spherical transforms for geophysical applications". In: *Geophysical Journal International* 139.2, pp. 547–555 (cit. on p. 12).
Lorenzani, S., Tilgner, A., (2001). "Fluid instabilities in precessing spheroidal cavities". In: *Journal of Fluid Mechanics* 447, pp. 111–128 (cit. on p. 43).
Lütjens, H., Luciani, J.-F., (2010). "XTOR-2F: A fully implicit Newton–Krylov solver applied to nonlinear 3D extended MHD in tokamaks". In: *Journal of Computational Physics* 229.21, pp. 8130–8143 (cit. on p. 44).
Manglik, A., Wicht, J., Christensen, U. R., (2010). "A dynamo model with double diffusive convection for Mercury's core". In: *Earth and Planetary Science Letters* 289.3-4, pp. 619–628 (cit. on p. 40).
Marti, P., **Schaeffer, N.**, Hollerbach, R., Cébron, D., Nore, C., Luddens, F., Guermond, J.-L., Aubert, J., Takehiro, S., Sasaki, Y., (2014). "Full sphere hydrodynamic and dynamo benchmarks". In: *Geophysical Journal International* 197.1, pp. 119–134 (cit. on pp. 11, 162).
Matsui, H., Heien, E. M., (2014). "A performance geodynamo benchmark". In: *AGU Fall Meeting Abstracts*, B4271 (cit. on pp. 11, 13).
Mohlenkamp, M. J., (1999). "A Fast Transform for Spherical Harmonics". In: *The Journal of Fourier Analysis and Appications* 5.2/3 (cit. on p. 12).
Monteux, J., **Schaeffer, N.**, Amit, H., Cardin, P., (2012). "Can a sinking metallic diapir generate a dynamo?" In: *Journal of Geophysical Research: Planets* 117.E10 (cit. on pp. 14, 40).
Nataf, H.-C., **Schaeffer, N.**, (2015). "8.06 - Turbulence in the Core". In: *Treatise on Geophysics (Second Edition)*. Ed. by G. Schubert. Second Edition. Oxford: Elsevier, pp. 161–181 (cit. on pp. 1, 8, 29, 31–33).

Net, M., Garcia, F., Sánchez, J., (2012). "Numerical study of the onset of thermosolutal convection in rotating spherical shells". In: *Physics of Fluids (1994-present)* 24.6, pp. 064101+ (cit. on p. 7).

Olson, P., (2015). "8.01 - Core Dynamics: An Introduction and Overview". In: *Treatise on Geophysics (Second Edition)*. Ed. by G. Schubert. Second Edition. Oxford: Elsevier, pp. 1–25 (cit. on pp. 6, 7, 29).

Olson, P., Aurnou, J., (1999). "A polar vortex in the Earth's core". In: *Nature* 402.6758, pp. 170–173 (cit. on p. 26).

Oruba, L., Dormy, E., (2014). "Predictive scaling laws for spherical rotating dynamos". In: *Geophysical Journal International* 198.2, pp. 828–847 (cit. on pp. 5, 8).

Pais, M. A., Jault, D., (2008). "Quasi-geostrophic flows responsible for the secular variation of the Earth's magnetic field". In: *Geophysical Journal International* 173.2, pp. 421–443 (cit. on p. 25).

Potts, D., Steidl, G., Tasche, M., (1998). "Fast algorithms for discrete polynomial transforms". In: *Mathematics of Computation* 67, pp. 1577–1590 (cit. on p. 12).

Rieutord, M., Espinosa Lara, F., (2013). "Ab Initio Modelling of Steady Rotating Stars". In: *Studying Stellar Rotation and Convection*. Ed. by M. Goupil, K. Belkacem, C. Neiner, F. Lignières, and J. J. Green. Vol. 865. Lecture Notes in Physics. Springer Berlin Heidelberg, pp. 49–73 (cit. on p. 43).

Rieutord, M., Zahn, J.-P., (1997). "Ekman Pumping and Tidal Dissipation in Close Binaries: A Refutation of Tassoul's Mechanism". In: *The Astrophysical Journal*, pp. 760+ (cit. on p. 44).

Roberts, P. H., (1967). *An introduction to magnetohydrodynamics*. Elsevier (cit. on p. 19).

— (1968). "On the Thermal Instability of a Rotating-Fluid Sphere Containing Heat Sources". In: *Philosophical Transactions of the Royal Society of London. Series A, Mathematical and Physical Sciences* 263.1136. roberts1968, pp. 93–117 (cit. on p. 25).

Roberts, P. H., Aurnou, J. M., (2011). "On the theory of core-mantle coupling". In: *Geophysical & Astrophysical Fluid Dynamics* 106, pp. 1–74 (cit. on p. 9).

Roberts, P. H., Glatzmaier, G. A., (2001). "The geodynamo, past, present and future". In: *Geophysical & Astrophysical Fluid Dynamics* 94.1-2, pp. 47–84 (cit. on p. 40).

Rogister, Y., Rochester, M. G., (2004). "Normal-mode theory of a rotating Earth model using a Lagrangian perturbation of a spherical model of reference". In: *Geophysical Journal International* 159.3, pp. 874–908 (cit. on p. 43).

Sakuraba, A., Roberts, P. H., (2009). "Generation of a strong magnetic field using uniform heat flux at the surface of the core". In: *Nature Geoscience* 2.11, pp. 802–805 (cit. on p. 31).

Schaeffer, N., (2013). "Efficient spherical harmonic transforms aimed at pseudospectral numerical simulations". In: *Geochemistry, Geophysics, Geosystems* 14.3, pp. 751–758 (cit. on pp. 1, 12, 50).

Schaeffer, N., Cardin, P., (2005). "Quasigeostrophic model of the instabilities of the Stewartson layer in flat and depth-varying containers". In: *Physics of Fluids* 17, p. 104111 (cit. on p. 44).

— (2006). "Quasi-geostrophic kinematic dynamos at low magnetic Prandtl number". In: *Earth and Planetary Science Letters* 245.3-4, pp. 595–604 (cit. on p. 25).

Schaeffer, N., Jault, D., Cardin, P., Drouard, M., (2012). "On the reflection of Alfvén waves and its implication for Earth's core modeling". In: *Geophysical Journal International* 191.2, pp. 508–516 (cit. on pp. 1, 18, 20, 21, 23, 24).

Schaeffer, N., Lora Silva, E., Pais, M. A., (2016). "Can Core Flows inferred from Geomagnetic Field Models explain the Earth's Dynamo?" In: *Geophysical Journal International* (cit. on pp. 1, 27, 28, 38).

Schaeffer, N., Pais, M. A., (2011). "On symmetry and anisotropy of Earth-core flows". In: *Geophysical Research Letters* 38.10 (cit. on pp. 1, 25, 26).

Schmalzl, J., Hansen, U., (2000). "A fully implicit model for simulating dynamo action in a Cartesian domain". In: *Physics of the Earth and Planetary Interiors* 120.4, pp. 339–349 (cit. on p. 44).

Schmitt, D., Alboussière, T., Brito, D., Cardin, P., Gagnière, N., Jault, D., Nataf, H.-C., (2008). "Rotating spherical Couette flow in a dipolar magnetic field : Experimental study of magneto-inertial waves". In: *J. Fluid Mech.* 604, pp. 175–197 (cit. on p. 15).

Schmitt, D., (2010). "Magneto-inertial waves in a rotating sphere". In: *Geophysical and Astrophysical Fluid Dynamics* 104.2-3, pp. 135–151 (cit. on pp. 29, 43).

Sheyko, A., (2014). "Numerical investigations of rotating MHD in a spherical shell". PhD thesis. ETH-Zürich (cit. on p. 32).

Simitev, R., Busse, F. H., (2005). "Prandtl-number dependence of convection-driven dynamos in rotating spherical fluid shells". In: *Journal of Fluid Mechanics* 532.-1, pp. 365–388 (cit. on p. 40).

Simitev, R. D., (2011). "Double-diffusive convection in a rotating cylindrical annulus with conical caps". In: *Physics of the Earth and Planetary Interiors* 186.3–4, pp. 183–190 (cit. on p. 7).

Soderlund, K. M., King, E. M., Aurnou, J. M., (2012). "The influence of magnetic fields in planetary dynamo models". In: *Earth and Planetary Science Letters* 333-334, pp. 9–20 (cit. on p. 9).
Sprague, M., Julien, K., Knobloch, E., Werne, J., (2006). "Numerical simulation of an asymptotically reduced system for rotationally constrained convection". In: *Journal of Fluid Mechanics* 551. sprague2006, pp. 141–174 (cit. on p. 25).
Sreenivasan, B., Jones, C. A., (2011). "Helicity generation and subcritical behaviour in rapidly rotating dynamos". In: *Journal of Fluid Mechanics* 688, pp. 5–30 (cit. on pp. 26–28).
Stelzer, Z., Jackson, A., (2013). "Extracting scaling laws from numerical dynamo models". In: *Geophysical Journal International* 193.3, pp. 1265–1276 (cit. on p. 8).
Suda, R., Takami, M., (2002). "A fast spherical harmonics transform algorithm". In: *Mathematics of Computation* 71.238, pp. 703–715 (cit. on p. 12).
Takahashi, F., (2014). "Double diffusive convection in the Earth's core and the morphology of the geomagnetic field". In: *Physics of the Earth and Planetary Interiors* 226, pp. 83–87 (cit. on p. 7).
Tilgner, A., (2005). "Precession driven dynamos". In: *Physics of Fluids (1994-present)* 17.3, pp. 034104+ (cit. on p. 40).
— (2015). "8.07 - Rotational Dynamics of the Core". In: *Treatise on Geophysics (Second Edition)*. Ed. by G. Schubert. Second Edition. Oxford: Elsevier, pp. 183–212 (cit. on p. 40).
Tygert, M., (2008). "Fast algorithms for spherical harmonic expansions, II". In: *Journal of Computational Physics* 227.8, pp. 4260–4279 (cit. on p. 12).
Vidal, J., **Schaeffer, N.,** (2015). "Quasi-geostrophic modes in the Earth's fluid core with an outer stably stratified layer". In: *Geophysical Journal International* 202.3, pp. 2182–2193 (cit. on p. 43).
Wang, D., Ruuth, S. J., (2008). "Variable step-size implicit-explicit linear multistep methods for time-dependent partial differential equations". In: *Journal of Computational Mathematics* 26.6, pp. 838–855 (cit. on p. 170).
Weber, R. C., Lin, P.-Y., Garnero, E. J., Williams, Q., Lognonné, P., (2011). "Seismic Detection of the Lunar Core". In: *Science* 331.6015, pp. 309–312 (cit. on p. 39).
Weiss, B. P., Tikoo, S. M., (2014). "The lunar dynamo". In: *Science* 346.6214, p. 1246753 (cit. on pp. 5, 39).
Wicht, J., (2014). "Flow instabilities in the wide-gap spherical Couette system". In: *Journal of Fluid Mechanics* 738, pp. 184–221 (cit. on p. 15).

Zhan, X., Chen, R., Cai, X. C., Zhang, K., (2014). "A fully implicit dynamo model for long-term evolution of the geomagnetic field". In: *AGU Fall Meeting Abstracts*, B4273 (cit. on p. 44).